Investigation of snow melt dynamics and boundary layer processes over a melting snow surface

PAR

Sebastian SCHLÖGL

EPFL

ÉCOLE POLYTECHNIQUE
FÉDÉRALE DE LAUSANNE

Suisse
2018

Acknowledgements

Abstract

The energy balance of a snow pack determines snow melting rates and the knowledge about the different contributions in the energy balance is an important but challenging requirement to predict e.g. meltwater runoff. In this thesis, we investigate the surface energy balance of a snow pack for a continuous and a patchy snow cover. Snow surface temperatures have been validated to assess the accuracy of the surface energy balance of a continuous snow pack for individual points. As the four radiation components contribute largest to the surface energy balance, accurate radiation measurements (typically only available for the shortwave radiation) are required for the model input. A model error (up to 5 K in snow surface temperatures) is introduced to the surface energy balance of a continuous snow pack by parametrizing the incoming longwave radiation, which is typically not measured. Turbulent heat fluxes are typically calculated in physics-based models with Monin-Obukhov bulk formulations and its parametrization contributes to model errors in the surface energy balance up to 2 K. The parametrization of the turbulent fluxes was found to be the largest error source in the case of measured incoming longwave radiation. Very stable atmospheric conditions over snow and a non-equilibrium boundary layer have a strong but very difficult to quantify influence on turbulent surface fluxes. Stability corrections were typically developed over non-snow surfaces and applied over snow in complex terrain, where several mandatory assumptions of the Monin-Obukhov bulk formulation are heavily violated. Therefore, our validation shows a much better model representation of the surface energy balance in idealized flat terrain in comparison with complex terrain. In this thesis, we develop new stability corrections over snow and assess the error of the Monin-Obukhov bulk formulation with 6 W m^{-2} and an additional error of 1-5 W m^{-2} due to state-of-the-art parametrizations of the stability correction. Additionally, the surface energy balance is sensitive to uncertainties in the physical properties of snow (e.g. snow emissivity, effective thermal conductivity of snow and the extinction coefficient of snow). The relative percentages of these parameters contributing to model errors in the surface energy balance of a snow pack are around one order of magnitude smaller than uncertainties due to the parametrization of turbulent sensible heat fluxes.

The energy balance of a snow pack significantly alters for heterogeneous land-surfaces in the late ablation period. Warm air from the bare ground can be efficiently transported over the snow patch and modifies the near-surface air temperature field. Terrestrial laser scanning measurements reveal that local snow ablation rates at the upwind edge of the snow patch are 25 % larger than further inside of the snow patch. The strong thermal contrast in surface temperatures in combination with calm wind conditions leads to the development of a stable internal boundary layer, which grows along the fetch and reduces turbulent mixing of warm air masses. Small-scale boundary layer dynamics are typically not resolved in hydrological models. Numerical simulations with the atmospheric model Advanced Regional Prediction System (ARPS) reveal a mean air temperature increase above the patchy snow cover of 2-5 K in comparison with a continuous snow cover, which could lead to an increase in daily mean snow ablation rates up to 30 %. Above-average snow ablation rates at the upwind edge of a snow patch could be resolved by the development of a temperature footprint approach. However, the effect of increasing near-surface mean air temperatures to snow ablation from lateral transport processes is small when considering an entire melting period. Uncertainties in measured precipitation, parametrized incoming longwave radiation and calculated turbulent fluxes with Monin-Obukhov bulk formulation lead to larger errors in modelled snow heights than neglecting lateral transport processes. Additionally, a coarse horizontal resolution of numerical simulations in hydrological model in Alpine terrain leads to larger model errors in the amount of SWE than neglecting small-scale boundary-layer processes. However, in regions with a large spatial variability of snow depths at the time of peak accumulation, favouring the development of many small snow patches in the later stage of the ablation period as well as in flat regions and/or regions with high wind velocities, small-scale boundary layer processes such as the advection of warm air and the development of stable internal boundary layers are more important and need to be considered in hydrological models.

Keywords

Zusammenfassung

Die Energiebilanz einer Schneedecke bestimmt Schmelzraten von Schnee, welche benötigt werden um beispielsweise den Abfluss einer Region zu bestimmen. In dieser Arbeit wurde die (Oberflächen) Energiebilanz einer kontinuierlichen und einer fleckigen Schneedecke bestimmt. Oberflächentemperaturen der Schneedecke wurden validiert um die Genauigkeit der Oberflächenenergiebilanz einer kontinuierlichen Schneedecke abzuschätzen. Da die vier Strahlungskomponenten am Meisten zur Energiebilanz einer Schneedecke beitragen, sind exakte Messungen als Modellinput erforderlich, welche in den meisten Fällen nur für die kurzwellige solare Strahlung vorhanden ist. Ein grosser Fehler von bis zu 5 K in den Oberflächentemperaturen wird durch die Parametrisierung der einfallenden langwelligen Strahlung verursacht, welche in der Regel nicht gemessen wird. Turbulente Flüsse werden in physikalisch basierten Schneemodellen mit der Monin-Obukhov Ähnlichkeitstheorie berechnet, und tragen zu Modellfehlern in Oberflächentemperaturen bis zu 2 K bei. Im Falle von gemessenen einfallender langwelliger Strahlung ist die Berechnung der turbulenten Flüsse die grösste Fehlerquelle in der Energiebilanz der Schneedecke. Eine sehr stabile Schichtung über Schnee und eine Grenzschicht im Ungleichgewicht haben einen sehr starken, und gleichzeitig schwer abzuschätzenden, Einfluss auf die Oberflächenflüsse. Stabilitätskorrekturen werden im Normalfall über schneefreien Oberflächen entwickelt und dennoch über Schneeoberflächen angewandt. Ausserdem wird die Monin-Obukhov Ähnlichkeitstheorie in komplexem Gelände benutzt, wo einige Anwendungsbedingungen nicht erfüllt werden können. Daher können physikalische Modelle die Energiebilanz in flachen, idealisierten Gebieten viel besser wiedergeben als in komplexem Gelände. In dieser Arbeit wurden Stabilitätskorrekturen über Schnee entwickelt und der Fehler in der Monin-Obukhov Ähnlichkeitstheorie mit 6 W m^{-2} bestimmt mit einem zusätzlichen Fehler von 1-5 W m^{-2} durch die Parametrisierung der Stabilitätskorrekturen. Zusätzlich ist die Energiebilanz einer kontinuierlichen Schneedecke abhängig von physikalischen Eigenschaften von Schnee wie zum Beispiel der Rauigkeitslänge von Schnee, dem Emissionsvermögen von Schnee, der thermischen Leitfähigkeit von Schnee und der Extinktion von Schnee. Die relativen Beiträge der einzelnen Parameter zu den Fehlern in der Energiebilanz der Schneedecke werden in dieser Arbeit untersucht.

Die Energiebilanz der Schneedecke ändert sich stark in der späten Ablationsphase, wenn die Schneedecke fleckig wird. Warme Luftmassen können über den Schneefleck transportiert werden und das oberflächennahe Temperaturfeld verändern. Auf der Windseite des Schneeflecks wurden mit einem terrestrischen Laserscanner 25 % höhere Ablationsraten als auf der windabgewandten Seite gemessen. Aufgrund der Warmluftadvektion entwickelt sich zudem eine interne stabile Grenzschicht die windwärts wächst. Diese kleinskaligen atmosphärischen Prozesse können in hydrologischen Modellen nicht aufgelöst werden. Numerische Simulationen mit einem atmosphärischen Modell zeigen eine Erhöhung der mittleren Lufttemperatur von 2-5 K für fleckige Schneedecken im Vergleich zu einer kontinuierlichen Schneedecke. Diese Erhöhung in der Lufttemperatur kann bis zu 30 % grössere tägliche Schmelzraten führen. Die numerischen Resultate sind stark abhängig von der mittleren Windgeschwindigkeit und werden von einem neu entwickelten „Temperatur Footprint" Ansatz bestätigt. Allerdings ist die Erhöhung der Schmelzraten durch laterale Transportprozesse klein wenn eine komplette Ablationsperiode simuliert wird. Modellfehler in gemessenem Niederschlag, Unsicherheiten in der einfallenden langwelligen Strahlung und Unsicherheiten in der Berechnung der turbulenten Flüsse sind grösser als die Vernachlässigung der lateralen Transportprozesse. Eine zu grobe horizontale Auflösung in hydrologischen Modellen führt bereits zu grösseren Fehlern in alpinen Regionen als die Vernachlässigung der atmosphärischen kleinskaligen Prozesse über Schneeflecken. In Regionen mit grosser Schneehöhenvariabilität im Hochwinter, welche eine Entwicklung von ganz kleinen Schneeflecken in der später Ablationsphase begünstigt, in flachen Regionen und in Regionen mit starken Windgeschwindigkeiten führt die Vernachlässigung von kleinskaligen atmosphärischen Prozessen wie die Advektion warmer Luft und die Entwicklung einer internen stabilen Grenzschicht zu erheblichen Fehlern in der Abschätzung der mittleren Schneeschmelze.

Contents

List of Abbreviations

ARPS	Advanced Regional Prediction System
ASL	Atmospheric surface layer
AWS	Automatic weather stations
C2SM	Center for Climate Systems Modeling
CLM	Community land model
CNF	Cumulative normalized contribution to flux measurements
CORINE	Coordination of Information on the Environment
DEM	Digital elevation model
DISCHMEX	Dischma experiment
DISKUS	Dischmatal Klimauntersuchungen
ENVIDAT	Environmental data portal
FC	Flux contribution
FOEHN	Federal office in Switzerland
GCM-RCM	Global Climate Model - Regional Climate Model
HS	Snow height
IDW	Inverse distance weighting
ILWR	Incoming longwave radiation
IMIS	Interkantonales Mess- und Informationssystem
IR	Infrared
ISWR	Incoming shortwave radiation
JIM	JULES investigation model
JULES	Joint UK land environment simulator
MOST	Monin-Obukhov similarity theory
PREVAH	Precipitation-Runoff-Evapotranspiration HRU Model
PS	Patchy snow cover
RMSE	Root mean square error
SC	Snow cover
SCF	Snow cover Fraction
SIBL	Stable internal boundary layer
SL	Snow line
SLF	WSL Institute for Snow and Avalanche Research SLF
SWE	Snow water equivalent
TLS	Terrestrial laser scanning

List of Symbols

a_1	-	Empirical coefficient of the buoyancy term in the multivariate stability correction (momentum)
a_2	-	Empirical coefficient of the shear term in the multivariate stability correction (momentum)
b_1	-	Empirical coefficient of the buoyancy term in the multivariate stability correction (scalar)
b_2	-	Empirical coefficient of the shear term in the multivariate stability correction (scalar)
B	-	Non-dimensional buoyancy term
c_p	J kg^{-1} K^{-1}	Heat capacity of the air
C_H	-	Exchange coefficient for stable conditions
g	m s^{-2}	Free fall acceleration of the Earth
H	W m^{-2}	Turbulent sensible heat flux
HS	m	Snow height
IQR		Interquartile range
k	-	von Kármán constant
L	m	Obukhov length
m_1	-	Empirical coefficient of the univariate stability correction (momentum)
m_2	-	Empirical coefficient of the univariate stability correction (scalar)
MAE		Mean absolute error
MBE		Mean bias error
Q_l	W m^{-2}	Turbulent latent heat flux
Ri	-	Gradient Richardson number
Ri_{cr}	-	Critical Richardson number
R_f	-	Flux Richardson number
S	-	Non-dimensional shear term
T_*	K	Temperature scale
TA	K	Air temperature
u_*	m s^{-1}	Friction velocity
$\bar{U}$	m s^{-1}	Mean wind velocity
w'	m s^{-1}	Fluctuation in the vertical wind velocity
x_L	m	Fetch distance
z_{0M}	m	Aerodynamic momentum roughness length
z_{0T}	m	Aerodynamic scalar roughness length
z_{ref}	m	Height of the measurement
ζ	-	Stability parameter
ψ_m	-	Stability correction for momentum

ψ_m	-	Stability correction for scalars
ρ	kg m^{-3}	Density of the air
θ'	K	Potential temperature fluctuation
θ_s	K	Potential temperature at the surface
θ_z	K	Potential temperature at the height z

Chapter 1   Introduction

1.1   Snow covered areas modify the Earth's climate, water cycle and the energy balance

Snow covers a significant fraction of the Earth's northern hemisphere (Kapnick and Delworth, 2013) and influences ecosystems (Wipf and Rixen, 2010), the Earth's energy balance (Hunt et al., 1986; Kiehl and Trenberth, 1997), permafrost (Haeberli and Beniston, 1998; Stieglitz et al., 2003), large scale atmospheric circulation (Clark and Serreze, 2000; Morinaga et al., 2003) and the economic sector in mountainous regions due to e.g. winter tourism (Abegg et al., 2007). In many locations of the Earth's land surface the snow cover remains as glaciers, ice caps or ice shields throughout the year. The largest part of snow covered areas at the northern hemisphere show a seasonal snow cover with vanishing snow cover in spring and summer and recurrent snow cover in autumn and winter. The Earth's water cycle is strongly affected by the seasonal snow cover, as a large part of the available water is stored as snow in winter and finally released as water in spring. The amount of stored water in winter is a mandatory information for practitioners in several parts of the economics as e.g. in agriculture, hydropower generation (Schaefli et al., 2007) or flood prevention (Wever et al., 2017).

The presence of snow significantly alters the surface energy balance of the Earth due to a large snow albedo, which leads to a large reflectance of the shortwave radiation. In times of a changing climate and a rapid increase in mean annual air temperatures of the Earth's surface, the assessment of the correct amount of snow on the Earth's land surface is a desirable goal to e.g. correctly assess the positive snow-albedo feedback mechanism (Déry and Brown, 2007), estimate Arctic albedo changes (Chapin III et al., 2005; Winton, 2006; Bintanja and van der Linden, 2013) or analyse changes in the winter precipitation (Feng and Hu, 2007).

Snow cover influences not only large scale mean air temperatures of the Earth's surface, but could affect small-scale regional weather patterns and strongly influences the lower atmospheric boundary layer, which typically results in a very stable stratification (Andreas, 2002). Additionally, the presence of snow could lead to e.g. a strong longwave radiative flux divergence and radiative cooling in the lower atmospheric boundary layer (Hoch et al., 2007) and cold-air pooling in complex terrain (Lareau et al., 2013) on a very small scale.

1.2   Measuring snow cover and snow ablation rates

Several different measurement techniques have been established in the last decades to measure snow ablation rates, which are distinguished in point measurements and two-dimensional measurements. Single point melt measurements have been developed in the course of the 20th century, e.g. by estimating snow melting recorded with a lysimeter at the bottom of the snow pack (Haupt, 1969). Single point measurements of the snow water equivalent (SWE), which is expressed as the product of snow height and snow density and measured by weighing a snow sample, are conducted to assess the stored water within the snow pack (Martinec and Rango, 1981).

Two-dimensional measurements of SWE are required to estimate the stored water of an entire catchment, as SWE extremely varies on a very small-scale due to different elevation, aspect or slope (Grünewald and Lehning, 2015). For this purpose, several remote sensing techniques have been launched, which provide measurements of SWE, snow height and snow ablation rates in different horizontal resolution and spatial coverage.

An accurate measurement of the snow height can be provided by terrestrial laser scanning (Prokop, 2008; Fig. 1.1 left), which allows a fine horizontal resolution and typically covers measurement areas in the order of several kilometres. Terrestrial laser scanning (TLS) is used to estimate a point cloud of the surface by sending a laser signal in a certain frequency from the laser scanner in all directions. The laser signal is reflected at the surface and the distance between the surface and the laser scanner is calculated by the travel time of the signal. Note that this technique provides only valuable results in case of no snowfall or no rain. Additionally, clouds and fog in between the scanning location and the surface lead to a signal reflection of the laser at the cloud particles and prevent valuable results. Fixed reflectors in the surroundings of the measurement area are used to convert the scanner own coordinate system into a global coordinate system. Terrestrial laser scanning provides high-resolution snow ablation rates by subtracting two consecutive measurement days. TLS measurements have not only been used to analyse snow accumulation in steep rock walls (Sommer et al., 2015; Gerber et al., 2017) or to record snow ablation rates on a very fine horizontal resolution (Grünewald et al., 2010; Egli et al., 2012; Mott et al., 2013; Schlögl et al., submitted), but have been used to measure forest structures (Watt and Donoghue, 2005), analyse rock fall events (Abellán et al, 2009) and detect avalanches (Deems et al., 2015).

Fig 1.1 Terrestrial laser scanner (left) and an eddy-covariance tower (right) at the Gletschboden area, Davos, Switzerland

Estimating snow ablation rates by recording the snow surface with unmanned aerial systems have become a valuable alternative to TLS measurements in the last years (Bühler et al., 2016) and will likely become more important in the future, as the measurement devices are very cheap and easy to maintain. The measurement technique is based on photogrammetry (Colomina and Molina, 2014) and allows a similar accuracy and horizontal resolution as TLS measurements.

SWE, snow height, and snow ablation rates could additionally be detected on larger scales with airborne laser scanning (ALS) (Schirmer et al., 2011; Vallet et al., 2011; Bühler et al., 2012; Vögeli et al., 2016). This measurement technique is very similar to the TLS measurements with the difference that the position of the laser scanner is not fixed but moving in the helicopter or airplane. Large areas could be easily covered with sufficient horizontal resolution. However, these measurements are very expensive and typically cannot be provided on a daily basis.

Two dimensional measurements of SWE, snow height or snow ablation are either limited in time (e.g. TLS measurements could not be made during precipitation events) or space (e.g. snow heights from single point measurements are not representative for an entire catchment (Grünewald and Lehning, 2015)). However, the representation of SWE for the entire catchment and snow season is a mandatory requirement for e.g. flood warning systems. As measurements could not provide sufficient spatial and temporal information of the snow pack, hydrological and snow models were developed to receive continuous information about the snow pack in time and space.

1.3 Snow cover modelling

Three different types of snow models have been established in the last decades. The very simple temperature index model (Hock, 2003) is typically dependent on the air temperature (and in the extended version on the yearly cycle of the solar radiation (Walter et al., 2005)). Temperature index models are limited in their accuracy and cannot resolve small-scale variations in snow melting due to different slope angles and aspects. Additionally, the temporal resolution of temperature index models is limited to one day, which prohibits a snow melting analysis on sub-daily scales. Further, the performance of simple temperature index models is strongly dependent on model calibrations.

Simple physics-based models, which fully solve the energy balance of a snow pack, are more accurate than simple temperature index models (Kumar et al., 2013) and do not require calibration factors. Meteorological input data (typically recorded from standard automatic weather stations) are required to solve the energy balance of a snow pack. Air temperature, relative humidity, wind velocity, precipitation and net longwave and shortwave radiation are necessary input data to describe the vertical exchange from the snow pack with the atmosphere. Simple physics-based snow models (e.g. ISNOBAL (Marks et al. 1999)) consist of one (or two) snow layers with a constant snow density.

Physics-based detailed multi-layer snow pack models as Crocus (Brun et al., 1989) or SNOWPACK (Bartelt and Lehning, 2002) are more complex than single-layer models and were developed to e.g. improve avalanche warnings. The detailed multi-layer snow model (such as SNOWPACK) is based on governing differential equations of mass, momentum and energy conservation for the

three constituent phase's ice, water and air, which are numerically solved by the finite-element method. The relevance of physics-based snow pack models significantly increased in the 1990s, as they were used for hydrological forecasting, climate modelling and numerical weather prediction.

Essery et al. (2013) analysed more than 1000 different snow pack models and found large model spreads for snow water equivalents and no clear best model, but a group of models with similar good results, a group of models with a consistently weak model performance and a group of models with a good model performance in some cases, but a weak model performance during other conditions. Essery et al. (2013) showed that the model spread is small in the accumulation period but strongly increases in the ablation period. This implies that estimating the energy balance of the snow pack does not work sufficiently in the ablation period. Hence, the energy balance of a snow pack will be analysed in this thesis for a continuous snow cover and a patchy snow cover (Fig. 1.2).

The model error of the surface energy balance of a continuous and patchy snow cover is expressed in this thesis in errors of snow surface temperatures or in those of vertical fluxes.
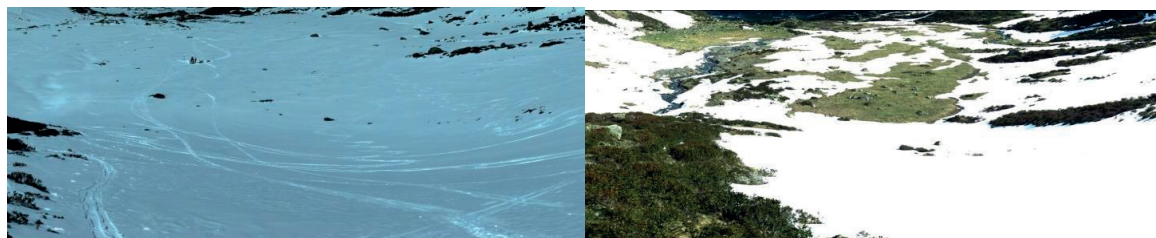
Fig 1.2 Panoramic image of the Gletschboden area, Davos, Switzerland recorded with a terrestrial laser scanner (TLS) for a continuous snow cover (left, 17.04.2014) and a patchy snow cover (right, 21.05.2014).

1.3.1 Surface energy balance of a continuous snow cover

Modelled snow ablation rates are calculated by assessing the energy balance of a snow pack. The required energy for heating and (once the melting point is reached) melting snow is dependent on net shortwave radiation, net longwave radiation, turbulent sensible and latent heat fluxes, advective heat from precipitation and blowing snow and heat exchange with the ground. The largest uncertainties in snow melt modelling are typically caused by inaccuracies in net longwave radiation and turbulent fluxes, as measurements of net shortwave radiation are typically of good quality and the contributions of advective heat from precipitation and heat exchange with the ground are small. The energy balance over snow was assessed in several publications for different surface characteristics (e.g. over an ideal flat test site in Greenland (Ohmura et al., 1994; Hoch, 2006) or in complex mountain terrain (Fierz et al., 2003)).

Incoming longwave radiation is often parametrized (Flerchinger et al., 2009) than measured and can lead to uncertainties up to 40 W m^{-2} (Schlögl et al., 2016), especially if clear-sky parameterizations instead of all-sky parametrizations are used, i.e. in case of no reliable cloud estimates. The temporal and spatial coverage of eddy-covariance measurements recorded from 3-D ultrasonic anemometer (Fig. 1.1 right) in snow covered areas is insufficient to drive physics-based snow models. Therefore, turbulent surface fluxes are typically calculated with a traditional bulk formulation (Blanc, 1987) of the Monin-Obukhov similarity theory (Obukhov, 1946). This approach accounts for the differences in temperature, specific humidity and local wind velocities of two vertical levels. One measurement level should be located at the surface and the second measurement level should be located close to the surface in order to achieve satisfactory model results for turbulent fluxes at the surface. Stability corrections are introduced in the model approach to account for the reduced turbulent exchange in stable stratification (Dyer, 1974). In this thesis, we developed new stability corrections over snow and assessed the model error due to the Monin-Obukhov bulk formulation.

1.3.2 Surface energy balance of a patchy snow cover

The energy balance of a snow pack significantly changes once the snow cover becomes patchy in the late ablation period, as small-scale boundary layer dynamics cannot be neglected for heterogeneous land-surfaces (Essery et al., 2006; Mott et al., 2013, 2015). Hence, the assumption of a constant vertical transport invalidates as soon as the snow pack becomes patchy. The advection of warm air masses from the bare ground towards the upwind edge of a snow patch modifies near-surface air temperatures. Near-surface air temperatures increase at the upwind edge of a snow patch and lead to larger snow ablation rates in comparison with an area further inside of a snow patch (Liston, 1999; Pomeroy et al., 2003). Above-average snow ablation rates at the upwind edge of a snow patch increase with increasing wind velocity, strong mechanical turbulence and increasing soil temperatures of the bare ground.

A stable internal boundary layer (SIBL) develops at the border between snow and no snow (Mahrt and Vickers, 2005; Mott et al., 2016, 2017) and grows along the fetch (Garatt, 1990; Granger et al., 2006) due to thermal differences in surface temperatures of a

heterogeneous land-surface. The formation of a SIBL favours boundary layer decoupling and could lead to smaller snow ablation rates further downwind of the snow patch. The SIBL typically develops for weak mechanical turbulence, calm wind conditions and concave topography (Mott et al., 2013).

Small-scale boundary layer dynamics over a heterogeneous land-surface are typically not resolved in hydrological models, as lateral transport processes are neglected. In current hydrological models, the energy balance of a snow pack is calculated for each pixel separately by estimating the vertical exchange between the snow and the atmosphere. Neighbouring pixels in hydrological models do not interact with each other, which would strongly modify the near-surface wind and air temperature fields.

Model parametrizations accounting for patchy snow surfaces and lateral transport processes are rare. A parametrization has been developed depending on the Weisman stability parameter (Weisman, 1977), the soil temperature of the bare ground and the fetch distance on condition that the height of the SIBL is known (Granger et al., 2002). In this thesis, we present two new approaches to account for lateral transport processes and modified near-surface air temperatures in a hydrological model.

1.4   Open research questions

The following open research questions are dealing with the model performance of the energy balance of a snow pack and are answered in this thesis:

How large is the model error in turbulent sensible heat fluxes by using Monin Obukhov similarity theory for a continuous snow cover?

How well perform well-established and newly developed stability corrections over a continuous snow cover for different atmospheric conditions?

Are turbulent sensible heat fluxes in physics-based models better represented in ideal flat terrain than in complex terrain?

How large is the model uncertainty in snow surface temperatures by using different parametrizations of the incoming longwave radiation and different stability corrections?

How large is the model uncertainty in snow surface temperatures caused by uncertainties in physical properties of the snow?

How large is the model error by neglecting lateral transport processes in a hydrological model during patchy snow covers and for an entire ablation period?

Is the temperature footprint approach able to resolve the small-scale variability in snow ablation rates during patchy snow covers?

1.5   Outline of this thesis

The thesis consists of two main parts, dealing with (1) the vertical exchange of heat, momentum and mass of a snow pack with the atmosphere for a continuous snow cover for an individual location and (2) the two-dimensional surface energy balance of a patchy snow cover in the late ablation period. Both main parts focus on the improvement of modelled snow ablation rates in the ablation period to better predict snow height, snow water equivalent and finally meltwater runoff of a catchment.

The thesis is divided into five main chapters, corresponding to two peer-reviewed, published journal articles (Chapter 2 and 6), two papers in revision (Chapter 4 and 5) and one paper in preparation (Chapter 3). A published co-authored paper (Mott et al., 2017) is included in the Appendix A.

Chapter 2: Schlögl, S., Lehning, M., Nisimura, K., Huwald, H., Cullen, N. J., and Mott, R. (2017) How do stability corrections perform in the stable boundary layer over snow? Boundary-Layer Meteorology, 165, 161–180, 2017.

The model performance of turbulent sensible heat fluxes is analysed for a stable boundary layer over snow by testing (a) the validity of Monin-Obukhov similarity theory, (b) several already published stability corrections and (c) two newly developed stability corrections. Five different test sites with different topographical and climatological characteristics were selected to compare eddy-covariance measurements with modelled surface turbulent sensible heat fluxes from the physics-based model SNOWPACK.

Chapter 3: Schlögl, S., and Lehning, M., The surface energy balance revisited: Predicting correct snow surface temperatures as influenced by meteorological input and snow properties, In Preparation.

The model performance of the surface energy balance of a continuous snow pack is estimated by validating snow surface temperatures for three different test sites. The error in the surface energy balance could be divided in (a) uncertainties of model input data due to measurement uncertainties or necessary parametrizations (e.g. turbulent fluxes and incoming longwave radiation) and (b)

uncertainties in physical properties of snow (snow emissivity, effective thermal conductivity of snow, extinction coefficient of snow).

Chapter 4*: Schlögl, S., Lehning, M., and Mott, R., Representation of horizontal transport processes in snowmelt modelling by applying a footprint approach, Submitted to Frontiers in Earth Science.*

Modelled snow ablations rates could not resolve small-scale variations in measured rates from terrestrial laser scanning, as lateral transport processes are neglected in a hydrological model. This indicates that the additional energy for melting snow in the late ablation period due to the advection of warm air from the bare ground towards the snow pack is significant. A new temperature footprint approach is introduced to calculate near-surface air temperature fields and account for lateral transport processes during patchy snow covers.

Chapter 5*: Schlögl, S., Lehning, M., and Mott, R., How are turbulent sensible heat fluxes and snow melt rates affected a changing snow cover fraction? Submitted to Frontiers in Earth Science.*

The non-hydrostatic model ARPS is used to calculate near-surface air temperature and wind velocity fields for different snow cover fractions, snow patch sizes and initial wind velocities. ARPS meteorological fields were used as input for the hydrological model Alpine3D in order to calculate snow ablation rates and the surface energy balance of a patchy snow cover.

Chapter 6*: Schlögl, S., Marty, C., Bavay, M., and Lehning, M. (2016) Sensitivity of Alpine3D modelled snow cover to modifications in DEM resolution, station coverage and meteorological input quantities, Environmental Modelling and Software,83, 387-396.*

The sensitivity of snow water equivalent to several input parameters is assessed in the hydrological model Alpine3D. The horizontal resolution of the digital elevation model, the station coverage and several meteorological input quantities (boundary layer parameters, incoming longwave radiation, precipitation undercatch, variations in the albedo and the incoming shortwave radiation) were modified.

Chapter 7 presents an overall discussion and conclusion of all different studies. Chapter 8 gives an outlook for possible future studies improving (1) the surface energy balance for continuous snow covers for an individual location and (2) the small-scale boundary layer dynamics over a heterogeneous land-surface. This Chapter covers (a) the Eddy-covariance method tool, (b) sky-view factors for an individual location, (c) a tool to automatically redistribute snow from terrain properties and wind velocities, (d) the validation of the atmospheric model ARPS during patchy snow covers, (e) the uncertainties in near-surface air temperatures of large-scale atmospheric models during patchy snow covers and (f) the use of thermocouples to validate the temperature footprint approach.

Appendix A*: Mott, R., Schlögl, S., Dirks, L., and Lehning, M. (2017) Impact of Extreme Land Surface Heterogeneity on Micrometeorology over Spring Snow Cover, Journal of Hydrometeorology, 18, 2705-2722.*

Turbulent sensible heat fluxes were recorded with eddy-covariance measurements at three different vertical levels in the ablation period for (a) a continuous snow cover, (b) a strict snow line and (c) patchy snow covers.

Chapter 2 How do stability corrections perform in the stable boundary layer over snow?

Schlögl, S.[1,2], Lehning, M.[1,2], Nisimura, K.[3], Huwald, H.[2], Cullen, N. J.[4], and Mott, R.[1]

[1] WSL-Institute for Snow and Avalanche Research SLF, Davos, Switzerland
[2] School of Architecture, Civil and Environmental Engineering, École Polytechnique Fédérale de Lausanne, Lausanne, Switzerland
[3] University of Nagoya, Graduate School of Environmental Studies, Nagoya, Japan
[4] Department of Geography, University of Otago, Dunedin, New Zealand

Abstract We assess sensible heat-flux parametrizations in stable conditions over snow surfaces by testing and developing stability correction functions for two alpine and two polar test sites. Five turbulence datasets are analysed with respect to, a) the validity of the Monin-Obukhov similarity theory, b) the model performance of well-established stability corrections, and c) the development of new univariate and multivariate stability corrections. Using a wide range of stability corrections reveals an overestimation of the turbulent sensible heat flux for high wind speeds and a generally poor performance of all investigated functions for large temperature differences between snow and the atmosphere above (> 10 K). Applying the Monin-Obukhov bulk formulation introduces a mean absolute error in the sensible heat flux of 6 W m^{-2} (compared with heat fluxes calculated directly from eddy covariance). The stability corrections produce an additional error between 1 and 5 W m^{-2}, with the smallest error for published stability corrections found for the Holtslag scheme. We confirm from previous studies that stability corrections need improvements for large temperature differences and wind speeds, where sensible heat fluxes are distinctly overestimated. Under these atmospheric conditions our newly developed stability corrections slightly improve the model performance. However, the differences between stability corrections are typically small when compared to the residual error, which stems from the Monin-Obukhov bulk formulation.

2.1 Introduction

The energy balance of a snow pack is mainly determined by net radiation and turbulent heat fluxes (Plüss and Mazzoni, 1994), the latter contributing up to 50 % of the melt energy (Föhn, 1973; Funk, 1984; Pohl et al., 2006; Mott et al., 2011), especially in regions with generally high wind speeds. Modelling turbulent heat fluxes is a challenging task because atmospheric stability often has an influence that is significant but difficult to quantify. Based on the assumption of a constant-flux layer, Monin-Obukhov similarity theory (MOST, Obukhov 1946) leads to a bulk formulation of the turbulent heat fluxes (Blanc, 1987). This technique has been deployed in almost all numerical models describing surface exchange, from climate research to the engineering of airplane wings.

Several studies (e.g. Cullen et al., 2007) investigated uncertainties in the bulk formulation and showed in general an acceptable agreement between eddy-covariance measurements and the bulk formulation over snow with some deficiencies caused by the violation of MOST assumptions:

1) For the stable boundary layer the applicability of the bulk formulation is limited to a certain range of the stability parameter ζ and the bulk Richardson number (e.g. Sharan and Kumar, 2011).
2) The bulk formulation underestimates turbulent heat fluxes if measurements are made outside of the atmospheric surface layer (ASL) (Arck and Scherer, 2002). Hence, the existence of constant fluxes is a mandatory assumption for the calculation of turbulent heat fluxes with the bulk formulation. This assumption ensures that the bulk fluxes are the same as the surface fluxes and is reasonably accurate in the ASL for near-neutral conditions ($0 < \zeta < 0.1$) (Grachev et al., 2005).
3) Stationarity and horizontal homogeneity are further mandatory assumptions in the similarity theory, investigated by several studies in the 1980s (e.g. Joffre, 1982; Högström, 1988). These assumptions are typically strongly violated for test sites in complex terrain.

For Earth science applications, choice of an atmospheric stability correction is usually required as modelled turbulent heat fluxes assuming a neutral boundary layer tend to overestimate measured heat fluxes. Many different stability corrections for momentum ψ_m and scalars ψ_s have been published during the last few decades but show variable performance over snow (Andreas, 2002). It has been noted that stability correction functions strongly depend on the chosen test site in such a way that no universal relation can be singled out as optimal (Martin and Lejeune, 1998). Most well-established stability corrections depend exclusively on the stability parameter ζ (Dyer, 1974 and references therein), with a few studies (e.g. Sorbjan, 2010, 2016) developing stability corrections based on the bulk Richardson number. One novelty of our study is the development of a parametrization assuming a two-parameter dependence on buoyancy and shear terms in a first-order statistical model. To our knowledge, this is the first presentation of a stability correction that separates the bulk Richardson number into buoyancy and shear terms.

The main objective is therefore to assess stability corrections, in particular for stable conditions over snow in an effort to improve existing heat-flux parametrization schemes. We develop stability corrections in a purely empirical way, which is a well-known approach in the literature (e.g. Vickers et al., 2015). The sensitivity of turbulent heat-flux parametrizations has been shown to be largest for wind speeds between 3 and 5 m s^{-1} (Dadic et al., 2013). Therefore, we explicitly analyse the performance of different stability corrections as a function of atmospheric conditions. The paper is organized as follows: in Section 2.2-2.4 we introduce the selected datasets, the data processing methodology and the model set-up. In Section 2.5, the results are shown and discussed with respect to, a) the applicability of MOST, b) the model performance of well-established stability corrections and c) the development of a univariate and a multivariate stability correction. Results are summarized in Section 2.6.

2.2 Turbulence and meteorological data

We used five different atmospheric turbulence datasets from four test sites, with these sites showing differences in their topographical characteristics. We chose one typical alpine test site with high topographical complexity (Weissfluhjoch, Davos, Switzerland) and three test sites consisting of one glacier site (Plaine Morte, Crans-Montana, Switzerland) and two polar sites (Greenland and Antarctica) representing a quasi-ideal site with homogeneous surface and quasi infinite fetch in all directions.

The turbulent sensible heat flux (H) was calculated using the eddy-covariance method: $H = \rho\, c_p \overline{w'\theta'}$, where ρ is the density of the air, c_p is the heat capacity of the air, w' is the fluctuation of the vertical wind speed and θ' is the virtual sonic temperature fluctuation. Note that the sonic temperature fluctuations have been converted into virtual temperature fluctuations.

Three-dimensional wind velocity and air temperature were processed using a linear detrending (Rannik and Vesala, 1999) and a planar fit approach (Massmann and Lee, 2002) to rotate the coordinate system. Air temperature, relative humidity and air pressure from weather stations were used to calculate air properties, which are required for the data processing. The weather stations are located in the immediate vicinity of the turbulence tower and are affected by the same air masses. Turbulence data were averaged to 30-min intervals, whilst changing to a 15-min time interval marginally affects the heat fluxes at the Weissfluhjoch test site (Mott et al., 2011). Note that we define a negative sensible heat flux as being directed towards the snow surface and a positive sensible heat flux as being directed upwards.

The selected datasets and corresponding test sites are summarized in Table 2.1 and briefly introduced below:

- **Weissfluhjoch 2007 (WFJ07)**: A vertical set-up of two three-dimensional ultrasonic anemometers (CSAT3, Campbell Scientific, Inc.) was used at the traditional field site Weissfluhjoch (2540 m asl.) to measure three-dimensional wind velocity and air temperature at a frequency of 20 Hz. The sensors were mounted 3 m and 5 m above the ground and provided reliable data for 50 days between 11 February 2007 and 24 April 2007. Further information on the field campaign can be found in Stössel et al. (2010) and Mott et al. (2011).
- **Weissfluhjoch 2011-13 (WFJ11)**: Three-dimensional wind velocity and air temperature were recorded at 5 m above the ground at a frequency of 10 Hz with a three-dimensional ultrasonic anemometer (CSAT3). The analysis was conducted for data obtained between February and March in the years 2011-13.
- **Plaine Morte 2007 (PM07)**: Two three-dimensional ultrasonic anemometers (CSAT3) were installed on a horizontal boom facing opposite directions (west-north-west vs. east-south-east) at 3.75 m above the ground to measure air temperature and three-dimensional wind velocity at 20 Hz. The data were collected at the almost flat field site on the Plaine Morte glacier (2750 m asl.) near Crans-Montana, Switzerland from February to April 2007. High quality meteorological data were additionally recorded and used to force the model. A detailed description about the set-up at the Plaine Morte glacier can be found in Huwald et al. (2009) and Bou-Zeid et al. (2010).
- **Greenland 2000 (GR00)**: High-frequency three-dimensional ultrasonic anemometer measurements (CSAT3) were recorded at 50 Hz at the Summit Camp (72.3 °N, 38.8 °W, 3208 m asl.) located on the northern dome of the Greenland ice sheet. Data were collected at 1 m and 2 m above the snow surface during summer in 2000 and 2001. Additionally, meteorological measurements were obtained for the post processing and used to force the model. More information about the field campaign can be found in Cullen et al. (2007, 2014).
- **Antarctica 2000 (AA00)**: A set-up of three vertical three-dimensional ultrasonic anemometers (DA-600, Kaijo Denki) were installed at Mizuho Station (70°42' S, 44°20' E, 2230 m asl.) in Eastern Antarctica at 0.2, 1 and 25 m and recorded turbulence data at a frequency of 100 Hz from October to November 2000. Longwave and shortwave radiation, relative humid-

ity, air and snow surface temperature were additionally measured and used to force the model. More information about the field campaign can be found in Nishimura and Nemoto (2005).

Area	Date	Number of days	Frequency	Level above ground
WFJ07	Feb-Apr 2007	50	20 Hz	3, 5 m
WFJ11	Feb+Mar, 2011-13	169	10 Hz	5 m
PM07	Feb-Apr 2007	37	20 Hz	3.75 m
GR00	Jun 2000-01	16	50 Hz	1, 2 m
AA00	Oct-Nov 2000	43	100 Hz	0.2, 1, 25 m

Table 2.1 Overview of the different datasets. The number of analysed days, the frequency of the sonic anemometer and the vertical level above the ground are shown.

2.3   Model

We calculated surface turbulent heat fluxes using the physically-based model SNOWPACK (Lehning et al., 2002). Meteorological data (air and snow surface temperature, relative humidity, incoming and outgoing shortwave and longwave radiation) were required to force the model and taken from weather stations or meteorological sensors close to the turbulence towers. Wind velocities were used directly from the three-dimensional ultrasonic anemometers and sensible heat fluxes calculated using Monin-Obukhov bulk formulation,

$$H = \rho \, c_p C_H \overline{U} \, \Delta\theta, \tag{2.1}$$

where $\Delta\theta = \theta_s - \theta_{z_{ref}}$ is the virtual potential temperature difference, $\theta_{z_{ref}}$ is the virtual potential temperature at the reference height, θ_s is the virtual potential temperature at the snow surface, $\overline{U}$ is the mean wind speed and C_H is the exchange coefficient for stable conditions,

$$C_H = \frac{k^2}{\left[\ln\left(\frac{z_{ref}}{z_{0M}}\right) - \psi_m(\zeta)\right]\left[\ln\left(\frac{z_{ref}}{z_{0M}}\right) - \psi_s(\zeta)\right]}, \tag{2.2}$$

where $k = 0.4$ is the von Kármán constant, $\zeta = (-k \, z_{ref} \, g \, T_*)/(\theta_s \, u_*^2)$ is the modelled stability parameter (stability parameter henceforth), $u_* = k \, \overline{U} \left(\ln(z_{ref}/z_{0M}) - \psi_m\right)^{-1}$ is the modelled friction velocity, $T_* = k(\theta_s - \theta_{z_{ref}})\left(\ln(z_{ref}/z_{0M}) - \psi_s\right)^{-1}$ is the modelled temperature scale, z_{0M} is the aerodynamic roughness length and ψ_m and ψ_s are the stability corrections for momentum and scalars. In our analysis, we used the simple approach that the roughness lengths for momentum and scalars are equal ($z_{0M} = z_{0T}$) although several studies (Andreas 1987, 2010; Smeets and van den Broeke, 2008b; Conway and Cullen, 2013) suggest $z_{0M} \gg z_{0T}$ in the case of fully rough flow in agreement with surface renewal theory. An analysis of the parametrization of the scalar roughness length z_{0T} is beyond the scope of the present study, though we note that assuming a separate scalar roughness length does not significantly improve the heat-flux parametrization (not shown).

2.4   Methods

We focus on meteorological conditions excluding the following situations:

1) Patchy snow cover: turbulent heat fluxes over a patchy snow cover are extremely variable and difficult to quantify as the advective heat transport significantly alters the boundary-layer characteristics (Essery et al., 2006; Mott et al., 2013, 2015).

2) Heavy precipitation: turbulence measurements are not reliable during heavy precipitation because snowflakes/raindrops passing through the three-dimensional ultrasonic sampling volume disturb the measurement.

3) An unstable boundary layer: unstable conditions above snow can occur, e.g. in summer over dry snow (Cullen and Steffen, 2001), but are generally rather infrequent. Herein we focus only on stability corrections for stable conditions.

The following analysis steps have been conducted for the different turbulence datasets:

2.4.1 Assessment of Monin-Obukhov validity by applying a non-parametrized ψ function

An estimation of the non-parametrized stability correction based on the measured heat-flux values was conducted. This separates the error due to the bulk formulation from that introduced through the parametrizations of the correction functions. Measured friction velocities ($u_{*,meas}$) and temperature scales ($T_{*,meas}$) from the three-dimensional ultrasonic anemometers are required to calculate non-parametrized stability correction values for momentum ψ_m and heat ψ_s,

$$\psi_m = \ln\left(\frac{z_{ref}}{z_{0M}}\right) - \frac{k\,\overline{U}}{u_{*,meas}}, \tag{2.3}$$

$$\psi_s = \ln\left(\frac{z_{ref}}{z_{0M}}\right) - \frac{k\,\Delta\theta}{T_{*,meas}}. \tag{2.4}$$

Note that changes to the measurement height z_{ref} due to a changing snow depth are taken into account.

2.4.2 Characterization of well-established stability corrections

We tested six different stability corrections (Stearns and Weidner, 1993; modified by Michlmayr et al., 2008; Holtslag and deBruin, 1988; Beljaars and Holtslag, 1991; Grachev et al., 2007 and a log-linear expression) with the SNOWPACK model and compared them against the assumption of a neutral atmosphere (see Table 2.6 in the Appendix). The six investigated stability parametrizations are exclusively dependent on the stability parameter ζ, which implies that all relevant information is found in one variable. The original Stearns and Weidner stability correction (original Stearns henceforth) for momentum recommends logarithmic and inverse tangent terms of the fourth root of ζ and differs only slightly for the stability correction for heat and was developed from measurements in Antarctica. The modified Stearns and Weidner stability correction (modified Stearns henceforth) contains the same functional form as the original stability correction of Stearns with different empirical coefficients. The original Stearns stability correction is recommended for low air temperatures (Stearns and Weidner, 1993). The stability correction of Holtslag and de Bruin (1988; Holtslag henceforth) for heat and momentum is identical and consists of linear and exponential terms with five empirical coefficients. This stability correction is recommended for very stable conditions (Andreas, 2002). The stability correction of Beljaars and Holtslag (1991; Beljaars henceforth) differs for heat and momentum. This stability correction for momentum contains the same functional form as Holtslag's stability correction with different empirical coefficients. Beljaars' stability correction for heat differs from those of Holtslag in one functional term. Holtslag's and Beljaars' stability corrections were both derived over a grass-covered surface at Cabauw, Netherlands. Grachev et al. (2007) proposed stability corrections developed from measurements in the Arctic separately for momentum and heat.

The stability correction using the simple log-linear expression is based on theoretical suggestions for weakly stable conditions (e.g. Munro, 1980) and exclusively consists of one empirical coefficient β, which varies between a value of 4 (Webb, 1970) and 7 (Large and Pond, 1982; Högström, 1988). We chose $\beta = 5$ for the stability correction for momentum and heat in our assessment, which is the coefficient used in the energy balance snow model SNOBAL (Marks and Dozier, 1992). A further variant of correction, used in the snow modelling community, e.g. in the community land model (CLM) (Zeng et al., 1998) or in the joint UK land environment simulator (JULES) investigation model (JIM) (Essery et al., 2013), distinguishes between near-neutral and stable cases. The stability corrections in the land-surface models CLM or JIM and in the energy balance snow model SNOBAL are identical for near-neutral cases and slightly differ for stable conditions. A comparison between both models indicates no significant improvement of the performance of the sensible heat fluxes in the CLM or JIM models (not shown).

We additionally separated our high quality data in sub-critical and supercritical cases according to Grachev et al. (2013) in order to account for the applicability of MOST in stable conditions. Gradient Richardson number $Ri = g\,\theta^{-1}\,(d\theta\,/\,dz)(d\overline{U}/dz)^{-2}$ and flux Richardson number $R_f = -g\,\theta^{-1}\,\overline{w'\theta'}\,u_*^{-2}\,(d\overline{U}/dz)^{-1}$ have been calculated for this purpose. Data points were separated in the turbulent part of the flow (sub-critical cases: $Ri < Ri_{cr} = 0.2$ and $R_f < R_{f,cr} = 0.2$) and the laminar part of the flow (supercritical cases: $Ri > Ri_{cr} = 0.2$ and $R_f > R_{f,cr} = 0.2$). Expressing these regimes in terms of the stability parameter, the flow is turbulent for $\zeta < 1$ and laminar for $\zeta > 1$ by assuming $\beta = 5$ (see above). Note that a hysteresis effect could lead to a turbulent flow regime until $Ri = 1$ or $\zeta = 5$, if the flow was previously turbulent. The applicability of MOST is theoretically limited to sub-critical cases.

2.4.3 Development of a simple alternative model

We developed test-site specific parametrizations and assessed a test-site independent, universal parametrization based on a randomly chosen subset of 67 % of the individual datasets (Section 2.5.3 and Section 2.5.4). The remaining 33 % of the individual datasets were used for a validation and comparison between our newly developed parametrizations and the well-established parametrizations (Section 2.5.5). The coefficients of the universal parametrization are calculated based on a combined large dataset from all experiments. Additionally, all datasets were artificially replicated to reach the size of the largest dataset (WFJ11) due to the

inhomogeneity of the size of separate datasets. This method is more robust than averaging the coefficients of the test-site-specific parametrizations.

Based on our high quality datasets we developed two alternative approaches: a) a univariate parametrization assuming a conventional linear dependence on the measured stability parameter $\zeta_{meas} = z_{ref} L^{-1}$ where $L = -u_{*,meas}^3 \, \theta / k \, g \, \overline{w' \theta'}$ is the Obukhov length, and b) a multivariate parametrization assuming a dependence on buoyancy and shear terms in a first- order statistical model. The development of both approaches was conducted for conditions in a stable atmosphere ($0 < \zeta_{meas} < 10$).

a) To avoid a large number of empirical coefficients, we decided to choose a linear functional form for the stability correction. This reduces the number of empirical coefficients to a minimum,

$$\psi_m = m_1 \, \zeta_{meas}, \tag{2.5a}$$

$$\psi_s = m_2 \, \zeta_{meas}, \tag{2.5b}$$

where m_1 and m_2 are dimensionless empirical coefficients, which are negative in the case of stable stratification.

In order to estimate the empirical coefficients, the non-parametrized ψ values (Eqs. 2.3 and 2.4) were plotted as a function of the measured stability parameter, and due to large scatter in the datasets we decided to conduct a logarithmic bin-averaging of the data. We chose logarithmic bin-averaging instead of equally-spaced bin-averaging as the frequency of near-neutral atmospheric conditions is large and decreases exponentially with increasing stability. We selected the median instead of the mean for averaging the ψ values because the median is less sensitive to outliers and leads to more robust results. Finally, the linear regression was conducted with a least-squares scheme.

Additionally, we tested polynomials of different orders to find the optimum agreement and highest regression coefficient. While the optimum agreement significantly changed between the chosen test sites, a linear regression with an offset b showed the highest correlation coefficient for most cases. However, in the following, we explicitly exclude a potential offset b because any offset would preclude recovering the asymptotic behaviour towards neutral conditions correctly. Additionally, exponential functions and other dependencies were analysed but gave inconsistent results and are therefore not discussed further.

b) The bulk Richardson number is separated into non-dimensional buoyancy $B = \Delta T / \overline{T}$ ($\overline{T}$ is the mean of the air (TA) and snow surface temperature (TSS)) and shear contributions $S = z_{ref} \, g / \overline{U}^2$. This relationship is used to conduct a second parametrization assuming a two-parameter dependence on buoyancy and shear terms in a first-order statistical model,

$$\psi_m(TA, TSS, \overline{U}) = a_1 \, B + b_1 \, S, \tag{2.6a}$$

$$\psi_s(TA, TSS, \overline{U}) = a_2 \, B + b_2 \, S, \tag{2.6b}$$

where a_1, a_2, b_1 and b_2 are the dimensionless empirical coefficients. The purpose of this test model is to simply determine whether undesirable effects due to combining shear and buoyancy into one term can be alleviated.

Statistical models of second or higher order were also evaluated, and we found no sufficient improvement of R^2, which leads to the presentation of a first-order statistical model only. We additionally tested statistical models with an offset and discuss the model performance in Section 2.5.4.

2.5 Results and Discussion

2.5.1 The uncertainty of the bulk formulation

We investigated differences between the eddy-covariance method and the bulk formulation and assessed the uncertainty occurring through application of the bulk formulation. This uncertainty in heat-flux parametrization is interpreted as the minimum error and defines the limitation of bulk formulations. The mean absolute error (MAE) due to the parametrization is on average 6 W m^{-2} (Table 2.3). The approach slightly underestimates measured sensible heat fluxes, quantitatively estimated by using the mean bias error ($MBE = 1$ W m^{-2}). A comprehensive evaluation has shown that small sensible heat fluxes (≤ 30 W m^{-2}) towards the snow surface are satisfactorily simulated with the bulk formulation, whereas larger heat fluxes are underestimated significantly (Fig. 2.1) in agreement with Guo et al. (2011).
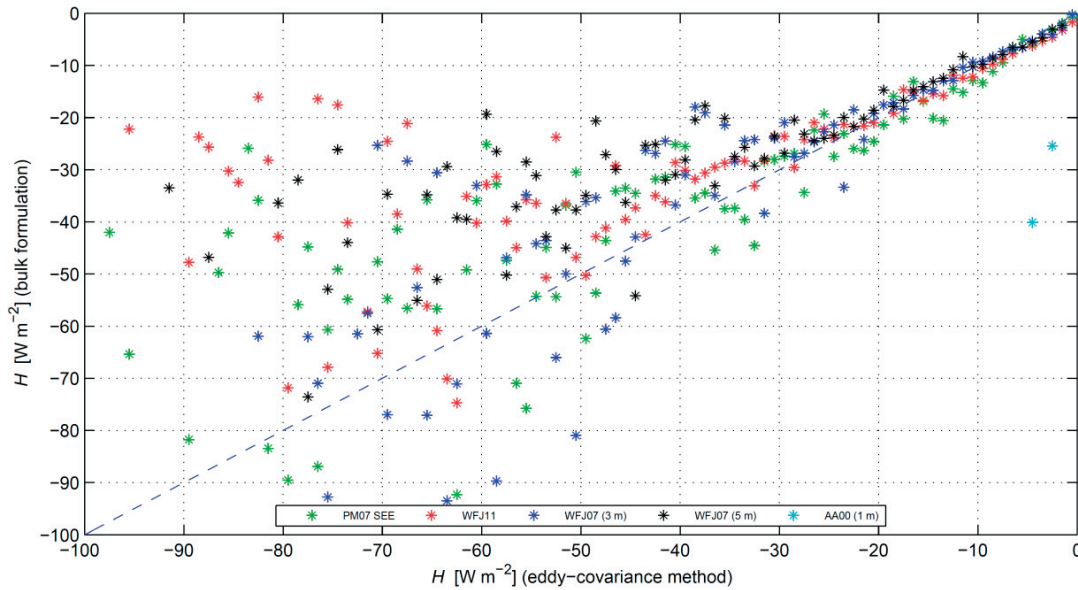
Fig 2.1 30-min sensible heat fluxes [W m^{-2}]: Measurements processed with the eddy-covariance method (*x*-axis) and model results calculated with the bulk formulation (*y*-axis) are shown for PM07 SEE (green), WFJ11 (red), WFJ07 (3 m) (blue), WFJ07 (5 m) (black) and AA00 (1 m) (cyan).

Two opposite effects explain these differences: the bulk formulation underestimates heat fluxes for large temperature differences, while on the other hand, heat fluxes are overestimated for wind speeds > 2 m s^{-1}. This observation has a strong ramification for simulating turbulent heat fluxes for the Antarctic test site, where data reveal a mean wind speed of 10 m s^{-1}. Despite near-neutral atmospheric conditions, high wind speeds lead to modelled sensible heat fluxes up to 100 W m^{-2}. In contrast, results from the eddy-covariance method show only small sensible heat fluxes up to 10 W m^{-2}. An uncertainty in the snow surface temperature of 1 K actually results in a modelled sensible heat flux uncertainty of up to 50 W m^{-2} for the meteorological conditions in Antarctica, and this uncertainty distinctly decreases with decreasing wind speeds and increasing temperature difference. We recommend careful attention when analysing turbulent sensible heat fluxes in the presence of high wind speeds and small temperature differences. Because of the high sensitivity to the snow surface temperatures for conditions found in Antarctica, we decided to develop the stability corrections without using the Antarctica dataset.

In summary, uncertainties in the bulk formulation may be due to the violation of the necessary assumptions for using MOST. For example, our investigations show that the assumption of a constant-flux layer (difference of sensible heat fluxes of two different vertical measurement level is smaller than 10 %, see Stull, 1988) is only valid 23 % of the time for the GR00 dataset and only 10 % of the time at the Weissfluhjoch test site by comparing measured turbulent sensible heat fluxes at two vertical levels. The MOST assumption of an ideal test site with a quasi-infinite fetch in all directions is only fulfilled for the Greenland test site, and for test sites in complex terrain mean absolute errors are distinctly larger than for Greenland.

2.5.2 Evaluation of well-established stability corrections

Applying different stability corrections clearly affects the absolute values of the sensible heat flux. The resulting MAE values (Table 2.2) show the optimum model performance of the sensible heat flux for the Holtslag, Beljaars and original Stearns stability corrections (MAE: 7 W m^{-2}), followed by the log-linear assumption (MAE: 8 W m^{-2}), Grachev et al. (2007) (MAE: 11 W m^{-2}) and the modified correction of Stearns (MAE: 11 W m^{-2}). It is remarkable that the simple log-linear stability correction performs better than the modified correction of Stearns. The assumption of a neutral boundary layer shows the largest MAE values (MAE: 22 W m^{-2}) and should not be used when modelling turbulent sensible heat fluxes in stable conditions. These findings are in agreement with e.g. Dadic et al. (2013). Note that for the WFJ11 and the GR00 (2 m) datasets some stability corrections provide even better results than the non-parametrized ψ function (Section 2.5.1), which could be interpreted as error compensation.

Additionally, the mean bias error (MBE) is calculated to indicate a systematic model error by applying different stability corrections (Table 2.2). Modified Stearns and the neutral boundary layer overestimate the turbulent sensible heat flux, whereas the Holtslag, Beljaars and Grachev stability corrections, the original Stearns stability correction, and the log-linear approach tend to underestimate the heat fluxes.

The results of the MAE values are consistent for the individual test sites with a highly variable magnitude of MAE values depending on the test site. The larger MAE in the PM07 dataset may be the result of katabatic flows, which may lead to a larger deviation from idealized conditions.

Area	Non-parametrized ψ	Holtslag	Beljaars	Grachev	Log-linear	Original Stearns	Modified Stearns	Neutral	Uni	Multi (with offset)
WFJ07 (3 m)	5.2	6.2	6.4	15.9	7.1	7.0	9.5	14.9	7.2	5.7 (5.9)
WFJ07 (5 m)	4.8	6.3	6.4	9.6	8.1	6.6	7.8	12.1	6.1	6.7 (5.9)
WFJ11	7.3	6.7	6.8	12.9	8.4	8.0	9.7	55.3	7.2	5.7 (6.9)
PM07 SEE	9.1	10.8	10.7	10.6	11.5	10.2	15.6	24.6	12.4	9.5 (10.6)
PM07 NWW	8.1	12.2	12.0	11.2	11.9	10.7	21.4	28.6	14.2	9.5 (11.1)
GR00 (1 m)	3.7	4.1	4.2	10.4	3.7	4.1	5.8	10.6	5.7	3.6 (6.4)
GR00 (2 m)	5.1	3.6	3.7	9.5	3.1	4.3	7.4	10.1	5.5	3.8 (7.1)
AA00 (1 m)	92.8	101.0	101.5	103.2	101.1	67.0	128.3	101.2	101.1	60.2 (120.2)
WFJ07 (3 m)	0.3	2.3	2.3	4.8	4.0	2.6	−0.7	−10.9	0.2	5.2 (1.3)
WFJ07 (5 m)	1.6	5.9	6.0	1.4	7.8	5.3	2.1	−7.6	3.4	6.5 (3.2)
WFJ11	3.3	4.3	4.3	8.3	6.7	−0.6	−2.5	−52.9	2.5	4.2 (0.8)
PM07 SEE	2.7	1.9	1.8	2.8	3.2	1.5	−5.1	−20.3	−1.2	7.7 (2.8)
PM07 NWW	3.7	−3.5	−3.4	0.1	−2.0	−0.6	−14.4	−24.1	−7.2	7.4 (0.1)
GR00 (1 m)	1.0	−0.3	0.1	−2.0	0.3	−0.1	−1.8	−3.4	−1.1	0.9 (−2.5)
GR00 (2 m)	1.0	−0.7	−0.4	−3.5	0.4	−0.8	−3.0	−3.7	−2.0	0.3 (−3.5)
AA00 (1 m)	−32.6	−36.5	−35.6	−35.0	−36.5	−39.7	0.3	−36.7	−36.4	−34.1 (−40.2)

Table 2.2 Mean absolute error (MAE) in [W m^{-2}] (upper table) and mean bias error (MBE) in [W m^{-2}] (lower table) for seven different datasets and ten approaches for stability corrections. Negative MBE values indicate an overestimation of the sensible heat flux towards the snow surface.

The performance of sensible heat-flux parametrizations strongly depends on atmospheric conditions. Therefore, as an example we investigated the quality of model results as a function of the air temperature TA, the temperature difference ΔT, the wind speed $\overline{U}$ and the stability parameter ζ, shown for the stability correction of Holtslag (Fig. 2.2) but also valid for the other investigated stability corrections.

The performance of sensible heat-flux parametrizations is not distinctly dependent on air temperature but decreases with an increase in wind speed and temperature difference as discussed above. Stability corrections perform reasonably well for a small temperature difference. In other words, stability corrections need improvements in very stable conditions and perform satisfactorily in near-neutral conditions where only a small correction is required.
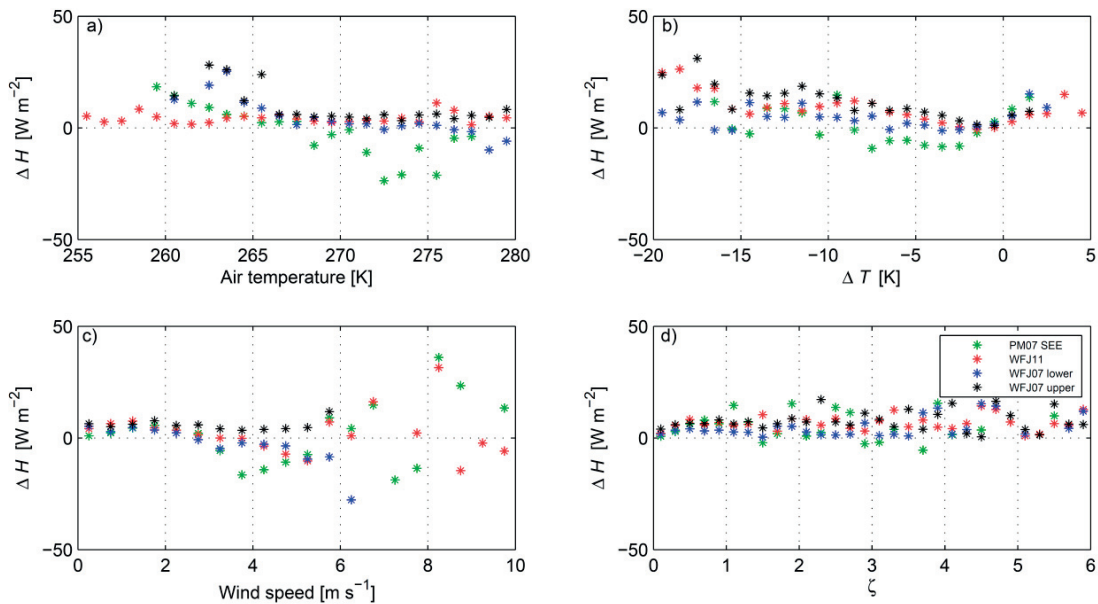
Fig 2.2 Differences between modelled (Holtslag) and measured sensible heat flux [W m^{-2}]. The differences are shown as functions of air temperature TA, temperature difference ΔT, wind speed $\bar{U}$ and stability parameter ζ. The test sites WFJ11 (red), WFJ07 lower (blue), WFJ07 upper (black) and PM07 SEE (green) were selected for the visualization.

Depending on the chosen test site, 50-70 % of the data consist of sub-critical cases. Sensible heat fluxes are modelled more accurately for the sub-critical cases shown for the WFJ11 dataset (Table 2.3); MAE values decrease by 2 W m^{-2} on average when considering only sub-critical cases. Additionally we found an improvement in MBE values. The improved representation of sensible heat fluxes in the sub-critical cases is caused by the fact that MOST is only applicable in this range and the trivial fact that sensible heat fluxes are on average larger in the supercritical cases, which causes in general larger absolute errors. However, we note that in model applications, e.g. model simulations of the seasonal snow cover, the supercritical cases need to be covered, too. Since to our knowledge no generally accepted or widely used alternative exists to simply extending the MOST parametrization, the values as presented in Table 2.2 are of practical validity.

MAE	Sub-critical	Supercritical	All
Modified Stearns	8.2	11.3	9.7
Original Stearns	6.1	10.0	8.0
Holtslag	6.2	7.0	6.7
Log-linear	7.4	9.1	8.4
Neutral	37.4	70.4	55.3

MBE	Sub-critical	Supercritical	All
Modified Stearns	−2.0	−2.8	−2.5
Original Stearns	0.4	−2.3	−0.6
Holtslag	2.9	5.0	4.3
Log-linear	4.8	7.7	6.7
Neutral	−35.2	−68.0	−52.9

Table 2.3 Mean absolute error (MAE) in [W m^{-2}] (upper table) and mean bias error (MBE) in [W m^{-2}] (lower table) for the WFJ11 dataset and five approaches for stability corrections. Negative MBE values indicate an overestimation of the sensible heat flux towards the snow surface. Data were separated in sub-critical cases, supercritical cases and all cases (same values as Table 2.2).

2.5.3 Parametrization for a stability correction based on the measured stability parameter (univariate parametrization)

To test how far the functional forms of established stability corrections provide extra value to our datasets, we developed a simple linear regression of the correction function with the measured stability parameter as an independent variable. As a first step, correction functions have been developed for the individual sites; coefficients of the parametrization strongly depend on the chosen test site and show a large spread in magnitude (Fig. 2.3).
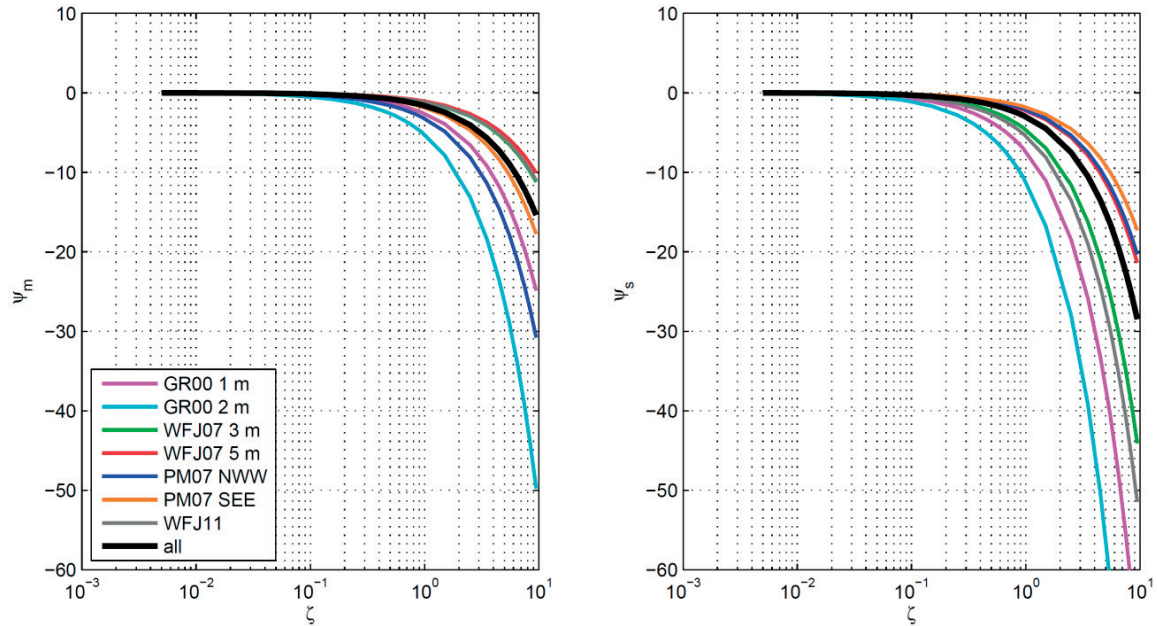
Fig 2.3 Stability correction functions ψ_m and ψ_s as a function of the measured stability parameter ζ for the different test sites separately and the universal parametrization (black line).

The largest stability correction for momentum was found for the GR00 (2 m) dataset ($m_1 = -5.24$), whereas the lowest correction is required for the WFJ07 (5 m) dataset ($m_1 = -1.06$). The spread for the test-site-specific stability corrections for scalars is larger and shows again the largest stability corrections for the Greenland test site and the lowest stability corrections for Weissfluhjoch. Hence, the stability correction for the quasi-ideal test site Greenland is large and decreases with increasing complexity of the topography. These findings need to be tested for more stations of different complexity to confirm this result.

The substantial dependence upon the test site has already been observed by Martin and Lejeune (1998) and is clearly confirmed herein. However, it is desirable to find a universal stability correction for terrain of different complexity covered in snow. As described in Section 2.4.3, we therefore also derived an overall model, and for the universal parametrization we estimated $m_1 = -1.63$ and $m_2 = -2.96$.

MAE values of this universal univariate parametrization, solely dependent on the stability parameter, amount on average to 7 W m^{-2}. This MAE value is split into a 6 W m^{-2} uncertainty due to the bulk formulation and additionally 1 W m^{-2} uncertainty by applying the parametrization. One exception holds for the Greenland ice sheet, and for this test site, the univariate parametrization performs better than the non-parametrized ψ values. In general, the univariate parametrization shows a systematic bias of 2 W m^{-2}. Compared with the well-established stability corrections we improved the model performance for moderate wind speeds (2-5 m s^{-1}) (Fig. 2.4).
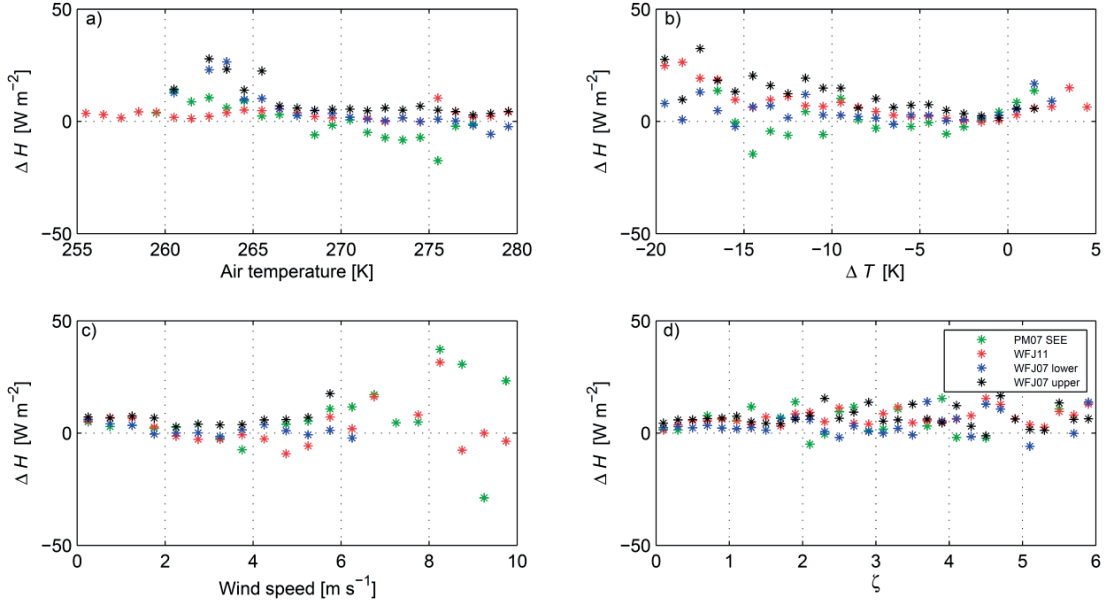
Fig 2.4 Differences between modelled and measured sensible heat flux [W m^{-2}] for the univariate parametrization. The differences are shown as functions of air temperature, temperature difference, wind speed and stability parameter. WFJ11 (red), WFJ07 lower (blue), WFJ07 upper (black) and PM07 SEE (green) were selected for the visualization.

2.5.4 Parametrization of the stability correction based on buoyancy and shear terms separately (multivariate parametrization)

The stability parameter represents the balance between buoyancy and shear term as a simple ratio, having both desirable properties but also mathematical problems for low wind speeds. We therefore test an independent treatment of buoyancy and shear terms in a linear model as a stability correction (Eqs. 2.6a, 2.6b). The MAE values of the universal parametrization for this approach are on average 7 W m^{-2}, with the multivariate parametrization having a systematic bias of 4 W m^{-2}. In summary the multivariate parametrization performs slightly worse than the univariate parametrization, confirming that the combination of buoyancy and shear terms is an acceptable choice.

Coefficients of the multivariate parametrization vary by one order of magnitude for the different test sites and are therefore shown to be highly sensitive to test-site-specific settings (Table 2.4).

test site	a_1	b_1	test site	a_2	b_2
WFJ07 (3 m)	3.227	0.0043	WFJ07 (3 m)	−982.90	−0.0005
WFJ07 (5 m)	−4.441	0.0025	WFJ07 (5 m)	−642.51	0.0009
WFJ11	−30.74	0.0008	WFJ11	−1135.4	−0.0015
PM07 NWW	−191.93	0.0008	PM07 NWW	−751.73	−0.0005
PM07 SEE	−29.55	0.0090	PM07 SEE	−692.74	−0.0123
GR00 (1 m)	−145.41	−0.0914	GR00 (1 m)	−378.92	−2.0489
GR00 (2 m)	−179.56	−0.0369	GR00 (2 m)	−243.93	−0.7448
Universal	−65.35	0.0017	Universal	−813.21	−0.0014

Table 2.4 Dimensionless empirical coefficients of the multivariate parametrization for ψ_m (left) and ψ_s (right) for different test sites.

The multivariate parametrization still tends to underestimate measured sensible heat fluxes, especially for large temperature differences and high wind speeds. However in terms of MAE, the universal multivariate parametrization performs better than all investigated stability corrections, especially for high wind speeds. A second advantage of the multivariate parametrization is related to the number of model uncertainties.

Physically-based models usually calculate the stability parameter for MOST in order to determine surface turbulent heat fluxes, and investigations have shown a large discrepancy between modelled and measured stability parameters. The modelled stability parameter tends to have larger values especially for low wind speeds and large temperature differences (not shown). These uncertainties directly affect stability corrections and hence modelled surface fluxes, where we found up to 20 W m^{-2} smaller sensible heat

fluxes by using the modelled stability parameter instead of the measured stability parameter. The approach of the multivariate stability correction is independent of the stability parameter and eliminates the uncertainty in the modelled stability parameter. Related to this aspect, we recommend the application of a multivariate stability correction on the condition that high quality meteorological variables are also recorded.

Including an offset c_1 and c_2 (in Eq. 2.6a and Eq. 2.6b) lowers the systematic bias of 4.6 W m^{-2} to 0.3 W m^{-2} and leads to a much better representation of the sensible heat fluxes. Investigations have shown that the offset for the stability correction of momentum is almost zero ($c_1 = -0.69$), but for the stability correction of heat we found an offset $c_2 = 6.73$. This offset can be interpreted as the offset $\ln(z_{ref}/z_0)$ in Eq. 2.4, which is valid for neutral conditions with no temperature difference. Results of the multivariate stability correction with offset are shown in Tables 2.2 and 2.5 in brackets.

2.5.5 Validation

In order to compare our newly developed parametrizations with well-established stability corrections, we used the remaining one-third of the datasets (not used for the parametrization development) for validation. Since the performances of stability corrections were shown to be highly sensitive to the chosen test site, we analyse the average MAE and MBE values of all datasets for the model performance test, considering a large range of air temperatures, temperature differences and wind speeds (Table 2.5).

Stability correction	MAE	MBE
Holtslag	7.0	1.5
Beljaars	7.2	1.5
Grachev	11.4	1.7
Modified Stearns	10.9	−3.6
Original Stearns	7.1	1.1
Log-linear	7.6	3.0
Neutral	21.9	−17.5
Univariate	6.7	2.0
Multivariate	6.4	4.6
(with offset)	(7.7)	(0.3)

Table 2.5 MAE [W m^{-2}] and MBE [W m^{-2}] averaged over the five different datasets for six well-established stability corrections, the assumption of a neutral boundary layer and the newly developed parametrizations.

The consideration of both errors (MAE and MBE) is required to allow a comprehensive analysis of the performance of the parametrizations. Stability corrections due to Holtslag, Beljaars, original Stearns, log-linear and our two newly developed parametrizations have a similar MAE value of 7 W m^{-2} on average and slightly underestimate the turbulent heat fluxes. The modified Stearns parametrization and the neutral boundary layer overestimate the heat fluxes at the measurement height. Note that modified Stearns was introduced by Michlmayr et al. (2008) in order to allow a more accurate simulation of snow-surface dynamics, in particular snow-surface temperature. Further investigations are required to assess how far near-surface flux divergence versus snow-model inaccuracies are responsible for surface temperatures being better simulated with modified Stearns but local heat fluxes at the measurement height are not more accurate. The multivariate stability correction with offset (shown in brackets) shows almost no systematic bias.

Additionally, spatial cross validations have been conducted for all datasets by using the test-site-specific parametrizations and the universal parametrization. As expected, the smallest MAE value averaged over the five different datasets was found for the test-site-specific parametrizations, which correspond to the related test sites. The test-site-specific parametrizations, developed from other test sites, provide similarly reliable results. The MAE value is merely increased by 1 W m^{-2} using parametrizations of other test sites, and the universal parametrization performs slightly better than the parametrizations of other test sites, but worse than the parametrizations of the same test site. In terms of MBE values we analysed the lowest systematical bias for the test-site-specific parametrizations, which correspond to the related test sites and a 1 W m^{-2} larger systematical bias for the universal parametrization and the test-site-specific parametrizations from other test sites.

Analysing seasonal dependencies, we investigated temporal cross validations for the WFJ11 dataset for March 2012. For this experiment, coefficients for the parametrizations were developed based on monthly subsets of the entire WFJ11 dataset. In general, we analysed no seasonal dependence and a similar MAE value with a difference of less than 1 W m^{-2} for parametrizations developed for different months.

Results from the spatial and temporal cross validations hold for the univariate and multivariate parametrizations and reveal that the choice of a test-site-specific parametrization is not crucial for the performance of heat-flux parametrizations. Finally, these results show the robustness of the developed stability corrections that are applicable for snow-covered terrain. Further it legitimises the creation of a universal parametrization developed from all five datasets.

2.5.6   Model performance as a function of meteorological conditions

We compare the performance of the nine different stability corrections against a range of typical atmospheric conditions for the WFJ11 validation dataset (Fig. 2.5), with results similarly found for the other datasets. Note that for this analysis the two universal parametrizations (univariate and multivariate) are used in order to compare the model performance with the well-established stability corrections.
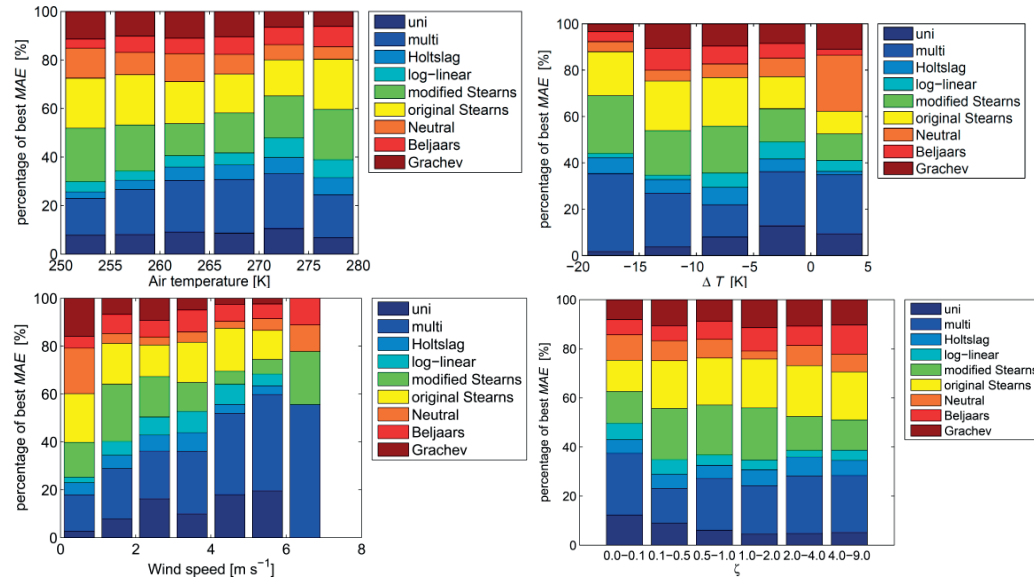
Fig 2.5 Frequency in [%] of the smallest MAE value depending on the air temperature (upper left), temperature difference (upper right), wind speed (lower left) and stability parameter (lower right) for the WFJ11 dataset.

- Air temperature: the model performance for different approaches for heat-flux parametrizations is generally robust to air temperatures. Modified Stearns provides acceptable heat-flux parametrizations for very low temperatures, whereas Holtslag provides better results for temperatures above 260 K. The univariate and multivariate parametrizations perform adequately in almost the whole range of air temperatures.
- Temperature difference: while original Stearns shows the optimum model performance for large temperature differences, the univariate parametrization has the optimum heat-flux estimates for low temperature differences. The newly developed multivariate parametrization is an acceptable alternative to original Stearns for large temperature differences.
- Wind speed: the univariate parametrization shows the largest percentage of optimum MAE values for moderate wind speeds (2-5 m s^{-1}) and the performance of the multivariate parametrization is optimum for wind speeds > 5 m s^{-1}.
- Stability parameter: the univariate parametrization performs optimum for near-neutral and weakly stable conditions. The results of the multivariate parametrization clearly improve in more stable conditions compared to the other approaches.

2.6   Conclusion

We tested existing and newly developed parametrizations to correct for atmospheric stability over snow, with turbulent heat-flux parametrizations improved by using two different approaches for a stability correction. We partitioned the error into a contribution from the bulk formulation and the model performance of the stability correction itself. We compared well-established stability corrections with two new stability corrections over snow and summarize the major findings as follows:

- Uncertainty in the bulk formulation: investigations have shown a modelled MAE value of 6 W m^{-2} using non-parametrized ψ values. This MAE value corresponds to the accuracy of the bulk formulation itself and has to be tolerated in current physically-based models. In particular, large sensible heat fluxes contribute to the error because they are significantly underestimated in the model.
- Validation of well-established stability corrections: the optimum heat-flux parametrizations are those of Holtslag and deBruin (1988) and Beljaars and Holtslag (1991) (MAE: 7 W m^{-2}), followed by the simple log-linear approach (MAE: 8 W m^{-2}), the stability correction of Grachev et al. (2007) and the stability correction of Stearns and Weidner (1993) (modified by Michlmayr et al., 2008) (MAE: 11 W m^{-2}). A neutral boundary layer strongly overestimates heat fluxes towards the snow surface (MAE: 22 W m^{-2}). All investigated stability corrections perform reasonably during low wind speeds and small temperature differences but show biases during high wind speeds.

- Uncertainty in the newly developed parametrizations: universal parametrizations for a univariate and multivariate approach have been developed herein. For the multivariate parametrization $MAE = 7$ W m^{-2} with a systematic bias of 4 W m^{-2}; the approach of the univariate parametrization has a similar MAE value and underestimates heat fluxes by 2 W m^{-2} on average. As none of the well-established parametrizations showed a reasonable performance for high wind speeds, our new multivariate parametrization presents itself as a viable alternative. In general the optimum performance was found for the multivariate parametrization with offset. The univariate parametrization could be an acceptable alternative for neutral atmospheric conditions and moderate wind speeds, and has additionally the advantage that only two empirical coefficients are required.

Stability corrections in general are affected by a large number of uncertainties. Many of these have not been systematically investigated in this study but could lead to a different performance of the stability corrections. The influence of a parametrization of the scalar roughness length, the uncertainty of the modelled stability parameter, uncertainties in the measurements of snow surface temperature and the measurement heights need further investigation to test the robustness of the results across all conditions.

2.7   Appendix

We used the following stability corrections (see also "Electronic Supplement Material" in Sharan and Kumar (2011) for further discussion and additional stability corrections):

Stability correction	ψ_m	ψ_s
Stearns and Weidner (1993)	$\left[\ln\left(1 + (1 + 5\,\zeta)^{1/4}\right)\right]^2 + \ln\left(1 + (1 + 5\,\zeta)^{1/2}\right) - 2\tan^{-1}\left[(1 + 5\,\zeta)^{1/4}\right] - 1.333$	$\left[\ln\left(1 + (1 + 5\,\zeta)^{1/2}\right)\right]^2 - 2(1 + 5\,\zeta)^{1/2} - 0.667(1 + 5\,\zeta)^{3/2} + 1.2804$
Stearns and Weidner (1993) (modified by Michlmayr et al., 2008)	$\left[\ln\left(1 + (1 + 5\,\zeta)^{1/4}\right)\right]^2 + \ln\left(1 + (1 + 5\,\zeta)^{1/2}\right) - 1\tan^{-1}\left[(1 + 5\,\zeta)^{1/4}\right] - 0.5\,(1 + 5\,\zeta)^{3/4} + 0.8247$	$\left[\ln\left(1 + (1 + 5\,\zeta)^{1/2}\right)\right]^2 - 1(1 + 5\,\zeta)^{1/2} - 0.3(1 + 5\,\zeta)^{3/2} + 1.2804$
Holtslag and deBruin (1988)	$-[0.7\,\zeta + 0.75\,(\zeta - 14.28)\exp(-0.35\,\zeta) + 10.71]$	$-[0.7\,\zeta + 0.75\,(\zeta - 14.28)\exp(-0.35\,\zeta) + 10.71]$
Beljaars and Holtslag (1991)	$-[\zeta + 0.667\,(\zeta - 14.28)\exp(-0.35\,\zeta) + 9.52]$	$-\left[(1 + 0.667\,\zeta)^{3/2} + 0.667\,(\zeta - 14.28)\exp(-0.35\,\zeta) + 8.52\right]$
Grachev et al. (2007)	$-19.5\left[(1 + \zeta)^{1/3} - 1\right] + 2.18\left[2\ln\left(\frac{(1+\zeta)^{1/3}+0.67}{1.67}\right) - \ln\left(\frac{(1+\zeta)^{2/3}-0.67(1+\zeta)^{1/3}+0.45}{0.78}\right) + 3.46\tan^{-1}\left(\frac{2(1+\zeta)^{1/3}-0.67}{1.16}\right) - 0.86\right]$	$-2.5\ln(1 + 3\,\zeta + \zeta^2) + 1.12\left[\ln\left(\frac{2\,\zeta^2 + 0.76}{2\,\zeta^2 + 5.24}\right) + 1.92\right]$
Log-linear	$-5\,\zeta$	$-5\,\zeta$
Neutral	0	0

Table 2.6: Stability correction functions for ψ_m and ψ_s used in our study.

Chapter 3   The surface energy balance revisited: Predicting correct snow surface temperatures as influenced by meteorological input and snow properties

Schlögl, S.[1,2], and Lehning, M.[1,2]

[1] WSL-Institute for Snow and Avalanche Research SLF, Davos, Switzerland
[2] School of Architecture, Civil and Environmental Engineering, École Polytechnique Fédérale de Lausanne, Lausanne, Switzerland

Abstract The surface energy balance of a snow pack strongly determines snow melting rates and dynamics of the atmospheric boundary layer but is difficult to accurately model both in hydrological as well as meteorological/climatological models. We investigate and validate snow surface temperature predictions in the physics-based model SNOWPACK for three test sites with different surface characteristics. The largest model error in snow surface temperatures (up to 5 K) was found for the test site Weissfluhjoch in highly complex terrain of the Swiss Alps, whereas model results from the flat test site Summit, Greenland suggest a much better model performance.

The model error is divided in (a) uncertainties of the model input due to measurement uncertainties or necessary model input parametrizations and (b) uncertainties in physical properties of snow. The largest error source in the surface energy balance of a snow pack stems from the parametrization of the incoming longwave radiation and can lead to a model error in snow surface temperatures of up to 5 K, followed by uncertainties of parametrized turbulent heat fluxes (2 K). The model performance significantly increases, if incoming longwave radiation and turbulent fluxes are measured. However, snow surface temperatures are negatively biased in highly complex terrain for measured incoming longwave radiation, as a result of terrain reflections/emissions and decreasing sky view factors, which are not considered in the one-dimensional physics-based snow model due to missing information of the surrounding digital elevation model. Uncertainties in the snow emissivity, the effective thermal conductivity of snow and the extinction coefficient of the snow are at least one order of magnitude smaller than model input parametrizations and lead to model errors in snow surface temperatures around 0.2 K.

Keywords Surface energy balance • Monin-Obukhov bulk formulation • turbulent sensible heat flux • snow • incoming longwave radiation • snow emissivity • effective thermal conduction of snow • extinction coefficient of snow

3.1   Introduction

An accurate estimation of the surface energy balance of a snow pack in physics-based models is a mandatory requirement to correctly assess snow melting rates in spring. Accurately modelled snow melting rates are of special interest for e.g. practitioners in hydropower generation (Schaefli et al., 2007) or flood prevention (Wever et al., 2017). But also for a correct snow representation in larger-scale meteorological and hydrological models, the energy balance is very important. Via the surface temperature, there is a strong feed-back on the atmosphere. In order to validate the energy balance of a snow pack (Etchevers et al., 2004), one often compares snow melting rates of the model with snow water equivalent measurements (e.g. Fierz et al., 2003). In our work, we will use measured surface temperatures to validate model predictions.

The model performance of the surface energy balance of a snow pack is strongly dependent on accurate measurements of the four radiation components, as these components mainly determine a major part of the surface energy balance. However, incoming

longwave radiation is typically not measured by standard automatic weather stations and needs to be parametrized or interpolated. Several all-sky parametrizations were developed as a function of air temperature and cloud cover in the last decades and summarized in Flerchinger et al. (2009). Applying parametrizations of the incoming longwave radiation lead to model errors of the surface energy balance of the snow pack, which are estimated in our study.

Turbulent heat fluxes can contribute up to 50 % to the available energy for melting snow in regions with high wind velocities and have been analysed in the last decades (Funk, 1984; Plüss and Mazzoni, 1994; Pohl et al., 2006; Mott et al., 2011; Schlögl et al., 2017). Turbulent heat fluxes are typically calculated with a bulk formulation (Blanc, 1987) of the Monin-Obukhov similarity theory (MOST, Obukhov, 1946). Stability corrections, which have been developed over non-snow surfaces, are applied in physics-based snow models, as the atmospheric stability is typically large over snow surfaces (Andreas, 2002). Schlögl et al. (2017) estimated the model error of turbulent sensible heat fluxes which stem from the Monin-Obukhov bulk formulation and the additional error due to different parametrizations of the stability corrections by comparing model results with eddy-covariance measurements recorded from 3-D ultrasonic anemometers. They found that model errors in turbulent sensible heat fluxes increase in complex terrain, where assumptions of the application of MOST (e.g. constant flux layer, infinite fetch in all directions) are heavily violated. In this study, we follow up on the work of Schlögl et al. (2017) by validating the entire surface energy balance. For this purpose, we compare modelled and measured snow surface temperatures for three different test sites.

Besides the parametrizations of incoming longwave radiation and turbulent surface fluxes, physical properties of snow could additionally contribute to uncertainties in the surface energy balance of a snow pack. We investigate the contribution of the snow emissivity, the effective thermal conductivity of snow and the extinction coefficient of snow to model errors in the snow surface temperature.

Outgoing longwave radiation and snow surface temperatures can be mutually estimated from the Stefan Boltzmann law if the snow emissivity is known. Therefore, the snow emissivity is a potential error source in the surface energy balance of a snow pack and has been measured in several publications with a wide range of dimensionless values from 0.8 to 0.99 (Griggs, 1968; Surdyk and Fily, 1995). Some studies suggest that the snow emissivity is not a fixed constant but decreases with increasing snow particle size and age of the snow (Burke et al., 1981; Hori et al., 2006).

The temporal and spatial development of snow temperatures within the snow pack is mainly governed by the diffusive process of heat conduction. Therefore, the effective thermal conductivity of snow is a potential error source in the surface energy balance and investigated in several studies (Sturm et al., 1997, 2002; Lehning et al., 1999; Fierz and Lehning, 2001; Schneebeli and Sokratov, 2004; Löwe et al., 2013). Values of the effective thermal conductivity of snow are ranged between 0.1 and 0.4 W m^{-1} K^{-1} and increase with increasing snow density (Calonne et al., 2011; Riche and Schneebeli, 2013).

Several studies (e.g. Colbeck, 1989a; Kuipers et al., 2009) suggest that close to the surface, snow temperatures are not only affected by the diffusive process of heat conduction but may be affected by non-diffusive processes like the absorption of the shortwave radiation or ventilation of snow (Bartlett and Lehning, 2011). This heating of the first few centimetres below the snow surface could lead to sub-surface melting and refreezing. The extinction coefficient of snow determines how far the shortwave radiation penetrates through the snow pack. Only around 1-2 % of the shortwave radiation typically reaches penetration depths of 1 m in the snow pack (Oke, 1987). The extinction coefficient of snow is typically dependent on the wavelength of the shortwave radiation and assessed in different wavelength bands (Bohren and Barkstrom, 1974). Increasing the extinction coefficient of snow leads to an energy redistribution within the snow pack and finally a modification in the surface energy balance of the snow pack.

The paper is organised as follows. In Section 3.2 the methods of the study are described. In Section 3.3, we assess the model error of snow surface temperatures with respect to (a) uncertainties in the model input due to necessary parametrizations or the measurement uncertainty and (b) uncertainties in the physical properties of snow. In Section 3.4 results are discussed and summarized.

3.2 Methods

3.2.1 Test sites

We recorded snow surface temperatures and standard meteorological parameters for three different test sites with different topographical characteristics. The test site Weissfluhjoch (Davos, Switzerland) is located in highly complex terrain, whereas the Plaine Morte (Crans-Montana, Switzerland) test site is located at a glacier and the Greenland dataset is located at a polar test site with a quasi-infinite fetch in all directions.

- Weissfluhjoch 2016 (WFJ16): Snow surface temperatures are measured with an infrared thermometer at the Versuchsfeld in 2540 m asl. 3-D wind velocities and air temperatures were recorded at 2.5 m above the snow surface at a frequency of 10 Hz with a 3-D ultrasonic anemometer (Young). Additionally the meteorological parameters air temperature, relative humidity, wind velocity and direction and four radiation components are measured and used as model input. The analysis was conducted for data measured between 8th December 2016 and 21st December 2016.

- Plaine Morte 2007 (PM07): Snow surface temperatures are measured with an infrared thermometer. An ultrasonic ane-mometer (CSAT3) was installed in 1.75 m above the snow surface to measure fluctuations in air temperatures and 3-D wind velocities at a frequency of 20 Hz. The data were collected at the almost flat field site on the Plaine Morte glacier (2750 m asl.) near Crans-Montana, Switzerland from February to April 2007. High quality meteorological data were additionally recorded and used as model input. A detailed description about the setup at the Plaine Morte glacier can be found in Huwald et al. (2009) and Bou-Zeid et al. (2010).
- Greenland 2000 (GR00): Snow surface temperatures were recorded at the Summit Camp (72.3 °N, 38.8 °W, 3208 m asl.) located on the northern dome of the Greenland ice sheet. Turbulent sensible heat fluxes were collected at 1 m above the snow surface. Additionally, meteorological measurements (air temperature, relative humidity, wind velocity and direction, all radiation components) were used as model input. The analysis was conducted for data measured between 19th June 2000 and 14th October 2000. More information about the field campaign can be found in Cullen et al. (2007, 2014).

Turbulent sensible heat fluxes for the PM07 and GR00 dataset were processed as described in Schlögl et al., 2017 (Section 2.2), whereas turbulent sensible heat fluxes for the WFJ16 data set were calculated with the Biomicrometeorology flux software (Thomas et al., 2009) including despiking (Vickers and Mahrt, 1997), rotating of the coordinate system and a frequence response correction (Moore, 1986). As a frequence response correction was not conducted for the PM07 and GR00 datasets, but for the WFJ16 dataset, we analysed the relative importance of the frequence response correction. A sensitivity analysis for the WFJ16 data set shows that the difference in turbulent sensible heat fluxes with and without applying a frequence response correction is small (not shown). Turbulence data of all datasets were averaged to 30-min intervals.

3.2.2 SNOWPACK model

We calculated snow surface temperatures (TSS) with the physics-based snow model SNOWPACK (Bartelt and Lehning, 2002; Lehning et al., 2002). The upper boundary condition at the snow surface ($z = h$) is expressed with the Neumann boundary condition in order to solve the snow temperature field T_s in SNOWPACK:

$$k_s \frac{\partial T_s(z=h)}{\partial z} = LW + H + q_l + q_{rr}, \qquad (3.1)$$

where k_s is the effective thermal conductivity of snow, LW is the net longwave radiation, H is the turbulent sensible heat exchange, q_l is the turbulent latent heat exchange and q_{rr} is the heat flux from rain. The effective thermal conductivity of snow k_s is calculated by a semi-empirical approach using many parameters of the snow microstructure (Lehning et al., 2002). Note that shortwave radiation is not treated as a boundary condition but a volume source, which penetrates the uppermost snow layers (Lehning et al., 2002b).

The net longwave radiation is calculated by the difference between the incoming longwave radiation ($ILWR$) and the outgoing longwave radiation ($OLWR$):

$$LW = ILWR - OLWR \ = \ ILWR - \varepsilon_{snow}\sigma\, TSS^4, \qquad (3.2)$$

where $\sigma = 5.67 \cdot 10^{-8}$ W m^{-2} K^{-4} is the Stefan-Boltzmann constant and $\varepsilon_{snow} = 0.98$ is the default snow emissivity in SNOWPACK, but modified in this study.

Sensible heat fluxes H (and latent heat fluxes q_l) are calculated in SNOWPACK with the Monin-Obukhov bulk formulation:

$$H = \rho\, c_p C_H \overline{U}\, \Delta\theta, \qquad (3.3)$$

where $\Delta\theta = \theta_s - \theta_{z_{ref}}$ is the virtual potential temperature difference, $\theta_{z_{ref}}$ is the virtual potential temperature at the reference height, θ_s is the virtual potential temperature at the snow surface, $\overline{U}$ is the mean wind speed and C_H is the exchange coefficient for stable conditions,

$$C_H = \frac{k^2}{\left[\ln\left(\frac{z_{ref}}{z_{0M}}\right) - \psi_m(\zeta)\right]\left[\ln\left(\frac{z_{ref}}{z_{0M}}\right) - \psi_s(\zeta)\right]}, \qquad (3.4)$$

where $k = 0.4$ is the von Kármán constant, ζ is the stability parameter, $z_{0M} = 0.002$ m is the aerodynamic roughness length for momentum, in agreement with Schlögl et al. (2017) and ψ_m and ψ_s are the stability corrections for momentum and scalars.

In this study, we exclude rainfall events and therefore do not consider the heat flux from rain q_{rr}.

3.2.3   Procedure

We conducted model simulations with SNOWPACK by using 5 different scenarios of the turbulent sensible heat flux and 5 different scenarios of the incoming longwave radiation. We combined each scenario of the turbulent sensible heat flux with all scenarios of the incoming longwave radiation, which results in totally 25 simulations. We estimated surface turbulent sensible heat fluxes in the model by using (a) measured turbulent sensible heat fluxes from the eddy-covariance tower at a certain height above the ground, (b) the stability correction of Holtslag and deBruin (1988, Holtslag henceforce), (c) the default stability correction in SNOWPACK Stearns and Weidner (modified by Michlmayr et al. (2008), modified Stearns henceforce), (d) the univariate stability correction developed in Schlögl et al. (2017), and (e) the assumption of a neutral boundary layer. The incoming longwave radiation is either (a) measured or parametrized by using a parametrization of Crawford and Duchon (b: 1999, Crawford henceforth), Unsworth and Monteith (c: 1975, Unsworth henceforth), Omstedt (d: 1990) and Konzelmann et al. (e: 1994). Measured turbulent sensible heat fluxes and Holtslags stability correction in combination with measured $ILWR$ and the parametrization of Konzelmann are highlighted in this study.

The error contribution of physical properties of snow to the surface energy balance of a snow pack is assessed for measured incoming longwave radiation and measured turbulent sensible heat fluxes.

We modified the snow emissivity ε_{snow} and the estimation of the $OLWR$ in SNOWPACK (Table 3.1). In the current standard version of SNOWPACK a constant snow emissivity and an estimation of $OLWR$ from measured TSS is used (simulation E1).

Simulation	Snow emissivity	$OLWR$
E1	Constant (0.98)	Calculated from TSS
E2	Constant (0.95)	Calculated from TSS
E3	Constant (0.99)	Calculated from TSS
E4	Constant (0.98)	measured
E5	measured	Calculated from TSS
E6	measured	measured

Table 3.1 Four different simulations have been conducted in order to account for the uncertainty of the snow emissivity and the uncertainty of a different setup of the $OLWR$ in the model.

Additionally, the effective thermal conductivity of snow and the extinction coefficient of snow have been modified to assess the model error of snow surface temperatures. We chose a modification of 50 %, 80 %, 120 % and 150 % of the default values, which were calculated in SNOWPACK.

Three widely used statistical parameters have been calculated to validate the surface energy balance and analyse the model performance of the snow surface temperatures TSS.

$$MAE = \frac{1}{n} \sum_{i=1}^{n} |TSS_{mod} - TSS_{meas}| \tag{3.5}$$

$$MBE = \frac{1}{n} \sum_{i=1}^{n} TSS_{mod} - TSS_{meas} \tag{3.6}$$

$$IQR = (TSS_{mod} - TSS_{meas})_{0.75} - (TSS_{mod} - TSS_{meas})_{0.25} \tag{3.7}$$

The mean absolute error MAE describes the average error of the model calculations, the mean bias error MBE describes a potential average bias and the interquartile range IQR describes the spread of the error.

3.3   Results

3.3.1   Representation of snow surface temperatures in the model

The model performance of the surface energy balance of a snow pack is strongly sensitive to model input uncertainties from the accuracy of the measurement or required parametrizations (if no measurements are available) and uncertainties in physical properties of snow. Both error sources are discussed in detail in Section 3.3.2 and 3.3.3:

- Parametrization of the incoming longwave radiation (Section 3.3.2.1)
- Parametrization of turbulent sensible (and latent) heat fluxes (Section 3.3.2.2)
- Measurement uncertainties of the surface energy balance (Section 3.3.2.3)
- The snow emissivity (Section 3.3.3.1)

- The effective thermal conductivity of snow (Section 3.3.3.2)
- The extinction coefficient of snow (Section 3.3.3.3)

In this section, we assess the overall error of modelled snow surface temperatures for three different datasets and 25 different model ensembles. The best model performance was found for the GR00 dataset, followed by the PM07 dataset and the WFJ16 dataset. The mean absolute error MAE varies between 0.6 K for the best model ensemble member of the GR00 dataset to 5.4 K for the worst model ensemble member of the WFJ16 dataset. The best model ensemble member of the WFJ16 dataset shows around 1 K larger values of MAE than the best model ensemble member of the GR00 dataset (Table 3.2). Additionally, the spread in the mean bias error MBE of the different model ensembles is much larger for the WFJ16 dataset in comparison with PM07 dataset and the GR00 dataset. These large differences in the model performance of snow surface temperatures can be explained by the different topographical characteristics of the sites. The Summit test site in Greenland is an ideally flat location, whereas the test site Weissfluhjoch is located in the Swiss Alps with steep slopes in the close surroundings of the measurement field (which is locally flat). In complex terrain, several assumptions of the Monin-Obukhov bulk formulation are heavily violated (e.g. constant flux layers, infinite fetch in all directions), which lead to model errors of the turbulent sensible heat fluxes (Schlögl et al., 2017) and hence model errors in the snow surface temperature.

Additionally, values of measured radiation components (and snow surface temperatures) at one specific point are strongly sensitive to the specific environment, in particular terrain. For example, the longwave radiation exchange of the snow surface with the upper hemisphere is altered on a slope, a local depression or if significant terrain is close to the site. Shortwave radiation can be affected by terrain reflections in highly complex terrain and especially if a snow cover is present. Both effects increase with a decreasing sky view factor (SVF), which describes the visible clear sky of the hemisphere, centred over the analysed position (Oke, 1981). The SVF is 1 for an idealized flat test site (e.g. PM07 or GR00) and decreases in complex terrain (e.g. WFJ16), where slopes in the direct surroundings of the measurement hinder a complete visibility of the clear sky hemisphere. The model performance of the surface energy balance decreases with decreasing SVF, as terrain reflections and SVF are typically not considered in one-dimensional snow models due to missing information of the surrounding digital elevation model. In principle, those effects are included in the measurements but in practice sensor sensitivity is such that radiation from low elevation angles will not fully be covered.

	MAE [K]	MBE [K]	IQR [K]
WFJ16	1.6…5.4	-3.4…5.0	3.3…9.2
PM07	0.9…4.9	-3.7…1.8	1.9…9.8
GR00	0.6…2.0	-1.4…0.6	1.4…6.1

Table 3.2 The minimum and maximum of the mean absolute error MAE [K], mean bias error MBE [K] and the interquartile range [K] of the 25 model ensemble members is shown for the three datasets WFJ16, PM07 and GR00.
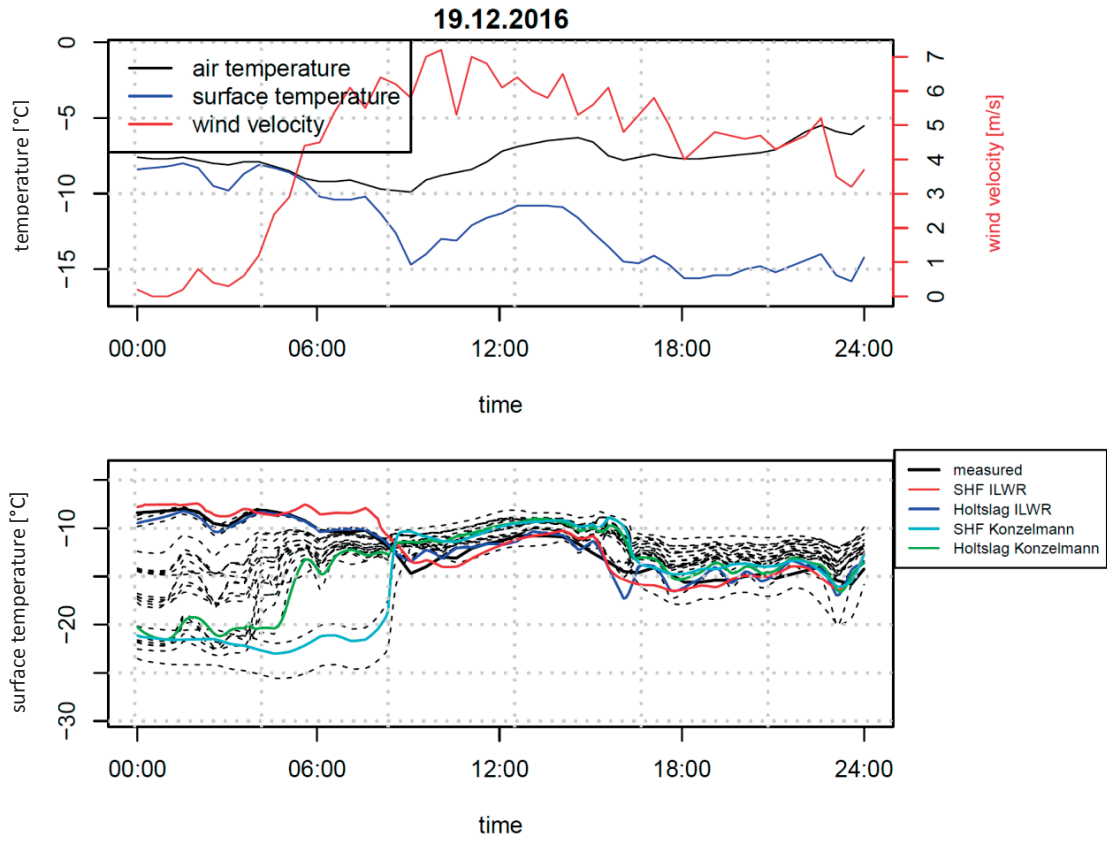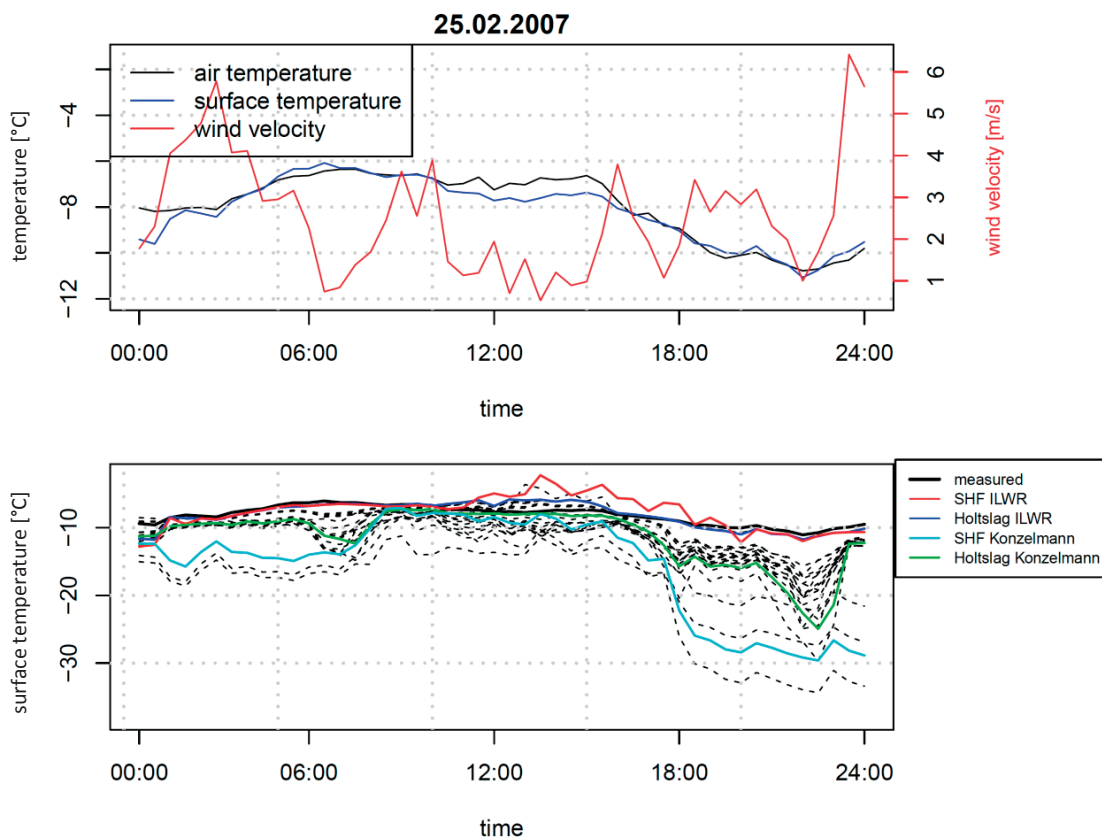
Fig 3.1 Two example days for the dataset WFJ16 for the 19.12.2016 (top) and the dataset PM07 for the 25.02.2007 (bottom). Measured air and snow surface temperatures[°C] and wind velocities [m/s] are shown in the upper panels. Modelled and measured snow surface temperatures are shown in the lower panels. The dashed lines indicate the 25 different model ensemble members. The model representation is shown in the coloured lines by using measured incoming longwave radiation and measured turbulent sensible heat fluxes in combination with *ILWR* parametrizations of Konzelmann and stability corrections of Holtslag.

The 25 different model ensemble members of snow surface temperatures and the measurement of the snow surface temperatures are exemplarily shown for one day at the WFJ16 test site and one day at the PM07 test site (Fig. 3.1). The model performance strongly varies for the different model ensembles in the early morning for the specific example (19.12.2016) of the WFJ16 dataset during calm wind conditions and a small temperature difference between the snow surface temperature and the air temperature. Some model ensembles strongly underestimate snow surface temperatures up to 15 K, whereas other model ensembles match well with measured snow surface temperatures in the early morning. The spread of the 25 model ensembles decreases with increasing wind velocity after sunrise. This underestimation of the surface temperature has repeatedly been observed over snow (Etchevers et al., 2004; Michlmayr et al., 2008) but has thus far remained unexplained.

The model performance for snow surface temperature predictions is analysed as a function of the measured snow surface temperature, measured turbulent sensible heat flux and measured wind velocity (Fig. 3.2) and will be analysed for varying cloud cover fractions. We found some general trends for the majority of the model ensembles, although the 25 different model ensembles often show strongly different behaviour for different atmospheric conditions.

The model ensembles tend to overestimate snow surface temperatures for very low snow surface temperatures, whereas we found an underestimation in the model ensembles for measured snow surface temperatures close to the freezing point. Additionally, we found a much larger model spread for calm conditions than for moderate to high wind velocities.
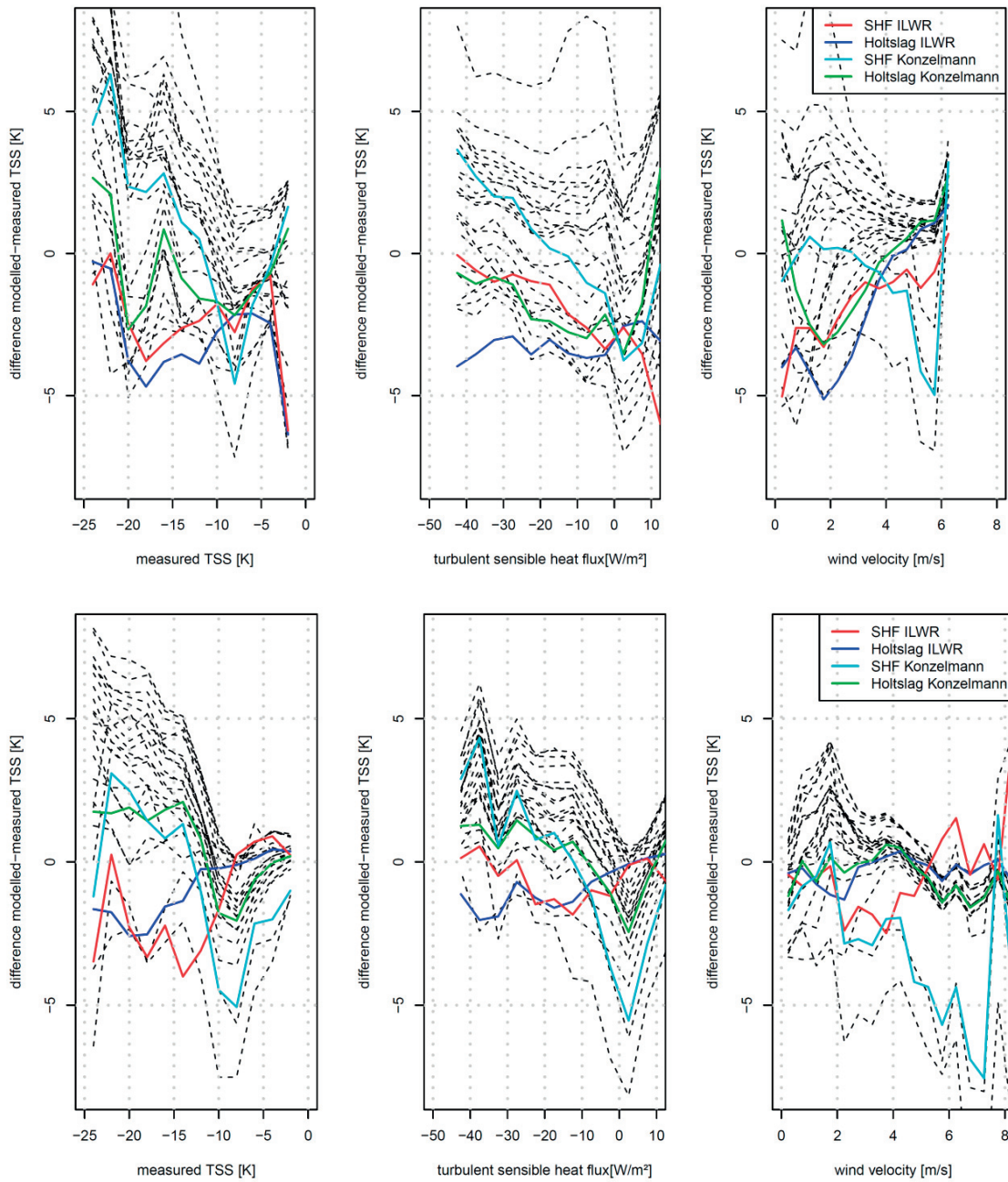
Fig 3.2 Difference between modelled and measured snow surface temperature for WFJ16 (upper panels) and PM07 (lower panels) as a function of different measured snow surface temperatures (left), measured turbulent sensible heat fluxes (middle) and measured wind velocities (right). The dashed lines indicate the 25 different model ensemble members. The model representation is shown in the coloured lines by using of measured incoming longwave radiation and measured turbulent sensible heat fluxes in combination with $ILWR$ parametrizations of Konzelmann and stability corrections of Holtslag. The results for the GR00 test site are similar (not shown).

Setup	Measured	Holtslag	Mod. Stearns	univariate	Neutral
Measured	4.4/4.3/3.1	3.6/2.0/1.5	5.1/2.1/1.7	3.3/1.9/1.4	3.3/2.4/1.5
Crawford	6.9/9.8/6.1	6.3/4.7/3.9	5.7/4.1/2.8	6.7/4.1/3.3	3.8/4.2/2.9
Omstedt	4.6/9.8/5.8	3.9/4.8/2.6	4.4/5.0/2.4	3.9/4.9/2.5	3.8/5.4/2.4
Konzelmann	5.5/8.9/5.5	7.0/4.4/2.9	4.9/4.4/2.5	6.4/4.2/2.7	3.6/4.7/2.6
Unsworth	9.2/6.3/5.7	6.3/4.4/2.9	5.1/4.8/2.8	5.6/4.7/2.8	4.0/5.0/2.8

Table 3.3 IQR [K] for the 5 different setups of the turbulent sensible heat flux and the 5 different setups of the incoming longwave radiation for the WFJ16 (first number), PM07 test site (second number) and GR00 test site (third number).
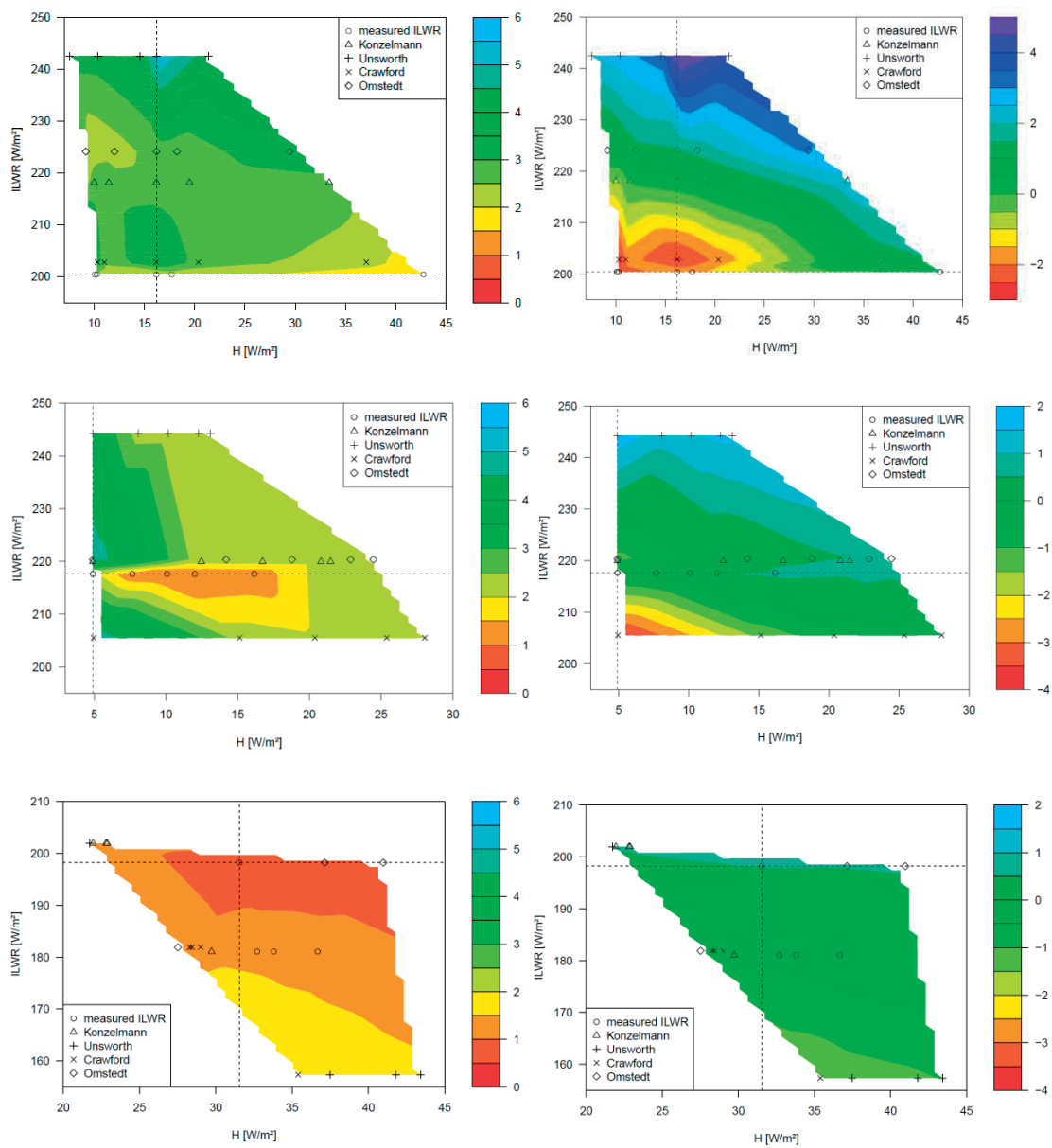
Fig 3.3 MAE [K] (left) and MBE [K] (right) for datasets from WFJ16 (upper panels), PM07 (middle panels) and GR00 (lower panels). Both errors are plotted as a function of the turbulent sensible heat flux and the incoming longwave radiation. Measured turbulent

sensible heat fluxes and incoming longwave radiation (averaged over the measurement period) are marked as dashed lines. The different setups of incoming longwave radiation are additionally shown in the legend.

3.3.2 Sensitivity to meteorological model input

The validation of snow surface temperatures is assessed with respect to uncertainties in the model input. Incoming longwave radiation and turbulent heat fluxes are typically not measured but parametrized. We assess the error contribution of uncertainties in parametrized $ILWR$ (Section 3.3.2.1) and turbulent fluxes (Section 3.3.2.2) to snow surface temperatures. Additionally, we assess model errors in snow surface temperatures by analysing typical measurement uncertainties (Section 3.3.2.3).

3.3.2.1 *Parametrization of the incoming longwave radiation*
The five different scenarios of the incoming longwave radiation strongly affect the model performance for snow surface temperatures (Fig. 3.3). For the WFJ16 dataset, the measured incoming longwave radiation ($ILWR = 200$ W m^{-2}) is on average smaller than that of all four different parametrizations (Crawford: $ILWR = 202$ W m^{-2}, Konzelmann: $ILWR = 219$ W m^{-2}, Omstedt: $ILWR = 224$ W m^{-2}, Unsworth: $ILWR = 242$ W m^{-2}). The best model performance was found for the Konzelmann parametrization with values of $MBE = 0.4$ K and values of $MAE = 2.7$ K in combination with measured turbulent sensible heat fluxes. Values of MAE are below 2 K but with a large negative bias ($MBE = -1.7$ K) when using measured $ILWR$ (and measured turbulent sensible heat fluxes). This underestimation in modelled snow surface temperatures at the Weissfluhjoch test site is consistent with the earlier study of Schmucki et al. (2014), who found a better model performance in the snow height during the ablation period by using a parametrization of the incoming longwave radiation instead of the measurement. The largest errors for snow surface temperatures were found when using the Unsworth parametrization. The model overestimates snow surface temperature on average by around 5 K. This implies that the modelled snow surface temperatures increase by around 1 K through an increase in the incoming longwave radiation of 5 W m^{-2}. Although the measured incoming longwave radiation is affected by a negative bias, the interquartile range IQR is lowest for this model scenario for all stability corrections (Table 3.3), showing that all parametrized forms have difficulties in representing the full range of environmental conditions. This implies that using a parametrization of the incoming longwave radiation (e.g. Konzelmann) leads to (on average) a smaller bias, but a larger model error spread (see Fig. 3.1) for this particular mountain site.

The strong sensitivity of the model performance of snow surface temperatures to the incoming longwave radiation is also observed for the PM07 dataset. For this test site, the average measured incoming longwave radiation is in good agreement with parametrizations of Konzelmann and Omstedt ($ILWR \approx 219$ W m^{-2}). All three model scenarios provide similar results in values of $MBE \approx -0.5$ K, but strongly vary in values of MAE. The scenario with measured incoming longwave radiation as model input performs best with values of $MAE = 2$ K, whereas the parametrizations of Konzelmann and Omstedt show values of MAE larger than 4 K. The parametrization of Crawford shows the lowest values ($ILWR = 205$ W m^{-2}) for the PM07 dataset similar as for the WFJ16 test site, whereas Unsworth's parametrization shows the largest incoming longwave radiation ($ILWR = 245$ W m^{-2}). Snow surface temperatures are negatively biased by using Crawford's parametrization and positively biased by using Unsworth's parameterization.

3.3.2.2 *Parametrization of the turbulent sensible (and latent) heat flux*
We analyse on the sensitivity of modelled snow surface temperatures to changes in turbulent sensible heat fluxes. As latent heat fluxes also contribute to uncertainties in modelled snow surface temperatures, we additionally separate uncertainties from turbulent sensible heat fluxes to those of latent heat fluxes.

Snow surface temperatures increase with increasing turbulent sensible heat fluxes towards the snow surface. The largest turbulent sensible heat fluxes and hence snow surface temperatures were found for the assumption of a neutral boundary layer, as stability corrections are zero in this specific scenario.

The second largest turbulent sensible heat fluxes were found by using the stability correction of Stearns and Weidner (1994, modified by Michlmayr et al., 2008). The original Stearns stability correction was modified by Michlmayr et al. (2008) in order to improve the model performance of snow surface temperatures. Hence, modified Stearns stability corrections better represent snow surface temperatures than the original stability correction of Stearns and Weidner (1994). However, Schlögl et al. (2017) showed that the modified Stearns stability correction lead to larger turbulent fluxes than the original Stearns stability correction and overestimates turbulent sensible heat fluxes and turbulent sensible heat fluxes are closer to measured values by using the original Stearns stability correction. In summary, turbulent sensible heat fluxes are better represented by using the original Stearns stability correction, whereas snow surface temperatures are better represented by using the modified Stearns stability correction. This finding is a typical example of an error cancellation in physics-based models. A worse representation of turbulent sensible heat fluxes could finally lead to a better representation of the surface energy balance of the snow pack (validated by the snow surface temperature) due to other error sources (such as e.g. the incoming longwave radiation).

For the WFJ16 dataset, the best values of MBE were found for the combination of an $ILWR$ parametrization of Konzelmann with the univariate stability correction of Schlögl et al. (2017) ($MBE = 0.15$ K). The lowest values of MAE were found for the combination of a negatively biased measured $ILWR$ with a positively biased neutral boundary layer ($MAE = 1.63$ K), which is another example of a well working error cancellation in a physics-based model. However, our analysis shows no best model ensemble member; rather many model ensembles provide good results for the WFJ16 dataset (Fig. 3.3). For example, the $ILWR$ parametrization

of Konzelmann performs well with all stability corrections ($MBE < \pm 1$ K) except the assumption of a neutral boundary layer. The combination of measured sensible heat fluxes with the $ILWR$ parametrization of Unsworth is an example of a worse model performance, where snow surface temperatures are overestimated on average around 5 K.

For the PM07 dataset, the best values of MBE were found for the combination of a parametrization of Konzelmann with a stability correction of Holtslag ($MBE = -0.05$ K). The lowest values of MAE were found for the combination of measured $ILWR$ with the univariate stability correction in Schlögl et al. (2017). In contrast to the WFJ16 dataset, we found a sufficiently good model performance of snow surface temperatures for measured $ILWR$ and measured turbulent sensible heat fluxes ($MAE = 2.12$ K, $MBE = -0.30$ K). The combination of measured turbulent sensible heat fluxes with the $ILWR$ parametrization of Crawford is an example of a poor model performance, where snow surface temperatures are underestimated on average around 4 K.

For the GR00 dataset, the best values of MBE were found for the combination of a parametrization of Konzelmann with a stability correction of modified Stearns ($MBE = -0.16$ K). The lowest values of MAE were found for the combination of measured $ILWR$ with the univariate stability correction in Schlögl et al. (2017) as for the PM07 dataset. The combination of the $ILWR$ parametrization of Crawford with the stability correction of Holtslag is an example of a poor model performance, where snow surface temperatures are underestimated on average around 1.5 K.

The sensitivity of the turbulent latent heat flux to snow surface temperatures is analysed by using measured $ILWR$ and measured turbulent sensible heat fluxes with a choice of different stability corrections as model input (Table 3.4).

	MAE [K]	MBE [K]	IQR [K]
Holtslag	1.95/2.21	−1.71/−0.26	4.38/4.51
Mod Stearns	2.17/2.48	−1.52/−0.32	4.60/4.90
Univariate	1.85/2.30	−1.63/−0.30	4.39/4.61
Neutral	1.72/2.13	−1.43/−0.30	4.15/4.34

Table 3.4 Mean absolute error MAE [K], mean bias error MBE [K] and the interquartile range [K] for measured incoming longwave radiation, measured turbulent sensible heat fluxes and varying stability corrections for the WFJ16 dataset (first number) an the PM07 dataset (second number).

The model error of snow surface temperatures caused by uncertainties in the latent heat flux contributes on average around 0.3 K for the WFJ16 dataset and lower values for the PM07 dataset. These small differences in the numerical model results of both test sites can be explained by the fact that average latent heat fluxes are much smaller than sensible heat fluxes.

3.3.2.3   *Sensitivity arising from limited accuracy of meteorological input*

The model performance of snow surface temperatures is strongly dependent on accurate measurements of longwave radiation and turbulent heat fluxes (Eq. 3.1) as shown above. However, uncertainties in measurements of the absorbed shortwave radiation could additionally lead to model errors in snow surface temperatures. The absorbed energy of the shortwave radiation can be estimated with the Beer-Lambert law for one snow layer as the difference of the absorbed shortwave radiation at the upper and lower boundary. Absorption is a function of snow density and other snow properties and decides at which depth the shortwave energy is deposited and heats the snow. Therefore, snow surface temperatures are sensitive not only to the energy balance terms in Eq. 3.1 but additionally to uncertainties in the shortwave radiation.

We modified the model input for $ILWR$, $ISWR$, absorbed shortwave radiation and turbulent sensible heat fluxes to their default input values (Table 3.5). The largest uncertainty in the surface energy balance of a snow pack stems from the incoming longwave radiation. Increasing the incoming longwave radiation about 10 (5) %, leads to an increase of 4.5 (2.1) K in snow surface temperatures. Investigations have shown an increase of 1.5 (0.7) K in snow surface temperatures by increasing the incoming shortwave radiation about 10 (5) %. Increasing turbulent sensible heat fluxes about 10 (5) % leads to 0.4 (0.2) K larger snow surface temperatures. Note that 10 % measurement uncertainty can be easily reached for turbulent sensible heat fluxes due to small absolute values (Massmann and Lee, 2002; Burba, 2013), whereas high-quality radiation measurements are typically affected by measurement uncertainties below 5 % (MacWhorter and Weller, 1991).

	$ILWR$	$ISWR$	H
90 %	−3.9	−1.4	−0.4
95 %	−2.0	−0.7	−0.2
105 %	2.1	0.7	0.2
110 %	4.5	1.5	0.4

Table 3.5 Sensitivity of the snow surface temperature [K] to uncertainties in the measurement of incoming longwave radiation, incoming shortwave radiation and the sensible heat flux. 90 %, 95 %, 105 % and 110 % of the default input values were chosen for the WFJ16 dataset.

3.3.3 Uncertainties in the physical properties of snow

We assess model errors in the surface energy balance of a snow pack with respect to three different uncertainties of the physical properties of snow: The snow emissivity (Section 3.3.3.1), the effective thermal conductivity of snow (Section 3.3.3.2) and the extinction coefficient of snow (Section 3.3.3.3). In this section, we used measured incoming longwave radiation and measured turbulent sensible heat fluxes as model input.

3.3.3.1 Snow emissivity
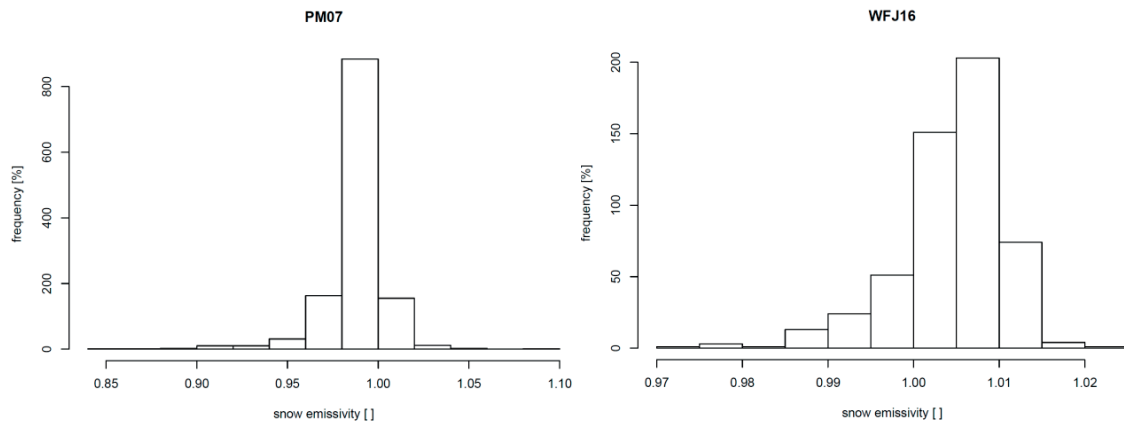
Fig 3.4 Distribution of the snow emissivity for the WFJ16 dataset (left) and the PM07 dataset (right)

The distribution of the snow emissivity is calculated by solving Stefan-Boltzmann law with the measured outgoing longwave radiation and measured surface temperatures for the WFJ16 and the PM07 datasets (Fig. 3.4). The majority of the snow emissivity values are unphysically above 1 for the WFJ16 dataset, whereas only 15 % of the snow emissivity values are above 1 for the PM07 dataset. Unphysical values above 1 must be attributed to measurement errors of snow surface temperatures and outgoing longwave radiation or to a vertical radiative flux divergence, which could be especially strong for very stable atmospheric conditions (Hoch et al., 2007). A small-scale spatial variability in snow surface temperatures (e.g. Mott et al., 2017) reveals that the location of snow surface temperature measurements and outgoing longwave radiation measurements has to be very close to each other.

Fig 3.5 Difference between modelled and measured snow surface temperature for WFJ16 (left) and PM07 (right) as a function of the measured snow emissivity. The dashed lines indicate the 25 different model ensemble members. The model representation is shown in the coloured lines by using measured incoming longwave radiation and measured turbulent sensible heat fluxes in combination with $ILWR$ parametrizations of Konzelmann and stability corrections of Holtslag.

The model performance of snow surface temperatures is estimated as a function of the measured snow emissivity (Fig. 3.5). Our analysis suggests that the model performance of snow surface temperatures is not sensitive to the measured snow emissivity for

the PM07 dataset. However, for unphysical values in the measured snow emissivity above 1 the model tends to strongly overestimate snow surface temperatures for the WFJ16 dataset.

The snow emissivity in the current standard version of SNOWPACK is set to a constant value equal to 0.98, which matches well with measured results from the PM07 dataset. However, many studies suggest a decreasing snow emissivity for increasing snow densities, which would increase snow surface temperatures. We estimated model errors in the surface energy balance by using the measured snow emissivity instead of a constant default value of $\varepsilon_{snow} = 0.98$. Additionally, we estimated the model uncertainty in the snow surface temperature by using measured $OLWR$, instead of the default SNOWPACK approach, where measured snow surface temperatures are used to calculate the $OLWR$ with Stefan-Boltzmann law.

The sensitivity analysis was conducted for measured incoming longwave radiation and measured turbulent sensible heat fluxes (Table 3.6). We focus on the analysis of the PM07 dataset, as the measured turbulent sensible heat flux in combination with measured incoming longwave radiation is negatively biased for the WFJ16 dataset.

Simulation	Snow emissivity	$OLWR$	MAE [K]	MBE $[K]$	IQR [K]
E1	Constant (0.98)	Calculated from TSS	1.95/2.20	−1.71/−0.25	4.39/4.51
E2	Constant (0.95)	Calculated from TSS	1.73/2.29	−1.33/−0.14	4.33/4.58
E3	Constant (0.99)	Calculated from TSS	2.01/2.26	−1.82/−0.26	4.41/4.74
E4	Constant (0.98)	measured	1.94/2.39	−1.72/−0.09	4.40/4.76
E5	measured	Calculated from TSS	2.00/2.30	−1.84/−0.23	4.38/4.71
E6	measured	measured	2.04/2.40	−1.89/−0.04	4.41/4.95

Table 3.6 MAE [K], MBE $[K]$ and IQR [K] for the four different snow emissivity scenarios for the WFJ16 dataset (first number) and PM07 dataset (second number).

Differences in the model performance of the snow surface temperatures for the four model simulations are small. The SNOWPACK default setting (E1) produces the largest negative bias ($MBE = −0.25$ K). The negative bias could be reduced to values of $MBE = −0.04$ K by using measured $OLWR$ and a measured snow emissivity (E6). Modelled snow surface temperatures increase around 0.4 K by decreasing the snow emissivity from 0.99 to 0.95 (E2 and E3).

3.3.3.2 *Effective thermal conductivity of snow*

We modified the effective thermal conductivity of snow as described in Section 3.2.3. The model error can be estimated around 1 K for the WFJ16 dataset and around 0.2 K for the PM07 dataset for a range from 50 % to 150 % of the default calculated effective thermal conductivity of snow in SNOWPACK (Table 3.7). The discrepancy between both datasets can be explained by smaller average snow conductivity values for the WFJ16 dataset (0.18 W m^{-1} K^{-1}) in comparison with the PM07 dataset (0.28 W m^{-1} K^{-1}). The smaller snow conductivity values in the WFJ16 dataset can be explained by the measurement period early in the season in December, where the snow density of the snow pack is typically low. The densification of the snow pack leads to larger snow conductivities in the course of the snow season (Riche and Schneebeli, 2013). Hence, snow conductivity values were almost doubled for the PM07 dataset, which were estimated from February to April, and lead to smaller relative differences in snow surface temperatures due to larger absolute values.

Simulation	MAE [K]	MBE $[K]$	IQR [K]
50 %	2.36/2.20	−2.23/−0.39	5.12/4.64
80 %	2.06/2.25	−1.89/−0.25	4.70/4.62
100 %	1.95/2.21	−1.71/−0.25	4.39/4.52
120 %	1.81/2.25	−1.52/−0.20	4.09/4.55
150 %	1.61/2.23	−1.31/−0.18	3.77/4.42

Table 3.7 MAE [K], MBE $[K]$ and IQR [K] for five different effective thermal snow conductivities for the WFJ16 dataset (first number) and PM07 dataset (second number).

Modelled snow surface temperatures increase with increasing effective thermal conductivity of snow, shown as a function of measured snow surface temperatures and wind velocities (Fig. 3.6). An increasing effective thermal conductivity of snow additionally reduces the negative bias for the WFJ16 and PM07 dataset.
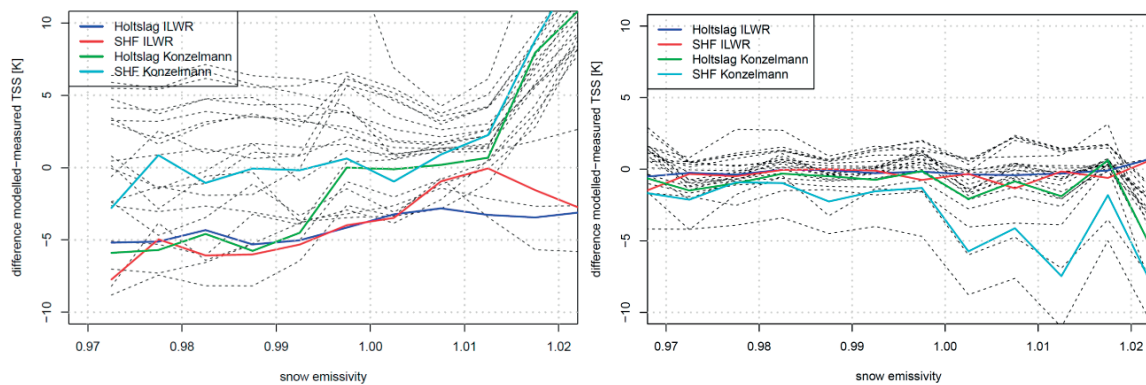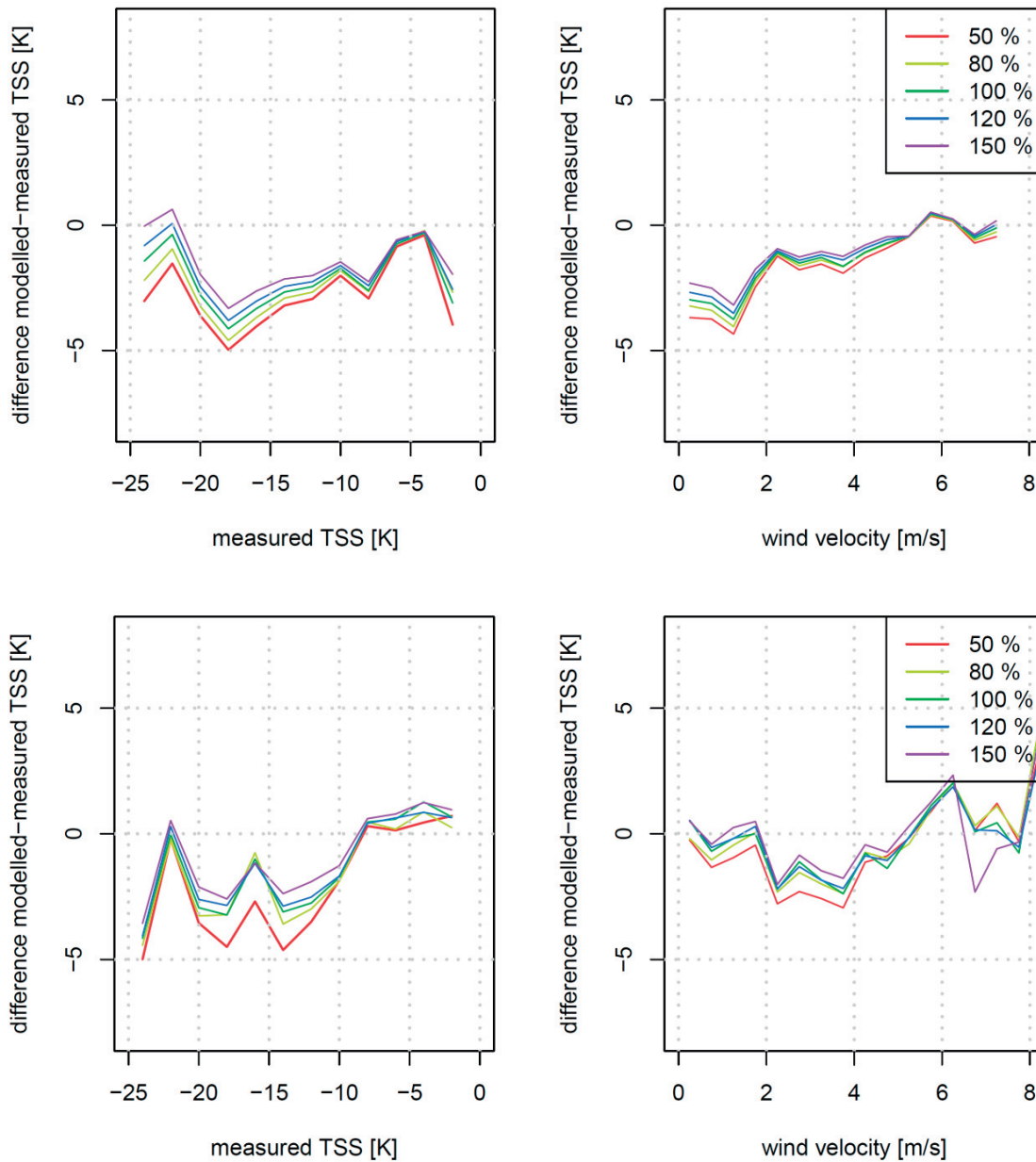
Fig 3.6 Difference between modelled and measured snow surface temperature for WFJ16 (upper panels) and PM07 (lower panels) as a function of the measured snow surface temperature (left) and the wind velocity (right). The effective thermal snow conductivity was modified to 50 %, 80 %, 120 %, and 150 % of their default values for the usage of measured incoming longwave radiation and measured turbulent sensible heat fluxes.

3.3.3.3   Extinction coefficient of snow

The extinction coefficient of snow additionally leads to model errors in the surface energy balance of a snow pack and is calculated in SNOWPACK by an empirical formula depending on the density and the grain size of the snow layer with two empirical constants, which are depending on five different wavelength bands of the shortwave radiation (Bohren and Barkstrom, 1974).

A modification of the extinction coefficient redistributes the energy from the absorbed shortwave radiation within the snow pack. Small extinction coefficients favours that the absorbed shortwave radiation deeply penetrates within the snow pack, whereas large

extinction coefficients lead to more energy in the first top layers of a snow pack. Increasing the extinction coefficient by 20 % of the default SNOWPACK setting leads to only 0.04 K larger snow surface temperatures for the WFJ16 dataset.

3.4 Discussion and conclusion

This study estimates the accuracy of the surface energy balance of a continuous snow pack for three different test sites with different surface characteristics, climates and topographical settings. For this purpose, snow surface temperatures have been validated by testing the sensitivity on measured and parametrized incoming longwave radiation, turbulent (sensible and latent) heat fluxes, shortwave radiation and physical properties of snow (snow emissivity, effective thermal conductivity of snow and extinction coefficient of snow). Additionally, we assessed the sensitivity of snow surface temperatures caused by typical measurement uncertainties.

Our analysis shows that the surface energy balance could be satisfactory estimated for the flat and idealized test site in Greenland with mean absolute errors in snow surface temperatures between 0.6 K and 2.0 K for 25 different ensemble members for different scenarios in turbulent sensible heat fluxes and incoming longwave radiation. The model performance of the surface energy balance decreases for the test site Weissfluhjoch in complex terrain and the mean absolute error of snow surface temperatures increases to values between 1.6 K and 5.4 K for the 25 different ensemble members. The decreasing model performance of the surface energy balance in complex terrain is mainly caused by the violation of assumptions in the Monin-Obukhov bulk formulation and the missing information about the surrounding terrain preventing e.g. an accurate estimation of the sky-view factor.

We separate the model error of the surface energy balance of a continuous snow pack in (1) uncertainties from the model input of standard meteorological parameters and (2) uncertainties in physical properties of snow:

(1)   Uncertainties of the model input of standard meteorological parameters
The largest uncertainty in the surface energy balance of a continuous snow pack stems from the parametrization of the incoming longwave radiation. Four different $ILWR$ parametrizations lead to differences in snow surface temperatures of up to 5 K. The second largest error source stems from the parameterization of the turbulent heat fluxes in the Monin-Obukhov bulk formulation, which leads to differences in snow surface temperatures of up to 2 K. The model error (especially the interquartile range) of snow surface temperatures decreases, if the incoming longwave radiation and turbulent sensible heat fluxes are measured instead of parametrized. However, snow surface temperatures are negatively biased for measured incoming radiation in highly complex terrain. Hence, model errors in the surface energy balance of a snow pack increase for decreasing sky-view factors, as sky-view factors are not considered in one-dimensional physics-based snow models due to the missing information of the surrounding digital elevation model.

Assuming that all radiation components and turbulent fluxes are affected by a measurement uncertainty of $\pm$ 5 %, the largest error in snow surface temperatures can be found for the incoming longwave radiation ($\pm$ 2 K), followed by the incoming shortwave radiation ($\pm$ 0.7 K) and the turbulent sensible heat flux ($\pm$ 0.2 K).

(2)   Uncertainties in the physical properties of snow
We assessed the model error contribution of uncertainties in the physical properties of snow (snow emissivity, effective thermal conductivity of snow, extinction coefficient of snow) to the surface energy balance of a continuous snow cover. Uncertainties in the snow emissivity are at least one order of magnitude smaller than uncertainties in the parametrization of turbulent heat fluxes and ranges up to 0.2 K. The uncertainty in the effective thermal conductivity of the snow is found to be in the same range as the uncertainty of the snow emissivity if the assessment of the snow conductivity is affected by an error lower than $\pm$ 15 %. The uncertainty of the extinction coefficient of snow is estimated with 0.04 K for a modification of the default settings of 20 %.

Chapter 4 Representation of horizontal transport processes in snowmelt modelling by applying a footprint approach

Schlögl, S.[1,2], Lehning, M.[1,2] and Mott, R.[1,3]

[1] WSL-Institute for Snow and Avalanche Research SLF, Davos, Switzerland
[2] School of Architecture, Civil and Environmental Engineering, École Polytechnique Fédérale de Lausanne, Lausanne, Switzerland
[3] Karlsruhe Institute of Technology, Institute of Meteorology and Climate Research, Atmospheric Environmental Research (IMK-IFU), KIT-Campus Alpin, Garmisch-Partenkirchen, Germany

Abstract The energy balance of an alpine snow cover significantly changes once the snow cover gets patchy. The local advection of warm air causes above-average snow ablation rates at the upwind edge of the snow patch. As lateral transport processes are typically not considered in models describing surface exchange, e.g. for hydrological or meteorological applications, small-scale variations in snow ablation rates are not resolved. The overall model error in the hydrological model Alpine3D is split into a contribution from the pure "leading edge effect" and a contribution from an increase in the mean air temperature due to a positive snow-albedo feedback mechanism. We found an overall model error for the entire ablation period of 4 % for the almost flat alpine test site Gletschboden and 14 % for the Wannengrat area, which is located in highly complex terrain including slopes of different aspects. Terrestrial laser scanning measurements at the Gletschboden test site were used to estimate the pure "leading edge effect" and reveal an increase in snow ablation rates of 25-30 % at the upwind edge of a snow patch and a total of 4-6 % on a catchment scale for two different ablation days with a snow cover fraction lower than 50 %. The estimated increase of local snow ablation rates is then around 1-3 % for an entire ablation period for the Gletschboden test site and approximately 4 % for the Wannengrat test site.

Our results show that the contribution of lateral heat advection is smaller than typical uncertainties in snow melt modelling due to uncertainties in boundary layer parameters and a parametrization of the incoming longwave radiation but increases in regions with smaller snow patch sizes and long-lasting patchy snow covers in the ablation period.

We introduce a new temperature footprint approach, which explains 15 % (out of 25 %) of the enhanced snow ablation rates at the upwind edge of the snow patch and could be used in hydrological models. In addition to improved snow ablation rates, the footprint model better represents snow mask maps and turbulent sensible heat fluxes from eddy-covariance measurements.

Keywords eddy-covariance measurements • patchy snow covers • snow ablation rates • temperature footprint approach • terrestrial laser scanning • turbulent sensible heat fluxes

4.1 Introduction

Modelling an alpine snow-cover is a challenging issue especially in the melting season when the snow cover becomes patchy (Essery et al., 2006; Fujita et al., 2010; Mott et al., 2011, 2013). Accurate modelled snow ablation rates are of special interest for e.g. practitioners in hydropower generation (Schaefli et al., 2007) or flood prevention (Wever et al., 2017) especially in the late snow ablation period. Snow and hydrological models are typically forced by single point meteorological measurements, which are interpolated to the grid of the digital elevation model. Turbulent fluxes in the atmosphere are often calculated with Monin-Obukhov similarity theory (MOST) based on this interpolated meteorological data. Therefore, snow and hydrological models do not include

lateral transport of sensible and latent heat in the atmosphere (Marks and Dozier, 1992; Marks and Winstral, 2001; Pellicciotti et al., 2008; Schlögl et al., 2016). Hence, the influence of the upward heat flux caused by local advection of warm air from the bare ground towards snow-covered areas is not considered and the development of a stable internal boundary layer (SIBL) is underestimated in the models. The effect of lateral transport of sensible heat on snow ablation rates on the catchment scale can be neglected as long as the snow cover remains continuous. However, when the snow cover fraction decreases in the later stages of the ablation period, the local effect of lateral heat transport becomes important (Marsh and Pomeroy, 1996) and snow ablation rates increase at the upwind edge of the snow patch (Liston, 1999; Pomeroy et al., 2003). This leads to an underestimation of the available energy in the model for melting snow and is compensated in some few studies by parametrizations in hydrological models (Granger et al., 2006). The physical basis for parametrizations of the advective heat flux was developed in the 1970s (Weisman, 1977), estimated as a function of the fetch distance (Liston et al., 1995) and refined in the boundary layer integration approach (Granger et al., 2002). Some studies (e.g. Helgason and Pomeroy, 2012; Harder et al., 2017) determined the local advection of sensible heat based on high resolution temperature profile measurements using thermocouples. These measurements are rare but crucial to calibrate model parametrizations. Contrary, eddy-covariance measurements over patchy snow covers are more frequent, but limited to large path lengths of the measurement devices which are not suitable to measure turbulence very close to the snow surface. However, measured turbulent sensible heat fluxes directly over the snow surface are recommended in order to assess the complex nature of heat-exchange processes over patchy snow-covers (Mott et al., 2016). As constant flux layers over patchy snow covers cannot develop to sufficient depth, turbulent sensible heat fluxes measured far away from the snow surface are not useful to assess snow ablation rates as the measurement is strongly influenced by the upwind air flow (Mott et al., 2017).

In this study, we present an approach to account for the local advection of sensible heat in order to improve the model performance in the late stage of the ablation period. The strength of this approach is the purely analytical origin which avoids introducing empirical coefficients in the model. We develop adapted footprint estimations (Schuepp et al., 1990) in order to resolve the spatial variability of near-surface air temperatures and turbulent sensible heat fluxes. This fundamental theory was originally deployed for eddy-covariance measurements revealing the origin of the measured turbulence as a function of the measurement height, atmospheric stability and wind speed.

This study is organized as follows. In Section 4.2, study site, measurements, model setup and the footprint approach are introduced. In Section 4.3, we assess the limitations of the Alpine3D model with respect to the calculation of snow ablation rates, the model error due to missing lateral transport processes, the model performance after applying the footprint approach, a validation of the footprint approach with respect to turbulent sensible heat fluxes, snow mask maps and snow ablation rates and finally a sensitivity analysis to transfer estimated results from our study site to different scales. In Section 4.4, the overall model error by neglecting lateral transport processes is discussed and major results of this study are summarized in Section 4.5.

4.2   Methods

4.2.1   Study Site

Our study site is located in the upper Dischma valley in the Swiss Alps near Davos. The investigated Gletschboden area (approximately 1 km south of Dürrboden) is almost flat with an extent of around 500 x 400 m (Fig. 4.1).
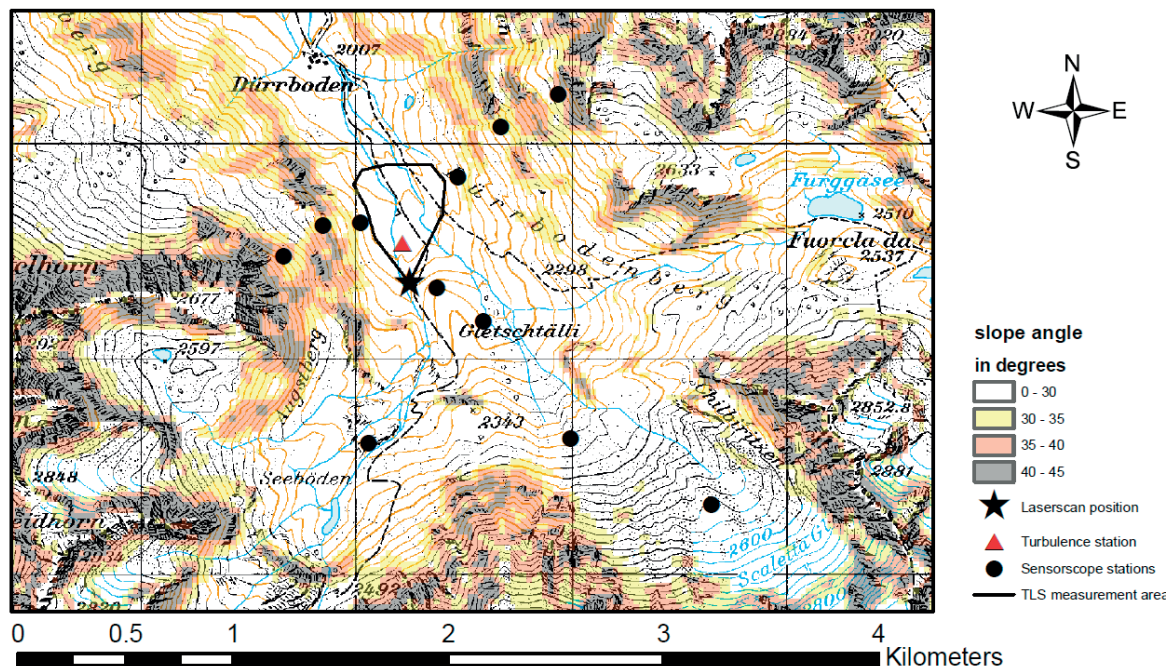
Fig 4.1 Measurement setup at the Gletschboden area in the upper Dischma valley: Mobile meteorological stations (black circle), terrestrial laser scanning (TLS) position (black asterisk), turbulence station (red triangle) and the TLS measurement area (solid black line) are shown.

Earlier studies during the extensive field campaign (Dischmatal Klimauntersuchungen), lead to several publications focusing on valley-scale meteorology in the 1980s (Egger, 1983; Hennemuth, 1986). More recent studies (Lehning et al., 2006; Bavay et al., 2009) were conducted in the Dischma valley focusing on hydrological questions and climate change. Additionally, the valley has been used to investigate the influence of locally varying radiation on runoff as a function of catchment size (Comola et al., 2015) and runoff temperatures (Gallice et al., 2016). An extensive field campaign, the Dischma experiment, has been conducted in the Dischma valley from 2014 to 2016 focusing on small-scale snow atmosphere interactions over patchy snow-covers in the late stage of the ablation period (Mott et al., 2017) and assessing small-scale variations in the atmospheric flow field in the surroundings of a steep rock wall and its influence on snow accumulation (Gerber et al., 2017).

Experimental results from the Gletschboden area are transferred to different horizontal scales in Section 4.3.6 by using artificial snow distributions for an idealized flat test site, which is described in detail in the companion paper (Schlögl et al., submitted). Additionally, earlier data from the Wannengrat field site (Mott et al., 2015) are re-analysed.

4.2.2   Measurements

4.2.2.1   *Terrestrial laser scanning*

We recorded snow ablation maps with a terrestrial laser scanner (TLS, Riegl-VZ6000) at the Gletschboden area (Fig. 4.1). The TLS position is located approximately 30 vertical meters above the Gletschboden area at a northerly exposed slope. In total 44 TLS measurement sets have been conducted in three consecutive years 2014-2016 (2014: 13 measurements; 2015: 17 measurements; 2016: 14 measurements). The TLS system has a single-point measurement frequency of 300 kHz and a beam divergence of 0.007°. This set-up allows a horizontal resolution of approximately 0.01 m in 100 m distance to the TLS position. One scan of the Gletschboden area lasts approximately 15 minutes. The travel time from the laser scanner towards the surface is recorded and afterwards converted into a point cloud of distances. 5 reflectors located at the Gletschboden area and in the closer surroundings were additionally scanned during each measurement to transform the point cloud from the scanner own coordinate system into Swiss coordinates. We tested the accuracy of the TLS measurement by repeating measurements from the same scan position and found a mean absolute error (MAE) of 0.5 ± 0.2 cm. Therefore, the small-scale variability of snow ablation rates is measured with high accuracy. Additionally, orthophotos have been created by using pictures recorded from the TLS in order to provide snow mask maps. Snow and bare ground can be distinguished by the RGB colour information of the orthophoto. Cells with blue band information greater than 175 were categorized as snow and all cells with values smaller or equal 175 were categorized as bare ground. The complete dataset can be found on ENVIDAT (http://dx.doi.org/10.16904/envidat.25).

4.2.2.2   Eddy covariance measurements

Eddy covariance measurements have been conducted at the Gletschboden test site in the ablation periods of three consecutive years 2014-2016. A vertical setup of three 3-D ultrasonic anemometers were installed at the Gletschboden area using a DA-600 Kaijo Denki for the lowermost measurement (0.3 m), using a CSAT3 (Campbell Scientific, Inc.) for the measurement in 2 m above the snow and a Young sonic in 3.2 m above the snow. Note that the height of the measurement varied during the three ablation periods. The post-processing of the eddy covariance measurements includes despiking, rotating of the coordinate system and a frequence response correction, which is described in detail by Mott et al. 2017. Turbulence data of all data sets were averaged to 30-min intervals. The complete dataset can be found on ENVIDAT (http://dx.doi.org/10.16904/10).

4.2.3   Models

The physics-based surface process model Alpine3D has been used to simulate snow melt processes. Alpine3D is a spatially distributed, three-dimensional (atmospheric) model for analysing and predicting dynamics of snow-dominated surface processes in mountainous topography. It includes modules for snow cover (SNOWPACK), vegetation and soil, snow transport, radiation transfer and runoff which can be enabled or disabled on demand (Lehning et al., 2006).

Snow ablation rates from TLS measurements were compared with Alpine3D snow ablation rates at the Gletschboden test site. The model is forced by 10 mobile meteorological stations which are located in the near surrounding of the simulated test site and have been installed specifically for this study. Meteorological fields (air temperature and wind velocity) are interpolated to a 1 x 1 m horizontal grid by inverse distance weighting. Turbulent fluxes were calculated with the Monin-Obukhov bulk formulation (Blanc, 1987), using the univariate stability correction developed in Schlögl et al. (2017) and an aerodynamic roughness length over snow of 0.007 m. Note that the aerodynamic roughness length over bare ground is larger than over snow. In 2015, incoming longwave radiation is measured (instead of parametrized in 2014 and 2016) at one full energy balance station installed at the Gletschboden area close to the turbulence station. Alpine3D is initialized with measured snow depth distributions from TLS measurements exemplarily for several days in the ablation period.

As Alpine3D is limited to pointwise simulating the vertical exchange between the ground and the atmosphere and does not include lateral transport of heat and moisture in the atmosphere except if the drifting and blowing snow module is switched on (Groot Zwaaftink et al., 2011, 2013), the small- scale variability in snow ablation rates during patchy snow covers could not be resolved (Mott et al., 2013). Note that lateral transport calculations in Alpine3D are based on external meteorological fields, which are very expensive to obtain and therefore not a common setup for hydrological simulations. Very high resolution three-dimensional atmospheric simulations are discussed in a companion paper (Schlögl et al., submitted). We introduce a footprint approach in the following subsection to account for the local advection of sensible heat.

4.2.4   Footprint approach

Flux footprints have been analytically calculated in the 1990s by solving the diffusion equation (Schuepp et al., 1990). They proposed that the flux footprint can be calculated by considering the cumulative normalized contribution to flux measurements (CNF):
$CNF_z(x_L) = \exp\left(-\frac{U\,z}{u_*\,k\,x_L}\right)$. This fundamental theory was deployed for eddy-covariance measurements revealing the origin of the measured turbulence as a function of the measurement height, atmospheric stability and wind speed. For neutral conditions, the flux contribution (FC) is the derivate of the CNF with respect to the upwind fetch distance x_L and shown for two different measurement heights (Figure 2):

$$FC_z(x_L) = \frac{U\,z}{u_*\,k\,x_L{}^2}\exp\left(-\frac{U\,z}{u_*\,k\,x_L}\right) \tag{4.1}$$

where U is the wind speed, z is the measurement height, u_* is the friction velocity and k is the von Kàrmàn constant. Note that the dimension of the flux contribution is [m^{-1}], whereas the CNF (after integrating over the fetch distance) is dimensionless.
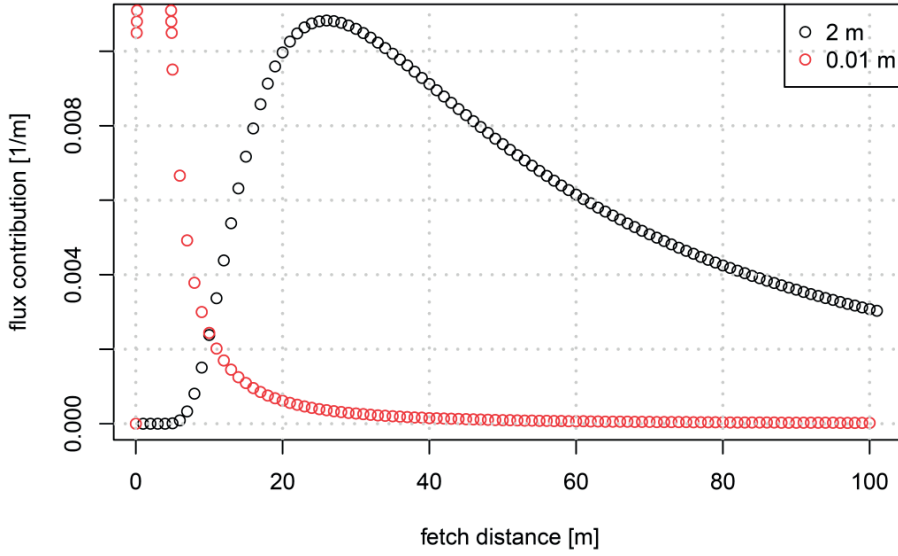
Fig 4.2 Flux contribution (FC) [m^{-1}] as a function of the fetch distance for a measurement height of 2 m (black) and a theoretical measurement height of 0.01 m (red). In this example the wind velocity is 1 m s^{-1} and the friction velocity is 0.1 m s^{-1}.

The footprint approach is adapted in our study to calculate the fetch dependent near-surface air temperatures (instead of turbulent sensible heat fluxes) for a height of $z = 0.01$ m above the surface in Alpine3D. We chose $z = 0.01$ m to realize a strictly monotonic decreasing flux contribution for a horizontal resolution of 1 m of the model grid, despite the fact that footprints decrease very close to the snow/bare ground transition (Fig. 4.2). Thus, the flux contribution is largest for the smallest fetch distance (1 m). The strictly monotonic decreasing flux contribution ensures that the additional energy from lateral transport processes is largest at the snow/bare ground transition and gradually decreases further inside of the snow patch. A (theoretical) decrease in the horizontal resolution from 1 m to e.g. 0.01 m could lead to a non-strictly monotonic decreasing flux contribution (see Fig 4.2). For those situations, the height z needs to be adapted again in order to realize a strictly monotonic decreasing flux contribution. The adapted footprint approach uses surface temperatures from Alpine3D as model input. To our knowledge, footprints for (surface) temperatures have not been developed yet, but separate scalar footprints exist, where concentrations instead of vertical fluxes are used to solve the diffusion equation (Schmid, 1994; Kljun et al., 2002). The maximum contribution of scalar footprints to the sensor/target pixel is located further upwind than for flux footprints. However, we used flux footprints instead of scalar footprints as a model for our weighting functions, as surface temperatures can be treated in a similar way as vertical fluxes. Monin-Obukhov bulk formulation suggests that – at first approximation - vertical fluxes of sensible heat are linearly dependent on the temperature difference between the surface and the air above. Vertical fluxes of sensible heat are therefore also linearly dependent on surface temperatures differences under the assumption of a constant air temperature and wind velocity at the reference height ($z = 2\,m$). This assumption of a constant air temperature and wind velocity field at the reference height is only valid for small and flat test sites as the Gletschboden area and cannot be made for larger distances e.g. for larger snow patches. The calculation of the near-surface air temperature field ($TA(0.01\,m)_{xy}$) contains three main analysis steps, which are explained in the following and were conducted for each pixel ($)_{xy}$ in the model domain and each time step of the model:

1. 30-min mean wind direction and the variation of the wind direction are estimated from the measurements at the eddy-covariance tower. We assume that the measured wind direction at the eddy-covariance tower is spatially homogenous inside the model domain. This assumption is a necessary requirement as only one meteorological station is available inside the model domain. However, a constant mean wind direction is a reasonable approximation of the true atmospheric conditions for our small and flat test site. Note that this approximation cannot be made for larger catchments. We define an upwind sector based on the wind direction and variation of the wind direction for each pixel in the model domain and each analysis time step. The width of the upwind sector corresponds to the standard deviation of the 30-min wind direction. Modelled surface temperatures from Alpine3D are used as input for the temperature footprint approach. All surface temperature pixels outside the upwind sector are not considered, whereas the surface temperature pixels inside the upwind sector are averaged as a function of the fetch distance ($\overline{TSS(x_L)}_{xy}$) (Fig. 4.3c).
2. The flux contribution (Eq. 4.1) is calculated for each time step and assumed to be equal for the entire model domain (Fig. 4.2, red dots). Measured wind speeds at the eddy-covariance tower and modelled friction velocity from Alpine3D are used to determine the flux contribution.
3. Finally, averaged surface temperatures $\overline{TSS(x_L)}_{xy}$, which are a function of the fetch distance x_L, have been multiplied with the flux contribution function $FC_{0.01}(x_L)$ (Eq. 4.1) and integrated over the fetch distance (Eq. 4.2).

The air temperature increase $\Delta TA(0.01\ m)_{xy}$ due to lateral heat transport processes is described in Eq. 4.2 and is always positive, as the mean surface temperature of the entire model domain in the late ablation period is always larger as the freezing point temperature $TA_f = 273.15$ K.

$$\Delta TA(0.01\ m)_{xy} = \int_0^\infty FC_{0.01}(x_L)\,\overline{TSS(x_L)}_{xy}\,dx_L - TA_f \tag{4.2}$$

Near-surface air temperature fields $TA(0.01\ m)_{xy}$ are calculated for the late ablation period by adding $\Delta TA(0.01\ m)_{xy}$ to the interpolated standard Alpine3D air temperature field in 2 m above the surface ($TA(2.0\ m)_{xy}$) (Eq. 4.3):

$$TA(0.01\ m)_{xy} = TA(2.0\ m)_{xy} + \Delta TA(0.01\ m)_{xy}. \tag{4.3}$$

Afterwards, near-surface air temperature fields $T_A(0.01\ m)_{xy}$ are used to calculate turbulent sensible heat fluxes with the Monin-Obukhov bulk formulation. Note that this approach is strongly sensitive to an accurate albedo of the bare ground and accurate information on the spatial distribution of the snow cover at time of peak accumulation.

The different analysis steps of the temperature footprint approach are exemplarily shown for one time step (21.05.2014 12 UTC) and one pixel ($x = 200, y = 150$) (Fig. 4.3). Modelled surface temperatures over snow are typically at the freezing point and typically much larger over bare ground during noon (Fig. 4.3a). The upwind sector is defined in Fig. 4.3b, based on an almost southern wind direction (171°) with a 30-min variation in the wind direction of 10°. The median of surface temperatures (inside the upwind sector) as a function of the fetch distance from the target pixel ($x = 200, y = 150$) indicate two snow-free areas upwind of the target pixel (Fig. 4.3c, black dots). The first snow-free area is located 25-75 m away from the target pixel and extremely influences $TA(0.01\ m)_{200,150}$, shown by the increase of $\int_0^{x_L} FC_{0.01}(x'_L)\overline{TSS(x'_L)}_{200,150}\,dx'_L$ (Fig. 4.3c, blue line) from 273.15 K to 276 K in the area of enhanced surface temperatures. The second snow-free area is located 210-230 m away from the target pixel. As the flux contribution in this area is almost 0, large surface temperatures from the snow-free ground do not influence $TA(0.01\ m)_{200,150}$, shown by a constant $\int_0^{x_L} FC_{0.01}(x'_L)\overline{TSS(x'_L)}_{200,150}\,dx'_L$ (Fig. 4.3c, blue line) between 210-230 m fetch distance. The term $\int_0^\infty FC_{0.01}(x_L)\overline{TSS(x_L)}_{200,150}\,dx_L$ is equal to 276.45 K, which implies an air temperature increase of 3.3 K due to the advection of warm air from the bare ground towards the target pixel. Finally, the near-surface air temperature field in 0.01 m above ground for all pixels in the model domain is shown in Fig. 4.3d.
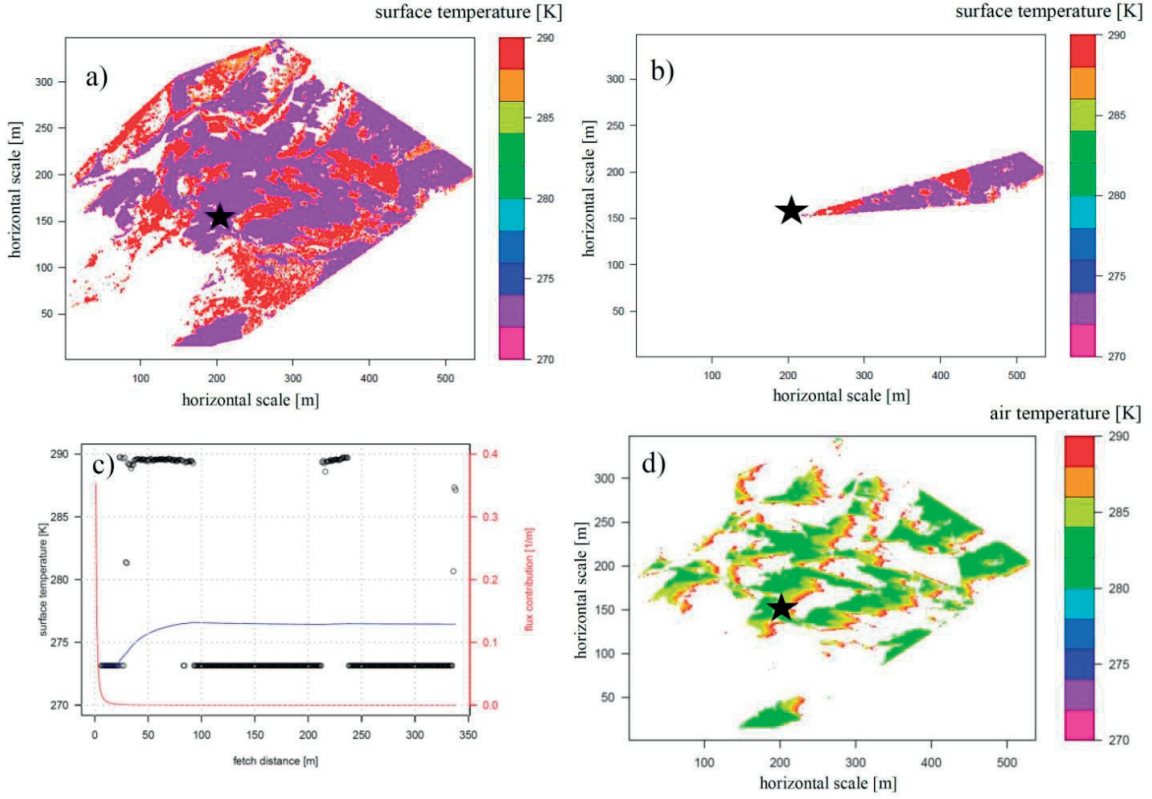
Fig 4.3 Stepwise explanation of the temperature footprint approach for one time step (21.05.2014 12 UTC): a) Alpine3D modelled surface temperatures [K] at the Gletschboden area. b) Upwind sector shown exemplarily for one pixel ($x = 200, y = 150$, black star). c) Averaged surface temperatures as a function of the fetch distance for a chosen pixel $\overline{TSS(x_L)}_{200,150}$ (black points), $\int_0^{x_L} FC_{0.01}\left(x_L'\right)\overline{TSS(x_L')}_{200,150} \, dx_L'$ [K] (blue line, both left y-axis) and flux contribution [m^{-1}] (red line, right y-axis). d) Near-surface air temperatures after the application of the temperature footprint approach [K] for the Gletschboden area. White colours indicate bare ground or measurement shadows.

To validate the approach with measured turbulent sensible heat fluxes at one specific point, the measurement height was chosen to be the mid-level height of the eddy-covariance measurements (2.0 m). We recalculated modelled surface turbulent sensible heat fluxes from Alpine3D (instead of the modelled surface temperatures) to conduct this validation (Section 4.3.5.1). This validation contains the same analysis steps as for the temperature footprint, but is based on modelled surface turbulent sensible heat fluxes in Alpine3D:

$$Q_s(2\,m)_{xy} = \int_0^\infty FC_{2.0}(x_L)\overline{Q_s(x_L)}_{xy} \, dx_L \qquad (4.4)$$

4.3 Results

4.3.1 Limitations of Alpine3D snow ablation rates

As long as the SCF is larger than 90 %, Alpine3D sufficiently captures daily snow ablation rates (Fig. 4.4). Both, daily snow ablation rates recorded from TLS and snow ablation rates from Alpine3D simulations show on average 0.05 m/day snow ablation. We found almost no systematic bias and a mean absolute error of 0.02 m/day in the Alpine3D simulation. However, the spatial variability in measured snow ablation rates is around one order of magnitude larger than for the snow ablation rates in Alpine3D.

Fig 4.4 Snow ablation rates [m/day] for the 06.05.2014 at the Gletschboden area in the upper Dischma valley: (a) Terrestrial laser scanning measurements, (b) Alpine3D model results, (c) model-measurement.

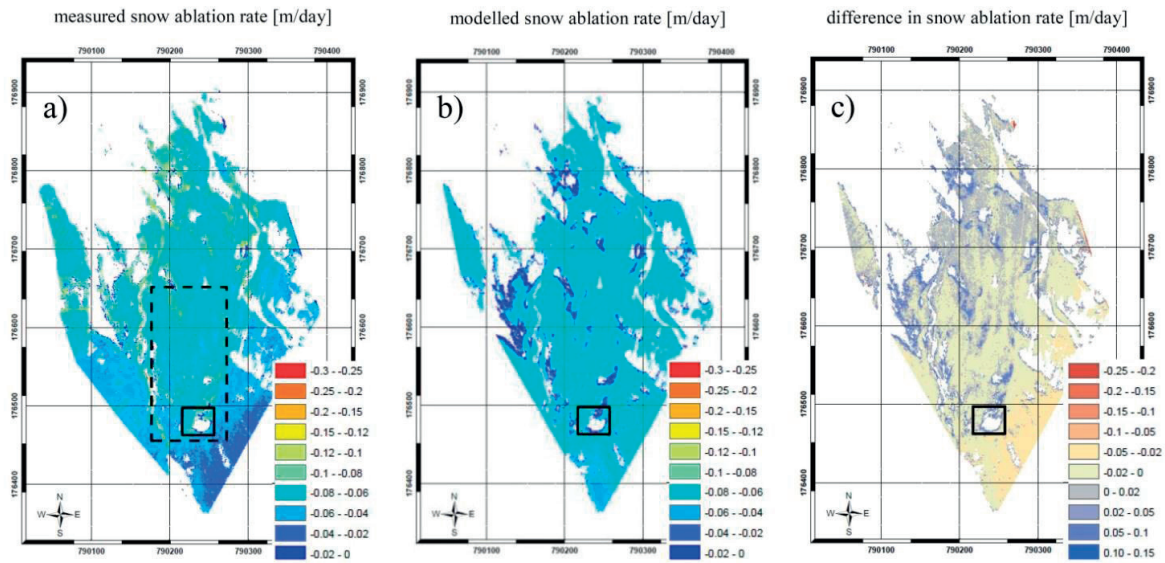Even in this early stage of the ablation period, local heat advection is observed around the snow-free area below the toe of the northern exposed slope (marked by the black rectangle in Fig. 4.4). Enhanced snow ablation rates were recorded with the TLS measurement in the close vicinity of snow-free areas, which are not resolved in the model (Fig. 4.4). This spatio-temporal dynamic in the melt-out of the snow cover is mainly a result of the end of winter snow distribution that is typically characterized by shallow snow covers at ridges and deep snow-covers in local depressions. Ridges become snow-free first and the near-surface atmosphere over snow-free areas at ridges is heated more than over persistent snow patches in local depressions, as the albedo of the bare ground is lower than the albedo of snow. Warmer air above the snow-free surface is efficiently transported towards the edge of the snow patches for high wind velocities, resulting in enhanced snow ablation rates at the upwind edge of the snow patches (Fig. 4.4a). Stable internal boundary layers develop at the border between bare ground and snow due to changes in surface temperatures and grow along the fetch (Garatt, 1990, Mahrt and Vickers, 2005; Mott et al., 2011, 2016). Mott et al. (2017) showed that decoupling of the near-surface atmospheric layers from the surrounding warmer air is favoured by the development of SIBLs. The complex interaction between the atmospheric boundary layer and the heterogeneous land-surface is therefore not resolved in our traditional model approach, as Alpine3D calculates the energy balance for each pixel separately based on the assumption of a boundary layer in equilibrium. This approach does not account for spatially varying boundary layer fields.

4.3.2   Above-average snow ablation rates at the upwind edge of snow patches

We assessed the increase of measured snow ablation rates at the upwind edge of the snow patch by analysing TLS snow ablation rates as a function of the fetch distance exemplarily for one day (21.05.2014) in the late ablation period 2014 with an already patchy snow cover ($SCF = 40$ %) (Fig. 4.5). For this example, we measured a mean snow height change of approximately 0.09 m/day at eight selected snow patches during a southern flow with a mean wind speed of 5 m s^{-1}. On the upwind edge of these snow patches, the maximum snow ablation rates increase to 0.11 m, which corresponds to 25 % larger snow ablation rates at the upwind edge due to local warm air advection. Additionally, we analysed a second ablation day (25.05.2014) in the late ablation period 2014 during a southern flow with a $SCF = 20$ %. We found locally 30 % larger snow ablation rates at the upwind edge of the snow patch. As the development of separate snow patches did not occur in the ablation period 2015 due to a long-lasting strict snow line and 2016 was determined by a rapid decrease of the snow cover fraction (Mott et al., 2017; Appendix A), the investigation above could only be provided for the two ablation days in 2014.
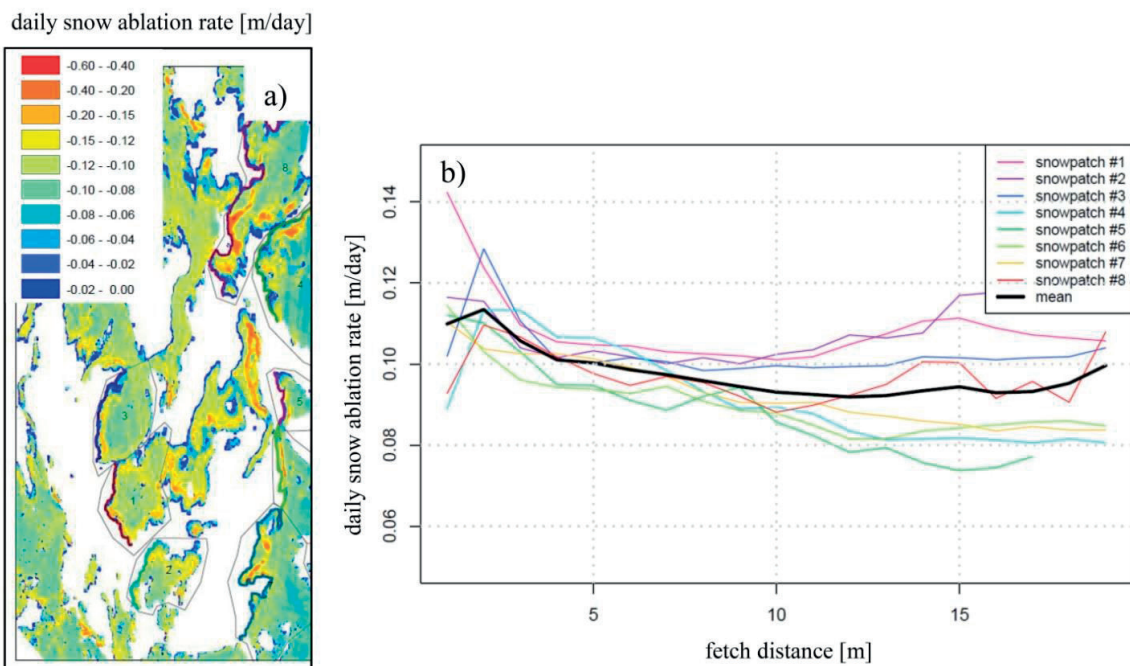
Fig 4.5 Snow ablation rates [m/day] for 21.05.2014 at the Gletschboden test site. The dashed box in Figure 4.4a shows the location of the investigated area. Eight different snow patches (a) were analysed to assess the daily snow ablation as a function of the fetch distance (b).

In both experimental cases, local warm air advection influences snow ablation rates over a fetch distance of 5 m downwind the leading edge, which is in agreement with Mott et al. 2011. However, this distance increases up to 15 m with increasing wind speed (Mott et al. 2011). An increase in mean snow ablation rates in the late stage of the ablation period due to an increase of the mean air temperature of the catchment is analysed in the companion paper Schlögl et al., submitted.

The local increase of snow ablation rates at the upwind edges contribute with 4 % ($SCF = 40$ %, 21.05.2014) and with 6 % ($SCF = 20$ %, 25.05.2014) to the total daily snow ablation rate of the entire catchment. The rather smaller contribution to the total snow ablation of the entire Gletschboden area in comparison with the enhanced snow ablation directly at the upwind edge of the presented snow patch is a result of the fetch distance distribution. As an example, for a given snow cover distribution at the Gletschboden area with a $SCF = 40$ % only 30 % of the snow-covered pixels have a smaller fetch distance than 5 m and are directly affected by local heat advection. A large fraction of snow-covered pixels further inside the snow patches is not affected by the leading edge effect (Fig. 4.S1). Thus, the contribution of local heat advection to the mean snow ablation on a catchment scale strongly depends on the fetch distance distribution. The fetch distance distribution itself is heavily dependent on the mean snow patch size. As the Gletschboden area is characterized by a rather homogeneous terrain, snow patches are relatively continuous with a mean snow patch size of approximately 30 x 30 m for $SCF = 40$ % and 20 x 20 m for $SCF = 20$ %.

The contribution of local heat advection to the mean snow ablation is expected to increase for regions with more heterogeneous surface characteristics, driving smaller snow patch sizes. Our calculations suggest that this increase in the contribution of local heat advection to the mean snow ablation rates can reach up to 12 % for a mean patch size of 10 x 10 m and converges to the measured increase in snow ablation rates at the leading edge of 25-30 % in the limiting case of a snow patch size smaller than 4 x 4 m (not shown). We found above-average snow ablation rates in comparison with snow ablation rates further inside the snow patch. However, the effect of local heat advection contributing to snow ablation additionally includes an increase in mean air temperatures and larger snow ablation rates further inside the snow patch, which are not directly affected by the "leading edge effect" but originated from a positive snow-albedo feedback and dirt or debris on the snow surface. Above-average snow ablation rates further inside the snow patch (in comparison with a continuous snow cover) cannnot be shown from our TLS measurements, but are analysed in the companion paper (Schlögl et al., submitted). In this study, near-surface air temperature fields were calculated with the non-hydrostatic atmospheric model ARPS for different snow cover fractions and used as input for the hydrological model Alpine3D, in which turbulent heat fluxes were calculated with the Monin-Obukhov bulk formulation. Numerical results reveal that above-average snow ablation rates further inside of the snow patch (in comparison to a continuous snow cover) are sensitive to varying snow cover fractions and wind velocities, but do not depend on the mean snow patch size.

4.3.3 Representation of snow patches in Alpine3D before the footprint correction

The representation of the spatial and temporal dynamics of snow patches in Alpine3D is assessed in the late ablation period. The model performance was statistically analysed by introducing a contingency table. The false alarm rate (model predicts snow, although the area is snow-free in the observation) is of special interest, as this model error can be related to the missing advective heat transport. The proportion correct (correctly forecasted pixels), miss rates and false alarm rates are calculated for two ablation periods 2014 and 2015 as a function of the SCF (Fig. 4.6). The model was initialized with the peak of winter snow distribution recorded with TLS mid of April at a horizontal grid resolution of 1 m.
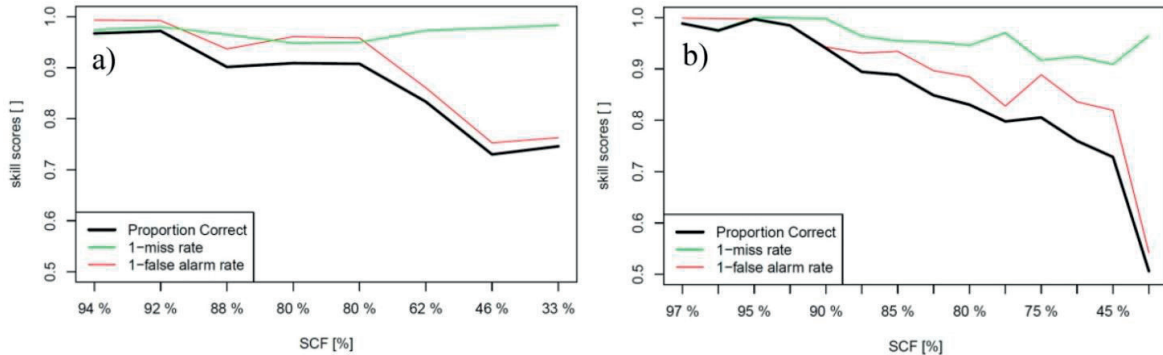

Fig 4.6 Skill score for 2014 (a) and 2015 (b) as a function of different snow cover fractions (SCF) for the Gletschboden area. Correctly forecasted pixels (black) and the error due to misses (green) and false alarm (red) are shown.

In both years, the proportion correct decreases with decreasing SCF. The proportion correct is above 0.95 as long as the snow cover is still continuous and decreases to 0.7 for SCF > 50 %. In 2015, the values even decrease towards 0.5 for SCF smaller than 50 %. This decrease in the proportion correct is mainly caused by the error due to the false alarm rates. A significant part of the false alarm rates is the result of the missing lateral transport of heat and moisture. Uncertainties in the parametrization of the incoming longwave radiation and uncertainties in the aerodynamic roughness length of snow and applied stability corrections are also assumed to contribute to differences in measured and modelled snow-cover distribution.

We assume that other external error sources (e.g. the small-scale spatial variability of the radiation or wind velocity in the catchment) can be neglected, as the investigated catchment is almost flat. However, both external error sources need to be considered in complex terrain, where turbulent sensible heat fluxes are strongly determined by slope winds.

4.3.4 Resolving small-scale variations in snow ablations rates by applying the temperature footprint approach

Near-surface air temperatures are recalculated with the temperature footprint approach for six analysis days (20.05.2014-25.05.2014) by initializing the model with the measured TLS snow distribution from 19.05.2014. We chose an initial snow distribution very close to the starting date of the analysis period instead of an initial snow distribution at the peak of winter in mid-April. This set-up better represents the location and size of the snow patches for the starting date of the analysis period and prevents a bias of around 20 % in the correct model prediction of the snow patches by initialising the model with a snow cover distribution in mid-April, mainly caused by the false alarm rate (Fig 4.6a).

Near-surface air temperatures are exemplarily shown for the 20.05.2014 12 UTC (Fig. 4.7 upper panels). Standard Alpine3D air temperatures over snow show almost no spatial variability ($\Delta TA = 0.1$ K) (Fig. 4.7a). After applying the temperature footprint approach however, near-surface air temperatures at a height of 0.01 m above the surface at the upwind edge of the snow patches are larger compared to further inside the snow patch ($\Delta TA = 6.1$ K) (Fig. 4.7b). For this specific example a southern flow leads to larger near-surface temperatures and larger snow ablation rates at the southern edge of the snow patch. For other days (e.g. 06.05.2014; Fig. 4.4) we observed larger daily snow ablation rates in all directions around the snow patch caused by changing diurnal wind directions. The changing diurnal wind directions at the Gletschboden area are a typical phenomenon in larger valleys, where anabatic winds during noon follow katabatic winds in the morning (Hennemuth, 1986; Mott et al., 2017). By applying the temperature footprint approach, we were able to provide snow ablation maps where the small-scale variation as observed in the TLS measurements could be resolved.
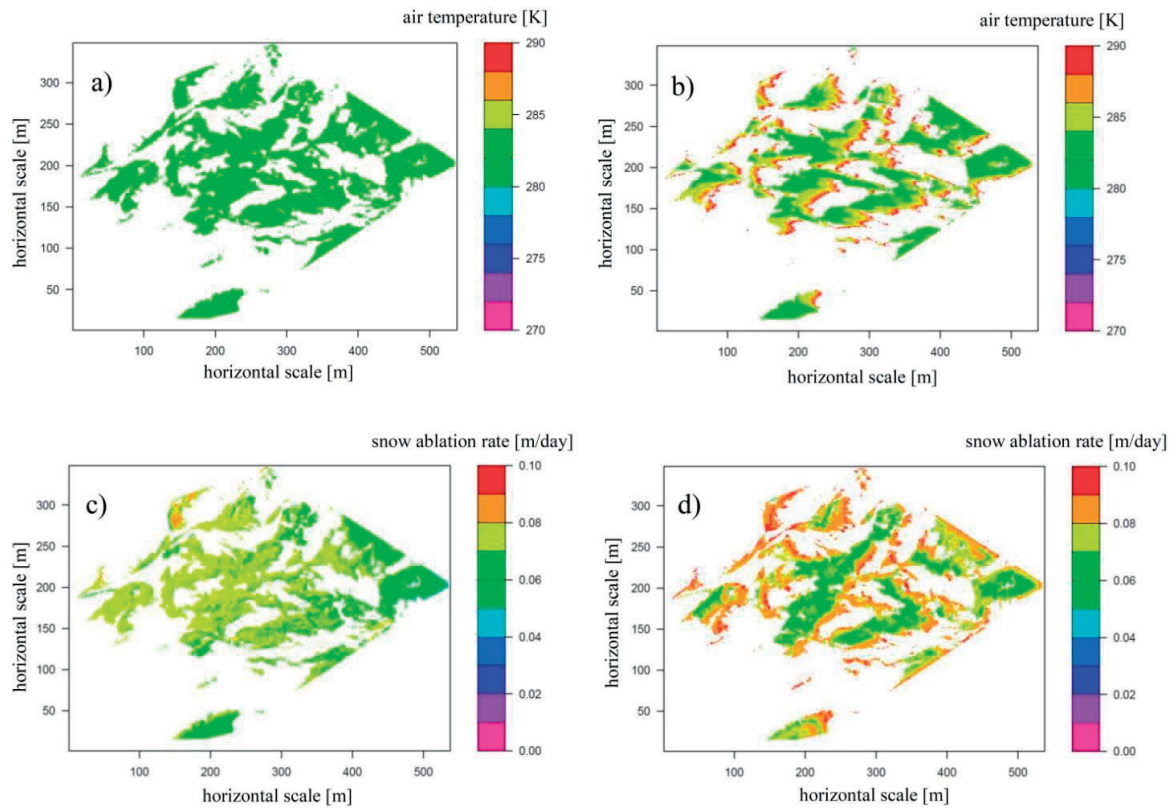
Fig 4.7 Near-surface air temperatures [K] (top panels) for the Gletschboden area for the 20.05.2014 12 UTC as input in Alpine3D before applying the temperature footprint approach (a) and after applying the temperature footprint approach (b). Modelled snow ablation rate [m/day] for the Gletschboden area for the 20.05.2014 (bottom panels) before applying the temperature footprint approach (c) and after applying the temperature footprint approach (d). White colours indicate bare ground or measurement shadows.

In the following we analyse the increase of the mean near-surface air temperature $\overline{\Delta TA(0.01\,m)}_{xy}$ over snow-covered pixels by applying the temperature footprint approach (Fig. 4.S2). The air temperature increase $\overline{\Delta TA(0.01\,m)}_{xy}$ is highly correlated with the surface temperature of the adjacent bare ground. The adjacent bare ground is heated after sunrise, which leads to an increase in values of $\overline{\Delta TA(0.01\,m)}_{xy}$. Values of $\overline{\Delta TA(0.01\,m)}_{xy}$ increase from 6 K (for a $SCF = 40$ %) to 14 K (for a $SCF = 20$ %) as a function of the SCF at noon. We found a 24 hours mean value of $\overline{\Delta TA(0.01\,m)}_{xy} = 5.3$ K for six analysis days (20.05.2014-25.05.2014), with a mean wind velocity of 4 m s^{-1} and a mean surface temperature of the adjacent bare ground of 282 K. The strong sensitivity of the temperature footprint approach to surface temperatures of the adjacent bare ground and SCF is further discussed in Section 4.3.6 for an idealized test site.

4.3.5   Validation of the footprint approach

We analysed the model performance of Alpine3D before and after applying the footprint approach with respect to a validation of turbulent sensible heat fluxes for an individual location and a validation of two-dimensional snow mask maps and snow ablation rates.

4.3.5.1   Turbulent sensible heat fluxes

Modelled turbulent sensible heat fluxes are sufficiently simulated for $SCF > 60$ %, but once the snow cover gets patchy and the fetch distance over snow decreases, measured turbulent sensible heat fluxes in 2 m above the surface are typically directed upwards, whereas modelled surface turbulent sensible heat fluxes are directed downwards (Fig. 4.8a). This difference is mainly caused by the development of a SIBL over snow patches, which is not resolved in the model. As turbulent fluxes are calculated with MOST, which is exclusively applicable for constant flux layers extending to the first grid point in the atmosphere or the level of meteorological measurements, MOST is typically not applicable over patchy snow covers.

The model performance of turbulent sensible heat fluxes for a single point could be significantly improved by applying the flux footprint approach (Fig. 4.8b). Modelled turbulent sensible heat fluxes after applying the flux footprint approach represent the flux in 2 m above the surface and are validated against eddy-covariance measurements at the same height. For this example, the measurement height is located above the height of the SIBL and the unstable boundary layer in upwind direction of the snow patch is taken into account by applying the flux footprint approach. Hence, model results after applying the flux footprint approach are more accurate to measured turbulent heat flux at the eddy-covariance tower than modelled surface turbulent sensible heat fluxes with MOST. This example clearly demonstrates that an eddy-covariance measurement height of 2 m above the surface in the late ablation period is located to far from the surface in order to get information on turbulent heat exchange above the melting snow surface.
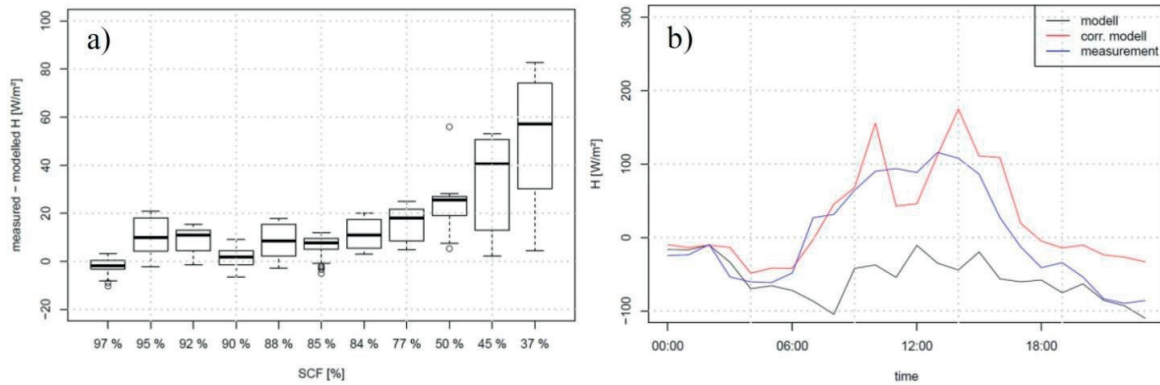
Fig 4.8 Difference between modelled surface turbulent sensible heat fluxes and measured turbulent sensible heat fluxes in 2 m above the surface [W m^{-2}] at the eddy-covariance tower as a function of the snow cover fraction (SCF) [%] (a). Turbulent sensible heat fluxes for 18.05.2015 (SCF = 37 %) at the eddy-covariance tower (b): The eddy-covariance measurement in 2 m above the surface is shown in blue, Alpine3D surface turbulent sensible heat flux is shown in black, turbulent sensible heat flux in 2 m above the surface after applying the flux footprint approach is shown in red.

4.3.5.2   Snow mask maps

Snow mask maps have been analysed before and after applying the temperature footprint approach (Fig. 4.9) to test the improvement in representing snow patches in Alpine3D. Alpine3D was run in this specific example for two days (21-22.05.2014), initialized with the snow distribution of the TLS measurement from 21.05.2014. We choose this short period of two days in order to ensure no bias in mean snow ablation rates between model and TLS measurement. By initialising Alpine3D with snow distributions at the peak of winter mid of April, the proportion correct for the Gletschboden area is below 75 % at end of May (Fig. 4.6a). As this skill score is strongly dependent on different boundary layer parameters (e.g. the aerodynamic roughness length of snow or the stability correction) and correct input radiation, the improvement in Alpine3D model simulations by applying the temperature footprint approach would be masked by those uncertainties.

The improvement in the model performance is clearly visible by comparing Fig. 4.9a and Fig. 4.9b and is analytically expressed by calculating the false alarm rates. False alarm rates in the late ablation period are around 6 % before applying the temperature footprint approach and could be decreased to around 3 % after applying the temperature footprint approach. Hence, we were able to improve the Alpine3D model performance with respect to the size and location of snow patches in an Alpine catchment.

Fig 4.9 Snow mask map for the Gletschboden area for the 22.05.2014. Model correctly provides snow (dark blue), model correctly provides bare ground (light blue). False alarms are shown in red, misses are shown in light green. White 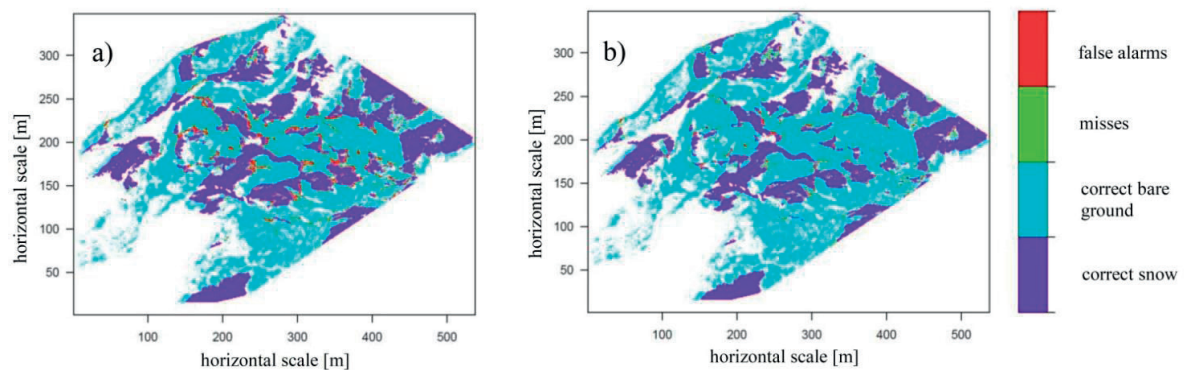colours indicate no data. Snow mask maps are shown without the temperature footprint approach (a) and with the temperature footprint approach (b).

4.3.5.3   Local snow ablation rates

The accuracy of the temperature footprint approach to local snow ablation rates in spring is shown in Fig. 4.10. Homogeneous standard Alpine3D snow ablation rates without applying the temperature footprint approach (Fig. 4.4) do not resolve the enhanced snow ablation rates on the upwind edge of the snow patch (Fig. 4.10a). Enhanced snow ablation rates at the upwind edge of the snow patch could be partly resolved by applying the temperature footprint approach. The improved representation of snow ablation rates at the upwind edge of the snow patches could also be observed for measured snow ablation rates above 0.15 m/day (Fig. 4.10b). While modelled standard Alpine3D snow ablation rates stay constant at measured snow ablation rates around 0.15 m/day, snow ablation rates additionally increase for measured snow ablation rates above 0.15 m/day after applying the temperature footprint approach. The Pearson correlation coefficient between measured and modelled snow ablation rates could be increased from 0.73 (before applying the temperature footprint approach) to 0.85 after the application of the temperature footprint approach for the two ablation days in 2014.
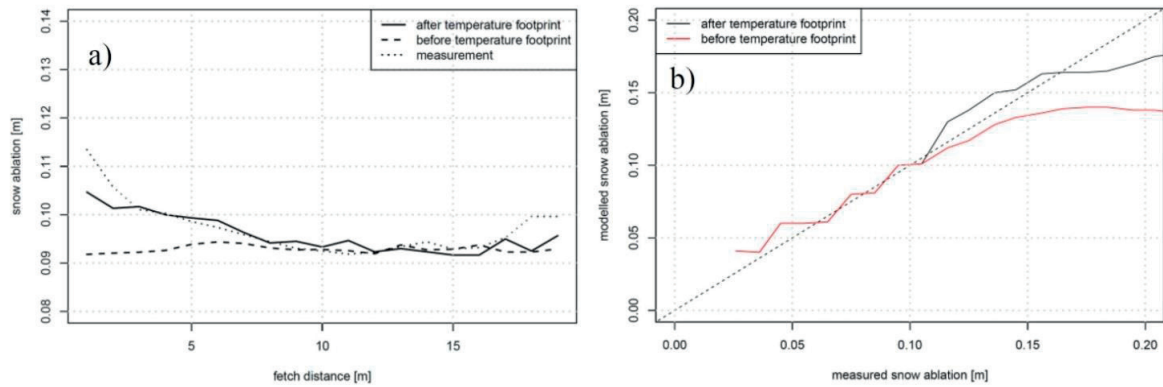
Fig 4.10 Snow ablation rate for the 21.05.2014 [m/day] as a function of the fetch distance [m] (a) for the terrestrial laser scanning measurement and the model results with and without applying the temperature footprint approach. Snow ablation rate [m/day] for the model results (with and without applying the temperature footprint approach) (y-axis) as a function of the measured snow ablation (x-axis) (b).

4.3.6   Sensitivity analysis

We analyse the sensitivity of major results from the temperature footprint approach by creating artificial snow cover distributions with varying SCF from 5-95 % and a varying number of snow patches from 1 to 36 (Schlögl et al., submitted). Additionally to varying snow cover distributions, the horizontal scale of the domain and meteorological conditions (soil temperature and wind velocity) are modified (Table 4.1) and compared with results from the Gletschboden area $(\overline{\Delta T_A(0.01\,m)_{xy}} = 5.3$ K). In summary, we modified 5 parameters in order to assess the differences in enhanced air temperature by the temperature footprint approach $\overline{\Delta TA(0.01\,m)}_{xy}$.

Parameter	Modification	Default	$\overline{\Delta TA(0.01\,m)_{xy}}$
SCF	5 - 95 %	25 %	5.4 K … 0.2 K
#patches	1, 4, 9, 16, 25, 36	16	3.9 K … 5.8 K
Horizontal scale	200, 400, 1000, 2000 m	400 m	5.4 K … 1.2 K
Wind velocity	0.5 - 5 m s^{-1}	2 m s^{-1}	1.5 K … 4.9 K
Soil temperature	2 -15 °C	10 °C	0.7 K … 4.9 K

Table 4.1 Parameter of the sensitivity analysis and $\overline{\Delta TA(0.01\,m)_{xy}}$ (averaged over snow covered pixels).

The value of $\overline{\Delta TA(0.01\,m)}_{xy}$ is equal to 3.3 K using all default values in Table 4.1 and increase from 0.2 K to 5.4 K by varying the SCF from 95 % to 5 % as long as the remaining four parameters were not modified. The values of $\overline{\Delta TA(0.01\,m)}_{xy}$ for the modification of the other parameters are shown in Table 4.1. In summary, four parameters are strongly sensitive to modifications with a

similar spread in values of $\overline{\Delta TA(0.01\,m)}_{xy}$ from 1-5 K, except the modification of the number of snow patches. Modifying more than one parameter could lead to much larger values of $\overline{\Delta TA(0.01\,m)}_{xy}$ than 5 K. A large number of snow patches and small SCF lead to values of $\overline{\Delta TA(0.01\,m)}_{xy}$ up to 10 K (Fig. 4.S3). Increasing the horizontal scale of the model domain lowers values of $\overline{\Delta TA(0.01\,m)}_{xy}$, as the snow patch size increases and a larger percentage of snow-covered pixels is not affected by lateral transport of sensible heat (Fig. 4.S4). High wind velocities and high surface temperatures of the adjacent bare ground lead to large values of $\overline{\Delta TA(0.01\,m)}_{xy}$ (Fig. 4.S5).

4.4 Discussion

We discuss the overall model error caused from neglecting lateral transport processes as found for the Gletschboden area and compare it to a second test site, which has been analysed previously (Mott et al., 2015). The split of the overall model error in a contribution from the pure "leading edge effect" and a contribution from an increase in the mean air temperature due to a positive snow-albedo feedback is maintained (Table 4.2). We presented the contribution of enhanced snow ablation from the pure "leading edge effect" at the upwind edge, for an entire catchment and for an entire catchment and entire ablation period by using snow ablation rates further inside the snow patch as a reference. Based on the analysis of high-resolution snow ablation data of two ablation days at the Gletschboden test site, the local advection of warm air causes 25-30 % more snow ablation at the upwind edge of a single snow patch and contributes 4-6 % to the total snow ablation of the entire catchment. 4-6 % additional snow ablation due to local warm air advection at the patch boundaries has been found for the specific snow distributions observed at the Gletschboden test site for the two analysis days late in the ablation period. The snow cover at the Gletschboden test site in the ablation period remains continuous for around 80 % of the ablation period and SCF rapidly decreases afterwards (Fig. 4.11a). Normalized snow depth ablation rates are almost constant throughout the ablation period and slightly increase towards the end of the ablation period. Based on this information, we found almost no contribution of the pure effect of local heat advection to snow ablation in the first 80 % of the ablation period, as the snow cover remains continuous. In the late ablation period (last 20 %) the contribution of the local heat advection to snow ablation steadily increases from 4 % (SCF = 40 %) to 6 % (SCF = 20 %) and finally up to 25-30 % for a snow patch size smaller than 4 x 4 m. By integrating over the entire ablation period, the consideration of the pure "leading edge effect" increases the total seasonal snow ablation approximately 1-3 %. Note that numbers are valid for the Gletschboden area and may only be transferable to regions with a similar snow patch size distribution.

Reference	Snow ablation rates inside the snow patch			Continuous snow cover
Domain	Leading edge	Entire catchment	Entire catchment and ablation period	Entire catchment and ablation period
Gletschboden	25-30 %	4-6 %	1-3 %	3-5 %
Wannengrat	25-30 %	~ 5 %	~ 4 %	13-15 %
Key Parameters	Bare ground temperature wind velocity	Mean snow patch size	Terrain features	Snow cover fraction wind velocity

Table 4.2: Above-average snow ablation rates [%] for the Gletschboden and Wannengrat test site due to lateral transport processes at the leading edge of a snow patch, for the entire catchment and for the entire catchment and ablation period. Snow ablation rates further inside the snow patch are used as the reference (first three columns). The last column represents the model error when using a continuous snow cover as the reference. Key parameters are additionally shown.

Based on existing data sets and model estimations, we could also estimate the leading edge effect, mean snow patch size and the relative duration of patchy snow covers during the ablation period for a second test site. The Wannengrat area (Davos, Switzerland) is more than one order of magnitude larger than the Gletschboden test site and located in highly complex terrain including steep slopes of different aspects. Further information about the Wannengrat area can be found in Egli et al. (2012) and Mott et al. (2011; 2015). For this analysis, we used mean perimeters of the snow patches for different snow-covered areas estimated in Mott et al., (2015) for the Wannengrat area by simply applying a constant melting rate to the snow depth distribution at peak of winter accumulation, which has been shown to yield correct statistics of important parameters such as SCF (Egli et al., 2012).

Similar to what we found for the Gletschboden test site, Mott et al. (2011) found up to 25-30 % above-average snow ablation rates at the leading edge for the Wannengrat test site. The mean snow patch size during similar SCF values is slightly larger for the Wannengrat test site than for the Gletschboden test site (SCF = 40 %: 30 m Gletschboden vs. 32 m Wannengrat; SCF = 20 %: 20 m Gletschboden vs. 25 m Wannengrat). Also similar to what has been calculated for the test site Gletschboden, above-average snow ablation rates decrease from 30 % at the leading edge to approximately 5 % for the entire Wannengrat catchment for one specific day in the late ablation period.

Patchy snow covers dominate the entire ablation period for the Wannengrat area, where a SCF < 50 % was observed for the last 70 % of the ablation period (Egli et al., 2012; Fig. 4.11b). The Wannengrat test site is characterized by much higher snow depth heterogeneity at peak of winter accumulation than the flatter Gletschboden test site, resulting in a much longer duration of the patchy snow cover phase. By integrating over the entire ablation period, the consideration of the pure "leading edge effect" at the Wannengrat catchment (approximately 4 %) is larger than for the Gletschboden area (1-3 %), particularly due to a much larger relative duration of patchy snow covers.
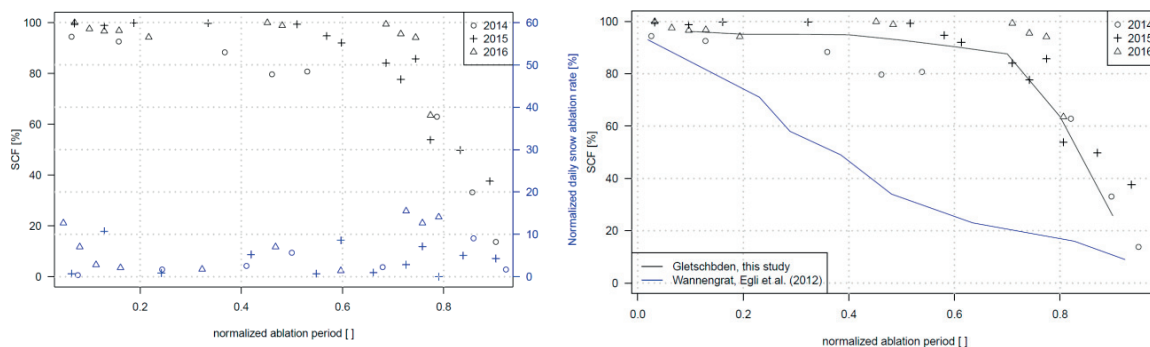

Fig 4.11 Snow cover fraction (SCF) [%] and normalized daily snow ablation rate [%] as a function of the normalized ablation period [ ] for 2014-2016 at the Gletschboden test site (left). SCF [%] as a function of the normalized ablation period [ ] for the Gletschboden test site (black) and the Wannengrat test site (blue, Egli et al., 2012). Results are based on terrestrial laser scanning measurements.

However, estimated model errors described above only consider the "leading edge effect". This local effect does not account for the stronger snow ablation over the entire snow patch area caused by an increase in the mean air temperature due to a positive snow-albedo feedback. This additional effect could not be captured by TLS measurements in this study but is assessed in the companion paper (Schlögl et al., submitted) by analysing the effect of varying snow cover fractions on near-surface air temperatures calculated with the non-hydrostatic atmospheric model ARPS. Numerical results reveal that mean snow ablation rates of snow patches (also for larger fetch distances than represented by the leading edge effect) are strongly sensitive to varying SCFs and wind velocities and robust to the mean snow patch size.

Based on sensitivity runs performed by Schlögl et al. (submitted), we compared mean snow ablation rates for different SCFs to mean snow ablation rates over a continuous snow cover. Mean snow ablation rates for different SCFs in combination with measured relative duration of patchy snow covers at the Wannengrat and the Gletschboden area were used to estimate the overall model error for the entire ablation period.

The overall model error by neglecting lateral transport processes is larger for the Wannengrat area (13-15 %) than for the Gletschboden area (3-5 %) (Table 4.2). Larger model errors for the Wannengrat area can be explained by the high sensitivity of numerical results to varying SCF and the relative duration of a patchy snow cover during the ablation period, which is much larger for the Wannengrat area. At the Gletschboden test site, above-average snow ablation from lateral transport processes can be split in 50 % contribution from the pure "leading edge effect" and 50 % contribution from the mean air temperature increase from a positive snow-albedo feedback. For the Wannengrat area, the positive snow-albedo feedback is larger than the pure "leading edge effect", mainly caused by a small relative duration of patchy snow covers within the ablation period.

4.5   Conclusion

We analysed the limited model performance of the physics based surface process model Alpine3D in calculating snow ablation rates over patchy snow covers, as Alpine3D neglects the spatial variability of near-surface air temperatures over patchy snow covers. Snow ablation rates at the upwind edge of a snow patch are distinctly underestimated in the model, as higher near-surface air temperatures due to local heat advection are not resolved. In this study, we applied a temperature footprint approach on near-surface air temperature fields, a technique originally deployed for eddy-covariance flux analysis. This approach correctly predicts enhanced snow ablation rates at the upwind edge of snow patches, as recalculated fetch-dependent near-surface air temperatures are enhanced in this region. The validation of the footprint approach with respect to turbulent sensible heat fluxes for a single point and two-dimensional snow mask maps and snow ablation rates show that Alpine3D model results could be significantly improved.

Modelled turbulent sensible heat fluxes over patchy snow covers at 2 m above ground are mostly directed upwards during noon after the application of the flux footprint approach and therefore correspond much better to eddy-covariance measurements. In

addition, two-dimensional snow mask maps and local snow ablation rates could be significantly better simulated by applying the temperature footprint approach. However, 25 % larger ablation rates at the upwind edge of the snow patch (in comparison with further inside of the snow patch) could not exclusively be explained by the implemented model approach (Fig. 4.10a). We were able to explain around 15 % (out of 25 %) above-average snow ablation rates at the upwind edge with the temperature footprint approach. This underestimation might be partly caused by an enhanced incoming longwave radiation in regions of enhanced air temperatures, as incoming longwave radiation increases with increasing air temperature. Additionally, the advection of latent heat is not resolved in this approach and could contribute to enhanced snow ablation at the upwind edge (Harder et al., 2017).

The strength of the temperature footprint approach is the universal use (not limited to warm air advection) of the method for horizontal transport processes in hydrological models. One might be interested e.g. in the advection of specific humidity in the air and could use the above described footprint approach.

We analysed the total model error through neglecting lateral transport processes due to the pure "leading edge effect" and due to a mean air temperature increase from a positive snow-albedo feedback for the almost flat test site Gletschboden. We compared values with those estimated for the Wannengrat area in highly complex terrain including slopes of different aspects. The total model error for an entire ablation period by neglecting lateral transport processes is larger for the Wannengrat area (approximately 14 %) than for the Gletschboden area (approximately 4 %) which is explained by the longer patchy snow cover duration at the Wannengrat area. For the Wannengrat area, the increase in the mean air temperature from a positive snow-albedo feedback is larger than the pure "leading edge effect", whereas both effects show a similar contribution to the overall model error for the Gletschboden area.

In summary, we were able to improve Alpine3D snow ablation rates by applying a temperature footprint approach on near-surface air temperatures over patchy snow covers. Enhanced snow ablation rates at the upwind edge of snow patches due to lateral transport of sensible heat could be resolved. The consideration of small-scale lateral transport processes is a fundamental investigation and complements e.g. a study of Helbig et al. 2015, who parametrized snow covered areas on larger scales up to 3 km.

Uncertainties in modelled snow ablation rates are mostly determined by uncertainties in the boundary layer parameters (e.g. roughness length or stability corrections) and the parametrization of the incoming longwave radiation (Schlögl et al., 2016). MOST model errors are strongly dependent on the chosen stability correction and significantly contribute to uncertainties in modelled snow ablation rates even over a continuous snow cover (Schlögl et al., 2017). In this study, we showed that MOST model errors significantly increase over patchy snow covers. In the late ablation period (SCF < 50 %), uncertainties in modelled snow ablation rates are partly determined by the complex interaction between the heterogeneous snow cover and the atmosphere (Mott et al., 2017).

Acknowledgements

4.6   Appendix

Diverse snow patch development

Earlier studies (e.g. Mott et al., 2011) suggest that the snow patch development in an ablation season is similar in different years and snow patches evolve at the same location. We confirm this statement for the ablation periods 2014 and 2016 at the Gletschboden test site, where the snow patch development is similar.
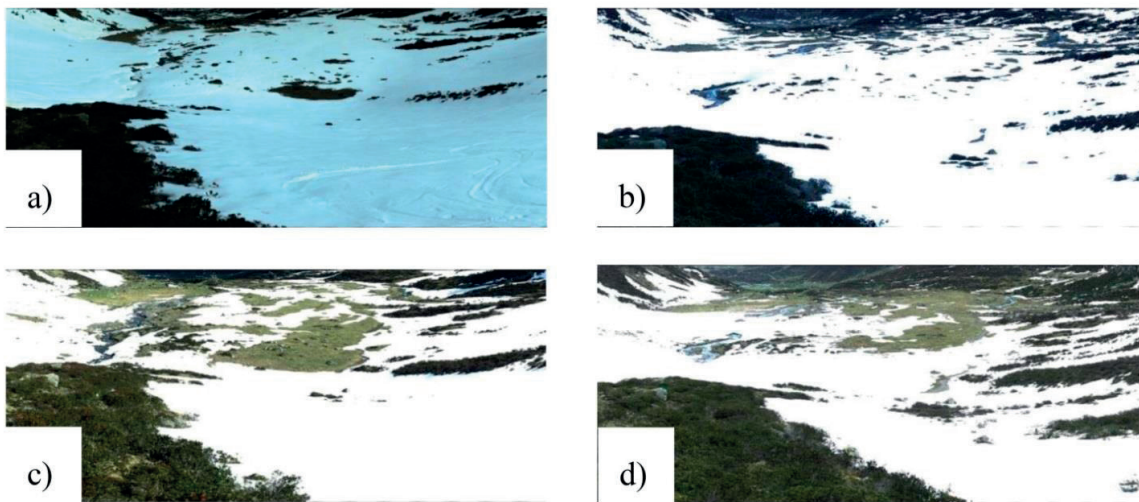
Fig 4.A Panoramic images of the Gletschboden area recorded from the scan position for the early ablation period (SCF = 80 %) (Upper panels) and the late ablation period (SCF = 50 %) (Lower panels). Images on the left are recorded in 2014 (08.05.2014: (a); 21.05.2014: (c)) and images on the right are recorded in 2015 (11.05.2015: (b); 16.05.2015: (d)).

However, we found for our test site that the development of snow patches is distinctly different for the years 2014 and 2015 (Fig. 4.A). The formation of isolated snow patches is predominant in 2014, whereas in 2015 a strict snow line develops from the northern, lower elevated part and the snow cover is influenced by a huge avalanche from the north eastern slope. In the following we tested three hypotheses which could explain the different development:

1.   Snow cover at peak accumulation

2.   Zero degree level and elevation gradient in snow height during the snow season

3.   Turbulent sensible heat fluxes in the ablation period

We tested if the snow cover at peak accumulation significantly differs between 2014 and 2015 (Fig. 4.Ba). The snow height at the beginning of the measurements in April was larger in 2015, but highly correlated with snow heights in 2014 (R^2 = 0.91). Despite the large correlation coefficient some very small-scale differences in the snow height have been detected at the slope toe of the northern-exposed slope. Snow could efficiently be transported to the toe of the slope in 2015, resulting in much larger snow heights in this area compared to 2014 (Fig. 4.Bb). These small-scale differences in snow heights could be explained by different wind directions during mid-winter snowfall events. Snowfall events in 2014 typically occurred during a southern flow, whereas the wind direction during snowfall events was mainly north in 2015, leading to an efficient snow transport towards the toe of northern-exposed slope (Gerber et al., 2017).

Fig 4.B Comparison of the Alpine snow cover at Gletschboden in 2014 and 2015: Pearson correlation coefficient of the snow height of both years as a function the snow cover fraction (a). Cross section of digital elevation model for summer and the time of peak accumulation 2014 and 2015 (b).

We observed a shallow snow pack at the slope toe in 2014 at peak accumulation and a development of a bare ground patch in this area early in the ablation period (see bare ground at the slope toe in Fig. 4.Aa). From this early state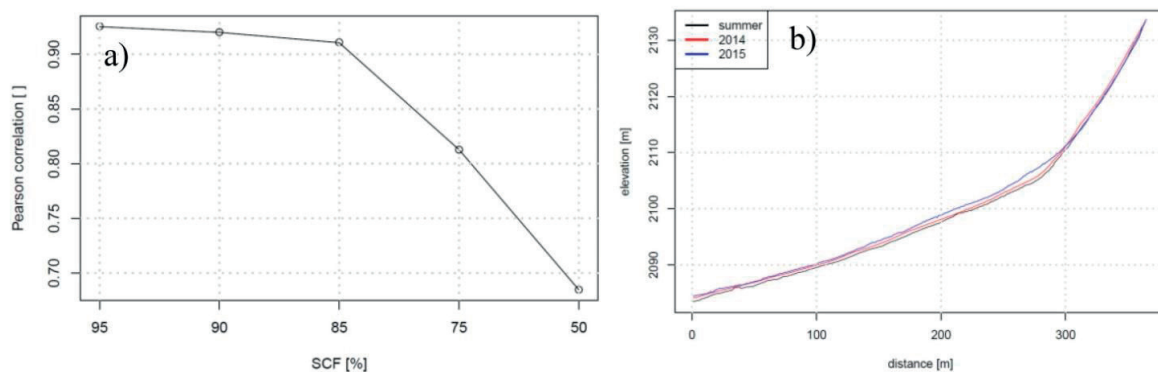 in the ablation period the Pearson correlation coefficient rapidly decreases to 0.7 during the course of the ablation period which analytically describes the different development of the snow patches (Fig. 4.Ba). Hence, snow melting in 2014 is mainly initialized by the snow-free area at the slope toe and develops starting from this area, whereas snow melting in 2015 is mainly initialized by the northern (lower elevated) parts of Gletschboden.

The initialization of snow melting from the lower elevated parts in the north is favoured by a strong elevation gradient of the snow height in 2015, which could be partly explained by a long-lasting zero degree level close to the mean elevation of the catchment. The snow height in regions above 2300 m asl was deep at the time of peak accumulation whereas the surface was already snow-free at the same time in 1700 m asl. The elevation gradient of the snow height was much smaller in 2014.

The third hypothesis tests different local heat advection directions in 2014 and 2015. As the wind direction in the ablation period 2014 and 2015 do not significantly differ (not shown), local heat advection acts similarly on the patchy snow cover. We expect that local heat advection from different directions as a consequence of different wind directions play a minor role in different snow patch developments. This assumption is caused by the fact that wind directions in the entire ablation periods are typically similar.

In summary, the different development of the Alpine snow patches in the Gletschboden area in 2014 and 2015 is mainly caused by a different peak accumulation due to different wind directions during mid-winter snowfall events and due to different elevation gradients of the snow height. This result cannot be generalized to other test sites and ablation periods. There might be years of a very similar snow patch development (as in 2014 and 2016) if the snow cover at peak accumulation, the wind direction in the ablation period and the elevation gradient of the snow height are similar.

Supplementary material

Percentage of fetch distance lower 5 m (15 m)
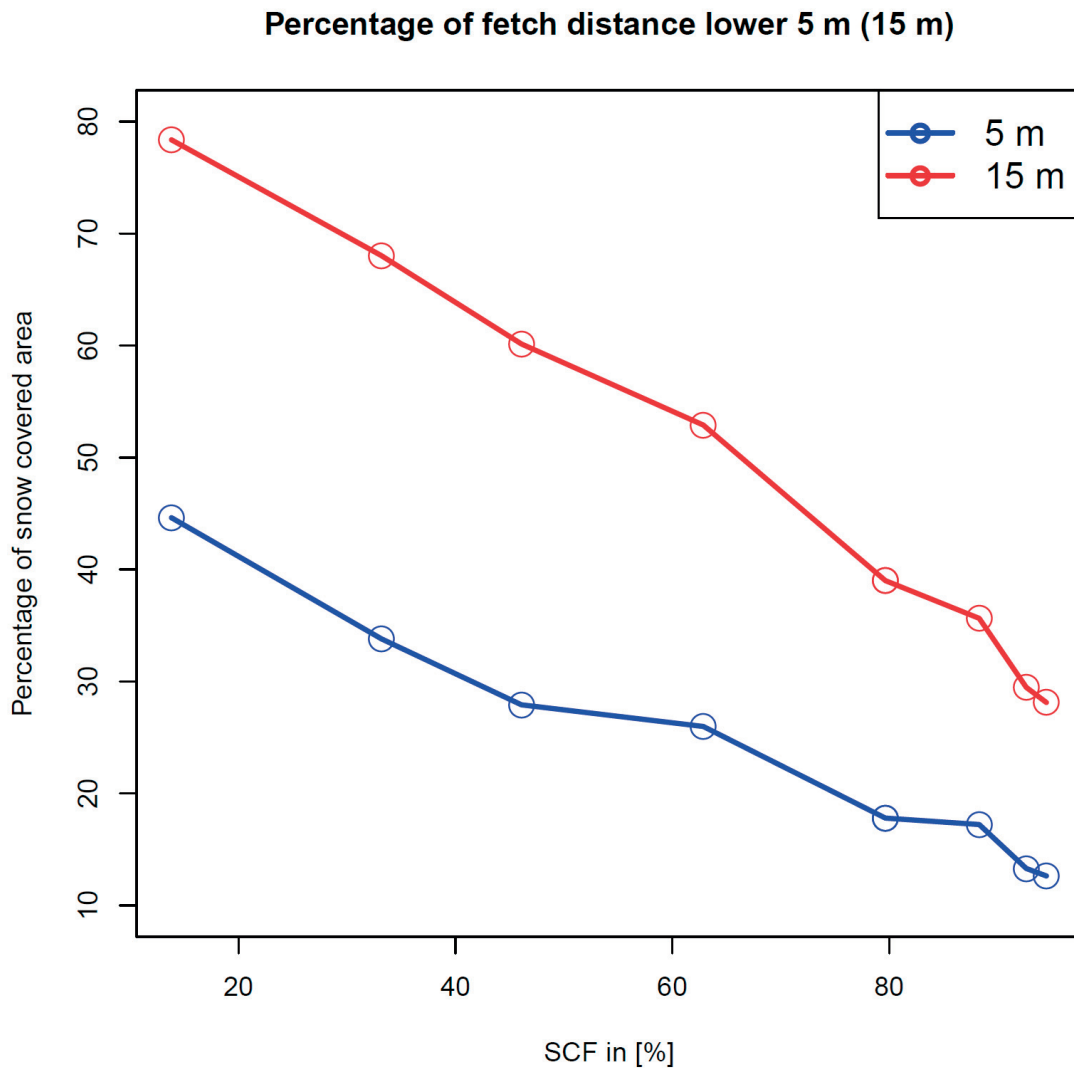
Fig 4.S1: Percentage of snow covered areas with a fetch distance below 5 m (blue) and below 15 m (red) estimated for the Gletschboden area for several different *SCF* in the ablation period 2014.
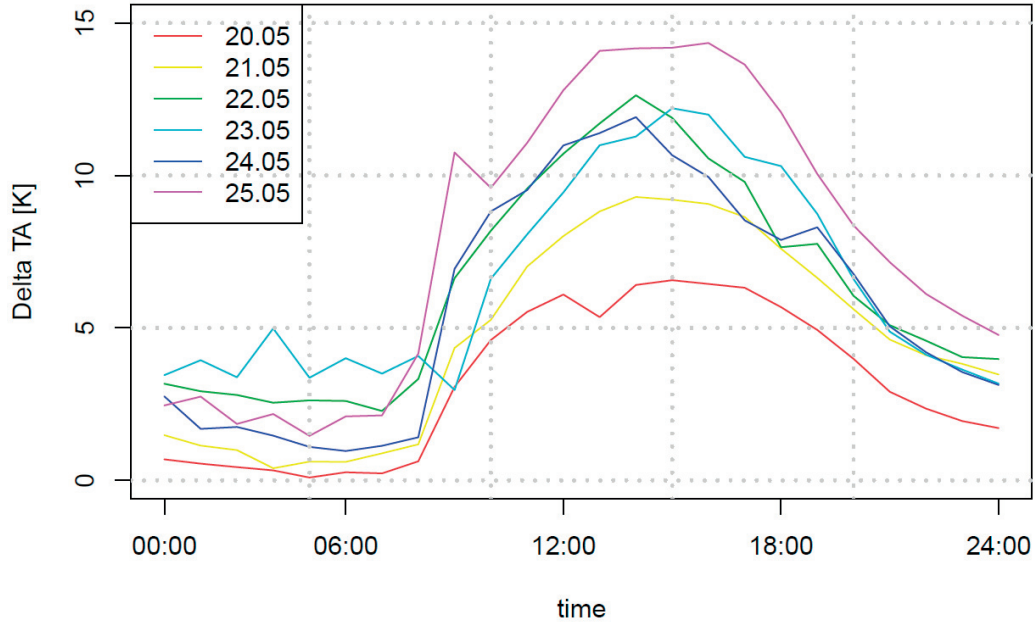
Fig 4.S2 Values of $\overline{\Delta TA(0.01\,m)}_{xy}$ [K] (averaged over snow covered pixels) as a function of the local time for 6 different analysis days in the late ablation period 2014.
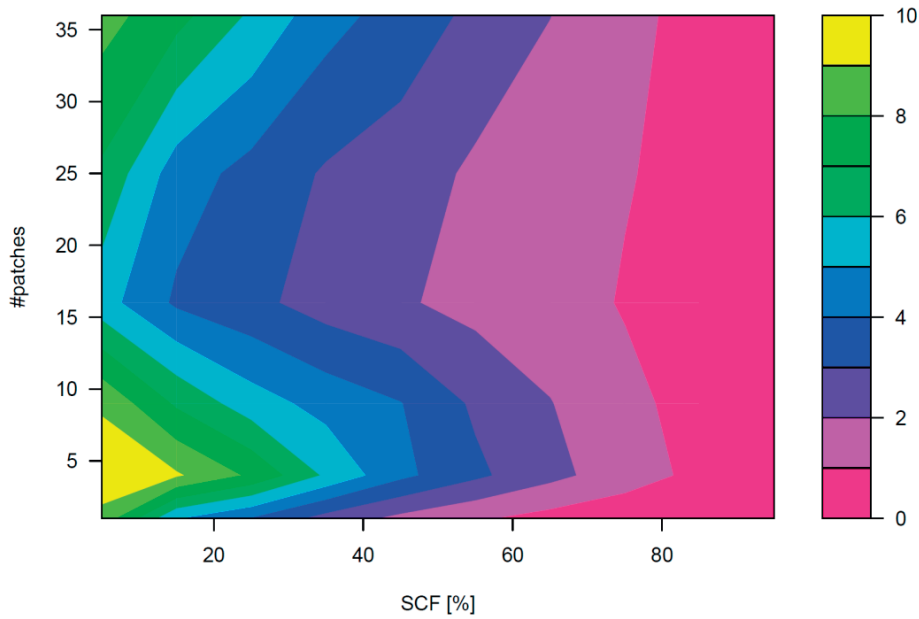
Fig 4.S3 $\overline{\Delta TA(0.01\,m)}_{xy}$ [K] (averaged over snow covered pixels) as a function of the SCF [%] and the number of snow pixels. Default values were used for the non-modified parameters (Table 4.1).
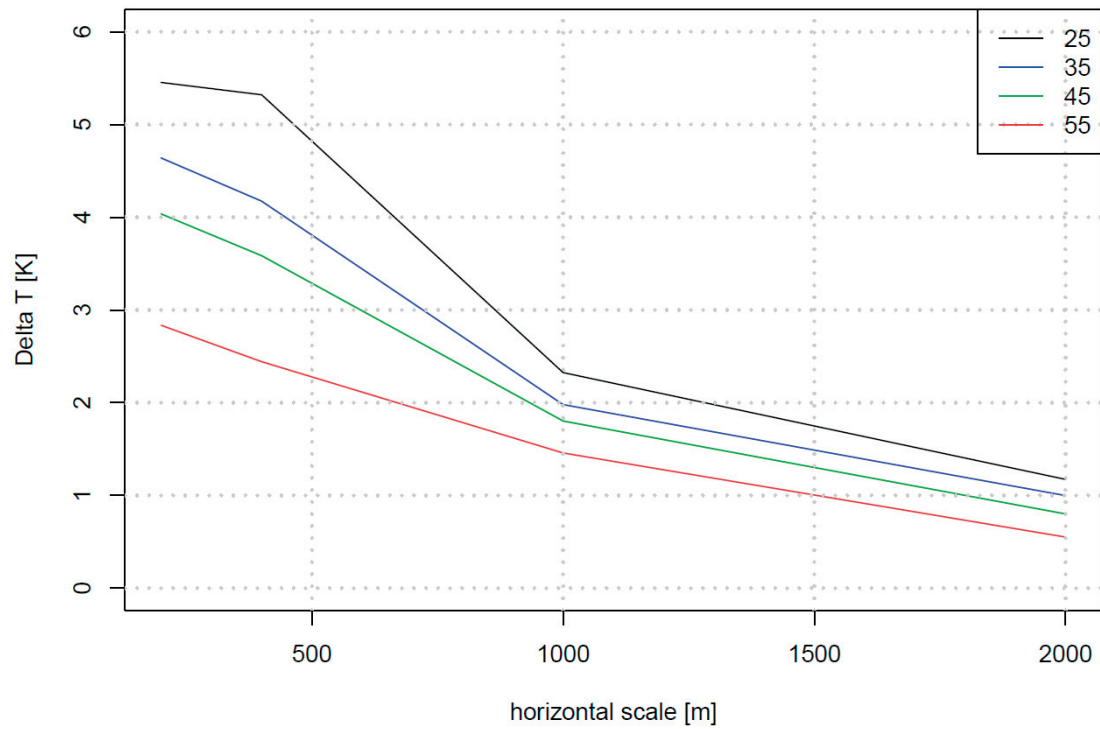
Fig 4.S4 $\overline{\Delta TA(0.01\,m)}_{xy}$ [K] (averaged over snow covered pixels) as a function of the horizontal scale [m] of the catchment for several different SCF. Default values were used for the non-modified parameters (Table 4.1).
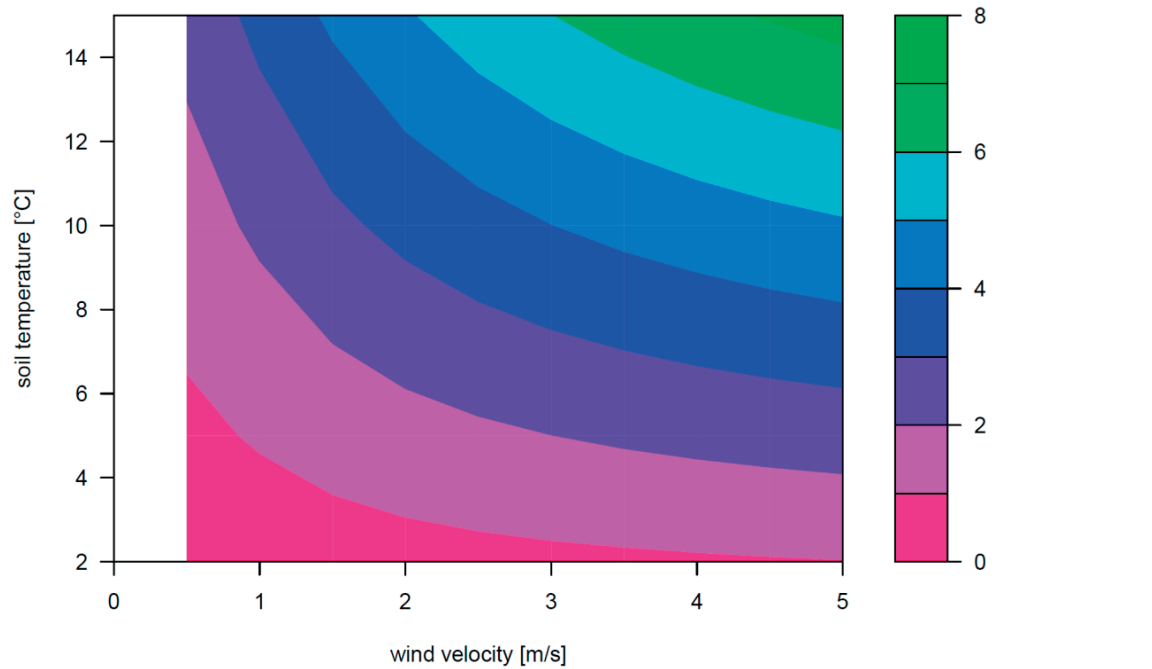
Fig 4.S5 $\overline{\Delta TA(0.01\,m)}_{xy}$ [K] (averaged over snow covered pixels) as a function of the wind velocity [m s^{-1}] and temperature of the adjacent bare ground [°C]. Default values were used for the non-modified parameters (Table 4.1).

Chapter 5   How are turbulent sensible heat fluxes and snowmelt rates affected by a changing snow cover fraction?

Schlögl, S.[1,2], Lehning, M. [1,2] and Mott, R.[1,3]

[1] WSL-Institute for Snow and Avalanche Research SLF, Davos, Switzerland
[2] School of Architecture, Civil and Environmental Engineering, École Polytechnique Fédérale de Lausanne, Lausanne, Switzerland
[3] Karlsruhe Institute of Technology, Institute of Meteorology and Climate Research, Atmospheric Environmental Research (IMK-IFU), KIT-Campus Alpin, Garmisch-Partenkirchen, Germany

Abstract The complex interaction between the atmospheric boundary layer and the heterogeneous land surface is typically not resolved in numerical models approximating the turbulent heat exchange processes. In this study, we consider the effect of the land surface heterogeneity on the spatial variability of near-surface air temperature fields and on snow melt processes. For this purpose we calculated turbulent sensible heat fluxes and daily snow depth depletion rates with the physics-based surface process model Alpine3D. To account for the effect of a heterogeneous land surface (such as patchy snow covers) on the local energy balance over snow, Alpine3D is driven by two-dimensional atmospheric fields of air temperature and wind velocity, generated with the non-hydrostatic atmospheric model ARPS. The atmospheric model is initialized with a set of snow distributions (snow cover fraction and number of snow patches) and atmospheric conditions (wind velocities) for an idealized flat test site.

Numerical results show that the feedback of the heterogeneity of the land surface (snow, no snow) on the near-surface variability of the atmospheric fields result in a significant increase in the mean air temperature $\Delta TA = 1.8$ K (3.7 K, 4.9 K) as the snow cover fraction is decreased from a continuous snow cover to 55 % (25 %, 5 %). Surface turbulent sensible heat fluxes and daily snow depth depletion rates are strongly correlated to mean air temperatures, leading to 22-40 % larger daily snow depth depletion rates for patchy snow covers. Mean air temperatures over snow heavily increase with increasing initial wind velocities and weakly increase with an increasing number of snow patches.

Numerical results from the idealized test site are compared with a test site in complex terrain. As slope-induced atmospheric processes (such as the development of katabatic flows) modify turbulent sensible heat fluxes, the variation of the surface energy balance is larger in complex terrain than for an idealized flat test site.

Keywords ARPS • heat advection • patchy snow covers • sensible heat flux • temperature footprint approach

5.1   Introduction

Snow melt modelling in an alpine environment is challenging especially in the late ablation period when the snow cover becomes patchy. A satisfactory model performance is a mandatory condition for many practical applications and has important implications for e.g. flood prevention or hydropower generation. The spatio-temporal development of snow patches in the late ablation period is mainly driven by the heterogeneous snow distribution at the end of winter due to redistribution processes, avalanches and heterogeneous precipitation (Lehning et al., 2008; Groot Zwaaftink et al., 2011; Mott et al., 2014; Gerber et al., 2017). Additionally, the snow patch development is strongly sensitive to several terrain features, e.g. slope or aspect of the terrain. Egli et al. (2012) proposed that spatially distributed snow melting in an alpine catchment could be well simulated with a uniform melt rate (mainly driven by the radiation components) if the snow depth at the beginning of the ablation period is well known. The assumption of a uniform melt rate is particularly valid for a continuous snow cover as long as the snow melting is mainly driven by the vertical turbulent heat fluxes between the snow surface and the atmosphere. However, once an alpine snow cover gets patchy during spring,

the relative importance of boundary layer processes driving the turbulent heat exchange changes significantly. The counteracting processes of local heat advection (larger melting rates at the leading edge of a snow patch) and boundary layer decoupling due to the development of a stable internal boundary layer (SIBL) (e.g. Mahrt and Vickers, 2005; Mott et al., 2016, 2017) (lower melting rates at the downwind edge of a snow patch) significantly modify local snow melting rates (Liston, 1999; Pomeroy et al., 2003; Essery et al., 2006). Heat advection is the dominant process for high wind velocities and strong mechanical turbulence, whereas boundary layer decoupling becomes important for calm conditions, a shallow SIBL, weak mechanical turbulence and a concave topography (Mott et al., 2013, 2015, 2016, 2017). The effect of the land surface heterogeneity modifies not only local snow melting rates but additionally drives a snow-breeze circulation (Johnson et al., 1984; Taylor et al., 1998) due to a strong thermal contrast between snow and bare ground. Snow-breeze circulations can interact in complex terrain with the development of diurnal wind systems (Letcher and Minder, 2015). We put the main focus of this paper on the effect of land surface heterogeneity on the spatial variability of near-surface air temperature and wind velocity fields resulting in a change of snow melt processes in the course of a melting season.

Sensible heat could be advected from the adjacent bare ground towards a snow patch, resulting in an additional energy input for melting snow (Marsh and Pomeroy, 1996). This local heat advection leads to an increase of snow melting rates at the leading edge of the snow patch and is well known since the 1970s (Weisman, 1977) and could be observed by new remote sensing technologies (Mott et al., 2011; Schlögl et al., submitted). Theoretical suggestions recommend the existence of heat advection as a function of the fetch distance (Liston et al., 1995). The boundary layer integration approach (Granger et al., 2002) deterministically describes the magnitude of heat advection as a function of the fetch distance on condition that the height of the SIBL is known. As the SIBL height is typically not measured but rather parametrized (Garratt, 1990 and references therein, Savelyev and Taylor, 2005), several parametrizations of heat advection have been published the last decade (e.g. Granger et al., 2002; Essery et al., 2006), which are functions of the Weisman stability parameter, fetch distance and the difference in surface temperatures between the bare ground and snow. More recent studies (Granger et al., 2006; Helgason and Pomeroy, 2012; Harder et al., 2017) determined the advection of sensible heat based on high resolution temperature profile measurements using thermocouples. However, these measurements are very rare. Fujita et al. (2010) experimentally analysed the snow ablation of a long-lasting snow patch over four decades and found a large correlation between snow ablation and wind speed and a small correlation between snow ablation and air temperatures during summer.

Numerical investigations over a heterogeneous land-surface on large scales have been conducted to analyse the development of katabatic and anabatic wind systems (Segal et al., 1991), to assess local advection of sensible heat (Liston, 1995), to estimate the warming feedback due to changing snow covered areas (Ménard et al, 2014) and to analyse the effect of spatial heat flux variations on a mountain glacier (Sauter and Galos, 2016). In contrast to large scale assessments over patchy snow covers, Mott et al. (2015) numerically analysed atmospheric flow field dynamics and boundary layer processes for an alpine catchment characterized by complex terrain on a small-scale. They showed that thermally driven flow fields over single snow patches and the warming of the near-surface atmosphere due to sensible heat advection significantly change the mean turbulent heat flux over snow and validated numerical results from turbulent sensible heat fluxes with measurement from an ultrasonic anemometer. The purpose of this study is to follow up the work of Mott et al. (2015) for an idealized flat test site separating the pure effect of highly resolved near-surface atmospheric fields from the effect of thermally-induced wind systems over snow on the surface energy balance of patchy snow covers.

In a companion paper (Schlögl et al., submitted) we investigate normalized daily snow depth depletion rates as a function of the fetch distance on the basis of terrestrial laser scanning (TLS). Mott et al. (2011) proposed that local advection of sensible heat influences daily snow depth depletion rates in the first 5 m fetch distance for low wind velocities and in the first 15 m for high wind velocities. This so-called "leading-edge effect" is well described in literature (e.g. Savelyev and Taylor, 2005), however with little quantitative investigations. In this paper we focus on the boundary layer development in connection with a patchy snow surface exchange and assess the effects on the basis of numerical simulations.

This study is organized as follows. In Section 5.2, the test site, model setup and the procedure of this work are described. In Section 5.3, results are shown with respect to, a) the variation of the near-surface meteorological fields by varying snow distributions and atmospheric conditions, b) their influence on turbulent sensible heat fluxes and snow depth depletion rates and c) the comparison of numerical results from the idealized test site with a test site in complex terrain. Section 5.4 offers a discussion and the conclusions of this study.

5.2   Methods

5.2.1   Idealized test site

We analyse the surface energy balance of a patchy snow cover for an idealized flat test site located at 2000 m asl. More than 100 artificial snow cover distributions have been created on a 400 x 400 m horizontal grid, which are characterized by the snow cover fraction (SCF) and the number of snow patches. These characteristics of the snow cover distributions were used as model input for the initial state with a horizontal resolution of 2 m. In this study, we show results of SCFs of 5 %, 25 % and 55 % and a varying

number of snow patches (1 patch, 16 patches and 36 patches) (Fig. 5.1). The mean snow patch size ranges from 18 m for SCF = 5 % and 36 snow patches to 298 m for SCF = 55 % and 1 snow patch.
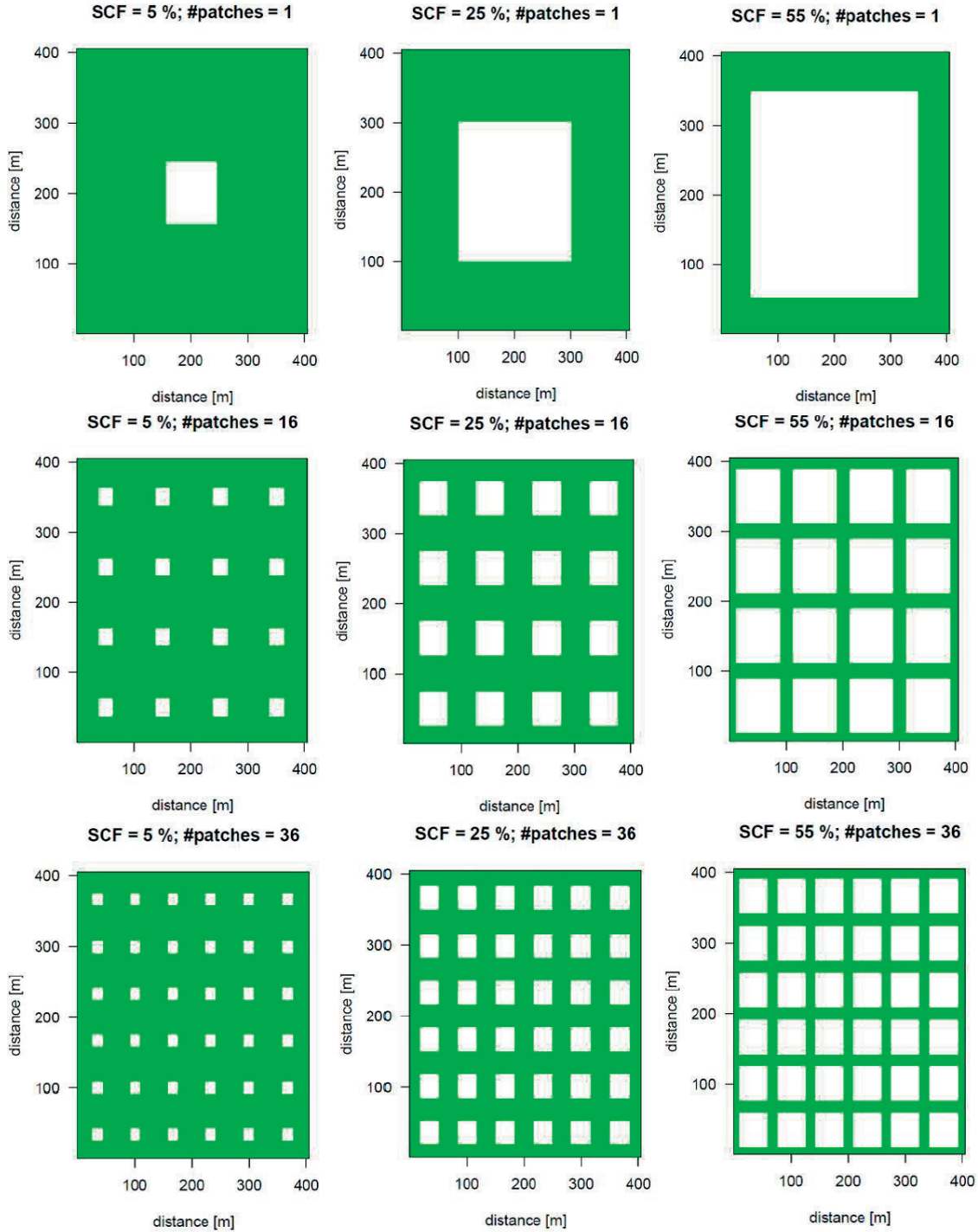

Fig 5.1 Initial idealized snow cover distributions, where the green colours indicate bare ground and white colours indicate snow. We choose a SCF of 5 %, 25 % and 55 % and the number (#) of patches is equal to 1, 16 and 36.

5.2.2   Model setup

The physics-based surface process model Alpine3D has been used to simulate snow melt accounting for the patchiness of the snow cover. Alpine3D is a spatially distributed, three-dimensional model for analysing and predicting dynamics of snow-dominated surface processes in mountainous topography (Lehning et al., 2006). In its standard version Alpine3D is limited to simulate pointwise the vertical turbulent exchange between the ground and the atmosphere and do not include lateral transport. Thus, the horizontal small scale variability in daily snow depth depletion rates (as observed from TLS measurements) could not be resolved (Mott et al., 2013; Schlögl et al., submitted). Air temperatures and wind velocity fields were calculated with the three-dimensional, non-hydrostatic atmospheric model ARPS (Advanced Regional Prediction System) (Xue et al., 2004). We used the 1.5-order turbulent kinetic energy scheme to parametrize the sub-grid scale turbulence (Deardorff, 1972). Turbulent fluxes were parametrized by using Monin-Obukhov bulk formulations and stability corrections of Deardorff (1972) in stable conditions. The radiative transfer model is given by Chou and Suarez (1994), which includes radiative cooling and forcing as well as topographical shading. The smaller time step was set to 0.001 s to integrate acoustic wave modes, the larger time step was set to 0.01 s to integrate the model. More details about the chosen setup in ARPS are described in detail in Mott et al. (2015).

Two-dimensional fields of snow cover distributions (Fig. 5.1), aerodynamic roughness length and surface temperatures are used to initialize the base state of a force-restore land-surface soil-vegetation model (Noilhan and Planton, 1989). Vertical profiles of atmospheric variables (potential air temperature, relative air humidity, wind velocity, wind direction) are used to initialize the atmospheric base state of ARPS. ARPS was initialized with a neutral boundary layer assuming a potential air temperature of 295 K in all vertical levels. Relative air humidity ($RH = 50$ %) and wind direction ($WD = 315°$) were assumed to be constant in all vertical levels. We chose a logarithmic wind profile for the initial model forcing. ARPS was run from 1st April 06:00 to 18:00 local time for a clear-sky day in 2 m horizontal resolution. We used periodic boundary conditions in all directions, as this setup leads to less numerical instabilities than open (radiation) lateral boundary conditions. Numerical simulations were conducted for an initial ARPS surface temperature of the bare ground of 283.15 K and for three initial ARPS wind velocities (0.5 m s^{-1}, 2 m s^{-1} and 5 m s^{-1}).

The spatial variability of air temperature and wind velocity fields induced by the patchiness of the snow cover is resolved by the atmospheric model ARPS. Thus heat is laterally transported from one grid point to the next in ARPS. Air temperature and wind velocity fields, generated with ARPS, are finally used as input for Alpine3D. Hence, the coupling of the two different models works only from the atmospheric model ARPS to the hydrological model Alpine3D and not vice versa.

In the physics-based surface process model Alpine3D, turbulent fluxes (sensible heat (H) and latent heat (Q_l)) were calculated with Monin-Obukhov bulk formulation by using the univariate stability corrections ψ_m for momentum and ψ_s for scalars according to Schlögl et al. (2017),

$$H = C \, \rho \, c_p \, \overline{U} \, \Delta\theta, \tag{5.1}$$

where $\Delta\theta = \theta_s - \theta_{z_{ref}}$ is the potential air temperature difference, $\theta_{z_{ref}}$ is the virtual potential air temperature at the reference height z_{ref}, θ_s is the virtual potential temperature at the snow surface, $\overline{U}$ is the mean wind velocity and C is the exchange coefficient for stable conditions over snow,

$$C = \frac{k^2}{\left[\ln\left(\frac{z_{ref}}{z_{0M}}\right) - \psi_m\right]\left[\ln\left(\frac{z_{ref}}{z_{0M}}\right) - \psi_s\right]}, \tag{5.2}$$

where $k = 0.4$ is the von Kármán constant and $z_{0M} = 0.007$ m is the aerodynamic surface roughness length over snow (Bavay et al., 2012; Schlögl et al., 2016). For bare ground, we chose alpine meadow with a surface roughness length of 0.03 m according to Wieringa (1993).

The full surface energy balance and the melt energy for snow (Q_m) were calculated in Alpine3D for one day from 6:00 to 18:00 by forcing the model with ARPS meteorological fields each 15 minutes:

$$Q_m = SW\downarrow - SW\uparrow + LW\downarrow - LW\uparrow + H + Q_l. \tag{5.3}$$

Radiation components (incoming shortwave radiation $SW\downarrow$, outgoing shortwave radiation $SW\uparrow$, incoming longwave radiation $LW\downarrow$ and outgoing longwave radiation $LW\uparrow$) were selected from a clear-sky day of beginning of April at a test site with an elevation of 2000 m asl. The incoming longwave radiation is parametrized with a clear-sky algorithm of Dilley and O'Brien (1998) in combination with the cloud correction algorithm of Unsworth and Monteith (1975). This setup allows changes in the incoming longwave radiation due to changes in the air temperatures. Incoming and outgoing shortwave radiation are measured and avoid a model-based snow surface albedo estimation.

In the following we focus on snow depth depletion rates $\Delta HS = HS_{18:00} - HS_{06:00}$ instead of the melt energy for snow Q_m, in order to compare numerical results with snow depth depletion rates recorded from terrestrial laser scanning in the companion paper (Schlögl et al., submitted). The conversion from Q_m to ΔHS is done for each model pixel by the physics-based surface process model SNOWPACK (Lehning et al., 2002), which is the physical core of the Alpine3D model.

5.2.2.1 Model setup for the Wannengrat test site

Numerical results of the idealized flat test site have been compared with numerical results for the test site Wannengrat, Davos, Switzerland (Mott et al., 2015). The Wannengrat test site has been mapped on a regular grid with a horizontal resolution of 5 m and includes 547 x 579 pixels with an elevation between 2069 m asl and 2647 m asl. The average slope angle of the Wannengrat test site is 19° with a standard deviation of 10°. More detailed information about the Wannengrat test site can be found in Mott et al. (2015). ARPS was initialized with measured snow distributions recorded with terrestrial laser scanning at the Wannengrat test site. Meteorological fields of air temperature and wind velocity are calculated in ARPS for SCF = 15 %, 23 %, 37 %, 50 % and 65 % and one quiescent (0 m s^{-1}) and one synoptic forcing (3 m s^{-1}).

Open (radiation) boundary conditions and an integration time of 700 seconds have been used for the Wannengrat test site, as the model becomes numerical unstable afterwards. The model was initialized for 12:00 local time for a clear sky day. In order to compare both test sites (Section 5.3.3), the Wannengrat specific model setup is additionally used for the idealized test site.

5.2.3 Procedure

We analysed ARPS meteorological fields and Alpine3D turbulent sensible heat fluxes and daily snow depth depletion rates for 7 different initial conditions. We modified the SCF (5, 25 and 55 %), the number of snow patches (1, 16 and 36) and the wind velocity (0.5, 2 and 5 m s^{-1}). Additionally, we simulated one continuous snow cover with a wind velocity of 2 m s^{-1} (Table 5.1). We calculated ARPS meteorological fields for the lowermost model level at $z_{ref} = 0.8$ m above the surface and a model level at $z_{ref} = 5.7$ m above the surface. By analysing ARPS meteorological fields for both model levels, we investigate a potential bias by using standard input meteorological stations which typically provide measurements between 2 and 10 m above the surface and only record spatially averaged values of atmospheric fields from a heterogeneous land surface.

Parameter	Default	Modification	Continuous snow cover
SCF	25 %	5 %, 25 %, 55 %	100 %
Number of snow patches	16	1, 16, 36	1
Wind velocity	2 m s^{-1}	0.5 m s^{-1}, 2 m s^{-1}, 5 m s^{-1}	2 m s^{-1}

Table 5.1 Default values and their modifications of the initial wind velocity and the snow distributions (SCF and number of patches) are shown. Additionally values for SCF, number of snow patches and wind forcing of the continuous snow cover are shown.

The variation in near-surface air temperatures ΔTA, turbulent sensible heat fluxes ΔQ_s and snow depth depletion rates $\Delta(\Delta HS)$ of the 7 model simulations are calculated with respect to the simulation of the continuous snow cover (csc):

$$\Delta TA = TA_{sim} - TA_{csc} \tag{5.4a}$$

$$\Delta H = H_{sim} - H_{csc} \tag{5.4b}$$

$$\Delta(\Delta HS) = \Delta HS_{sim} - \Delta HS_{csc} \tag{5.4c}$$

The variation in near-surface ARPS air temperatures ΔTA are compared with results from the temperature footprint approach in the companion paper (Schlögl et al, submitted). The temperature footprint approach is developed from adapted footprint estimations (Schuepp et al., 1990) in order to resolve the spatial variability of near-surface air temperatures and turbulent sensible heat fluxes. This fundamental theory was originally deployed for eddy-covariance measurements revealing the origin of the measured turbulence as a function of the measurement height, atmospheric stability and wind speed.

5.3   Results

5.3.1   Variation of atmospheric fields

ARPS air temperature and wind velocity fields are simulated for two different heights above the ground as a function of the local time (Fig. 5.2). Air temperatures in the lowest model level decrease in the first time step about 1 K indicating that the base-state potential air temperature of 295 K and the surface are not in equilibrium. Afterwards, air temperatures increase with sunrise, strongly for the near-surface model level but also for the model level at 5.7 m above the surface. The near-surface air temperature increase is heavily dependent on the chosen wind conditions and snow distributions (Fig. 5.3).
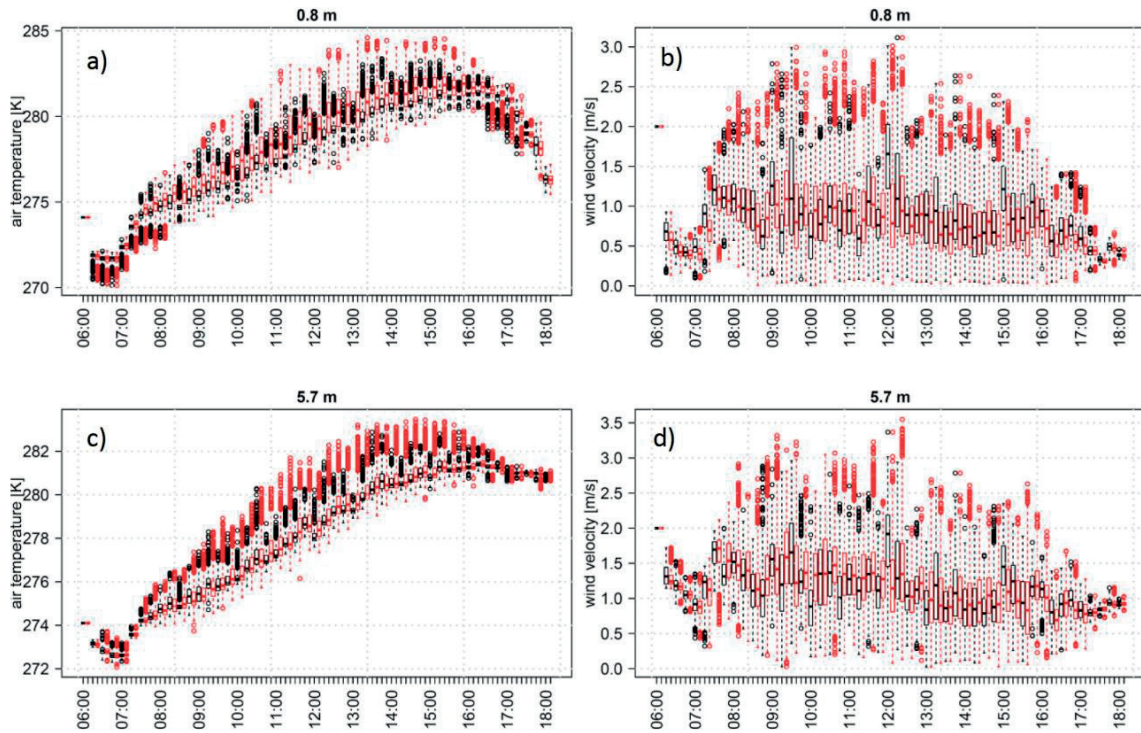
Fig 5.2 Development of the diurnal ARPS air temperature (left) and ARPS wind velocity (right) in 0.8 m (upper panels) and in 5.7 m (lower panels) above the surface for SCF = 25 % and a number of snow patches = 16. Initial values for the wind velocity are 2 m s^{-1} and temperature of the adjacent bare ground is 283.15 K. Results are shown as boxplots for snow-covered pixels (black) and all pixels (red) as a function of the local time.

Over snow covered pixels, daily averaged near-surface air temperatures increase around ΔTA = 1.8 ±0.4 K (3.7±0.5 K, 4.9±0.5 K) by lowering the SCF from a continuous snow cover to 55 (25, 5) % (Fig. 5.3c). For SCF = 25 %, the lowest ARPS near-surface air temperatures are found for small initial wind velocities. Near-surface air temperatures exceed 280 K for a calm wind forcing (0.5 m s^{-1}) at 15:00 local time (ΔTA = 3.2 K). Near-surface air temperatures increase to 282 K (ΔTA = 4.8 K) for a synoptic wind forcing (5 m s^{-1}) (Fig. 5.3a). ARPS near-surface air temperatures are not sensitive to variations in the number of snow patches. For SCF = 25 %, we found the smallest near-surface air temperatures for one large snow patch and the largest near-surface air temperatures for many smaller snow patches, but differences are smaller than 0.5 K (Fig. 5.3b). We additionally modified initial soil temperatures of the adjacent bare ground from 278 to 288 K. Near-surface air temperatures slightly increase with increasing soil temperatures, but numerical results are insensitive to modifications in the soil temperature as differences are smaller than 0.5 K (not shown).

Air temperatures at 0.8 m and 5.7 m for snow-covered pixels are almost similar from sunrise until sunset. However, air temperatures close to the snow surface rapidly decrease after sunset, whereas air temperatures higher up in the atmosphere are less affected by the cooling snow surface and stay almost constant in the first hour after sunset. In summary, variations between both vertical levels can be neglected as long as the energy balance of the snow pack remains positive ($Q_m > 0$) and the surface temperature consistently stays at its melting point.

The air temperatures differences between the model levels in 0.8 m and 5.7 m above surface for snow-covered pixels are shown as a function of the fetch distance and local time (Fig. 5.4). Warm air advection influences the snow covered pixels with a fetch distance lower than 5-10 m in the lowermost model level. The hourly variations in air temperature differences for small fetch distances explain the variations in Fig. 5.3c for small snow cover fractions. As the relative percentage of small fetch distances is small for large SCFs, the curves in Fig. 5.3c are smoothed for large SCFs.
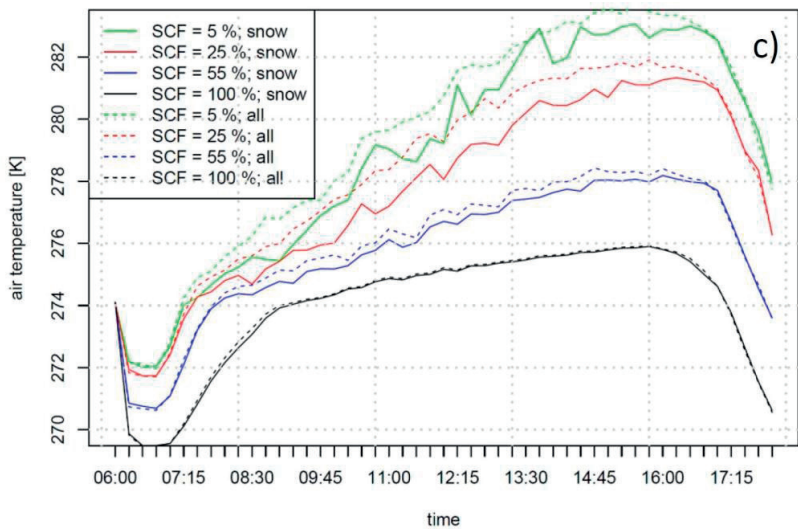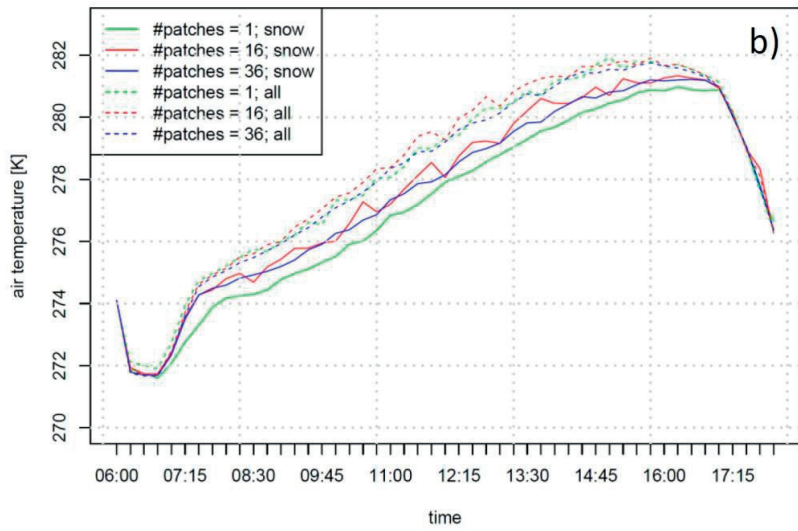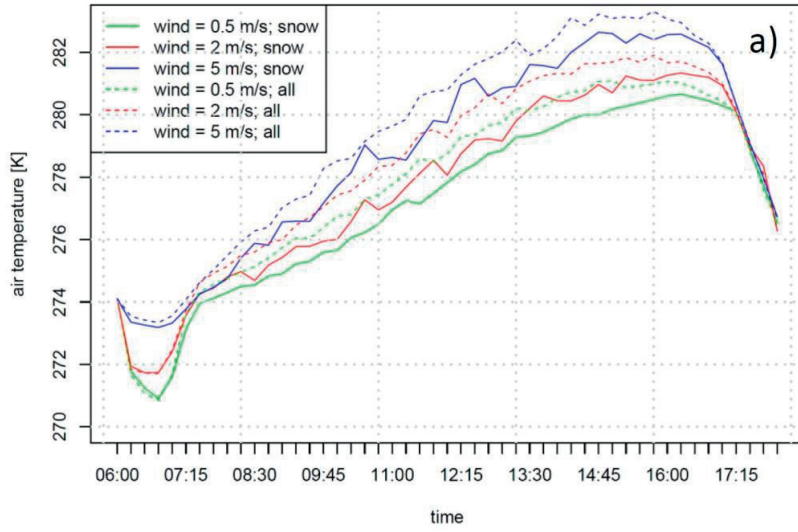
Fig 5.3 Development of the diurnal air temperature [K] for a set of different wind velocities (0.5, 2, 5 m s^{-1}) (top), for a set of a different number of snow patches (1, 16, 36) (middle) and for a set of different SCF (5 %, 25 %, 55 %, 100 %) (bottom). The default values are SCF = 25 %, number of snow patches = 16 and wind velocity = 2 m s^{-1}.
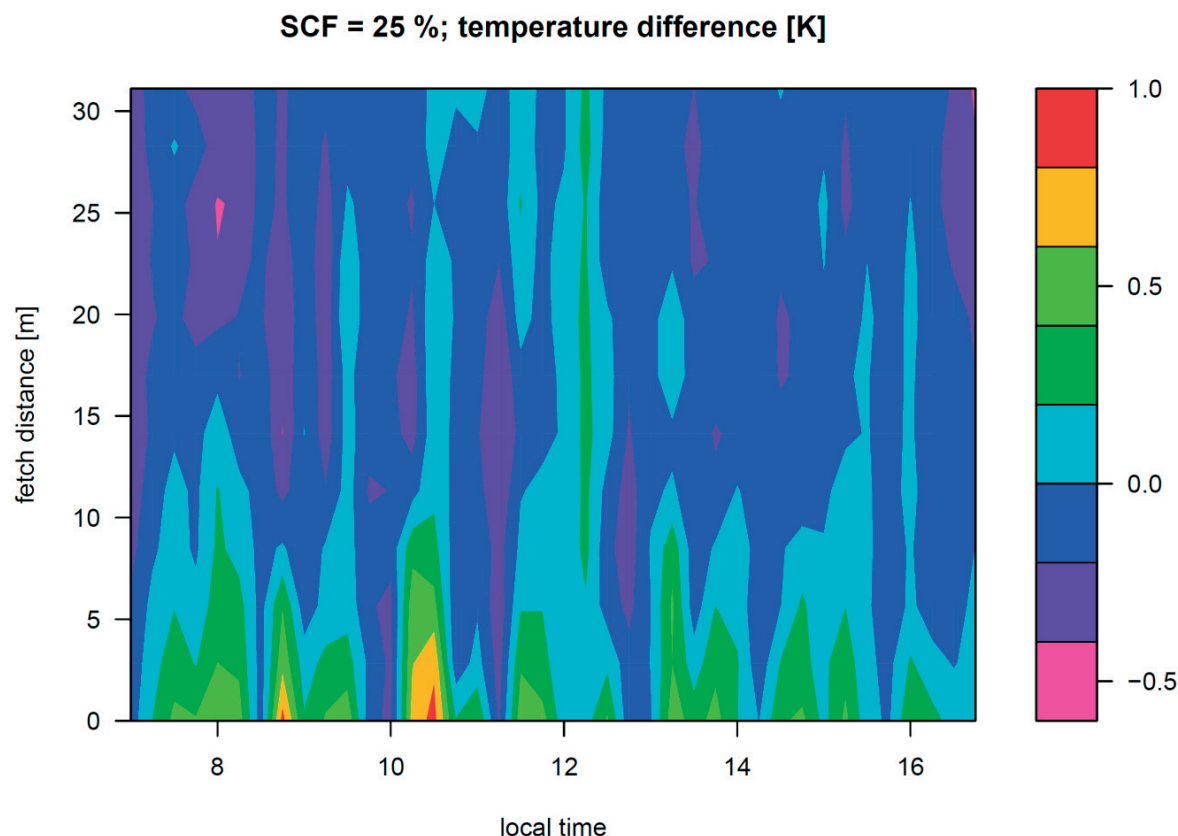
Fig 5.4: Temperature difference [K] between the lowest model level (0.8 m) and the model level in 5.7 m as a function of the local time and the fetch distance [m] for a SCF = 25 % and a wind velocity of 2 m s^{-1}. Positive values indicate warmer temperatures in 0.8 m above the surface than in 5.7 m above the surface.

Air temperatures for snow-covered pixels and all pixels are similar at 5.7 m above the surface. However, near-surface air temperatures for all pixels are up to 1 K larger than for only snow-covered pixels. This difference increases with decreasing SCF caused by the fact that smaller snow-covered areas lead to less cooling of the first model level than a land surface with a larger fraction of snow.

Accurate wind velocity fields are required to calculate Alpine3D surface turbulent sensible heat fluxes and snow depth depletion rates correctly. ARPS wind velocities increase with sunrise, stay constant throughout the day and decrease with sunset. Wind velocities for the first model level are smaller than higher up in the atmosphere, especially in the morning. Turbulent mixing of air masses becomes more important with increasing air temperatures after sunrise, leading to small differences in wind velocities between both model levels (0.8 m vs. 5.7 m) during noon.

We analysed the correlation between ARPS air temperature and wind velocity fields close to the snow surface for snow-covered pixels. For a synoptic forcing (5 m s^{-1}), we found a strong negative correlation mainly attributed to a change in the aerodynamic roughness length at the transition between the rougher snow-free ground and the smoother snow patch. Close to the ground-snow transition, air temperatures are 1-2 K larger than further inside the snow patch, whereas wind velocities are slightly smaller at the upwind edge of the snow patch than further inside the snow patch. This increase in wind velocity over the snow patch in downwind direction was not yet observed experimentally and explains that daily averaged wind velocities over snow decrease approximately 10 % by decreasing the SCF from a continuous snow cover to 5 %. For calm wind conditions (0.5 m s^{-1}), the formation of a snow-breeze circulation favours a low-level jet at the border between snow and bare ground in our numerical simulations. This phenomenon leads to a decrease in wind velocities in downwind direction and therefore a weak positive correlation between wind velocity and air temperature fields.

5.3.2 Turbulent sensible heat fluxes and snow depth depletion rates

In this section, we investigate the sensitivity of surface turbulent sensible heat fluxes (Fig. 5.5) and daily snow depth depletion rates (Table 5.2) to different initial wind conditions and snow cover distributions. Surface turbulent sensible heat fluxes typically show slightly larger positive values by using air temperature and wind velocity fields at 0.8 m instead of meteorological fields at 5.7 m (mean turbulent sensible heat fluxes for all simulations: 16 W m^{-2} at 0.8 m vs. 6 W m^{-2} at 5.7 m), which is discussed in detail in Section 5.4. The largest turbulent sensible heat fluxes towards the snow patch occur at around 15:00 local time for our specific example of 1st April, where air temperatures typically reach the daily maximum, and decrease afterwards in strong correlation with the air temperatures. The standard deviation of the turbulent sensible heat fluxes is largest at around 13:00 local time and increase with decreasing snow cover fraction and increasing wind velocity (not shown). In the following we present the Alpine3D surface energy balance for varying SCF, initial wind velocities and number of snow patches:

1. Snow cover fraction: A varying SCF heavily affects surface turbulent sensible heat fluxes and daily snow depth depletion rates. The largest snow depth depletion rates were simulated for a $SCF = 5$ %, as ARPS air temperatures and surface turbulent sensible heat fluxes are largest for this model setup. By using near-surface meteorological fields, daily snow depth depletion rates increase from $29 \cdot 10^{-3}$ m/day to $44 \cdot 10^{-3}$ m/day by varying the snow distribution from an almost continuous snow cover to $SCF = 5$ %. For $SCF = 55$ %, snow depth depletion rates are significantly larger by using meteorological fields at 5.7 m above the surface instead of near-surface meteorological fields ($37 \cdot 10^{-3}$ m/day vs. $40 \cdot 10^{-3}$ m/day). This is mostly caused by the formation of a SIBL in the model and a cooling of near-surface air temperatures by the presence of the snow. This cooling of the near-surface atmosphere could also be observed for the continuous snow cover (initial wind velocity = 2 m s^{-1}), where daily snow depth depletion rates are 25 % smaller by using near-surface meteorological fields as model input ($29 \cdot 10^{-3}$ m/day vs. $37 \cdot 10^{-3}$ m/day).

2. Initial wind velocity: For a synoptic forcing (wind velocity = 5 m s^{-1}), surface turbulent sensible heat fluxes are large throughout the day (up to 60 W m^{-2}), whereas surface turbulent sensible heat fluxes are small (up to 20 W m^{-2}) for calm conditions (wind velocity = 0.5 m s^{-1}). This surface reaction to the decrease in the initial wind velocity is then represented in daily snow depth depletion rates, which slightly decrease from $44 \cdot 10^{-3}$ m/day to $39 \cdot 10^{-3}$ m/day. The Alpine3D surface energy balance show similar results for the usage of meteorological fields at 0.8 m and 5.7 m above the surface.

3. Number of snow patches: The sensitivity of turbulent sensible heat fluxes and daily snow depth depletion rates to modifications in the number of snow patches is small. Differences in the surface energy balance are small by using ARPS meteorological fields in different heights.
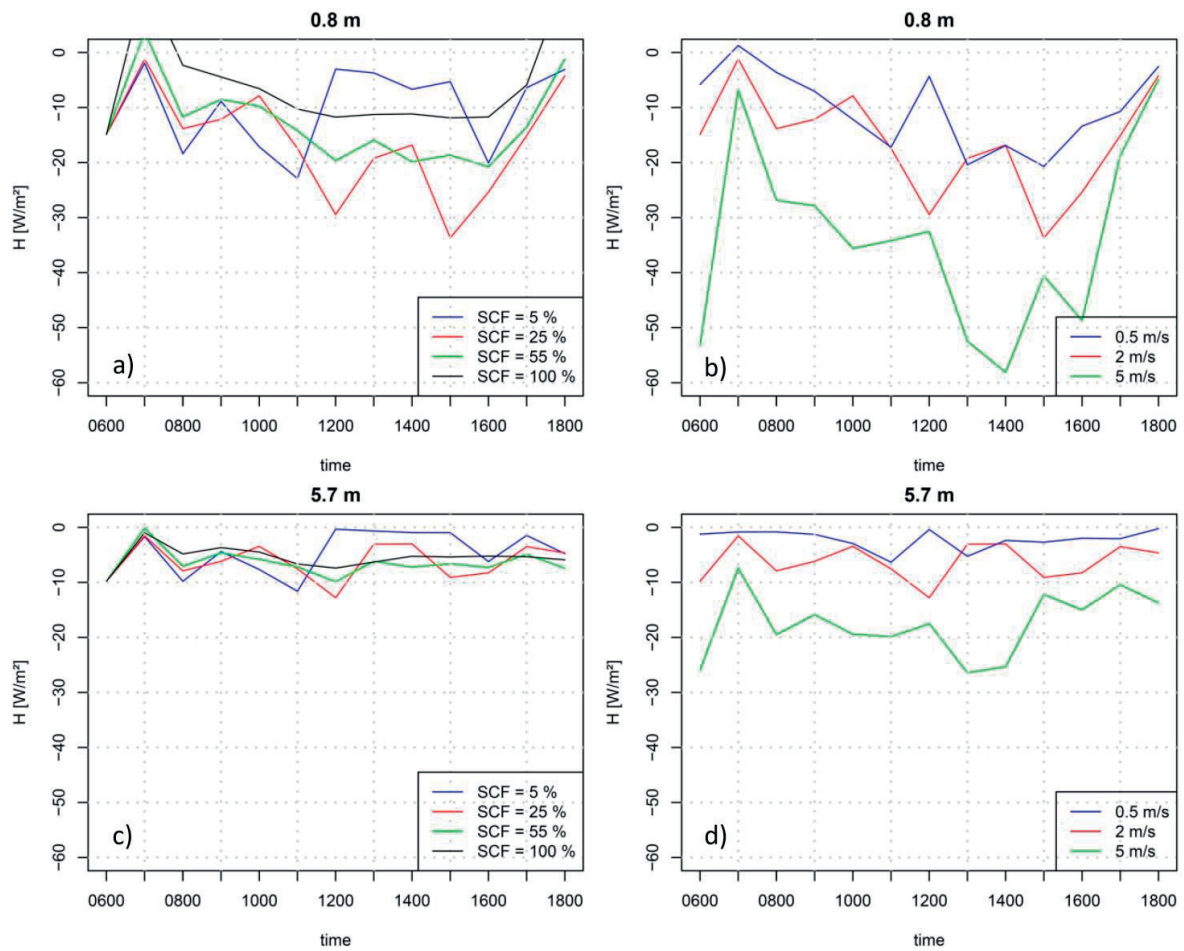
Fig 5.5 Surface turbulent sensible heat flux over snow [W m^{-2}] as a function of the local time by using ARPS meteorological fields of the near-surface model level (0.8 m, top) and a model level higher up in the atmosphere (5.7 m, bottom). Simulations with varying SCF (left) and varying initial wind velocity (right) are shown. Negative values indicate an downward sensible heat flux towards the snow pack.

	$SCF = 5\%$	$SCF = 25\%$	$SCF = 55\%$	$SCF = 100\%$
0.8 m	44 ± 0.5	40 ± 0.5	37 ± 0.7	29 ± 1.5
5.7 m	45 ± 0.4	40 ± 0.1	40 ± 0.3	37 ± 0.5

	#patches = 1	#patches = 16	#patches = 36
0.8 m	40 ± 0.6	40 ± 0.5	40 ± 0.6
5.7 m	40 ± 0.5	40 ± 0.1	40 ± 0.6

	$\overline{U} = 0.5 \, \text{m s}^{-1}$	$\overline{U} = 2 \, \text{m s}^{-1}$	$\overline{U} = 5 \, \text{m s}^{-1}$
0.8 m	39 ± 0.3	40 ± 0.5	44 ± 0.7
5.7 m	38 ± 0.0	40 ± 0.1	45 ± 1.0

Table 5.2 Daily snow depth depletion rates ΔHS [10^{-3} m/day] were shown as a function of different SCF, number of snow patches and wind forcing. The default values are $SCF = 25\,\%$, number of snow patches = 16 and wind velocity = 2 m s^{-1}.

On average, daily snow depth depletion rates are around 40 % larger for a patchy snow cover with $SCF = 5\,\%$ in comparison with a continuous snow cover (Table 5.3). This large difference is mainly caused by an increase in mean air temperatures causing an increase in surface turbulent sensible heat fluxes from 5 W m^{-2} for a continuous snow cover to 15 W m^{-2} for a $SCF = 5\,\%$. For $SCF = 55\,\%$, we analysed an increase in surface turbulent sensible heat fluxes of 73 %, which leads to 22 % larger snow depletion rates in comparison with a continuous snow cover.

	$SCF = 5\,\%$	$SCF = 25\,\%$	$SCF = 55\,\%$
ΔH	9.7 W m^{-2} (106 %)	6.9 W m^{-2} (89 %)	4.9 W m^{-2} (73 %)
$\Delta(\Delta HS)$	15 (40 %)	12 (33 %)	7 (22 %)

Table 5.3 Daily mean ΔH [W m^{-2}] and $\Delta(\Delta HS)$ [10^{-3} m/day] by using meteorological fields close to the snow surface for different SCF, a wind velocity of 2 m s^{-1} and the number of snow patches =16. Numbers in brackets are relative values in %.

We investigated turbulent sensible heat fluxes and snow depth depletion rates as a function of the fetch distance. The small horizontal small-scale variability in near-surface air temperature fields of ARPS leads to almost constant turbulent sensible heat fluxes and snow depth depletion rates throughout the snow patch. For synoptic forcing situations, ARPS near-surface air temperatures are 1-2 K larger at the leading edge of the snow patches than further inside of the snow patch. For calm conditions, ARPS near-surface air temperatures are only 0.5 K larger at the leading edge of snow patches. Therefore, the "leading edge effect" in daily snow depth depletion rates as recorded with TLS (Schlögl et al., submitted) could not sufficiently be resolved and possible reasons will be discussed in Section 5.4.

5.3.3   Comparison of the idealized test site with the Wannengrat test site

We compared surface turbulent sensible heat fluxes between the idealized flat test site and the Wannengrat test site (Fig. 5.6). Numerical findings of the surface energy balance for the idealized test site are in a similar range as results for the Wannengrat test site. However, we found significant differences in surface turbulent sensible heat fluxes between both test sites, as slope-induced atmospheric processes become significant in complex terrain. Hence, the variation of surface turbulent sensible heat fluxes due to different SCF is larger in complex terrain. The development of katabatic flows was observed for a quiescent forcing and lead to a decrease of turbulent sensible heat fluxes with decreasing SCF (Mott et al., 2015). In contrast, surface turbulent sensible heat fluxes increase with decreasing SCF for the idealized flat test site for a quiescent forcing as described in detail in Section 5.3.2.
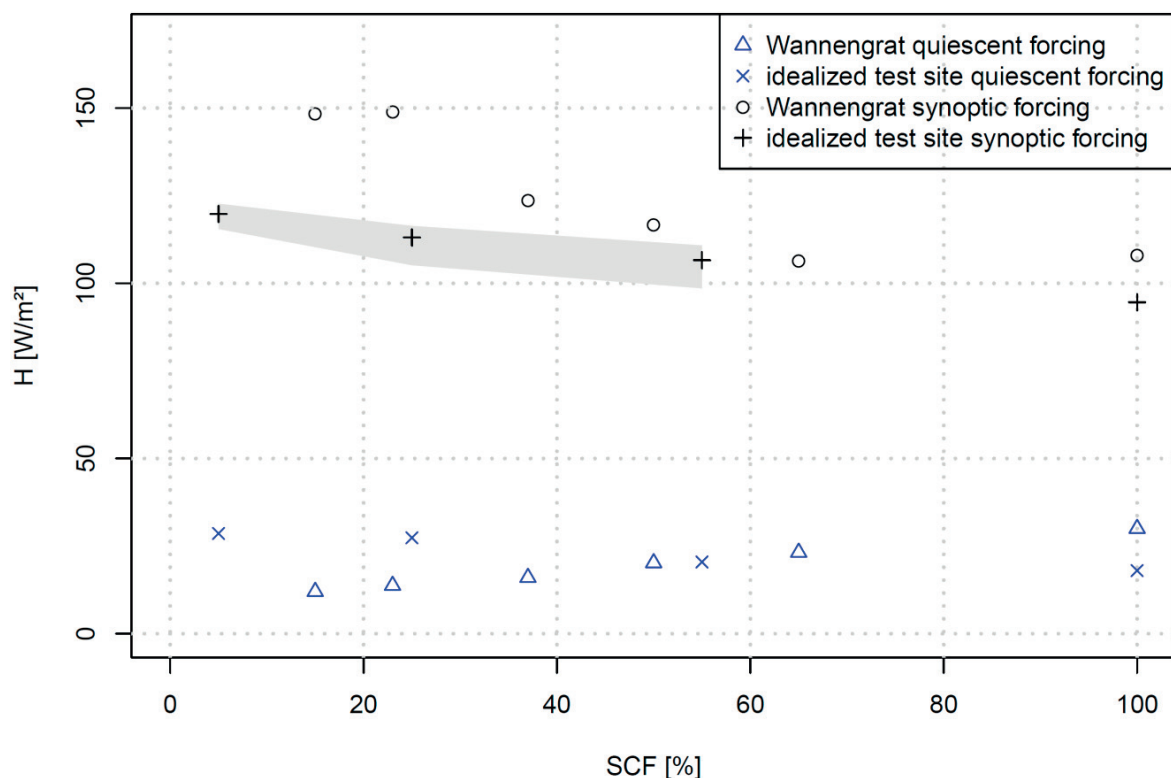
Fig 5.6: Surface turbulent sensible heat flux over snow [W m^{-2}] as a function of SCF for the idealized test site and the Wannengrat test site for a quiescent (blue) and synoptic forcing (black). The shaded area for the synoptic forcing of the idealized test site represents the uncertainty caused by the different number of snow patches.

For a synoptic forcing, surface turbulent sensible heat fluxes over snow increase for the idealized test site and the Wannengrat test site with decreasing SCF. However, the sensitivity of surface turbulent sensible heat fluxes to SCF is weaker for the idealized test site than for the Wannengrat test site caused by the fact that ARPS near-surface air temperatures und wind velocities are negatively correlated for the idealized test site, which leads to a damping of surface turbulent sensible heat fluxes. For the Wannengrat test site, however, the strong negative correlation was not observed, as changes in the wind velocity due to changes in the aerodynamic roughness length are less dominant than thermally-driven horizontal small-scale variations in the wind velocity field.

5.4 Discussion and conclusion

We showed that patchy snow covers significantly alter the surface energy balance of a snow pack. Once the snow cover gets patchy and the SCF decreases to 55 % (25 %, 5 %), the mean air temperature significantly increases ΔTA =1.8 K (3.7 K, 4.9 K) leading to a significant increase in daily mean snow depth depletion rates $\Delta(\Delta HS)$ = 22 % (33 %, 40 %). The sensitivity of daily snow depth depletion rates to varying snow distributions is mostly caused by a positive snow-albedo feedback which leads to an increase in mean air temperatures with decreasing SCF stimulating an increasing heat exchange towards the snow cover.

The small-scale variability of near-surface air temperatures at the first ARPS model level (0.8 m) is around one order of magnitude smaller than results from the temperature footprint approach, where near-surface air temperatures are calculated at a height of 0.01 m above the surface (Schlögl et al., submitted). This difference in the small-scale variability of near-surface air temperatures could be explained by the different height above ground. Alpine3D is not able to resolve the "leading-edge effect" (as recorded with TLS) by forcing the model with ARPS meteorological fields at 0.8 m above the surface. Our model resolution for this study is already much higher than usual for a meteorological model. Increasing the resolution even more will not be practical for real-world applications such as in hydrology or meteorology due to computational limitations.

Figure 5.7 compares the mean air temperature increase ΔTA averaged over snow-covered pixels between ARPS model results and the temperature footprint approach (Schlögl et al., submitted) as a function of the SCF and wind velocity. Although ARPS could not sufficiently resolve the leading-edge effect, the mean air temperature increase ΔTA averaged over snow-covered pixels (and hence the additional energy due to lateral transport processes) is similar for a large range of snow patch distributions and meteorological conditions. The correlation coefficient between the temperature footprint approach and ARPS model results is larger for the near-surface model level in 0.8 m than for the model level at 5.7 m above the surface. Differences in values of ΔTA between both ap-

proaches are large for a calm wind forcing (0.5 m s^{-1}), which could be explained by the fact that the formation of a SIBL is not fully resolved for the ARPS model simulation with a calm wind forcing and a $SCF = 25$ %.
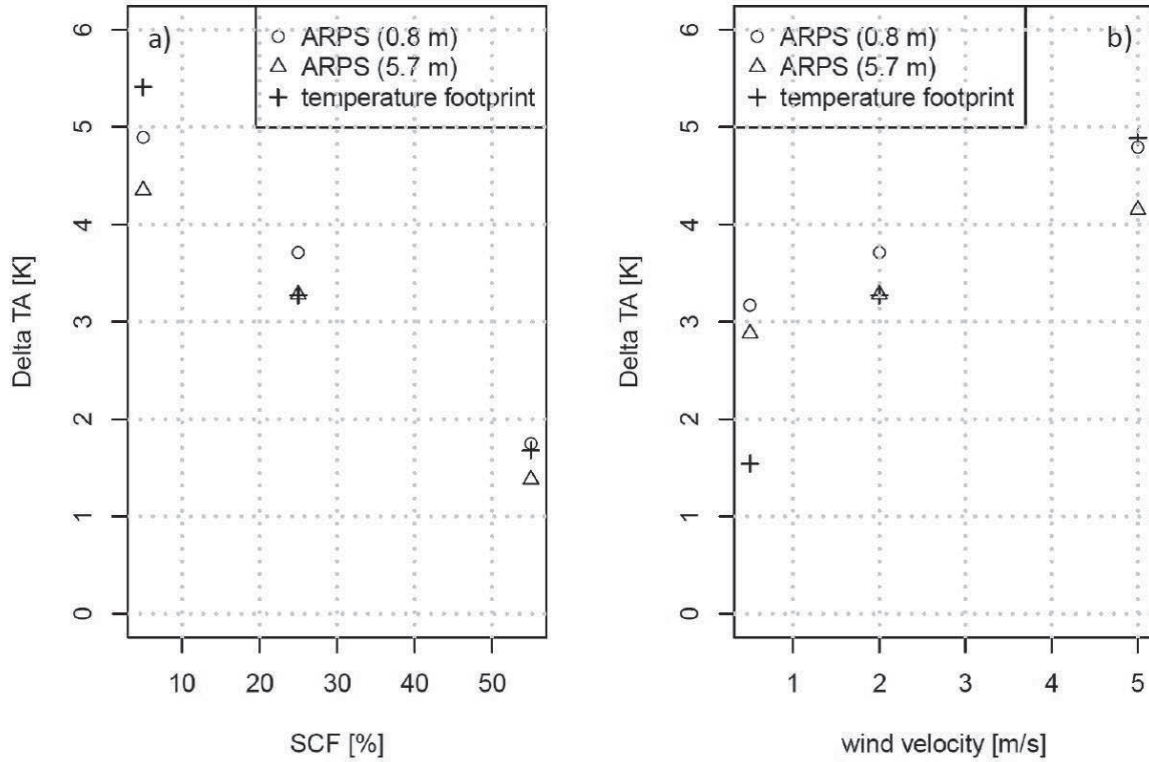

Fig 5.7 ΔTA [K] over snow as a function of SCF [%] (left) and wind velocity [m s^{-1}] (right) for the usage of ARPS meteorological fields in 0.8 m and 5.7 m above the surface and for the temperature footprint approach (Schlögl et al., submitted). The default values are $SCF = 25$ %, number of snow patches = 16 and wind velocity = 2 m s^{-1}.

We investigated differences in surface turbulent sensible heat fluxes by using meteorological fields in different heights above the surface (Fig. 5.3). For idealized conditions (e.g. continuous land surface, constant flux layer), the Monin-Obukhov bulk formulation predicts identical surface turbulent sensible heat fluxes if meteorological fields in different measurement heights are used. However, idealized conditions, which are required for the application of Monin-Obukhov bulk formulation, are heavily violated for patchy snow covers and the developing internal boundary layers of small vertical extent. Therefore, Monin-Obukhov formulations with the stability corrections, which are typically developed for situations with a continuous snow cover (Schlögl et al., 2017), could not account for the specific conditions over patchy snow covers, where strongly turbulent, warm air masses (originating from the adjacent bare ground) were advected towards snow patches with highly different surface characteristics. This warm air advection leads to very large temperatures differences over a short vertical distance, resulting in a very stable atmosphere directly above the snow surface. Schlögl et al. (2017) showed that stability corrections for a very stable atmosphere already show large errors over a continuous snow cover. Hence, surface turbulent sensible heat fluxes over patchy snow covers could strongly differ and will give erroneous estimations of the true surface heat exchange when using meteorological fields in different heights above the surface especially if the height of the SIBL is located close to the ground. The difference in turbulent sensible heat fluxes could be interpreted as the model uncertainty over patchy covers by violating necessary requirements in the Monin-Obukhov bulk formulation.

Our results have shown that knowledge about the snow cover distribution is a necessary requirement to correctly assess the additional energy to the surface energy balance from lateral transport processes of heat, momentum and moisture. Snow cover distributions are heavily dependent on different terrain parameters (Moore et al., 1991) of the digital elevation model (DEM). A patchy snow cover typically has a large mean snow patch size for a small horizontal scale of local depressions in the DEM. The mean snow patch size decreases when the horizontal scale of local depressions increases. A parametrization of a patchy snow cover distribution on a very small scale as a function of different terrain parameters would be complementary to the study of Helbig et al. (2015), where snow covered areas on larger scales up to 3 km were parametrized.

We tested the sensitivity of major numerical results to varying initial wind velocities. A sensitivity analysis with respect to varying aerodynamic roughness lengths for both snow and bare ground, cloud cover, the horizontal resolution of the model grid, analyse

period and parametrizations of stability corrections and incoming longwave radiation, goes beyond the scope of this study, but will be addressed in a future work.

Chapter 6 Sensitivity of Alpine3D modelled snow cover to modifications in DEM resolution, station coverage and meteorological input quantities

Schlögl, S.[1], Marty, C.[1], Bavay, M.[1], and Lehning, M. [1,2]

[1] WSL-Institute for Snow and Avalanche Research SLF, Davos, Switzerland
[2] School of Architecture, Civil and Environmental Engineering, École Polytechnique Fédérale de Lausanne, Lausanne, Switzerland

Abstract This study presents a comprehensive sensitivity and uncertainty assessment of important input parameters on the Alpine3D modelled snow water equivalent (SWE) for two different alpine catchments. Horizontal resolution of the DEM grid, station coverage and several meteorological input quantities were modified. Decreasing the horizontal resolution from 25 m to 1000 m leads to a 10 % higher SWE. Modifications in the spatial coverage of meteorological stations influence the SWE up to 20 %. Modifications of meteorological input quantities within some plausible ranges lead to changes in SWE up to 30 %. The results demonstrate that Alpine3D input uncertainties are in general in the same range as the typical measurement uncertainty of SWE and the uncertainty of the typical scenario spread of GCM-RCM ensemble runs.

Keywords Alpine3D • Model sensitivity • Snow cover • Climate change scenario

6.1 Introduction

Mountains have an exceptional position in the water cycle because they act as a fresh water storage in winter and as a melt water source in summer. Investigations on the snow cover provide the amount of stored and released fresh water which have important consequences for e.g. local winter tourism (Abegg et al., 2007; Schmucki et al., 2015), hydropower generation (Schaefli et al., 2007) and flood prevention (Weingartner et al., 2003). The information of the few meteorological and nivological point measurements is insufficient to answer hydrological questions e.g. the assessment of the released melt water in a certain catchment. Therefore, spatial models are used to simulate the snow cover and melt water runoff in mountainous areas. Historical studies show that simple temperature index models (Hock, 2003) simulate melt rates quite well but current physics-based models (Jin et al., 1999; Gelfan et al., 2004) are able to quantify spatial and temporal differences better (Walter et al., 2005). But even the results of physics-based models depend on some preconditions and assumptions, which are usually given by the setup of the modelling investigation.

Several studies on snow cover sensitivities have been published during the last decade. Keller et al., 2005 investigated the sensitivity of the snow cover to a climate change signal and their impact on plant habitats in an Alpine terrain. The influence of horizontal resolution, snow physical parametrizations and atmospheric forcing on the seasonal snow cover was analysed by Dutra et al., 2011). Ménégoz et al., 2014 assessed the snow cover sensitivity to black carbon deposition in the Himalayas. Berezowski et al., 2015 analysed snow cover sensitivities in a catchment in Poland.

In this study, we systematically investigate the impact of different model setups by changing some typical input parameters, like DEM resolution, data coverage or meteorological input quantities. To accomplish this task we use the physics-based model Alpine3D (Lehning et al., 2006), which has already been used in various mountain regions to assess e.g. snow water resources in mountain catchments (Michlmayr et al., 2008), simulate future snow cover on the basis of climate change scenarios (Bavay et al., 2009) and provide snow surface temperatures on ski pistes e.g. for the winter olympics in Vancouver and Sochi. All these studies used their own input parameter setup, which introduces some yet non-quantified uncertainties. For that purpose we investigate the robustness of the modelled snow water equivalent (SWE) by changing seven important model input parameters within some plausible ranges. It is important to realize that the absolute uncertainty of the modelled SWE is highly dependent on the potentially

insufficient spatial coverage of the meteorological measurements and their associated errors. We therefore focus on relative differences in SWE to Alpine3D default settings in this study and less in absolute values of SWE.

This paper is organized as follows. In Section 6.2, we present a description of the input data and the used model. Section 6.3 presents the methods of the study. In Section 6.4, the major results from the sensitivity studies are presented separately for each parameter. Further, these uncertainties are compared with the uncertainty induced by the common spread of a set of GCM-RCM models and the typical uncertainty of SWE measurements.

6.2   Data

6.2.1   Input data

The sensitivity analysis has been performed for two different catchments in the Swiss Alps in order to see how the elevation and topography influences the results (Fig. 6.1): The catchment of the river Gürbe (145.08 km^2) south of the capital Bern and an area around the city Davos in the Swiss canton Graubünden in Eastern Switzerland (346.08 km^2). The Gürbe catchment represents an area at the edge of the Swiss Plateau (mean elevation of 758 m asl.) with a temperature mean of 2.3 °C and a precipitation sum of 498 mm during the winter half year (Nov–Apr). The Davos catchment features high alpine characteristics (mean elevation of 2142 m asl.) with a temperature mean of −3.9 °C and a precipitation sum of 560 mm during the winter half year. The Gürbe catchment drains into the river Gürbe which later flows into the river Rhine and finally into the North Sea. The catchment of the area around Davos drains mostly into the river Landwasser, which discharges into the Rhine and finally into the North Sea.
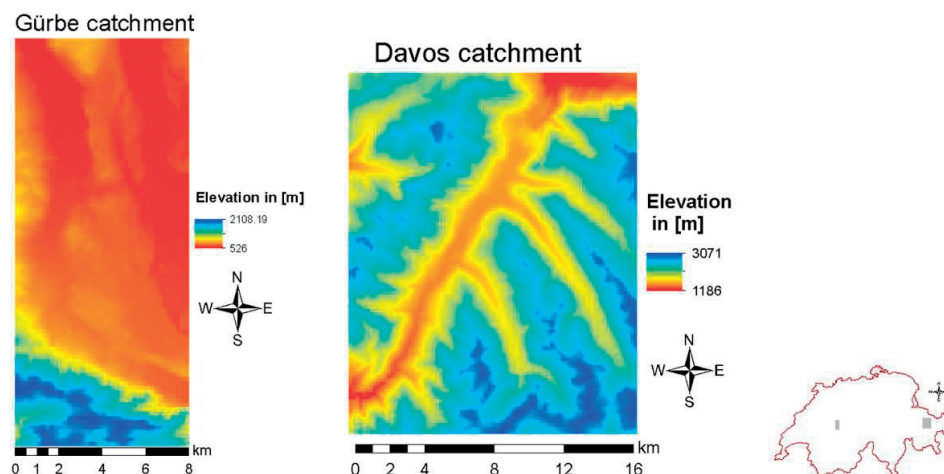
Fig 6.1 Elevation in [m asl.] of the Gürbe catchment (left) and the Davos catchment (right). The location of the two areas is shown in the map of Switzerland in the grey shaded areas (lower right panel). Note that the same colours indicate different elevation bands in the individual catchments.

The meteorological input data to drive the model are available from 48 automatic weather stations (AWS) in the Gürbe catchment and 34 AWS in the Davos catchment with hourly resolution. The data of the AWS were provided by the national weather service MeteoSwiss and by the Interkantonales Mess-und Informationssystem (IMIS), operated by the Institute for Snow and Avalanche Research (SLF). The IMIS stations are only equipped with unheated rain gauges, which prevented the use of its precipitation data for our purpose. Otherwise, air temperature, relative humidity, wind velocity, precipitation, incoming shortwave radiation and (if available) snow and ground surface temperatures were used as input data. Snow accumulation and snow ablation were simulated for 13 years from October 1999 until September 2012.

6.2.2   Model setup

The physics-based surface process model Alpine3D has been used to simulate the snow cover in the two catchments. Alpine3D is a spatially distributed (surface), three dimensional (atmospheric) model for analysing and predicting dynamics of snow-dominated surface processes in mountainous topography. It includes modules for snow cover (SNOWPACK), vegetation and soil, snow transport, radiation transfer and runoff which can be enabled or disabled on demand (Lehning et al., 2008; Kuonen et al., 2010). We used Alpine3D without the drift module. The Alpine3D input consists of two different surface grids (a digital elevation model (DEM) and the land cover data) and time series of different meteorological parameters measured by AWS.

The horizontal resolution of the DEM can be chosen as well as the horizontal resolution of the land cover data taken from CORINE (Coordination of information on the Environment) (Bossard et al., 2000), which uniformly classifies the most important types of land use in Europe. Before importing the land cover data in Alpine3D, the CORINE classification was transformed to the PREVAH classification (Viviroli et al., 2009) as the PREVAH classification is also used in Alpine3D. The PREVAH classification is less detailed than the CORINE classification, but sufficient for our simulations.

All meteorological input parameters of the stations were spatially interpolated to the grid of the DEM by an inverse distance weighting (IDW) except the radiation components which are physically calculated in the energy balance module. These interpolations of the meteorological data were done using MeteoIO, a pre-processing library of numerical models (Bavay and Egger, 2014). Linear elevation gradients of the meteorological quantities were calculated based on the data of the AWS on an hourly time step by IDW. In a variant of a robust regression approach, outliers are step by step eliminated from the dataset until a correlation coefficient of the linear regression reaches 0.7.

Note that only 20 % of the number of AWS can be omitted and in minimum four AWS are mandatory for the calculation of the altitudinal gradients. If this threshold cannot be reached, a default vertical gradient is assumed for the meteorological quantities except precipitation. In this case, the gridded precipitation is calculated with IDW. For each pixel of the DEM grid the snow cover model SNOWPACK (Lehning et al., 2002), which is the snow cover module in Alpine3D, calculates different snowpack parameters based on the interpolated meteorological input parameters in a temporal resolution of 30 min. The different soil and vegetation types (known from the CORINE land cover data) are considered in the SNOWPACK model as well as different parameters for the boundary layer, for example the height of the wind measurement and the roughness length of the snow. Since stability corrections based on interpolated meteorological parameters are not well defined, we chose the robust method of prescribing a neutrally forced boundary layer where the surface heat fluxes are parameterized using the Monin-Obukhov similarity theory. This assumption overestimates the surface fluxes up to 30 W m^{-2} in very stable conditions (see Section 6.4.3).

6.3   Methods

In this section we investigate the sensitivity of the snow cover for all seven modifications which are given in Table 6.1. In order to assess the impact of the individual parameter, only one parameter at a time has been changed in each model run. Changing one parameter at a time does not give a comprehensive picture of the model sensitivity as correctly pointed out by Saltelli and Annoni (2010). However, we are mainly interested in a comparative analysis of model sensitivity on specific parameters and note that investigating all possible combinations of our sensitivity parameters would cause over 400,000 simulations. Another limitation comes from using a specific climate setting and limited length time series (Shin et al., 2013). This limitation is considered to be small. We distinguish between Alpine3D "specific parameters" like the resolution of the grid and the data coverage on the one hand and "meteorology related parameters" which could vary due to climate change, natural variability or parameterizations on the other hand. The results of the Alpine3D specific parameters are only valid in the two chosen catchments but give a good estimate of the expected uncertainty in typical mountainous terrain. The changes of the meteorological input quantities would be similar in most catchments.

Parameter	Default	Modifications
Resolution	200 m	25 m, 500 m, 1000 m
Data coverage	all AWS	omitting one AWS
Roughness length	7 mm	1 mm, 2 mm, 4 mm, 10 mm, 13 mm
Undercatch	yes	no
$ILWR$ parameterization	Dilley Unsworth	Dilley clear sky, Dilley Crawford, Brutsaert clear sky, Brutsaert Crawford, Brutsaert Unsworth
Albedo	100 %	90 %, 95 %, 99 %, 101 %, 105 %, 110 %
Incoming shortwave radiation ($ISWR$)	100 %	90 %, 95 %, 99 %, 101 %, 105 %, 110 %

Table 6.1 The seven modified input parameters. For an explanation of the different parametrizations of the incoming longwave radiation ($ILWR$) see the references in Section 6.4.4.2.

The mean relative difference D (equation (6.1)) of SWE is a meaningful metric to estimate the effect of the modified parameters on the snow pack in Alpine3D.

$$D = \frac{Y_{mod} - Y_{def}}{0.5(Y_{mod} + Y_{def})}$$

(6.1)

where Y_{mod} is the modified response and Y_{def} is the response with the default parameters. Default parameters were taken from Bavay et al. (2012). The results are based on an average winter (mean of 1999–2012). This averaging leads to a smoothing of extreme weather events and represents the current climate best.

6.4   Results and Discussion

6.4.1   Resolution

The horizontal resolution of the DEM is often limited by computational power. However, the spatial resolution of a model domain highly impacts the model topography, which in turn influences the snow distribution e.g. by changing the input of shortwave radiation. Four different resolutions (25 m, 200 m, 500 m, 1000 m) were selected for the DEM grid and the land cover data, respectively. Note that the finest resolution of the CORINE land cover data is 100 m. For the 25 m grid a linear interpolation was necessary.

Using different horizontal resolution can change the distribution of the DEM, slope and aspect as shown in Fig. 6.2: The spatial distribution (PDF) of the elevation depends only little on the resolution. This is shown in a nearly identical mean elevation and an identical X-value, defined as the ratio of pixels which are higher than the mean elevation plus the standard deviation. But in a coarser resolution the mountain peaks are lower and the valley floors have a higher elevation. Accordingly, the slope angles are significantly lower, which demonstrates the well known flattening of the topography. A decrease of the mean slope angle from 10.9° (25 m resolution) to 4.9° (1000 m resolution) was observed in the Gürbe catchment and from 25.2° to 10.6° in the Davos catchment, respectively. The distribution of the aspect is highly determined by the chosen catchment. A dominating aspect of the distribution (in Gürbe the east sector (45–135°) and in Davos the west sector) gets more dominant in a coarser grid. Conversely, in an aspect with a low number of pixels the pixel percentage decreases with coarser resolution. In both regions the lowest ratio was observed for southern aspects consistent with the location of both areas north of the main Alpine divide. The ratio in southern aspects (135–225°) decreased from 13.0 % (25 m) to 4.9 % (1000 m) in the Gürbe catchment, respectively from 21.6 % (25 m) to 9.4 % (1000 m) in Davos. Regarding the impact on the simulated catchment wide SWE our results show that in comparison to the horizontal resolution of 200 m a 25 m resolution causes a negative bias of −2 % for both catchments, whereas in a 1000 m grid the SWE is +10 % (Gürbe), respectively +3 % (Davos) larger (Fig. 6.3a).

To investigate the reasons for this increase of SWE with coarser resolution of the DEM a closer look on Fig. 6.4 is helpful. This figure shows the influence of two different horizontal resolutions in dependence of the slope angle and the aspect for April. Three main observations can be made:

–   In flat terrain the horizontal resolution affects the SWE rarely.
–   Southern slopes (135–225°) show more SWE in coarser resolution for slope angles above 20°. This is caused by the flattening of the topography in coarser resolution. Flat slopes in southern aspects get less solar energy and there is less melting in the simulation with a coarser resolution.
–   Northern exposed slopes show less SWE in the coarser resolution, because the slopes are flatter. Thus the available energy for melting snow is larger.

These results are only valid if the slopes show already ablation. During the accumulation season SWE is uniformly distributed across aspects, which is caused by the fact that preferential deposition of snow or snow transport by wind or gravity have not been calculated for our investigations. The differences in SWE for the mid-winter of around 2 % (Table 6.2) are caused by melting events due to the low mean elevation of the Gürbe catchment and were not observed at high elevation.

In summary the effect of the southern slopes slightly predominates in spring which explains the increase of the SWE with coarser resolution in Fig. 6.3a. But all these results cannot be generalized because the mean elevation and main aspect of the catchment influence the results strongly. Thus, results for another catchment e.g. south of the main Alpine divide may show quantitative differences.
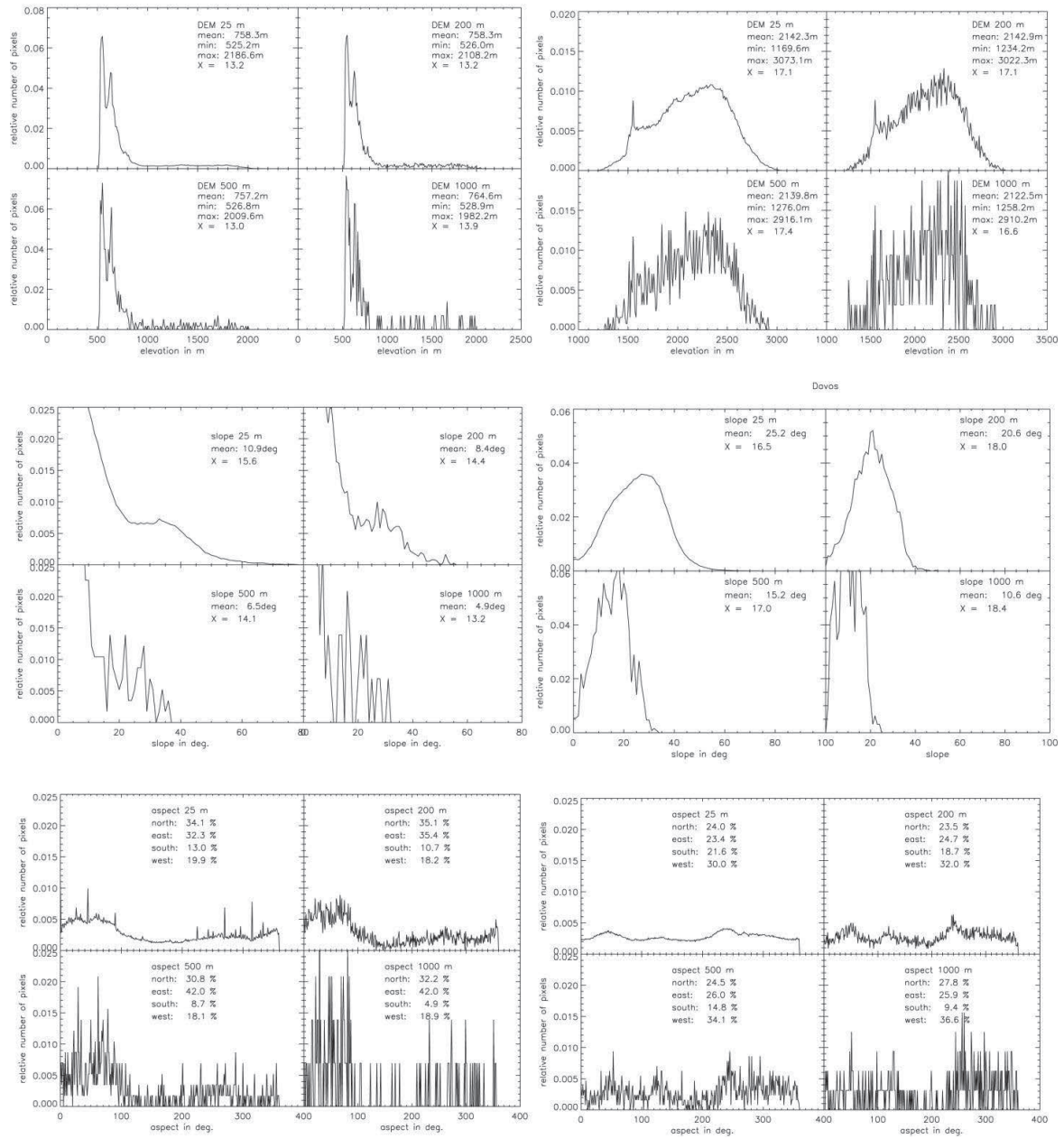
Fig 6.2 Standardized histogram of the DEM (top), slope angle (middle) and aspect (bottom) of the catchment Gürbe (left) and Davos (right) for the four different resolutions (25 m, 200 m, 500 m and 1000 m).
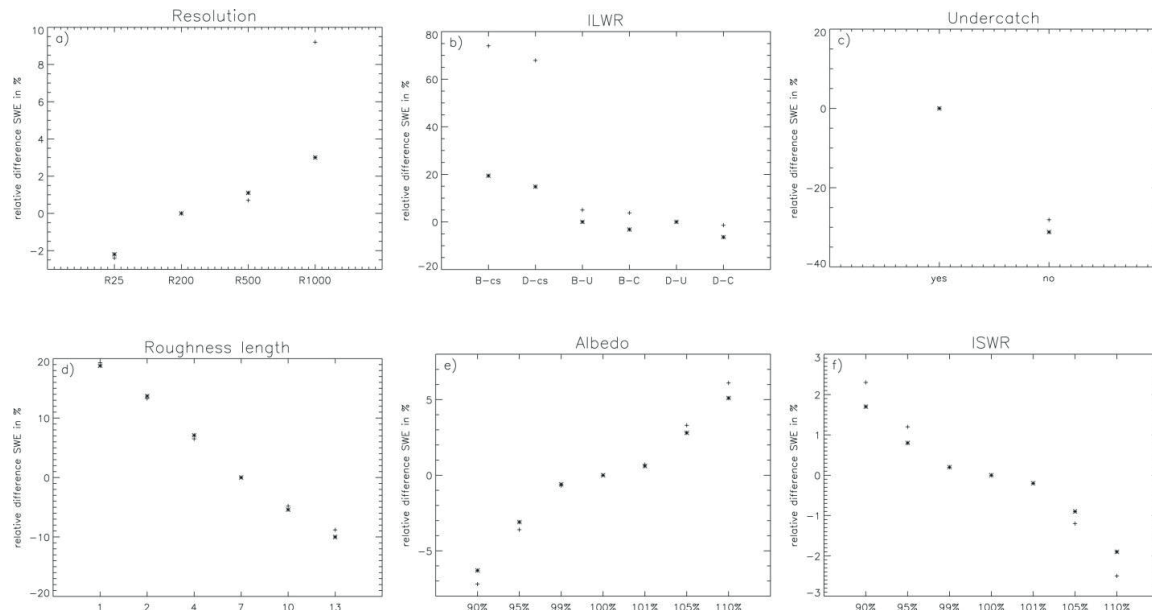
Fig 6.3 Mean relative difference in the simulated SWE [%] when the following input parameters are modified and compared to their default settings: resolution (a), $ILWR$ (b), precipitation undercatch (c), roughness length (d), albedo (e) and $ISWR$ (f) for the Gürbe domain (plus sign) and the Davos domain (asterisk).

Fig 6.4 Changes of SWE in mm for April dependent on the slope angle and aspect, when the R500 and the R25 grid are compared.

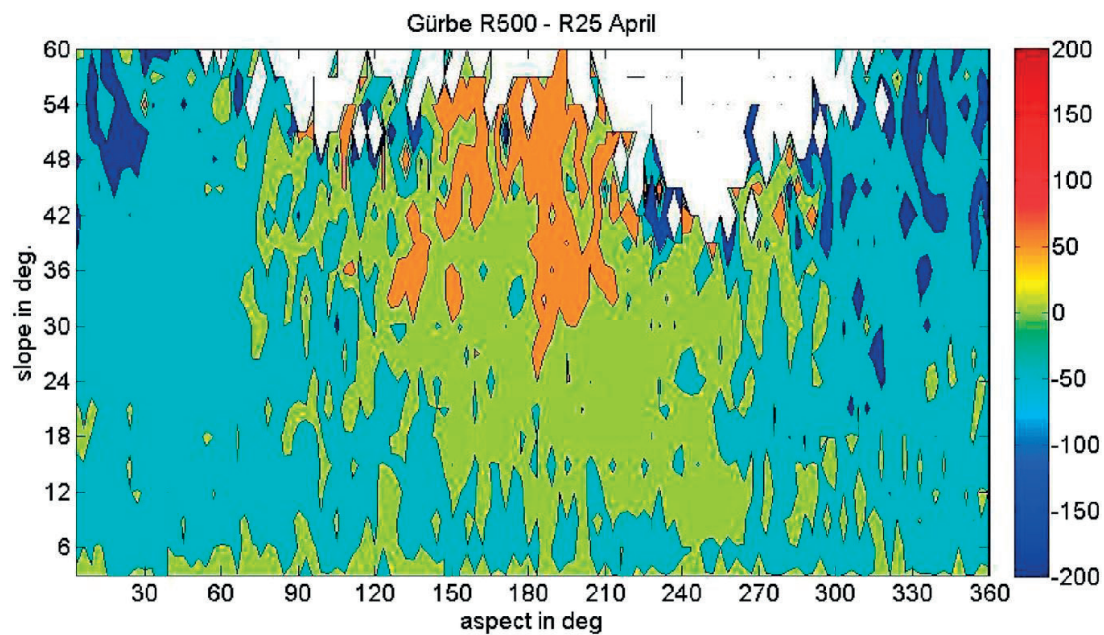| Parameter	Modification	Oct	Nov	Dec	Jan	Feb	Mar	Apr	Mai	Jun	Year
Resolution	R25	−2.3	−1.3	−1.4	−1.4	−1.4	−1.9	−4.6	−14.7	−9.5	−2.4 (−0.8)
	R500	0.2	0.4	0.5	0.5	0.5	0.6	1.1	5.2	−13.2	3.1 (1.0)
	R1000	13.5	6.4	5.5	5.2	4.6	7.8	19.4	38.9	29.1	11.6 (2.7)
ILWR	Brutsaert cs	45.1	49.7	65.9	74.2	72.2	75.3	66.2	126.3	169.3	74.0 (23.8)
	Dilley cs	40.3	45.6	61.2	68.8	66.4	68.7	60.2	118.7	163.4	67.9 (20.8)
	Brutsaert Unsworth	2.8	2.3	3.6	4.1	4.0	5.0	6.8	14.0	12.6	5.0 (1.0)
	Brutsaert Crawford	−1.9	2.6	6.1	7.2	5.9	3.5	−1.5	−7.4	−9.4	3.8 (0.7)
	Dilley Crawford	−4.4	0.3	2.3	2.8	1.5	−1.7	−8.7	−21.9	−19.0	−1.4 (−0.3)
Undercatch	no	−16.5	−22.4	−22.4	−24.0	−27.0	−28.6	−33.8	−58.3	−44.0	−28.1 (−5.0)
Roughness length	1 mm	15.6	10.8	15.3	17.1	17.0	18.6	21.8	53.7	63.2	19.3 (4.3)
	2 mm	10.0	7.2	10.7	11.6	11.7	12.8	15.6	37.8	40.6	13.3 (2.9)
	4 mm	4.3	3.4	5.3	5.8	5.8	6.4	7.8	18.5	16.8	6.5 (1.3)
	10 mm	−3.0	−2.4	−3.9	−4.3	−4.2	−4.8	−6.0	−13.2	−9.0	−4.8 (−1.0)
	13 mm	−5.2	−4.2	−7.0	−7.8	−7.7	−8.7	−11.1	−24.0	−14.9	−8.8 (−1.7)
Albedo	90 %	−4.7	−2.5	−3.5	−4.2	−4.7	−7.4	−13.2	−32.6	−26.2	−5.6 (−1.4)
	95 %	−2.3	−1.2	−1.7	−2.0	−2.3	−3.6	−6.3	−16.1	−13.7	−3.6 (−0.7)
	99 %	−0.5	−0.2	−0.3	−0.4	−0.5	−0.7	−1.2	−3.1	−3.0	−0.7 (−0.1)
	101 %	0.4	0.2	0.3	0.4	0.4	0.7	1.2	3.2	2.9	0.7 (0.1)
	105 %	2.2	1.2	1.6	1.9	2.1	3.4	5.6	15.3	15.3	3.3 (0.8)
	110 %	4.1	2.2	2.9	3.5	3.8	6.1	10.2	28.7	30.9	6.1 (1.3)
ISWR	90 %	1.7	0.8	1.1	1.3	1.3	2.3	4.0	11.2	10.2	2.3 (0.5)
	95 %	0.9	0.4	0.5	0.6	0.7	1.2	2.1	5.7	5.1	1.2 (0.2)
	99 %	0.2	0.1	0.1	0.1	0.1	0.2	0.4	1.2	0.9	0.2 (0.0)
	101 %	−0.2	−0.1	−0.1	−0.1	−0.1	−0.2	−0.4	−1.2	−1.0	−0.2 (0.0)
	105 %	−0.9	−0.4	−0.6	−0.6	−0.7	−1.2	−2.2	−5.8	−5.3	−1.2 (−0.2)
	110 %	−1.9	−0.9	−1.1	−1.3	−1.4	−2.5	−4.6	−11.8	−10.7	−2.5 (−0.5)

Table 6.2 Mean relative difference in the simulated SWE [%] for the Gürbe catchment when input parameters are modified and compared to their default settings. Shown are the monthly impact between October and June and the annual value. The values in the brackets indicate the yearly mean absolute difference in [mm].

6.4.2 Station coverage

The meteorological data of the automatic weather stations (AWS) were interpolated to the model grid by an inverse distance weighting algorithm including a linear elevation gradient. A uniform spatial distribution of the AWS is ideal to achieve robust results but is usually not given in reality.

To investigate the impact of the individual stations leave-one-out cross validations (48 + 1 in Gürbe, 34 + 1 in Davos) were performed for both catchments. These simulations were conducted from October 2008 until September 2010.

Omitting one MeteoSwiss station affects the SWE of the whole domain more than omitting an IMIS station (Fig. 6.5). This is caused by the fact that the MeteoSwiss station also provides precipitation which is a very sensitive meteorological parameter for the calculation of SWE. Omitting a low elevated MeteoSwiss stations can result in more SWE and omitting a high elevated MeteoSwiss station can result in a decrease in SWE for both catchments. Thus, neglecting several high elevated MeteoSwiss stations could lower the SWE artificially (Fig. 6.5). The highest differences up to 20 % occur if omitting high elevated stations in the precipitation abundant region of the main Alpine divide.

A part of these differences may be caused by the IDW interpolation which does not include topographically induced climate effects. This is explained by a simple example. A station in the target valley has the same weighting as a station in a neighbouring valley, if the distance to the target grid point is the same. This assumption is not correct, because the target grid point is climatologically more influenced by the station in the target valley than by the station of the neighbouring valley.

The different AWS should ideally be located in the same climate region with same temperature and precipitation patterns. Otherwise altitudinal gradients especially for the precipitation would be averaged by two different climate regions and applied for the whole catchment. The assumption of one elevation gradient per catchment can often not be realized due to the fact that large catchments often contain more than one climate region. Additionally one climate region may contain not enough stations to calculate altitudinal gradients.
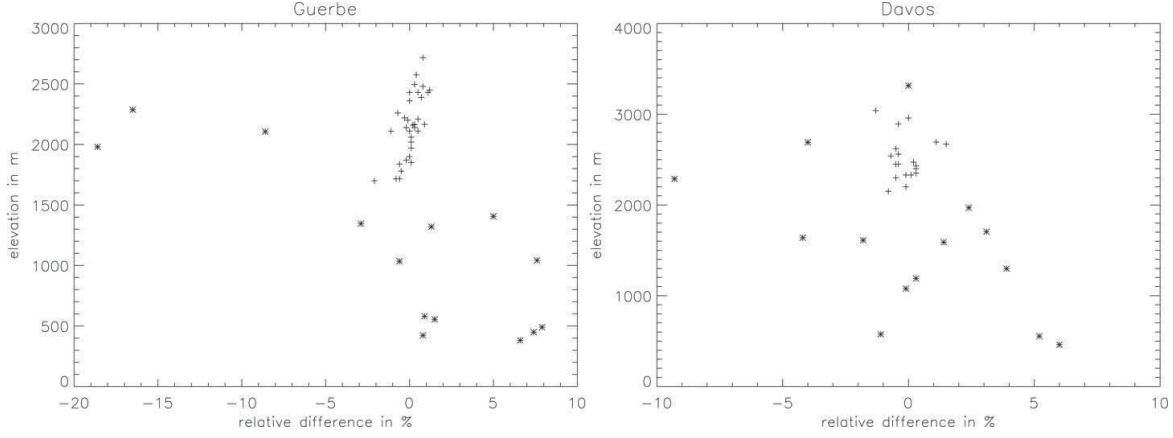
Fig 6.5 Impact on the simulated SWE [%] when omitting one station for Gürbe (left) and Davos (right). The elevation of the omitted station is shown on the y-axis. The plus sign marks the IMIS stations and the asterisk marks the MeteoSwiss stations. The simulation was conducted from October 2008 until September 2010.

6.4.3   Boundary layer parameters

Boundary layer processes determine the energy balance of a snowpack. Knowledge of the size of turbulent fluxes in complex terrain is required in order to calculate the energy balance correctly (Martin and Lejeune, 1998). We focus on the modification of the roughness length, which is difficult to measure. Additionally, we also investigate height of the wind measurement, which depends on the station design and the depth of the snow on the ground. These parameters determine among others the available energy of melting snow.

The available energy for melting snow (M_0) is determined by the energy balance of the snow pack and is calculated as follows:

$$M_0 = SW + LW + H + Q_l + P + Q_g, \tag{6.2}$$

where SW is the net shortwave radiation, LW is the net longwave radiation, H is the sensible heat flux, Q_l is the latent heat flux, P is the advective heat from precipitation and Q_g is the heat exchange with the ground (including advection by meltwater). In the following it will be shown that a variation of the roughness length or the height of the measured wind speeds will affect the latent and sensible heat flux and hence M_0.

The sensible heat flux H and latent heat flux Q_l is given by:

$$H = \rho \, c_p C_H \bar{U} \left(T_{z_{ref}} - T_s \right) \tag{6.3}$$

$$Q_l = \rho \, L_v C_H \, \bar{U} \left(q_{z_{ref}} - q_s \right) \tag{6.4}$$

where ρ is the air density, c_p is the heat capacity of air, $\bar{U}$ is the mean wind velocity, L_v is the latent heat of sublimation for ice, $T_{z_{ref}}$ is the air temperature at the reference height, T_s is the snow surface temperature, $q_{z_{ref}}$ is the specific humidity at the reference height, q_s is the specific humidity at the surface and C_H is the bulk transfer coefficient for heat, momentum and water vapor. In an unstable or stable atmosphere stability corrections have been taken into account to calculate the bulk transfer coefficient. For neutral conditions C_H simplifies to the following expression:

$$C_H = \frac{k^2}{[\ln(z/z_0)]^2}, \tag{6.5}$$

where k is the von Karman's constant, u is the wind speed at the height of the wind measurement z and z_0 is the aerodynamic roughness length.

A decreasing roughness length decreases the bulk transfer coefficient and the sensible and latent heat fluxes. This would lower the available energy for melting the snow in a snow pack and result in an increase of the SWE. The roughness length is changed in this experiment between 1 mm and 13 mm (Lehning et al., 2006) which accounts for the range of physically realistic values due to changes in the surface condition during the snow season. The results show a strong impact of the roughness length on the simulated SWE. Increasing the roughness length from 1 mm to 13 mm reduces the SWE in both domains by up to 30 % (Fig. 6.3d). The highest relative differences were found at the beginning and the end of the snow season (Table 6.2). The 1000–1500 m elevation zone shows the lowest relative differences (Fig. 6.6d).
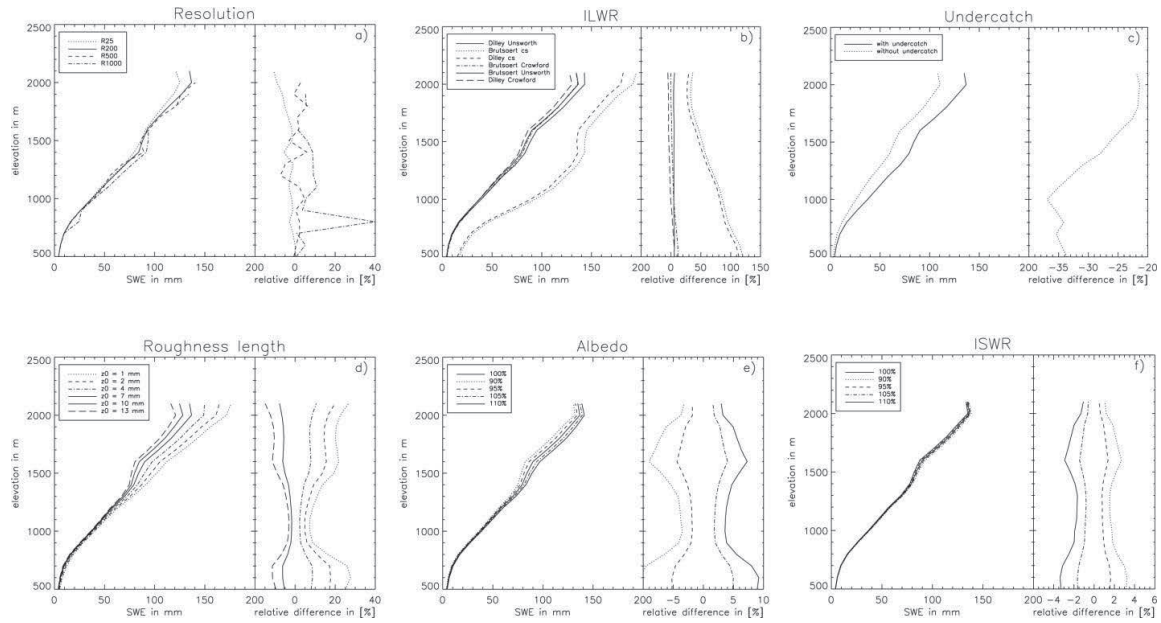
Fig 6.6 Altitudinal profile of the SWE in [mm] and the relative difference in [%] to the default settings for the Gürbe catchment is shown for resolution (a), $ILWR$ (b), precipitation undercatch (c), roughness length (d), albedo (e) and $ISWR$ (f). The elevation bands were calculated in a 100 m mean. Note the same SWE x-axis scaling for the six modifications but a different x-axis scaling for the relative difference.

Assuming 1.5 m – 3 m snow depth, the height of the wind measurements is changed between 3.5 m and 8.5 m. These values were chosen because MeteoSwiss stations measure the wind in 10 m and IMIS stations in 6.5 m above ground. Increasing the height of the wind measurements from 3.5 m to 8.5 m, the total amount of SWE increases 8.7 %. This can be explained by a lower wind speed near the surface for the 8.5 m measurement height, which causes lower surface heat fluxes in the melting period.

The Alpine3D default setting represents a neutrally forced atmospheric surface layer using Monin-Obukhov similarity theory for the calculation of the turbulent fluxes. Alpine3D alternatively provides a setting which considers a stability correction by Stearns and Weidner (1993) (modified by Michlmayr et al., 2008). Using this stability correction increases the SWE of +23.3 % in the Gürbe catchment caused by lower turbulent heat fluxes (not shown). These findings are in agreement with a study of Mott et al. (2013), where the two opposite effects of the advective heat transport and the near-surface boundary layer decoupling were discussed.

6.4.4 Meteorology related parameters

6.4.4.1 *Precipitation undercatch*

Several studies (e.g. Sevruk, 1982) summarized in the WMO report of Goodison et al. (1998) demonstrate that the measured precipitation at the rain gauge underestimates the true precipitation of a catchment due to high wind speeds. This underestimation of the measured precipitation is negligible in valleys with low wind speeds and becomes more important in mountainous and windy areas. We applied the Hamon (1973) correction algorithm since Schmucki et al. (2014) found good results for stations in our domain with this method. The undercatch corrected precipitation P_{cor} is defined as:

$$P_{cor} = P_{meas} \exp\left(b\,\overline{U}\right), \tag{6}$$

where P_{meas} is the measured precipitation of the rain gauge, $\overline{U}$ is the wind speed in m s^{-1} and b is a temperature dependent coefficient. No undercatch correction is applied for temperatures above 1.2 °C. Accordingly solid precipitation only is corrected.

The differences between the undercatch corrected precipitation and the raw data from the measured precipitation of the rain gauge are only substantial in elevations above 2000 m (Fig. 6.7). In this elevation zone, mean relative differences of 27.6 % for Davos (22 stations), respectively 22.4 % for the Gürbe catchment (26 stations) were found for the precipitation. If we only regard the stations in the elevation zone between 1000 m and 2000 m, the correction amounts to only 5.2 % (Davos) and 1.5 % (Gürbe). Below 1000 m the effect of the undercatch correction is negligible for both domains. Alpine3D has been running with and without this precipitation correction to quantitatively investigate the impact on the distribution of the snow cover. Looking at the entire catchment, the SWE is 28.1 % higher in the Gürbe catchment, respectively 31.2 % in the Davos catchment if the application of Hamon undercatch is applied (Fig. 6.3c). Regarding seasonal differences the undercatch impact is small at the beginning of the snow season and has its maximum at the end of the snow season due to the accumulation of snow during the season (Table 6.2).

Corresponding to the high wind speeds at high elevations, the absolute SWE is sensitive to the precipitation undercatch at greater heights (Fig. 6.6c).
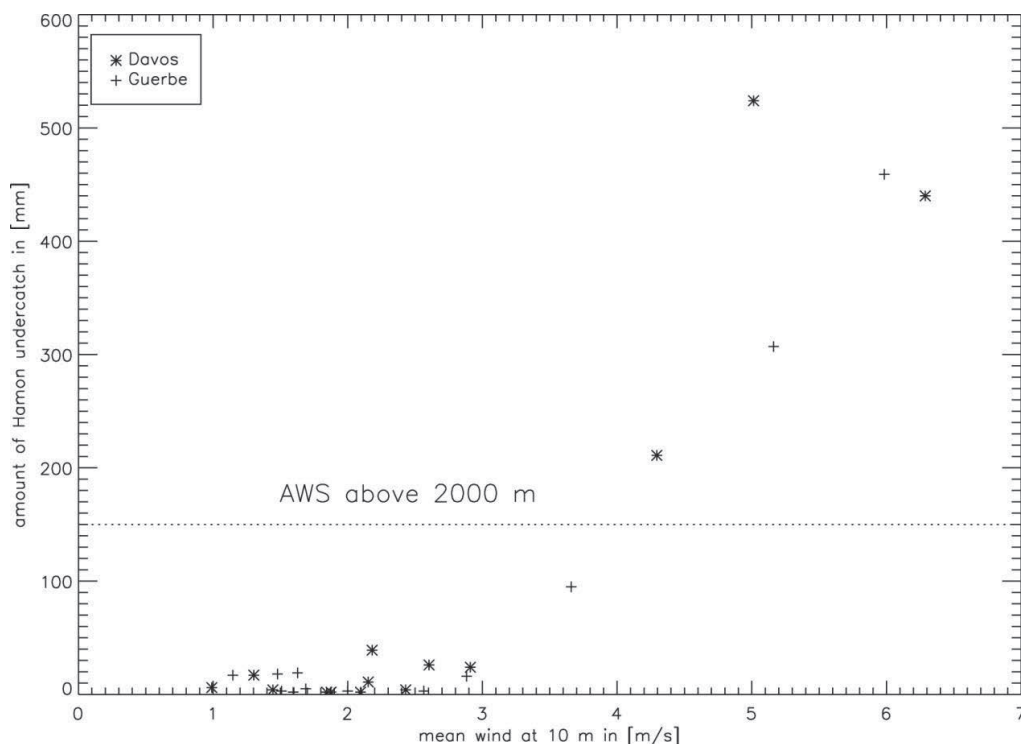

Fig 6.7 Annual undercatch correction as a function of the wind speed for the MeteoSwiss stations in the Gürbe (plus sign) and the Davos catchment (asterisk sign).

6.4.4.2 Incoming longwave radiation

Incoming longwave radiation is usually not measured by standard AWS's, but is an essential input parameter to solve the energy balance in physics-based models. Therefore $ILWR$ is often parameterized with the help of standard meteorological parameters. We selected six different $ILWR$ parameterizations, which were used by Schmucki et al. (2014) in the same climate region to investigate changes in the energy balance of the snow pack and finally differences in the snow distribution.

The $ILWR$ parameterizations depend on temperature, relative humidity and cloud cover fraction, which we estimated by dividing the measured $ISWR$ with the theoretical $ISWR$ at the top of the atmosphere. Including other parameters like the atmospheric turbidity would improve the estimation of the cloud cover fraction, but the above estimation is sufficient for our requirements. The clear sky parameterization of Dilley and O'Brien (1998) in combination with the cloud correction algorithm of Unsworth and Monteith (1975) was used in our simulations as the default because this parameterization shows a good performance in the Alpine domain according to Schmucki et al. (2014). As an alternative to the default clear sky and all sky radiation schemes we tested the Brutsaert (1975) clear sky and the Crawford and Duchon (1999) all sky schemes.

In order to estimate cloud cover during night, we use a running mean of 24 h by averaging 12 h backward and 12 h forward in time, as detailed described in Schmucki et al. (2014). This is conducted for every time step in one hour resolution. This averaging has a smoothing effect on the $ILWR$ day data.

Our investigations show nearly identical values for all investigated all-sky $ILWR$ parameterizations in winter. Clear sky schemes alone have also been investigated because some models parameterize the $ILWR$ by assuming only a clear sky scheme. As expected, the parametrized clear sky $ILWR$ gave significantly lower absolute values than the all-sky $ILWR$ (Table 6.3).

	Clear sky	Unsworth	Crawford
Dilley	228.6	269.5	273.0
Brutsaert	219.3	263.9	268.1

Table 6.3 Spatial and temporal (November–April) mean of the six $ILWR$ parameterization in [W m^{-2}] averaged over 13 years for the stations of the Gürbe catchment.

The results of the parameterized $ILWR$ were validated with time series of measured $ILWR$ from six different stations in the vicinity of the two investigated catchments. This comparison was done from October 2010 to September 2012 for Altdorf (449 m), Payerne (490 m), Bern (555 m), Ulrichen (1345 m), Napf (1406 m) and Gütsch (2287 m). The root mean square errors (RMSE), which has shown to be useful in the evaluation of environmental models (Bennett et al., 2013), show high values for the clear sky parameterizations of Dilley and Brutsaert (10 W m^{-2}) and lower values for the all sky parameterizations (3–5 W m^{-2}) (Fig. 6.8). The Dilley parameterization shows lower $RMSE$ than the Brutsaert parameterization, both for clear sky and for the combination with the cloud correction methods. The Unsworth cloud correction method was found to be the better cloud correction scheme than Crawford. The lowest RMSE was found for the Dilley-Unsworth parameterization, in agreement with the findings in Schmucki et al. (2014). The other three all-sky parameterizations show higher RMSE up to 5 W m^{-2}. The RMSE does not differ significantly between valley and mountain stations.
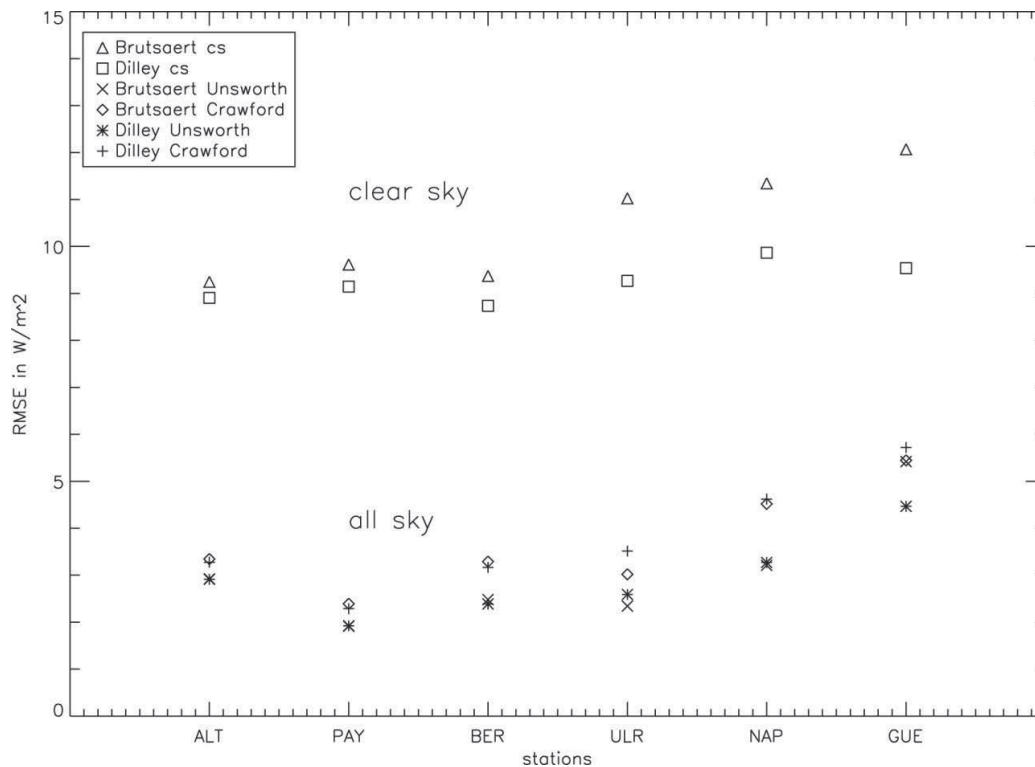
Fig 6.8 $RMSE$ in [W m^{-2}] comparing 6 different $ILWR$ parameterizations with measured data. The shown RMSE is a mean value of six stations between 450 and 2300 m asl.

The mean relative difference D between the default settings and the modifications is higher in Gürbe than in Davos, especially for the clear sky parameterizations. The SWE is overestimated in case of the clear sky parameterizations around 70 % in Gürbe and around 20 % in Davos in terms of relative differences. However, in terms of absolute differences we found a similar overestimation for both catchments. The Gürbe area has a lower elevation, therefore lower mean absolute SWE values and therefore shows higher relative changes. The differences for the all sky parameterizations are much smaller (around 5 %) and do not differ significantly for the two catchments (Fig. 6.3b). The highest relative differences were observed at end of the snow season (Table 6.2). For the all sky parameterizations no elevation dependency was found, whereas the clear sky parameterizations have higher differences in the valleys (Fig. 6.6b). These results demonstrate that clear sky parameterizations should definitely not be used.

6.4.4.3 Variation of the $ISWR$ and the albedo

A study of Wild (2009) shows the variation of $ISWR$ in the past century. Between the 1950s and 1980s a "global dimming" (4 % decrease of the $ISWR$ measured on the Earth's surface) and afterwards a weak recovery ("global brightening") was observed. The origin of these variations are caused by the turbidity of the atmosphere and not forced by the sun. Changes in the cloud cover (Houghton, 2001; Giorgi et al., 2004), aerosol emissions and volcanic eruptions are mainly responsible for these effects.

Several processes can change the snow surface albedo e.g. deposition of black carbon (Hadley and Kirchstetter, 2012), dust discharge from local slopes or remote deserts. These uncertainties in the snow surface albedo cause model errors especially in the melting period. Schmucki et al., 2014 show that the snow melting in the simulations starts too late in the season due to an overestimation of the albedo especially in lower elevations.

The albedo value and the $ISWR$ of the MeteoSwiss stations were modified to 90 %, 95 %, 99 %, 101 %, 105 %, 110 % of their default values in order to assess the effect on the snow pack. These modifications affect the amount of supplied energy of the snow pack and change the date of the melting period. The SWE varies $\pm$ 6 % due to the albedo modification (Fig. 6.3e) and $\pm$ 2 % due to the $ISWR$ modification (Fig. 6.3f) using the range of $\pm$ 10 % of the default values. The results of the albedo modification clearly demonstrate the effect of the snow albedo feedback mechanism and are therefore highly relevant for an assessment of climate change impacts.

6.4.5 Further input uncertainties

The calculation of wind induced precipitation undercatch for highly elevated alpine stations could be affected by the following problem: Freezing of non-heated wind sensors in the winter season can happen from time to time. Wind speeds are thus zero and the applied undercatch does not change the precipitation. This leads to an underestimation of the precipitation data and finally an underestimation of the snow depths at high elevation. Additional uncertainties may also occur because several physical processes like wind drift, preferential deposition or advective heat transport were not considered in the model version. Due to the large number of input uncertainties and their dependencies it is not possible to find the best value for each parameter separately. Therefore the results may affected by error cancellation or error addition.

6.4.6 Uncertainties in the climate change signal

The comparison of the so far investigated input uncertainties with uncertainties of the ensemble spread of a climate change scenario from different climate models are mandatory to assess the relative importance of the input uncertainties. Ensemble projections for temperature and precipitation have been taken from the CH2011 platform (Fischer et al., 2012). We investigated the non-interventional scenario A2 for the end of the century (2070–2099) for the Gürbe catchment. The simulations for the time period 2020–2049 support the conclusions as drawn for the time period 2070–2099 and are not shown for simplicity. We used the upper, lower and median datasets which contains the 97.5 %, respectively 2.5 % quantile and the median of 20 member ensembles of the GCM-RCM model chains. The mean remaining amount of SWE at the end of the century is 12 % compared to the reference period. This percentage represents the median of the ensemble members of the predicted temperature and precipitation changes. The percentage increases to 20 % when choosing the lower ΔT dataset in combination with the upper ΔP dataset. On the other hand, the percentage decreases to 3 % by applying the upper ΔT in combination with the lower ΔP dataset. Therefore, the remaining SWE is predicted to be between 3 % and 20 %, which translates into an uncertainty of 17 % due to climate change. By applying the two moderate cases (upper ΔT, upper ΔP vs. lower ΔP, lower ΔT), the climate change uncertainty is reduced to 10 %. The climate change uncertainty of the temperature and precipitation has a similar effect on the SWE as the uncertainties in our study. In particular, uncertainty of input parameters can be neglected if the relative change of SWE is calculated for future time periods. The remaining SWE – expressed as percentage change – for future time periods is not significantly affected by roughness lengths or other modified parameters. For example, using the range in the roughness length from 1 to 13 mm an uncertainty of only 2 % was simulated for the remaining SWE towards the end of the century. This allows very robust results for climate change simulations independent of the choice of different specific model input parameters for the snow model.

6.4.7 Uncertainties in the SWE measurements

The uncertainties of the simulations must also be set in perspective to the uncertainties of the measured SWE. Jonas et al. (2009) quantified the uncertainty of SWE measurements with 18 % in the early winter, 13 % in the mid-winter and 30 % in the late winter in the Swiss Alps. Sturm and Liston (2003) found an uncertainty of 23 % in the mid-winter in Alaska. Similar results show Kershaw and McCulloch (2007) for a region in Canada. Note that these values represent the uncertainties of point measurements. Additional uncertainty is added by the interpolation of SWE point measurements to the model grid (Grünewald et al., 2009).

6.5 Concluding remarks

We modified seven Alpine3D input parameters and analysed their relative impact on the simulated SWE for two different catchments. Based on our results, we recommend the following model strategies. A representative value of the roughness length and the precipitation undercatch should be used. The modelled SWE is also very sensitive to the station coverage, especially in catchments with different climate regimes. The choice of different $ILWR$ parametrizations, resolution, albedo and $ISWR$ are in contrast not crucial parameters compared to the upper three parameters (see Table 6.4). As already discussed in the methods, the full model sensitivity can only be assessed by combining parameter changes (Saltelli and Annoni, 2010), which has been beyond the scope of this analysis. While we could not perform such a systematic investigation of combined parameter variations, we expect from our experience with the model that uncertainties in such combinations will be smaller than the simple sum of sensitivities of individual parameters. This remains to be shown in future investigations.

Input parameter	Uncertainty
Resolution	5–15 %
Station coverage	15–25 %
Boundary layer	25–40 %
Undercatch	25–40 %
$ILWR$ parameterization	5–15 %
Albedo, $ISWR$	0–5 %

Table 6.4 Assessment of the uncertainties for different input parameters in four categories.

The low-elevation Gürbe catchment is more sensitive to changes of the model input parameters than the high-elevation Davos catchment due to a shallower snow pack and the fact that the temperatures are closer to the threshold temperature of zero degree. This statement also explains the larger sensitivities towards the end of the snow season.

In contrast to former studies, this is the first study quantifying uncertainties of model input parameters for a complex physics-based and fully distributed model and comparing it to the uncertainties from climate predictions.

Our findings for the individual input parameters can be summarized as follows:

- Resolution: Changing the horizontal resolution from 25 m to 1000 m caused a SWE increase by approximately 10 %. Coarser horizontal grids overestimate the SWE in the ablation period due to the flattening of the topography with coarser resolution, which leads to an underestimation of snow melting.
- Station coverage: Leave-one-out experiments show an input uncertainty of up to 20 % in omitting meteorological stations for our specific settings. Meteorological stations which provide precipitation data show the highest uncertainties whereas stations without precipitation data show an input uncertainty of only 2 %. Neglecting stations in precipitation abundant regions would lower the SWE artificially. The minimum number of input stations highly depends on the chosen catchment and could vary (based on experience) between 1 and 2 in flat terrain and 5–10 in catchments with complex surfaces.
- Boundary layer: A very high input uncertainty was observed by modifying several boundary layer parameters. Varying the roughness length between 1 and 13 mm results in an SWE uncertainty of 30 %. Using a stability correction instead of an assumption of a neutral boundary layer increases the SWE about 24 %.
- Precipitation undercatch: 30 % more SWE with the precipitation correction setup and a better agreement with SWE measurements demonstrates that the wind induced precipitation undercatch must be taken into account.
- $ILWR$ parametrization: Using a clear sky parameterization should be avoided, because the SWE is overestimated significantly up to 70 %. The choice of an adequate all-sky parametrization is not that important because the input uncertainties are below 10 %.
- Variation of the $ISWR$ and the albedo: The input uncertainties in modifying the albedo and $ISWR$ in a range of ± 10 % are relatively small (± 5 %) compared to the other modifications in this study.

Alpine3D input uncertainties are in the same range as the typical measurement uncertainty of SWE and the uncertainty of the GCM-RCM ensemble spread of an expected climate change scenario. These findings are of high relevance for practitioners, which are e.g. responsible for water resource management or ski area operations.

Acknowledgements

Chapter 7   Summary and conclusions

Physics-based snow models typically satisfactorily represent the snow height in the accumulation period in the case of high quality input data, but once the ablation period starts in spring, the model error of the snow height strongly increase (Essery et al., 2013). However, recording high quality precipitation input data in the accumulation period is a challenging issue, due to spatially heterogeneous precipitation input in mountainous regions and wind drifts during heavy snow falls (Gerber et al., 2017). This thesis focuses on the model performance of snow melt prediction in the ablation period. For this purpose, the (surface) energy balance of the snow pack is analysed to correctly model snow melting in a physics-based model.

Based on the snow coverage we divided the ablation period of a snow season in two parts: the continuous snow cover part and the patchy snow cover part. The surface energy balance of the snow pack is typically calculated by the vertical energy exchange of a snow pack with the atmosphere as long as the snow cover remains continuous. This assumption could lead to large model errors especially for patchy snow cover situations. The advection of warm air from the bare ground towards the snow patch becomes important with decreasing snow cover fraction and could act as an additional energy source. Hence, near-surface air temperatures and finally the surface energy balance of a patchy snow pack are strongly modified by the horizontal transport of heat.

Analysing snow ablation rates for several stations in the Swiss Alps reveals a non-linear decrease of snow heights in the ablation period with an accelerated decrease in snow heights in the late ablation period (Fig. 7.1). This is caused by (1) shorter nights and larger incoming shortwave radiation throughout the day, which increase mean air temperatures, and finally incoming longwave radiation and (2) the additional energy due to lateral transport processes and the modification of the near-surface air temperatures.
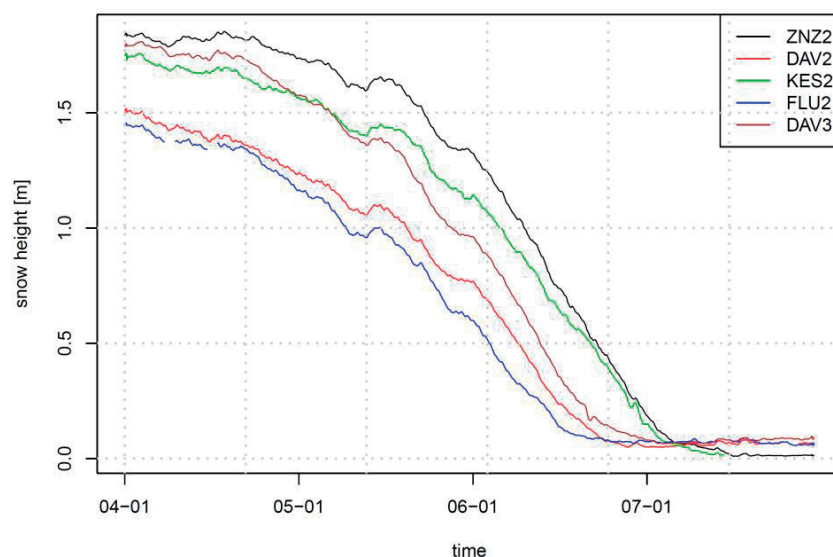
Fig 7.1 Snow height [m] of five IMIS stations in the Swiss Alps during the ablation period. The mean values from a 10 year analysis period are shown.

7.1   Continuous snow cover

In the first part of the thesis we focused on the surface energy balance of a continuous snow cover for an individual location and analysed the model performance of turbulent sensible heat fluxes (Chapter 2) as one part of the entire surface energy balance, which is assessed by validating snow surface temperatures.

We found three main errors sources which contribute to model uncertainties in the surface energy balance of a continuous snow cover:

1. Incoming longwave radiation

2. Turbulent sensible (and latent) heat fluxes

3. Snow properties

7.1.1 Incoming longwave radiation

The largest error source is introduced in the surface energy balance of a snow pack by the parametrization of incoming longwave radiation, which is often not measured. Our analysis shows uncertainties in modelled snow surface temperatures up to 5 K for different parametrizations of the incoming longwave radiation, which is equivalent to a flux uncertainty of around 20 W m^{-2}. This result clearly underlines the importance of high quality measurements of the incoming longwave radiation (and the other radiation components).

7.1.2 Turbulent sensible (and latent) heat fluxes

The second largest error contribution stems from the parametrization of turbulent fluxes by the Monin-Obukhov bulk formulation (uncertainties in modelled snow surface temperatures up to 2 K), which is analysed in detail in Chapter 2 and summarized as follows:

We found three main error sources which contribute to model uncertainties in turbulent sensible heat fluxes:

1. Violation of assumptions for the applicability of the Monin-Obukhov bulk formulation

2. Stability corrections

3. Aerodynamic roughness length of snow

Further smaller error sources, which were estimated to contribute to model uncertainties of turbulent sensible heat fluxes, are (1) the assumption that the aerodynamic roughness length of momentum is identical to the aerodynamic roughness length of scalars, and (2) uncertainties in the density of the air and the heat capacity of the air.

We found an average model uncertainty in turbulent sensible heat fluxes of 6 W m^{-2} by using Monin-Obukhov bulk formulation and additional 1-5 W m^{-2} from the parametrizations of the stability corrections. The choice of a stability correction strongly influences the date of the first snow-free day in the model and could vary around several days. The assumption of a neutral boundary layer (no stability correction) strongly overestimates turbulent sensible heat fluxes towards the snow surface ($MAE = 22$ W m^{-2}; $MBE = -18$ W m^{-2}) and lead to a too short snow season in the model, whereas the stability correction of Holtslag and deBruin (1988) produces small model errors for turbulent sensible heat fluxes ($MAE = 7$ W m^{-2}; $MBE = 2$ W m^{-2}). However, we also found that no single best stability correction function exists, as the stability corrections perform different for varying meteorological conditions. As an example, the newly developed multivariate stability correction performs best for high wind velocities, whereas the newly developed univariate stability correction performs best for moderate wind velocities. A combination of several different stability corrections for different meteorological conditions could be used to find the best possible model performance of turbulent sensible heat fluxes. However, this procedure would (disproportionally) increase the number of empirical coefficients in the model.

The application of Monin-Obukhov bulk formulations in physics-based models is based on a number of assumptions (e.g. constant flux layers, quasi infinite fetch in all directions) which are heavily violated in complex terrain. Hence, turbulent sensible heat fluxes and snow surface temperatures are much better represented in the model for idealized flat test sites in comparison with test sites in complex terrain. This is empirically confirmed by our analysis.

The uncertainty in the aerodynamic roughness length of snow is additional one large error source in the Monin-Obukhov bulk formulation. The snow water equivalent increases around 13 % by changing the initial aerodynamic roughness length of snow from 7 mm to 2 mm (Chapter 6). However, it is very unlikely that the aerodynamic roughness length does not change in the course of a snow season, which could partly explain model errors of the turbulent sensible heat fluxes by applying Monin-Obukhov bulk formulation.

Dozens of different stability corrections have been published in the last decades, which were mostly developed over snow-free surfaces (Andreas, 2002). Stability corrections could be easily used to tune a physics-based model and compensate other model errors (e.g. uncertainties in the incoming longwave radiation). A typical example of this error cancellation in the physics-based model SNOWPACK was observed when a combination of the assumption of a neutral boundary layer with the negatively biased measured incoming longwave radiation leads to the lowest mean absolute errors for the Weissfluhjoch test site. Additionally, the

aerodynamic roughness length of snow could be used as a tuning parameter in physics-based snow models as several studies suggest values for the aerodynamic roughness length, which span the range of at least one order of magnitude (Gromke et al., 2011).

7.1.3 Snow properties

The third largest model uncertainty in the surface energy balance of a continuous snow pack stems from physical properties of snow. The extinction coefficient, which is responsible for the shortwave radiation energy distribution within the snow pack, could lead to errors in the snow surface temperature of around 0.1 K, which is equivalent to a flux uncertainty of around 0.5 W m^{-2}. The snow emissivity is set to a constant value and could lead to errors of around 0.2 K. Uncertainties in the effective thermal conductivity of snow of around 15 % lead to similar model errors as for the constant snow emissivity.

The surface energy balance of a continuous snow pack for one individual location is additionally affected by measurement uncertainties of all four radiation components and the fact that sky-view factors are not included in a one-dimensional snow model due to missing information of the surrounding DEM.

7.2   Patchy snow cover

The surface energy balance of a snow pack significantly changes once the snow cover becomes patchy in the course of the ablation period (Chapter 4 and 5). Small-scale boundary layer processes over a heterogeneous land-surface are typically not considered in hydrological models, as the surface energy balance is calculated separately for each pixel based on the vertical exchange between the snow pack and the atmosphere. Hence, an error is introduced in the surface energy balance of hydrological models, due to the missing interaction between neighbouring pixels. The key parameters to estimate this model error were found to be the mean snow patch size and the wind velocity in the later stages of the ablation period. Additionally, the relative duration of patchy snow covers in the ablation period is an essential information to assess the model error for an entire ablation period.

For the investigated almost flat test site Gletschboden, we found a continuous snow cover for the majority (> 80 %) of the ablation time and a patchy snow cover for around 20 % of the time in the ablation period. However, estimated numbers are only valid in the investigation area and change for different test sites. The relative percentage of patchy snow covers in the ablation period is larger in regions with a large spatial heterogeneity of the snow depth at peak of winter accumulation, e.g. for the Wannengrat area in the Swiss Alps (Egli et al., 2012). We will assess the relative duration of patchy snow covers in the ablation period and the mean snow patch size for different slopes, aspects and scales in future work.

TLS measurements at the Gletschboden test site revealed 25-30 % above-average snow ablation rates at the leading edge of the snow patch and a contribution of totally around 5 % to snow ablation rates by local heat advection (Chapter 4). These numbers represent the pure effect at the "leading edge" of the snow patch, neglecting that snow ablation rates increase additionally further inside the snow patch due to an increase in the mean air temperature above the snow. In order to estimate the total increase in snow ablation as a patchy snow cover evolves by complex surface-atmosphere interactions, we coupled the atmospheric model ARPS with the hydrological model Alpine3D (Chapter 5). Numerical results suggest that turbulent sensible heat fluxes over patchy snow covers increase by 5-10 W m^{-2} (range for decreasing snow cover fractions from 55 % to 5 %) compared to continuous snow covers.

We developed a temperature footprint approach to calculate near-surface air temperature fields (Chapter 4). This purely analytical approach accounts for warm air advection during patchy snow covers, where pixels in a hydrological model interact with each other. The footprint approach was validated with snow mask maps, eddy-covariance measurements and snow ablation rates from TLS. The small-scale heterogeneity in snow ablation rates as observed from TLS measurements could be reproduced in a hydrological model, which significantly increased the model performance. Additionally, the increase in mean air temperatures (for increasing wind velocity and decreasing snow cover fraction) estimated with the temperature footprint approach is strongly correlated with air temperature fields modelled with the atmospheric model ARPS.

In the following, we compare the amount of different model errors to uncertainties in SWE predictions for the entire snow season. The largest uncertainty for modelling SWE for an entire snow season stems from the correct input precipitation. Winter precipitation is difficult to measure in high elevated regions and typically connected with high wind velocities. Therefore, a precipitation undercatch is applied, which increases the snow water equivalent around 30 % (Chapter 6.4.4.1). Additionally, the strong sensitivity of SWE to precipitation was analysed by modifying the station coverage (Chapter 6.4.2). By omitting one standard meteorological station with measured precipitation, the mean SWE could vary up to 20 %. The model error in SWE is less than 1 % for the Gletschboden test site by neglecting lateral transport processes for an entire snow season but could be much larger in regions with a large spatial heterogeneity of the snow depth at peak of winter accumulation.

By simulating an entire ablation period, we estimated the model error in SWE for a continuous snow cover for an individual location and found the largest error contributions to the surface energy balance due to uncertainties in the parametrizations of incoming longwave radiation and turbulent fluxes. Modifications in the horizontal resolution in hydrological models could additionally lead to uncertainties in SWE up to 15 %, especially in the ablation period where coarser horizontal resolution leads to less steep slopes and hence less incoming radiation (Chapter 6.4.2). The model error in SWE is around 3-5 % for the Gletschboden test site by neglecting

lateral transport processes for the ablation period. In regions with high wind velocities and/or regions with a large spatial hetero-geneity of the snow depth at peak of winter accumulation, favouring the development of many small long-living snow patches, lateral transport processes are more important. We found a model error of 14 % for the Wannengrat test site by neglecting lateral transport processes in the ablation period. The model error is split in a contribution from the pure leading edge effect, which can be resolved by TLS measurements and a contribution from a positive snow albedo feedback, which increases the mean air temper-atures and leads to additional snow melt further inside the snow patches. The consideration of lateral transport processes in flat idealized terrain is more important than in complex terrain, as uncertainties in the surface energy balance of a continuous snow pack decrease in flat and idealized terrain.

Chapter 8   Outlook

8.1   Eddy-covariance method tool

Measurements of turbulent (sensible) heat fluxes recorded with 3-D ultrasonic anemometers have become more frequent in the last decades and were particularly conducted for short time periods during field campaigns. However, several eddy-covariance measurements were conducted permanently throughout the winter. As we found an average MOST uncertainty of 6 W m^{-2} and an additional error of 1-5 W m^{-2} due to the parametrizations of the stability corrections for the turbulent sensible heat fluxes, the representation of measured turbulent sensible heat fluxes in a physics-based snow model is a desirable goal. Measured turbulent sensible heat fluxes could not be used in the current standard SNOWPACK version in the same way as the four radiation components, but are parametrized with Monin-Obukhov bulk formulation. By including measured sensible (and if available latent) heat fluxes in a similar way as standard meteorological input parameters (such as e.g. air temperature, wind velocity and the radiation components) the model performance would significantly increase especially during strong melting periods.

An eddy-covariance method module in MeteoIO (Bavay and Egger, 2014) would be required to estimate turbulent sensible heat fluxes from high-frequency raw data recorded from a 3-D ultrasonic anemometer. This module could work in a similar way as the Biomicrometeorology flux software (Thomas et al., 2009), which was externally used in Chapter 4 and Appendix A. The required input data for the eddy-covariance method module are on the one hand meteorological input parameters (air temperature, relative humidity and air pressure) to calculate the physical properties air density and heat conduction of the air and on the other hand high-frequent time series of air temperature and vertical velocity in order to compute the covariance $\overline{w'\theta'}$. Several analysis steps such as despiking, detrending, highpass filter and rotation of the coordinate system with e.g. a planar fit approach need to be conducted in order to guarantee high quality turbulence data.

8.2   Sky-view factor for point measurements

The model performance of the surface energy balance of a snow pack is strongly dependent on the chosen test site and shows weaknesses in complex terrain and a satisfactory performance for idealized flat test sites. Besides the violation of mandatory assumptions of the Monin-Obukhov bulk formulation, missing sky-view factors in the one-dimensional physics-based model SNOW-PACK could lead to uncertainties in the surface energy balance of a snow pack. The sky-view factor is typically 1 (100 % of the clear sky can be seen from fisheye observations) in flat areas or on top of a mountain. However, in complex terrain (especially in narrow valleys) the sky-view factor decreases and radiation components are biased by terrain reflections/emissions and the fact that the outgoing longwave radiation cannot be emitted in all hemispheric directions. Model errors in the surface energy balance of a snow pack increase for decreasing sky-view factors, as sky-view factors are not considered in one-dimensional physics-based snow models due to the missing information of the surrounding digital elevation model (Chapter 3). However, sky-view factors are implemented in the hydrological model Alpine3D to interpolate the measured radiation components from one individual measurement location to the model grid. The consideration of the digital elevation model in the close surroundings of the point measurement would allow estimating sky-view factors for a specific point (Helbig et al., 2009) and improving the surface energy balance in complex terrain. The estimation of sky-view factors with a digital elevation model does not work under canopy, in settlements or for buildings close to the measurement devices. Fisheye photographs need to be recorded in order to estimate the sky-view factor for those specific areas.

8.3   Terrain properties of a digital elevation model used to automatically re-distribute snow

The temperature footprint approach (Chapter 4) requires two-dimensional snow depths measurements at the peak of winter accumulation (typically recorded with TLS or ALS) as input for a hydrological model, as the redistributed snow at peak of winter accumulation drives the size and location of snow patches later in the ablation period (Schlögl et al., submitted, Chapter 4). By applying an automatic routine for snow redistribution during heavy snowfall events (snow is redistributed from ridges towards local depressions) as a function of the prevailing wind direction, different terrain parameters and the assumption of uniformly distributed precipitation patterns on a small-scale (Winstral and Marks, 2002), time consuming two-dimensional measurements of snow depths are not required anymore and could be used for validation instead.

Similar work was conducted by Vögeli et al. (2016), who redistributed the precipitation input in the hydrological model based on snow height measurements from ALS flights. However, representative snow depth distributions are difficult to measure for larger catchments with large elevation gradients.

The location of snow patches late in the ablation period could be assessed for large areas on condition that the digital elevation model of the summer has a very fine horizontal resolution and accurate wind velocity and wind direction are available throughout the snow season. Neglecting the synoptic conditions would imply an identical snow patch development for all ablation periods, which might be correct for specific locations and winter seasons with similar meteorological conditions. However, we found a different snow patch development at the Gletschboden area in the ablation period 2014 and 2015 (described in detail in the Appendix of Chapter 4), which suggests that different wind directions should be considered when developing a tool for the redistribution of snow during heavy snowfall events.

8.4 Validation of ARPS near surface air temperature and wind velocity fields

The model performance of a hydrological model, driven by air temperature and wind velocity fields from an atmospheric model, is typically assessed by validating snow ablation rates with e.g. TLS measurements. Errors in the model performance could be caused by errors in the input data or errors in the model itself. In order to separate both errors, a second validation would be required to test the accuracy of the meteorological input data, which were generated with an atmospheric model. This validation requires many meteorological measurements on a very small-scale and would be expensive and very time consuming. However, the validation of meteorological fields would allow a good overview about the strength and weakness of the atmospheric model on a very small scale.

The two-dimensional snow surface temperature measurements recorded with the infrared camera at the Gletschboden test site (Appendix A) could be additionally used as a validation dataset for testing the accuracy of the atmospheric model. This measurement dataset has to be georeferenced first and could be additionally correlated with measured snow ablation rates recorded from TLS.

8.5 Uncertainties in large-scale atmospheric models during patchy snow covers

We assessed the air temperature increase for patchy snow covers in an atmospheric model on a very small-scale of 2 m horizontal resolution (Chapter 5). This setup allows resolving lateral transport processes, which can cause up to 30 % larger snow ablation rates for patchy snow covers. However, one might be interested in the model error of numerical weather prediction models during patchy snow covers. A typical horizontal resolution of numerical weather models is in the order of hundreds of meters to kilometres. This horizontal resolution does not resolve "leading-edge effects", which could be only observed for small scales below 10 m. However, we expect a model error in the mean air temperature in numerical weather prediction models due to a positive snow-albedo feedback mechanism. A large horizontal resolution in numerical weather prediction models prevents accurate information of the snow cover fraction on a small-scale. The amount of the air temperature increase for different horizontal resolutions could be assessed in a sensitivity study by using the setup in Chapter 5. Finally, the model error of the mean air temperature could be assessed in a numerical weather prediction model on condition that the error in the snow cover fraction of a large-scale numerical weather prediction model is known.

8.6 Using thermocouples to validate the temperature footprint approach

The measurement of vertical air temperature profiles with thermocouples over snow and the bare ground allows assessing the amount of advective heat, which is transported from the bare ground towards the snow patch (Harder et al., 2017). Air temperature measurements with thermocouples could additionally be used to validate the temperature footprint approach (Chapter 4) and confirm or reject numerical results from ARPS model simulations (Chapter 5). As numerical results from ARPS simulations (Chapter 5) match well with the temperature footprint approach (Chapter 4), the consideration of thermocouples measurements (as a third independent approach to test the small-scale variability of near-surface air temperatures over patchy snow covers) is required to increase the impact and plausibility of the estimated results in Chapter 4 and 5. Measurements with thermocouples could additionally be used (together with the results in Chapter 4 and 5) to develop a simple parametrization in hydrological models in dependence of the snow cover fraction and wind velocity. A simple parametrization based on the snow cover fraction and wind velocity would be easier to implement in hydrological models than the temperature footprint approach, which would require much computational power.

References

[1] Abellán, A., Jaboyedoff, M., Oppikofer, T., and Vilaplana, J. M. (2009) Detection of millimetric deformation using a terrestrial laser scanner: experiment and application to a rockfall event, Nat. Hazards Earth Syst. Sci., 9, 365-372.

[2] Abegg, B., Agrawala, S., Crick, F., and de Montfalcon, A. (2007) Climate change impacts and adaptation in winter tourism. S. Agrawala (Ed.), Climate Change in the European Alps: Adapting Winter Tourism and Natural Hazards Management, OECD Publishing, Paris

[3] Andreas, E. L. (1987) A theory for the scalar roughness and the scalar transfer coefficients over snow and sea ice. Boundary Layer Meteorol. 38: 159-184.

[4] Andreas, E. L. (2002) Parameterizing scalar transfer over snow and ice: a review. J. Hydrometeorol. 3: 417-432.

[5] Andreas, E.L, Persson, P.O.G., Jordan, R.E., Horst, T.W., Guest, P.S., Grachev, A.A., and Fairall, C.W. (2010) Parameterizing turbulent exchange over sea ice in winter. J. Hydrometeorol. 11(1): 87-104. DOI: 10.1175/2009JHM1102.

[6] Arck, M., and Scherer, D. (2002) Problems in the determination of sensible heat flux over snow. Geogr. Ann. 84 A (3–4): 157–169.

[7] Bartelt, P. and Lehning, M. (2002) A physical SNOWPACK model for the Swiss avalanche warning: Part 1: numerical model, Cold Regions Science and Technology, 35(3), 123-145.

[8] Bartlett, S. J., and Lehning, M. (2011) A theoretical assessment of heat transfer by ventilation in homogeneous snowpacks, Water Resources Research, 47, W04503.

[9] Bavay, M., Lehning, M., Jonas, T. and Löwe, H. (2009) Simulations of future snow cover and discharge in Alpine headwater catchments, Hydrol. Process., 23, 95-108.

[10] Bavay, M., Grünewald, T., and Lehning, M. (2012) Response of snow cover and runoff to climate change in high Alpine catchments of Eastern Switzerland. Adv. Water Resour. http://dx.doi.org/10.1016/j.advwatres.2012.12.009

[11] Bavay, M., and Egger, T. (2014) MeteoIO 2.4.2: a preprocessing library for meteorological data. Geosci. Model Dev. Discuss., 7, pp. 3595-3645, 10.5194/gmdd-7-3594-2014.

[12] Bennett, N.D., Croke, F.W., Guariso, G., Guillaume, J.H.A., Hamilton, S.H., Jakeman, A. J., Marsili-Libelli, S., Newham, L.T.H., Norton, J.P., Perrin, C., Pierce, S.A., Robson, B., Seppelt, R., Voinov, A.A., Fath, B.D., and Andreassian, V. (2013) Characterising performance of environmental models. Environ. Model. Softw., 40, pp. 1-20.

[13] Berezowski, T., Nossent, J., Chormanski, J., and Batelaan, O. (2015) Spatial sensitivity analysis of snow cover data in a distributed rainfall-runoff model. Hydrol. Earth Syst. Sci., 19 (2015), pp. 1887-1904

[14] Bintanja, R., and van der Linden, E. C. (2013) The changing seasonal climate in the Arctic, Nature Scientific Reports, 3, 1556.

[15] Blanc, T. (1987) Accuracy of bulk-method-determined flux, stability, and sea surface roughness. Journal of Geophysical Research Atmospheres. 92: 3867-3876.

[16] Bohren, C. F., and Barkstrom, B. R. (1974) Theory of the Optical Properties of Snow, Journal of Geophysical Reasearch, 79 (30), 4527-4535.

[17] Bossard, M., Feranec, J., and Otahel, J. (2000) CORINE Land Cover Technical Guide – Addendum 2000. European Environment Agency.

[18] Bou-Zeid, E., Higgins, C., Huwald, H., Meneveau, C., and Parlange, M. B. (2010) Field study of the dynamics and modelling of subgridscale turbulence in a stable atmospheric surface layer over a glacier. J. Fluid Mech. 665: 480–515.

[19] Brun, E., Martin, E., Simon, V., Gendre, C., and Coléou, C. (1989), An energy and mass model of snow cover suitable for operational avalanche forecasting, J. Glaciol.,35(121), 333–342.

[20] Brutsaert, W. (1975) Derivable formula for long-wave radiation from clear skies. Water Resour. Res., 11 (5), pp. 742-744

[21] Bühler, Y., Marty, M., and Ginzler, C. (2012) High Resolution DEM Generation in High-Alpine Terrain Using Airborne Remote Sensing Techniques, Transactions in GIS, 16(5), 635-647.

[22] Bühler, Y., Adams, M. S., Bösch, R., and Stoffel, A. (2016) Mapping snow depth in alpine terrain with unmanned aerial systems (UASs): potential and limitations, The Cryosphere, 10, 1075–1088.

[23] Burba, G. (2013) Eddy Covariance Method for Scientific, Industrial, Agricultural, and Regulatory Applications, LI-COR Biosciences, Lincoln, Nebraska.

[24] Burke, H. K., Bowley, C. J., and Barnes, J. C. (1981) Comparison of theoretical and actual satellite microwave brightness temperatures to determine snowpack properties, Final Rep. A653-F, Environ. Res. and Technol., Concord, Mass.

[25] Calanca, P. (2001) A note on the roughness length for temperature over melting snow and ice. Q. J. R. Meteorol. Soc. 127: 255-260.

[26] Calonne, N., Flin, F., Morin, S., Lesaffre, B., Rolland du Roscoat, S., and Geindreau, C. (2011) Numerical and experimental investigations of the effective thermal conductivity of snow, Geophysical Research Letters, 38 (23), L23501.

[27] Chapin III, F. S., Sturm, M., Serreze, M. C., McFadden, J. P., Key, J. R., Llody, A. H., McGuire, A. D., Rupp, T. S., Lynch, A. H., Schimel, J. P., Beringer, J., Chapman, W. L., Epstein, H. E., Euskirchen, E. S., Hinzmann, L. D., Jia, G., Ping., C.-L., Tape, K. D., Thompson, C. D. C., Walker, D. A., and Welker, J. M. (2005) Role of Land-Surface Changes in Arctic Summer Warming, Science, 310, 657-660.

[28] Chou, M. D., and Suarez, M. J. (1994) An efficient thermal infrared radiation parameterization for use in general circulation models. NASA Tech. Memo. 104606, Vol. 3, 85 pp.

[29] Clark, M. P., and Serreze, M. C. (2000) Effects of Variations in East Asian Snow Cover on Modulating Atmospheric Circulation over the North Pacific Ocean, Journal of Climate, 13, 3700-3710.

[30] Colbeck, S. C. (1989a) Snow-crystal growth with varying surface temperatures and radiation penetration, J. Glaciol., 35, 23-29.

[31] Colomina, I., and Molina, P. (2014) Unmanned aerial systems for photogrammetry and remote sensing: A review, Journal of Photogrammetry and Remote Sensing, 92, 79-97.

[32] Comola, F., Schaefli, B., Rinaldo, A., and Lehning, M. (2015) Scale-dependent effects of solar radiation patterns on the snow-dominated hydrologic response, Geophys. Res. Lett., 42/10, DOI:10.1002/2015GL064075.

[33] Crawford, T. M., and Duchon, C. E. (1999) An Improved Parametrization for Estimating Effective Atmospheric Emissivity for Use in Calculating Daytime Downwelling Longwave Radiation, Journal of Applied Meteorology, 38, 474-480.

[34] Cullen, N. J., and Steffen, K. (2001) Unstable near-surface boundary layer conditions in summer on top of the Greenland ice sheet. Geophys. Res. Lett. 28: 4491-4493.

[35] Cullen, N. J., Steffen, K., and Blanken, P. D. (2007) Nonstationarity of turbulent heat fluxes at Summit, Greenland. Boundary Layer Meteorol. 122: 439-455.

[36] Cullen, N. J., Mölg, T., Conway, J., and Steffen, K. (2014) Assessing the role of sublimation in the dry snow zone of the Greenland ice sheet in a warming world. J. Geophys. Res. Atmos. 119: 6563-6577.

[37] Dadic, R., Mott, R., Lehning, M., Carenzo, M., Anderson, B., and Mackintosh, A. (2013) Sensitivity of turbulent fluxes to wind speed over snow surfaces in different climatic settings. Advances in Water Resources. 55: 178-189.

[38] Deardorff, J. W. (1972) Numerical investigation of neutral and unstable planetary boundary layers. J. Atmos. Sci., 29, 91–115.

[39] Deems, J. S., Gadomski, P. J., Vellone, D., Evanczyk, R., LeWinter, A. L., Birkeland, K. W., and Finnegan, D. C. (2015) Mapping starting zone snow depth with a ground-based lidar to assist avalanche control and forecasting, Cold Regions Science and Technology, 120, 197-204.

[40] Déry, S. J. and Brown, R. D. (2007) Recent Northern Hemisphere snow cover extent trends and implations for the snow-albedo feedback, Geophysical Research Letters, 34(22), L22504.

[41] Dilley, A.C., and O'Brien, D. M. (1998) Estimating downward clear sky long-wave irradiance at the surface from screen temperature and precipitable water. Q. J. R. Meteorol. Soc., 124 (549), pp. 1391-1401

[42] Dutra, E., Kotlarski, S., Viterbo, P., Balsamo, G., Miranda, P., Schär, C., Bissolli, P., and Jonas, T. (2011) Snow cover sensitivity to horizontal resolution, parametrizations, and atmospheric forcing in a land surface model. J. Geophys. Res., 116, p. D21109

[43] Dyer, A. J. (1974) A review of flux-profile relationships. Boundary Layer Meteorol. 7: 363-372.

[44] Egger, J. (1983) Pressure Distributions in the Dischma Valley During Field Experiment DISKUS, Beitr. Phys. Atmos., 56, 163-176.

[45] Egli, L., Jonas, T., Grünewald, T., Schirmer, M., and Burlando, P. (2012) Dynamics of snow ablation in a small Alpine catchment observed by repeated terrestrial laser scans, Hydrol. Process., 26, 1574-1585.

[46] Essery, R., Granger, R., and Pomeroy, J. (2006) Boundary-layer growth and advection of heat over snow and soil patches: modelling and parameterization. Hydrol. Process. 20: 953-967.

[47] Essery, R., Morin, S., Lejeune, Y., and Menard, C. B. (2013) A comparison of 1701 snow models using observations from an alpine site. Advances in Water Resources. 55: 131-148.

[48] Etchevers, P., Martin, E., Brown, R., Fierz, C., Lejeune, Y., Bazile, E., Boone, A., Dai, Y.J., Essery, R., Fernandez, A., Gusev, Y., Jordan, R., Koren, V., Kowalczyk, E., Nasonova, N. O., Pyles, R. D., Schlosser, A., Shmakin, A. B., Smirnova, T. G., Strasser, U., Verseghy, D., Yamazaki, T., and Yang, Z. L. (2004) Validation of the energy budget of an alpine snowpack simulated by several snow models (SnowMIP project), Annals of Glaciology, 38, 150-158.

[49] Feng, S., and Hu, Q. (2007) Changes in winter snowfall/precipitation ratio in the contiguous United States, Journal of Geophysical Research, 112, D15109.

[50] Fierz, C., and Lehning, M. (2001) Assessment of the microstructure-based snow-cover model SNOWPACK: thermal and mechanical properties, Cold Regions Science and Technology, 33 (1-2), 123-131.

[51] Fierz, C., Riber, P., Adams, E. E., Curran, A. R., Föhn, P. M. B., Lehning, M., and Plüss, C. (2003) Evaluation of snow-surface energy balance models in alpine terrain, Journal of Hydrology, 282, 76-944.

[52] Fischer, A. M., Weigel, A. P., Buser, C. M., Knutti, R., Künsch, H. R., Liniger, M. A., Schärb, C., and Appenzeller, C. (2012) Climate change projections for Switzerland based on a Bayesian multi-model approach. Int. J. Climatol., 32, pp. 2348-2371.

[53] Flerchinger, G. N., Xaio, W., Marks, D., Sauer, T. J., and Yu, Q. (2009) Comparison of algorithms for incoming atmospheric longwave radiation, Water Resources Research, 45(3), W03423.

[54] Föhn, P. (1973) Short term snow melt and ablation derived from heat- and mass-balance measurements. J. of Glaciology. 12(65): 275-289.

[55] Fujita, K., Hiyama, K., Iida, H., and Ageta, Y. (2010), Self-regulated fluctuations in the ablation of a snow patch over four decades, Water Resour. Res., 46, W11541.

[56] Funk, M. (1985) Räumliche Verteilung der Massenbilanz auf dem Rhonegletscher und ihre Beziehung zu Klimaelementen. Zürcher Geographische Schriften. 24: 183 pp.

[57] Gallice, A., Bavay, M., Brauchli, T., Comola, F., Lehning, M., and Huwald, H. (2016) StreamFlow 1.0: an extension to the spatially distributed snow model Alpine3D for hydrological modelling and deterministic stream temperature prediction, Geosci. Model Dev., 9, 4491-4519.

[58] Garratt, J. R (1990) The internal boundary layer – A review, Boundary-Layer Meteorology, 50, 171-203.

[59] Gelfan, A. N., Pomeroy, J. W., and Kuchment, L. S. (2004) Modeling forest cover influences on snow accumulation, sublimation, and melt. J. Hydrom., 5, pp. 785-803

[60] Gerber, F., Lehning, M., Hoch, S. W., and Mott, R. (2017) A Close-Ridge Small-Scale Atmospheric Flow Field and its Influence on Snow Accumulation,

[61] Giorgi, F., Bi, X., and Pal, J. (2004) Mean, interannual variability and trends in a regional climate change experiment over Europe. II: climate change scenarios (2071–2100). Clim. Dyn., 23, pp. 839-858

[62] Goodison, B. E., Louie, P. Y. T., and Yang, D. (1998) WMO Solid Precipitation Measurement Intercomparison, WMO/TD – No. 872. Instruments and observing methods Report No. 67

[63] Grachev, A.A., Fairall, C.W., Persson, P.O.G., Andreas, E.L, and Guest, P.S. (2005) Stable boundary-layer scaling regimes: the SHEBA data. Boundary Layer Meteorol. 116(2): 201-235. DOI 10.1007/s10546-004-2729-0

[64] Grachev, A.A., Andreas, E.L, Fairall, C.W., Guest, P.S., and Persson, P.O.G. (2007) SHEBA flux-profile relationships in the stable atmospheric boundary layer. Boundary-Layer Meteorol. 124(3): 315-333. DOI 10.1007/s10546-007-9177-6

[65] Grachev, A.A., Andreas, E.L, Fairall, C.W., Guest, P.S., and Persson, P.O.G. (2013) The critical Richardson number and limits of applicability of local similarity theory in the stable boundary layer. Boundary-Layer Meteorol. 147(1): 51-82. DOI: 10.1007/s10546-012-9771-0

[66] Granger, R. J., Pomeroy, J. W., and Parviainen, J. (2002) Boundary-layer integration approach to advection of sensible heat to a patchy snow cover, Hydrol. Process., 16, 3559-3569.

[67] Granger, R. J., Essery, R., and Pomeroy, J. W. (2006) Boundary-layer growth over snow and soil patches: field observations, Hydrol. Process. 20, 943-951.

[68] Griggs, M. (1968) Emissivities of natural surfaces in the 8- to 14-micron spectral region, J. Geophys. Res., 73, 7545-7551.

[69] Gromke, C., Manes, C., Walter, B., Lehning, M., and Guala, M. (2011) Aerodynamic Roughness Length of Fresh Snow, Boundary-Layer Meteorology, 141(1), 21-34.

[70] Groot Zwaaftink, C.D., Löwe, H., Mott, R., Bavay, M., Lehning M. (2011) Drifting snow sublimation: A high-resolution 3-D model with temperature and moisture feedbacks, JGR Atmospheres, 116, D16107, doi: 10.1029/2011JD015754.

[71] Groot Zwaaftink, C. D., Mott, R. and Lehning, M. (2013) Seasonal simulation of drifting snow sublimation in Alpine terrain, Water Resour. Res., 49, 1581-1590, doi:10.1002/wrcr.20137.

[72] Grünewald, T., Schirmer, M., and Lehning, M. (2009) Can the total snow amount in an Alpine catchment be estimated from flat field snow measurements? Geophys. Res. Abstr., 11, pp. EGU2009-12885

[73] Grünewald, T., Schirmer, M., Mott, R., and Lehning, M. (2010) Spatial and temporal variability of snow depth and ablation rates in a small mountain catchment, The Cryosphere, 4, 215–225.

[74] Grünewald, T., and Lehning, M. (2015) Are flat-field snow depth measurements representative? A comparison of selected index sites with areal snow depth measurements at the small catchment scale, Hydrological Processes, 29(7), 1717-1728.

[75] Guo X., Yang K., Zhao L., Yang W., Li S., Zhu M., Yao T., Chen Y. (2011) Critical Evaluation of Scalar Roughness Length Parametrizations Over a Melting Valley Glacier. Boundary Layer Meteorol. 139: 307-332.

[76] Hadley, O. L., and Kirchstetter, T. W. (2012) Black-carbon reduction of snow albedo, Nat. Clim. Change, 2, pp. 437-440

[77] Haeberli, W., and Beniston, M. (1998) Climate Change and its Impacts on Glaciers and Permafrost in the Alps, Ambio, 27(4), 258-265.

[78] Hamon, W. R. (1973) Computing actual precipitation in mountainous areas. Proc. WMO-IAHS Symp on the Distribution of Precipitation in Mountainous Areas, WMO, No. 326, pp. 159-173

[79] Harder, P., Pomeroy, J. W., and Helgason, W. (2017) Local scale advection of sensible and latent heat during snowmelt. Geophys. Res. Let. doi: 10.1002/2017GL074394.

[80] Haupt, H. F. (1969) A simple snowmelt lysimeter, Water Resources Research, 5(3), 714-718.

[81] Helbig, N., van Herwijnen, A., Magnusson, J., and Jonas, T. (2015) Fractional snow-covered area parameterization over complex topography, Hydrol. Earth Syst. Sci., 19, 1339-1351.

[82] Helgason, W., and Pomeroy, J. (2012) Problems closing the energy balance over a homogeneous snow cover during midwinter, Journal of Hydrometeorology, 13(2), 557-572.

[83] Hennemuth, B. (1986) Thermal asymmetry and cross-valley circulation in a small Alpine valley, Boundary-Layer Meteorology, 36, 371-394.

[84] Hoch, S. W., Calanca, P., Philipona, R., and Ohmura, A. (2007) Year-Round Observation of Longwave Radiative Flux Divergence in Greenland, Journal of Applied Meteorology and Climatology, 46, 1469-1479.

[85] Hoch, S. W. (2006) Radiative flux divergence in the surface boundary layer. A study based on observations at Summit, Greenland, ETH Dissertation 16194.

[86] Hock, R. (2003) Temperature index melt modelling in mountain areas. J. Hydrol., 282 (1–4) (2003), pp. 104-115

[87] Högström, U. (1988) Non-dimensional wind and temperature profiles in the atmospheric surface layer: A re-evaluation. Boundary Layer Meteorol. 42: 55-78.

[88] Holtslag, A. A. M. and De Bruin, H. A. R. (1988) Applied modeling of the nighttime surface energy balance over land. Journal of Applied Meteorology. 27(6): 689-704.

[89] Hori, M., Aoki, T., Tanikawa, T., Motoyoshi, H., Hachikubo, A., Sugiura, K., Yasunari, T. J., Eide, H., Storvold, R., Nakajima, Y., and Takahashi, F. (2006) In-situ measured spectral directional emissivity of snow and ice in the 8-14 μm atmospheric window, Remote Sensing of Environment, 100(4), 486-502.

[90] Houghton, J. T. (Ed.) (2001) Climate Change 2001: the Scientific Basis, Cambridge University Press, Cambridge

[91] Hunt, G. E., Kandel, R., and Mecherikunnel, A. T. (1986) A history of presatellite investigations of the earth's radiation balance, Rev. Geophys., 24, 351-356.

[92] Huwald, H., Higgins, C. W., Boldi, M. O., Bou-Zeid, E., Lehning, M., and Parlange, M. B. (2009) Albedo effect on radiative errors in air temperature measurements. Water Resour. Res., 45:W08431, doi:10.1029/2008WR007600.

[93] Jin, J., Gao, X., Yang, Z. L., Bales, R. C., Sorooshian, S., Dickinson, R. E., Sun, S. F., and Wu, G. X. (1999) Comparative analyses of physically based snowmelt models for climate simulations. J. Clim., 12, pp. 2643-2657

[94] Joffre, S. M. (1982) Momentum and heat transfers in the surface layer over a frozen sea, Boundary Layer Meterology, 24, 211-229.

[95] Johnson, R. H., Young, G. S., and Toth, J. J. (1984) Mesoscale weather effects of variable snow cover over northeast Colorado. Mon. Wea. Rev., 112, 1141–1152.

[96] Jonas, T., Marty, C., and Magnusson, J. (2009) Estimating the snow water equivalent from snow depth measurements in the Swiss Alps. J. Hydrol., 378, pp. 161-167, 10.1016/j.jhydrol.2009.09.021

[97] Kapnick, S. B., and Delworth, T. L. (2013) Controls of global snow under a changed climate, J. Climate, 26(15), 5537–5562.

[98] Keller, F., Goyette, S., and Beniston, M. (2005) Sensitivity analysis of snow cover to climate change scenarios and their impact on plant habitats in alpine terrain. Clim. Change, 72, pp. 299-319

[99] Kershaw, G. P., and McCulloch, J. (2007) Midwinter snowpack variation across the Arctic Treeline, Churchill, Manitoba, Canada, Arctic Antarct. Alp. Res., 39 (No. 1), pp. 9-15

[100] Kiehl, J. T., and Trenberth, K. E. (1997) Earth's Annual Global Mean Energy Balance, Bulletin of the American Meteorological Society, 78(2), 197-208.

[101] Kljun, N., Rotach, M. W., and Schmid, H. P. (2002) A three-dimensional backward lagrangian footprint model for a wide range of boundary-layer stratifications, Boundary-Layer Meteorology, 103, 205-226.

[102] Konzelmann, T., van de Wal, R. S. W., Greuell, W., Bintanja, R., Henneken, E. A.C., Abe-Ouchi, A. (1994) Parametrization of global and longwave incoming radiation for the Greenland Ice Sheet, Global and Planetary Change, 9(1), 143-164.

[103] Kuipers Munneke, P., van den Broeke, M. R., Reijmer, C. H., Helsen, M. M., Boot, W., Schneebeli, M., and Steffen, K. (2009) The role of radiation penetration in the energy budget of the snowpack at Summit, Greenland, The Cryosphere, 3, 155-165.

[104] Kumar, M., Marks, D., Dozier, J., Reba, M., and Winstral, A. (2013), Evaluation of distributed hydrologic impacts of temperature-index and energy-based snow models, Adv. Water Resour., 56(0), 77–89.

[105] Kuonen, P., Bavay, M., and Lehning, M. (2010) POP-C++ and Alpine3D: petition for a new HPC approach. E. Asimakopoulou, N. Bessis (Eds.), Advanced ICTs for Disaster Management and Threat Detection: Collaborative and Distributed Frameworks, Information Science Reference, Hershey, PA, pp. 237-261, 10.4018/978-1-61520-987-3.ch015

[106] Lareau, N. P., Crosman, E., Whiteman, C. D., Horel, J. H., Hoch, S. W., Brown, W. O. J., and Horst, T. W. (2013) The Persistent Cold-Air Pool Study, Bulletin of the American Meteorological Society, 94, 51-63.

[107] Large, W. G., and Pond, S. (1982) Sensible and Latent Heat Flux Measurements over the Ocean. J. Phys. Oceanogr. 11: 324-336.

[108] Lehning, M., Bartelt, P., Brown, B., Russi, T., Stöckli, U., and Zimmerli, M. (1999) SNOWPACK model calculations for avalanche warning based upon a new network of weather and snow stations, Cold Regions Science and Technology, 30 (1-3), 145-157.

[109] Lehning, M., Bartelt, P., Brown, B., Fierz, C., and Satyawali, P. (2002) A physical SNOWPACK model for the Swiss avalanche warning: Part II: Snow microstructure, Cold Regions Science and Technology, Volume 35, Issue 3, 147–167.

[110] Lehning, M., Bartelt, P., Brown, B., and Fierz, C. (2002) A physical SNOWPACK model for the Swiss avalanche warning: Part III: meteorological forcing, thin layer formation and evaluation. Cold Regions Science and Technology. 35(3): 169–184.

[111] Lehning, M., Völksch, I., Gustafsson, D., Nguyen, T. A., Stähli, M., and Zappa, M. (2006) ALPINE3D: a detailed model of mountain surface processes and its application to snow hydrology, Hydrol. Process., 20, 2111-2128.

[112] Lehning, M., Löwe, H., Ryser, M., and Raderschall, N. (2008) Inhomogeneous precipitation distribution and snow transport in steep terrain, Water Resour. Res., 44, W07404.

[113] Letcher, T. W., and Minder, J. R. (2015) Characterization of the simulated regional snow albedo feedback using a regional climate model over complex terrain. J. Climate, 28, 7576–7595.

[114] Liston, G. E. (1995) Local Advection of Momentum, Heat, and Moisture during the Melt of Patchy Snow Covers, Journal of Applied Meteorology, 34, 1705-1715.

[115] Liston, G. E. (1999) Interrelationships among Snow Distribution, Snowmelt, and Snow Cover Depletion: Implications for Atmospheric, Hydrologic, and Ecologic Modeling, Journal of Applied Meteorology, 38, 1474-1487.

[116] Löwe, H., Riche, F., and Schneebeli, M. (2013) A general treatment of snow microstructure exemplified by an improved relation for thermal conductivity, The Cryosphere, 7, 1473-1480.

[117] Luce, C. H., Tarboton, D. G., and Cooley K. R., (1998) The influence of the spatial distribution of snow on basin-averaged snowmelt, Hydrol. Proc., 12, 1671-1683.

[118] MacWhorter, M. A., and Weller, R. A. (1991) Error in Measurements of Incoming Shortwave Radiation Made from Ships and Buoys, Journal of Atmospheric and Oceanic Technology, 8, 108-117.

[119] Mahrt, L., and Vickers, D. (2005) Boundary-Layer Adjustment over Small-Scale Changes of Surface Heat Flux, Boundary-Layer Meteorology, 116, 313-330.

[120] Marks, D., and Dozier, J. (1992) Climate and Energy Exchange at the Snow Surface in the Alpine Region of the Sierra Nevada. 2. Snow Cover Energy Balance. Water Resources Research. 28(11): 3043-3054.

[121] Marks, D., Domingo, J., Susong, D., Link, T., and Garen, D. (1999) A spatially distributed energy balance snowmelt model for application in mountain basins, Hydrol. Proc., 13 (12-13), 1935–1959.

[122] Marks, D., and Winstral, A. (2001) Comparison of Snow Deposition, the Snow Cover Energy Balance, and Snowmelt at Two Sites in a Semiarid Mountain Basin, Journal of Hydrometeorology, 2(3), 213-227.

[123] Marsh, P. and Pomeroy, J. W. (1996) Meltwater fluxes at an arctic forest-tundra site, Hydrological Processes, 10(10), 1383-1400.

[124] Marsh, P., Neumann, N., Essery, R. and Pomeroy, J. W. (1999) Model estimates of local advection of sensible heat over a patchy snow cover, Interactions Between the Cryosphere, Climate and Greenhouse Gases (Proceedings of IUGG 99 Symposium HS2, Birmingham, Juli 1999) IAHS Publ. no. 256.

[125] Martin, E., and Lejeune, Y. (1998) Turbulent fluxes above the snow surface. Annals of Glaciology. 26: 179-183.

[126] Martinec, J., and Rango, A. (1981) Areal distribution of snow water equivalent evaluatied by snow cover monitoring, Water Resources Research, 17(5), 1480-1488.

[127] Massmann, W. J., and Lee, X. (2002) Eddy covariance flux corrections and uncertainties in long-term studies of carbon and energy exchanges. Agricultural and Forest Meteorology. 113: 121-144.

[128] Ménard, C. B., Essery, R., and Pomeroy, J. (2014) Modelled sensitivity of the snow regime to topography, shrub fraction and shrub height, Hydrol. Earth Syst. Sci., 18, 2375-2392.

[129] Ménégoz, M., Krinner, G., Balkanski, Y., Boucher, O., Cozic, A., Lim, S., Ginot, P., Laj, P., Gallée, H., Wagnon, P., Marinoni, A., and Jacobi, H. W. (2014) Snow cover sensitivity to black carbon deposition in the Himalayas: from atmospheric and ice core measurements to regional climate simulations. Atmos. Chem. Phys., 14, pp. 4237-4249

[130] Michlmayr, G., Lehning, M., Koboltschnig, G., Holzmann, H., Zappa, M., Mott, R., and Schöner, W. (2008) Application of the Alpine 3D model for glacier mass balance and glacier runoff studies at Goldbergkees, Austria. Hydrological processes. 22(19): 3941-3949.

[131] Monin, A.S. and Obukhov, A.M. (1954) Basic laws of turbulent mixing in the surface layer of the atmosphere, Tr. Akad. Nauk SSSR Geophiz. Inst., 24(151), 163-187.

[132] Moore, C. J. (1986) Frequence response corrections for eddy correlation systems, Boundary-Layer Meteorology, 37(1-2), 17-35.

[133] Moore, I. D., Grayson, R. B., and Ladson, A. R. (1991) Digital terrain modelling: A review of hydrological, geomorphological, and biological applications, Hydrological Processes, 5(1), 3-30.

[134] Morinaga, Y., Tian, S. F., and Shinoda, M. (2003) Winter snow anomaly and atmospheric circulation in Mongolia, Journal of Climatology, 23(13), 1627-1636.

[135] Mott, R., Egli, L., Grünewald, T., Dawes, N., Manes, C., Bavay, M., and Lehning, M. (2011) Micrometeorological processes driving snow ablation in an Alpine catchment. The Cryosphere. 5: 1083-1098.

[136] Mott, R., Gromke, C., Grünewald, T., and Lehning, M. (2013) Relative importance of advective heat transport and boundary layer decoupling in the melt dynamics of a patchy snow cover. Advances in Water Resources. 55: 88-97.

[137] Mott, R., Scipion, D., Schneebeli, M., Dawes, N., Berne, A., and Lehning, M. (2014) Orographic effects on snow deposition patterns in mountainous terrain, J. Geophs. Res. Atmos., 119, 1419-1439.

[138] Mott, R., Daniels, M., and Lehning, M. (2015) Atmospheric flow development and associated changes in turbulent sensible heat flux over a patchy mountain snow cover. J. Hydrometeor. 16: 1315-1340.

[139] Mott, R., Paterna, E., Horender, S., Crivelli, P., and Lehning, M. (2016) Wind tunnel experiments: cold-air pooling and atmospheric decoupling above a melting snow patch, The Cryosphere, 10, 445-458.

[140] Mott, R., Schlögl, S., Dirks, L., and Lehning, M. (2017) Impact of extreme land-surface heterogeneity on micrometeorology over spring snow-cover, J. Hydrometeor., 18(10), 2705-2722.

[141] Munro, D. S. (1980) Exponential-linear stability correction functions for weak to moderate instability near the ground. Boundary Layer Meteorol. 19: 125-131.

[142] Nishimura, K., and Nemoto, M. (2005) Blowing snow at Mizuho station, Antarctica. Phil. Trans. R. Soc. A. 363: 1647-1662.

[143] Obukhov, A.M. (1946) Turbulence in an atmosphere with a non-uniform temperature. Trudy Inst. Teoret. Geophys. Akad. Nauk SSSR. 1: 95-115 (translation in: Boundary-Layer Meteorol. 1971. 2: 7-29).

[144] Ohmura, A., Konzelmann, T., Rotach, M., Forrer, J., Wild, M., Abe-Ouchi, A., and Toritani, H. (1994) Energy balance for the Greenland ice sheet by observation and model computation, Snow and Ice Covers: Interaction with the Atmosphere and Ecosystems, IAHS Publ. no. 223.

[145] Oke, T. (1981) Canyon geometry and the nocturnal urban heat island: comparison of scale model and field observations, J. Climatol.1, 237–254.

[146] Oke, T. (1987) Boundary layer climates (Second edition), London, Methuen; New York, Routledge Press.

[147] Omstedt, A. (1990) A coupled one-dimensional sea ice-ocean model applied to a semi-enclosed basin, Tellus, 42A, 568-582.

[148] Plüss, C., and Mazzoni, R. (1994) The Role of Turbulent Heat Fluxes in the Energy Balance of High Alpine Snow Cover. Nordic Hydrology. 25: 25-38.

[149] Pohl, S., Marsh, P., and Liston, G. E. (2006) Spatial-temporal variability in turbulent fluxes during spring snowmelt. Arct. Antarct. Alp. Res. 38: 136–146.

[150] Pomeroy, J., Toth, B., Granger, R. J., Hedstrom, N. R., and Essery, R. L. H. (2003) Variation in Surface Energetics during Snowmelt in a Subarctic Mountain Catchment, Journal of Hydrometeorology, 4, 702-719.

[151] Pellicciotti, F., Helbing, J., Rivera, A., Favier, V., Corripio, J., Araos, J., Sicart, J. E., and Carenzo, M. (2008) A study of the energy balance and melt regime on Juncal Norte Glacier, semi-arid Andes of central Chile, using melt models of different complexity, Hydrological Processes, 22(19), 3980-3997.

[152] Prandtl, L. (1932) 'Meteorologische Anwendungen der Strömungslehre'. Beitr. Phys. Atmosph. 19: 188-202.

[153] Prokop, A. (2008) Assessing the applicability of terrestrial laser scanning for spatial snow depth measurements, Cold Regions Science and Technology, 54, 155-163.

[154] Rannik, Ü., and Vesala, T. (1999) Autoregressive filtering versus linear detrending in estimation of fluxes by the eddy covariance method. Boundary-Layer Meteorol. 91: 259-280.

[155] Riche, F., and Schneebeli, M. (2013) Thermal conductivity of snow measured by three independent methods and anisotropy considerations, The Cryosphere, 7, 217-227.

[156] Saltelli, A., and Annoni, P. (2010) How to avoid a perfunctory sensitivity analysis. Environ. Model. Softw., 25 (12), pp. 1508-1517

[157] Sauter, T. and Galos, S. P. (2016) Effects of local advection on the spatial sensible heat flux variation on a mountain glacier, The Cryosphere, 10, 2887-2905.

[158] Savelyev, S. A. and Taylor, P. A. (2005) Internal boundary layers: I. Height formulae for neutral and diabatic flows, Boundary-Layer Meteorol, 115, 1-25.

[159] Schaefli, B., Hingray, B., and Musy, A. (2007) Climate change and hydropower production in the Swiss Alps: quantification of potential impacts and related modelling uncertainties, Hydrol. Earth Syst. Sci., 11(3), 1191-1205.

[160] Schirmer, M., Wirz, V., Clifton, A., and Lehning, M. (2011) Persistence in intra-annual snow depth distribution: 1. Measurements and topographic control, Water Resour. Res., 47, W09516

[161] Schlögl, S., Marty, C., Bavay, M., and Lehning, M. (2016) Sensitivity of Alpine3D modelled snow cover to modifications in DEM resolution, station coverage and meteorological input quantities. Environmental Modelling and Software, 83, 387-396.

[162] Schlögl, S., Lehning, M., Nishimura, K., Huwald, H., Cullen, N. J., and Mott, R. (2017) How do stability corrections perform in the stable boundary layer over snow?, Boundary-Layer Meteorology, 165,161-180.

[163] Schlögl, S., Lehning, M., and Mott, R. How are turbulent sensible heat fluxes affected by a changing snow cover fraction? Submitted to Frontiers.

[164] Schlögl, S., Lehning, M., and Mott, R. (2018) Representation of horizontal transport processes in snowmelt modelling by applying a footprint approach. Submitted to Frontiers.

[165] Schmid, H. P. (1994) Source areas for scalars and scalar fluxes, Boundary-Layer Meteorology, 67(3), 293-318.

[166] Schneebeli, M. and Sokratov, S. A. (2004) Tomography of temperature gradient metamorphism of snow and associated changes in heat conduction, Hydrological Processes, 18 (18), 3655-3665.

[167] Schmucki, E., Marty, C., Fierz, C., and Lehning, M. (2014) Evaluation of modelled snow depth and snow water equivalent at three contrasting sites in Switzerland using SNOWPACK simulations driven by different meteorological data input, Cold Regions Science and Technology, 99, 27-37.

[168] Schmucki, E., Marty, C., Fierz, C., Weingartner, R., and Lehning, M. (2015) Impact of climate change in Switzerland on socio-economic snow indices. Theor. Appl. Climatol., 114, p. 15

[169] Schuepp, P. H., Leclerc, M. Y., Macpherson, J. I., and Desjardins, R. L. (1990) Footprint Prediction of scalar fluxes from analytical solutions of the diffusion equation, Boundary-Layer Meteorology, 50, 255-373.

[170] Segal, M., Garratt, J. R., Pielke, R. A., and Ye, Z. (1991) Scaling and numerical model evaluation of snow-cover effects on the generation and modification of day time mesoscale circulations. J. Atmos. Sci., 48, 1024–1041.

[171] Sevruk, B. (1982) Methods of Correction for Systematic Error in Point Precipitation Measurement for Operational Use. World Meteorol. Org., Operational Hydrol. Rep. 21, WMO-No. 589. p. 91.

[172] Sharan, M., and Kumar, P. (2011) Estimation of upper bounds for the applicability of non-linear similarity functions for non-dimensional wind and temperature profiles in the surface layer in very stable conditions. Proc. R. Soc. A. 467(2126): 473-494. DOI:10.1098/rspa.2010.0220.

[173] Shin, M. J., Guillaume, J. H. A., Croke, B. F. W., and Jakeman, A. J. (2013) Addressing ten questions about conceptual rainfall-runoff models with global sensitivity analyses in R. J. Hydrol., 503, pp. 135-152

[174] Shook, K., and Gray, D. M. (1997) Synthesizing shallow seasonal snow covers, Water Resour. Res., 33, 419-420.

[175] Smeets, C. J. P. P., and van den Broeke, M. R. *(2008b)* The parameterization of scalar transfer over rough ice. Boundary Layer Meteorol. 128(3): 339–355*, DOI:10.1007/s10546-008-9292-z.*

[176] Sommer, C. G., Lehning, M., and Mott, R. (2015) Snow in a Very Steep Rock Face: Accumulation and Redistribution During and After a Snowfall Event, Front. Earth Sci., 3, 73.

[177] Sorbjan, Z. (2010) Gradient-based scales and similarity laws in the stable boundary layer. Q.J.R.Meteorol.Soc. 136(650A): 1243-1254. DOI: 10.1002/qj.638

[178] Sorbjan, Z. (2016) Similarity scaling systems for stably stratified turbulent flows. Q.J.R. Meteorol. Soc.142(695B): 805-810. DOI: 10.1002/qj.2682

[179] Stearns, C. R. and Weidner, G. A. (1993) Sensible and Latent heat flux estimates in Antarctica. Antarctic Research Series. 61:109-138.

[180] Stieglitz, M., Déry, S. J., Romanovsky, V. E., and Osterkamp, T. E. (2003) The role of snow cover in the warming of arctic permafrost, Geophysical Research Letters, 30(13), 1721.

[181] Stössel F., Guala M., Fierz C., Manes C., Lehning M. (2010) Micrometeorological and morphological observations of surface hoar dynamics on a mountain snow cover. Water Resources Research. 46(4).

[182] Sturm, M. and Liston, G. E. (2003) The snow cover on lakes of the Arctic Coastal Plain of Alaska, U.S.A. J. Glaciol., 49 (No. 166), pp. 370-380

[183] Surdyk, S., and Fily, M. (1995) Results of a stratified snow emissivity model based on the wave approach: Application to the Antarctic ice sheet, Journal of Geophysical Research, 100, 8837-8848.

[184] Taylor, C. M., Harding, R. J., Pielke Sr, R. A., Vidale, P. L., Walko, R. L., and Pomeroy, J. W. (1998) Snow breezes in the boreal forest. J. Geophys. Res.,103, 23087–23101.

[185] Thomas, C. K., Law, B. E., Irvine, J., Martin, J. G., Pettijohn, J. C., and Davis, K. J. (2009) Seasonal hydrology explains interannual and seasonal variation in carbon and water exchange in a semiarid mature ponderosa pine forest in central Oregon, J. Geophys. Res.,114, G04006.

[186] Unsworth, M. H., and Monteith, J. L. (1975) Long-wave radiation at the ground, Quart. J. R. Met. Soc., 101, 13-24.

[187] Vallet, B., Pierrot-Deseilligny, M., Boldo, D., and Brédif, M. (2011) Building footprint database improvement for 3D reconstruction: A split and merge approach and its evaluation, ISPRS Journal of Photogrammetry and Remote Sensing, 66(5), 732-742.

[188] Vickers, D., and Mahrt, L. (1997) Quality Control and Flux Sampling Problems for Tower and Aircraft Data, Journal of Atmospheric and Oceanic Technology, 14, 512-526.

[189] Vickers, D., Mahrt, L., Andreas, E.L. (2015) Formulation of the sea surface friction velocity in terms of the mean wind and bulk stability. J. Appl. Meteor. Climatol. 54(3): 691-703.

[190] Viviroli, D., Zappa, M., Gurtz, J., and Weingartner, R. (2009) An introduction to the hydrological modelling system PREVAH and its pre- and post-processing-tools. Environ. Model. Softw., 24 (10), pp. 1209-1222

[191] Vögeli, C., Lehning, M., Wever, N., and Bavay, M. (2016) Scaling Precipitation Input to Spatially Distributed Hydrological Models by Measured Snow Distribution, Frontiers in Earth Science, 4, 108.

[192] Walter, M. T., Brooks, E. S., McCool, D. K., King, L. G., Molnau, M., and Boll, J. (2005) Process-based snowmelt modeling: does it require more input data than temperature-index modeling? J. Hydrol., 300, pp. 65-75

[193] Watt, P. J., and Donoghue, D. N. M. (2005) Measuring forest structure with terrestrial laser scanning, Int. J. Remote Sens, 26(7), pp. 1437– 1446.

[194] Webb, E. K. (1970) Profile Relationships The Log-Linear Range and Extension to Strong Stability. Quart. J. Roy. Meteorol. Soc. 96: 67-90.

[195] Weingartner, R., Barben, M., and Spreafico, M. (2003) Floods in mountain areas – an overview based on examples from Switzerland. J. Hydrol., 282, pp. 10-24

[196] Wever, N., Comola, F., Bavay, M., and Lehning, M. (2017) Simulating the influence of snow surface processes on soil moisture dynamics and streamflow generation in an alpine catchment, Hydrol. Earth Syst. Sci., 21, 4053-4071.

[197] Weisman, R. N. (1977) Snowmelt: A Two-Dimensional Turbulent Diffusion Model, Water Resources Research, 13(2), 337-342.

[198] Wieringa, J. (1993) Representative roughness parameters for homogeneous terrain, Boundary-Layer Meteorology, 63, 323-363.

[199] Wild, M. (2009) Global dimming and brightening: a review. J. Geophys. Res. - Atmos., 114, p. D00D16, 10.1029/2008JD011470

[200] Winstral, A. and Marks, D. (2002) Simulating wind fields and snow redistribution using terrain-based parameters to model snow accumulation and melt over a semi-arid mountain catchment, Hydrological Processes, 16(18), 3585-3603.

[201] Winton, M. (2006) Amplified Arctic climate change: What does surface albedo feedback have to do with it? Geophysical Research Letters, 33(3), L03701.

[202] Wipf, S., and Rixen, C. (2010) A review of snow manipulation experiments in Arctic and alpine tundra ecosystems, Polar Research, 29, 95-109.

[203] Xue, M., Droegemeier, K. K., Wong, V., Shapiro, A., and Brewster, K. (2004) The Advanced Regional Prediction System (ARPS) – A multi-scale non-hydrostatic atmospheric simulation model. Part II: model physics and applications, Meteorol. Atmos. Phys., 76, 143-165.

[204] Zeng X., Zhao M., Dickinson R.E. (1998) Intercomparison of Bulk Aerodynamic Algorithms for the Computation of Sea Surface Fluxes Using TOGA COARE and TAO Data. Journal of Climate. 11: 2628-2644.

Appendix A: Impact of Extreme Land Surface Heterogeneity on Micrometeorology over Spring Snow Cover

Mott, R.[1,3], Schlögl, S.[1,2], Dirks, L.[1] and Lehning, M.[1,2]

[1] WSL-Institute for Snow and Avalanche Research SLF, Davos, Switzerland
[2] School of Architecture, Civil and Environmental Engineering, École Polytechnique Fédérale de Lausanne, Lausanne, Switzerland
[3] Karlsruhe Institute of Technology, Institute of Meteorology and Climate Research, Atmospheric Environmental Research (IMK-IFU), KIT-Campus Alpin, Garmisch-Partenkirchen, Germany

Abstract The melting mountain snow cover in spring typically changes from a continuous snow cover to a mosaic of patches of snow and bare ground, inducing an extreme heterogeneity of the land surface. A comprehensive measurement campaign, the Dischma experiment, was conducted during three entire ablation seasons. The aim of this study was to experimentally investigate the small-scale boundary layer dynamics over a melting snow cover with a gradually decreasing snow cover fraction and the associated heat exchange at the snow surface. This study presents a unique dataset combining eddy covariance measurements at different atmospheric levels with maps of snow surface temperatures and snow cover fractions. The experiments evidence diurnal mountain wind systems driving the diurnal cycle of turbulent sensible heat fluxes over snow and the formation of katabatic flows over long-lasting snow patches strongly affecting the temporal evolution of snow surface temperature patterns. The snow cover distribution is also shown to be of vital importance for the frequency of stable internal boundary layer development over snow. For situations with a clear evidence of stable internal boundary layer development over snow, the data reveal a very shallow atmospheric layer adjacent to the snow cover decoupled from the warm-air advection above. These measurements confirm previous wind tunnel experiments that also evidenced a decoupling of the air adjacent to the snow cover from the warmer air above, especially within topographical depressions and when ambient wind velocities are low. For these situations, in particular, all tested energy balance models strongly overestimated the turbulent sensible heat flux directed toward the snow cover.

Keywords: Atmosphere • Boundary layer • Atmosphere-land interaction • Small scale processes • Surface fluxes • Spring season

A.1   Introduction

The strong interaction between the near-surface atmosphere and the underlying ground via heat exchange processes makes the presence of snow a key component of the Earth system (Sauter and Obleitner, 2015) with vital consequences for the hydrological cycle (Lehning, 2013). Furthermore, snow albedo feedbacks are shown to enhance large- and small-scale variability of atmospheric warming and even change diurnal wind systems (Randall et al., 1994; Letcher and Minder, 2015).

The springtime snow cover typically changes from a continuous snow cover to a mosaic of patches of snow and bare ground, inducing an extreme heterogeneity of the land surface (Liston, 1995). In the absence of terrain, strong snow cover variations drive a snow-breeze type of circulation, responding to the strong thermal contrast between snow and bare ground (Johnson et al. 1984; Taylor et al., 1998). In mountainous regions, where springtime snow cover is mainly governed by complex terrain and elevation gradients, snow-breeze circulations and diurnal mountain wind systems interact (Letcher and Minder, 2015). Segal et al. (1991) showed that the presence of snow at higher elevations can counteract the diurnal upslope flow. Recent numerical results presented by Mott et al. (2015) have suggested that the presence of snow patches in spring significantly affects the diurnal mountain wind system. Thermally driven small-scale flow features are shown to develop over large snow patches, considerably changing the heat exchange process over the springtime snow cover. Furthermore, the special setup of the land surface in spring coincides with steps in surface roughness and surface temperature, inducing the development of dynamic and thermal internal boundary layers. As a result, mass and energy fluxes as well as the mean flow field characteristics show a high spatial variability not only in the horizontal but also in the vertical direction (Essery, 1999; Essery et al., 2006; Granger et al., 2006; Mott et al., 2013; Harder et al., 2017).

Long-lasting snow and ice patches are typically found in topographic depressions because of preferred snow accumulation and suppressed snow ablation in sheltered areas (Tabler, 1975; Dadic et al., 2010; Mott et al., 2014; Odegard et al., 2017). Large snow patches can significantly alter the near-surface flow field (Glazirin et al., 2004), and strong atmospheric decoupling and connected suppression of heat exchange slows down snow ablation in spring (Fujita et al., 2010). Recent wind tunnel experiments (Mott et al., 2016) on flow development over a melting snow patch gave evidence that wind sheltering effects result in atmospheric decoupling over snow and significantly suppress the turbulent heat exchange between the snow and adjacent atmosphere. Thus, atmospheric decoupling is promoted by— but at the same time counteracts —the effect of the warming of the atmosphere caused by heating of already snow-free areas. The interaction between these two counteracting processes is very complex and not well understood.

In winter, turbulent heat fluxes over snow show a high sensitivity to spatially variable wind velocities induced by complex terrain (Mott et al., 2011; Pohl et al., 2006; Dadic et al., 2013; Schlögl et al., 2017). Furthermore, surface energy, mass, and momentum fluxes are strongly linked to horizontally heterogeneous land surfaces (Cohen and Rind, 1991). Knowledge of the effect of spring land surface heterogeneity on local heat exchange processes and the consideration of the range of scales that needs to be accounted for remains a challenging part when attempting to represent relevant processes in, for example, Earth system modeling (de Vrese et al., 2016). There are some models that parameterize and assess subgrid fractional snow cover in global and regional models as simplified functions of snow depth, snow water equivalent, roughness length, and subgrid orography (Roesch et al., 2001; Liston, 2004; Takata et al., 2003; Essery, 2008; Dutra et al., 2010; Best et al., 2011; Nitta et al., 2014). The interaction between the fractional snow cover and the overlying atmosphere is, however, highly simplified. The estimation of average sensible heat by flux–gradient relationships is not valid over patchy snow cover because of the high spatial variability of air temperature and sensible heat fluxes. Close to the variable surface, constant flux layers and fully developed boundary layers do not exist and yield a high temporal and spatial variability of boundary layer characteristics on a very small scale. Local air temperature and sensible heat flux measurements are strongly dependent on the upwind distribution of snow patches and snow-free areas (Marsh et al., 1999). Experiments on heat exchange processes over patchy snow cover thus become very challenging during spring conditions. This is one reason that experimental studies on heat exchange in areas featuring extreme land surface heterogeneity such as patchy snow cover are very rare (Essery et al., 2006; Mott et al., 2013) and typically only represent a snapshot in time (Mott et al., 2013). Recent studies pointed out the necessity of field measurements conducted over a complete melting season covering the atmospheric boundary layer dynamics under different meteorological conditions and for a successively decreasing snow cover fraction that is, increasing heterogeneity in land surface characteristics (Mott et al., 2016).

In this study, we present a unique dataset monitored during the comprehensive measurement campaign, the Dischma experiment. We present eddy covariance measurements conducted over a long-lasting snow patch in a small alpine catchment. Since measurements were performed over three complete ablation periods, the dataset comprises different snow cover distributions and meteorological conditions. Additionally, snow cover warming, snow cover distribution, and mean flow field development have been monitored throughout the three melting periods. Since recent numerical investigations on boundary flow development over patchy snow cover suggested a high sensitivity of the near-surface flow field to the changing land surface in spring (Mott et al., 2015), we will analyse turbulent heat exchange and snow cover warming as a function of the prevailing wind situation and snow cover distribution. We will further discuss the effect of a decreasing snow cover fraction on the boundary layer development and on the associated heat exchange above the melting snow cover.

A.2 Methods

A.2.1 Field site

The test site Gletschboden is located in the upper Dischma valley, featuring a flat area surrounded by steep slopes to the southeast and northwest, a small hill to the south, and the lower Dischma valley to the north (Fig. A.1). The flat test site is located at approximately 2100 m MSL and is mainly covered by alpine meadow with some rocks. The Dischma valley discharges into the larger Landwasser valley, at Davos, Switzerland. The Dischma valley is approximately 15 km long, with the valley floor at 1600 m asl at the entrance and 2000 m asl at the end. Ridge-top elevations range from 2500 to 3000 m asl. The Dischma valley is v-shaped and is largely symmetrical. The Dischma valley contains a 43 km^2 hydrological catchment with a stream meandering along the valley floor, which is fed by smaller side streams and a glacier at the southern end. High-quality runoff data are available from the federal office in Switzerland (FOEHN) for the Dischma catchment. In the 1980s, the Dischma valley was the site of an extensive field campaign, Dischmatal Klimauntersuchungen (DISKUS), which lead to several publications in the following decade regarding valley-scale meteorology (Hennemuth and Köhler, 1984; Hennemuth and Schmidt, 1985; Hennemuth, 1986). The Dischma valley has been a site for snow hydrology studies (Lehning et al., 2006; Bavay et al., 2009; Griessinger et al., 2016). Very recently, the Dischma experiment was run in the Dischma valley from the winter season of 2013/14 until 2016/17, with the aim to investigate snow–atmosphere interactions driving snow accumulation (Gerber et al., 2017) and ablation in an Alpine catchment.
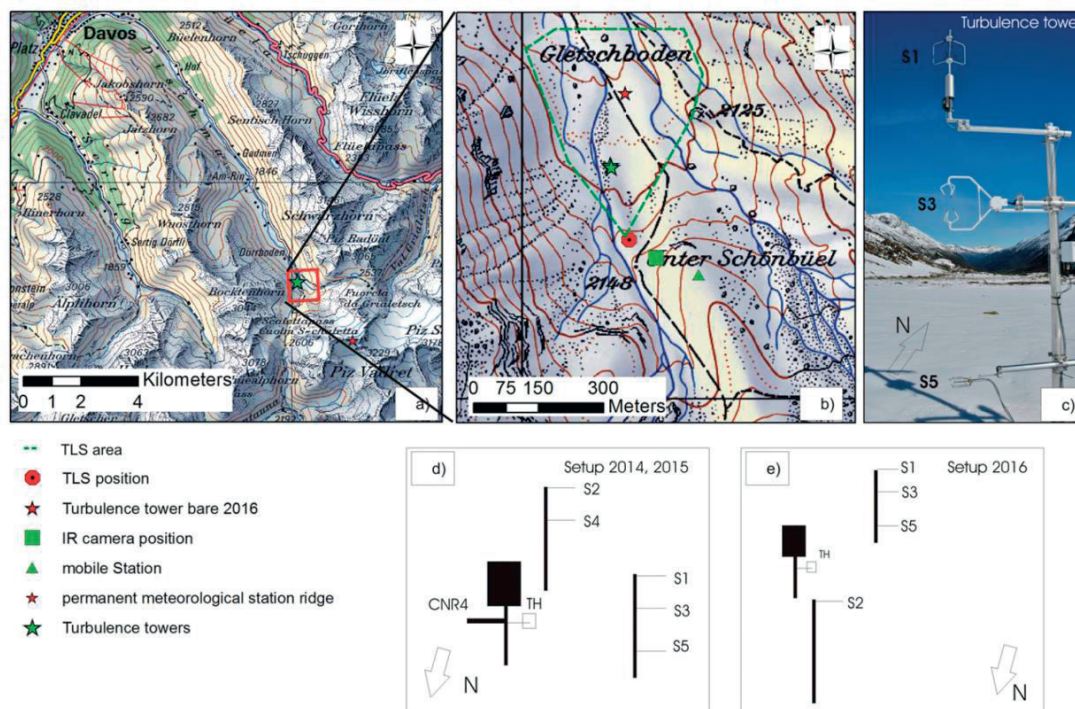
Fig A.1 (a) The upper Dischma valley (Davos, Switzerland) showing the location of (b) field site Gletschboden. (c) Picture of turbulence tower and illustrations of measurement setup in (d) 2014/15 and (e) 2016. Label descriptions: TH = temperature/humidity sensor, CNR4 = net radiometer, S = sonic anemometer.

A.2.2 Eddy-covariance measurements

As part of the Dischma experiment measurement campaign, a turbulence station was installed at the Gletschboden area during the ablation seasons of 2014, 2015, and 2016. For the seasons 2014 and 2015, the turbulence station consisted of two turbulence towers and was installed over a long-lasting snow patch. The turbulence towers were equipped with two Young ultrasonic anemometers mounted 0.7 m (in 2014) and 3.3 m (in 2015) above snow-free ground, two ultrasonic anemometers (CSAT3, Campbell Scientific, Inc.) mounted at 2.6 m (in 2014) and 2.2 m (in 2015) above snow-free ground, and one anemometer (DA-600, Kaijo Denki) mounted at 0.3 m above the snow surface.

Because of a changing snow height in winter, the height over snow changed for sensors S1 and S2 (upper level) and S3 and S4 (at medium level) during the ablation season (Fig. A.2a, Table A.1). Since sensor S5 at the lowest level has been installed only on a temporary basis, the height of approximately 0.3 m over the snow surface could be kept constant. Furthermore, in 2015, one additional tower was been equipped with a net radiometer (CNR4) and a temperature humidity sensor (Fig. A.1). Since the full energy balance station was only available for ablation period 2015, some of the analyses were only done with data recorded during this ablation season (see sections 3a and 3d).

The measurement setup changed for 2016 with the aim of improving footprint estimations for certain wind directions, with one turbulence tower installed over bare ground and a second one over the reference snow patch. The turbulence tower installed in the upwind snow-free area (for northerly winds) was equipped with one sonic anemometer installed at 3.2 m above bare ground. The turbulence tower over snow was equipped with one Young sonic anemometer at 3.5 m and one CSAT at 1.7 m above bare ground (Fig. A.2a, Table A.1). Sensor S5 (0.3 m above snow) was only installed during ablation days late in the ablation season. Unfortunately, predominantly southerly flows were observed during the time period when the snow cover became patchy in 2016. The dataset is thus not usable for footprint analysis, but is used in the following to show the frequency of the development of thermal internal boundary layers.

Turbulence data were sampled at a frequency of 20 Hz. The processing of the data to quality-controlled fluxes has been done with the Biomicrometeorology flux software (Thomas et al., 2009). The program applies plausibility tests and a despiking test after Vickers and Mahrt (1997) on the measured data. The routine further applies a time-lag correction and considers the deployment (e.g., the sonic azimuth). A frequency response correction (Moore, 1986) is done and a three-dimensional rotation is performed. Finally, quality assurance/quality control (QA/QC) flags after Foken et al. (2004) are issued and fast Fourier transform power and cospectra are calculated. The change in snow height is considered in the postprocessing for every measurement day. The turbulence data were averaged to 5- and 30-min intervals. Since a comparison between different averaging times showed that the random error introduced by the choice of averaging time is rather small during daytime and larger during night and in the morning, we chose an

averaging time of 30 min for the analysis on daytime turbulent heat fluxes applied in this study. Turbulence dataset analysed in this study is published at the Environmental Data Portal ENVIDAT (http://www.envidat.ch/dataset/10-16904-10).
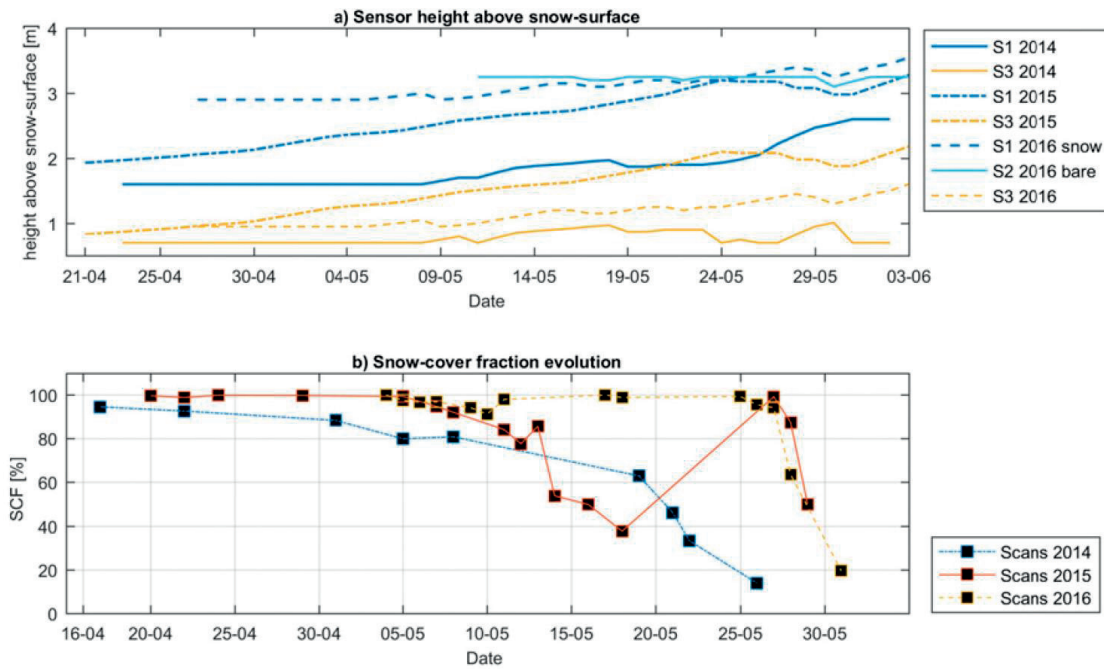

Fig A.2 (a) Sensor height above surface and (b) snow cover fractions at the field site Gletschboden, estimated from snow-depth maps obtained from terrestrial laser scans.

Sensors	Height above snow and year of deployment			
	2014	2015	2016	
Young, (S1, S2)	1.6–2.6 m	1.9–3.3 m	S1: 3.5–2.9 m	S2: 3.2 m
CSAT (S3, S4)	0.7–1 m	0.7–2.2 m	S3: 1.7–0.9 m	S4: No
Kaji Denki (S5)	0.3 m	0.3 m	0.3 m	
CNR4	No	2 m	No	
Temperature/humidity	No	2 m	2 m	

Table A.1: Deployed sensors, associated sensor height above ground, and year of deployment.

A.2.3   Snow surface temperature measurements

A thermal infrared camera (IR camera hereafter), VarioCAM HD research 900 (Infra Tec GMBH), was used to measure snow surface temperatures at the Gletschboden area with a high spatial and temporal resolution. Because of the diurnal cycle of avalanche danger in the Dischma valley in spring, measurements were conducted on an hourly basis during morning hours, when the snow cover warming rates are largest.

The camera uses an uncooled microbolometer array for the detection of thermal infrared radiation in the spectral range of 7.5–14 µm. The resolution of the camera is 1024 × 768 pixels with a measurement range from −40° to 1200°C and an accuracy of ±1.5 K for the measurement range. Surface temperatures measured by the IR camera were corrected according to the emissivity of snow, reflected radiation from the sky (sensed by the camera), and the atmospheric transmissivity. We used the incoming longwave radiation, vapor pressure, and air temperature from CNR4 and temperature/humidity sensors mounted at the turbulence station for the correction. The emissivity of snow was parameterized following the model of Hori et al. (2013). As the emissivity varies significantly with incident angle and snow type, an emissivity value for each pixel has been parameterized. The wavelength of peak emittance was calculated after Wien's law for the camera temperature. The calculation of atmospheric emissivity was done with the parameterization suggested by Idso (1981), as this formulation applied specifically to the 8–15-µm range of the thermal IR spectrum. Emissivity values were rather small for all measurement days, owing to the rather low temperature and relative humidity of the air. A comparison of corrected snow surface temperatures measured by the IR camera to snow surface temperatures derived from pyrgeometer measurement (CNR4 sensor) by applying the Stefan–Boltzmann law revealed a camera offset of approximately 4.5 K. A comparison of relative temperatures obtained from the IR camera, CNR4 sensor, and a mobile weather station shows that relative values coincide well, mainly not exceeding the arbitrary threshold of ±0.5 K (Fig. A.3).
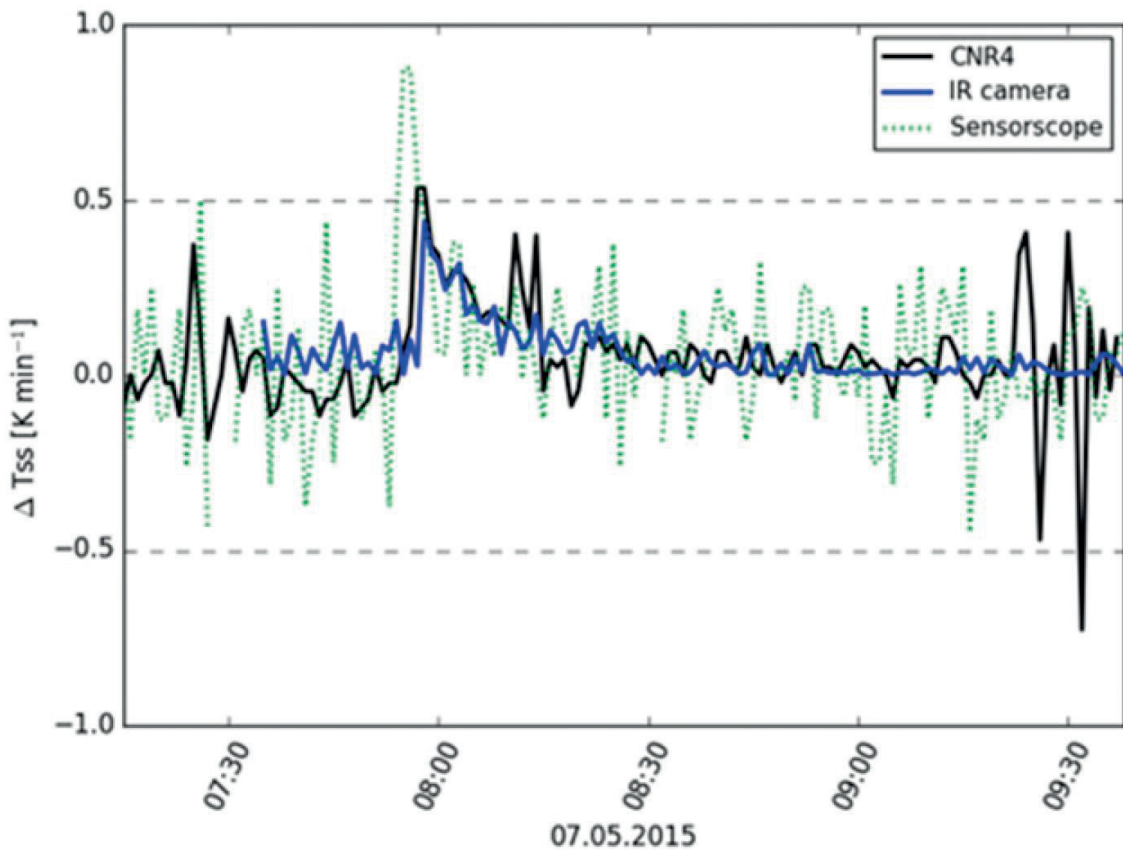
Fig A.3: Comparison of snow surface temperature change per minute for the IR camera, CNR4, and mobile weather station (Sensorscope).

A.2.4 Snow depth and snow cover fraction measurements

In total, 44 high-resolution snow depth measurements were conducted with the terrestrial laser scanner (TLS; Riegl VZ-6000) in the three consecutive years of 2014, 2015, and 2016. We used snow depth maps of the Gletschboden with an area of 400 m × 500 m (Fig. A.1) in order to estimate the temporal development of the snow cover fraction (SCF; Fig. A.2) and snow ablation rates. The Gletschboden area was recorded with a frequency of 300 kHz and a beam divergence of 0.007°, which implies a horizontal resolution of approximately 0.01 m in 100 m distance from the TLS position. Scans were done at intervals of a few days depending on weather conditions, with a reduction of scan intervals to 24–48 h if snow ablation was very strong (Fig. A.2b). A more general description of the TLS measurement setup and accuracy over snow can be found in Prokop et al. (2008), Schaffhauser et al. (2008), and Grünewald et al. (2010). We followed the postprocessing procedure described by Sommer et al. (2015), applying the multistation adjustment to improve the registration of scans conducted on different measurement days. Rasters of snow depths with a cell size of 0.2 m were calculated from georeferenced point clouds to estimate the snow cover fraction of the test site (Fig. A.2b) and the wind fetch distance over snow at the location of turbulence measurements at the reference snow patch.

Comparing the peak snow accumulation of the three winter seasons at the nearby Weissfluhjoch location (2540 m) with the long-term trend (http://www.slf.ch/schneeinfo/wochenbericht/2015-16/jahresbericht/Schneehoehenverlauf/index_DE), peak snow accumulation was below average in winter 2013/14, above average in winter 2014/15, and average in winter 2015/16. The temporal development of snow cover fractions (Fig. A.2b) show a more gradual decrease in snow cover fraction at the Gletschboden and an earlier end of the ablation season in 2014 than in the consecutive years.

A.3 Results

A.3.1 Prevailing wind situations and connected temporal patterns of mean turbulent heat fluxes

Earlier numerical results show a high sensitivity of turbulent sensible heat fluxes over patchy snow cover to prevailing wind situations (Mott et al., 2015). We thus analyse temporal patterns of measured turbulent heat exchange and turbulence characteristics over the whole ablation period of 2015 for different weather classes. In this analysis, we only include data collected during the

ablation period of 2015 because the full energy balance station was only available for this year. The main aim of this section is to investigate the interactions among the changing land surface, the boundary layer flow, and the mean turbulent heat exchange over snow.

The diurnal variation of the median of the turbulent sensible heat flux, wind velocity, and the stability parameter z/L (height above ground/Monin–Obukhov length) measured at sensors S3 and S4 (mounted at 2.2 m above the snow-free surface, 0.8 m in 2015 above the snow surface) are shown in Fig. A.4 for different weather classes. Analysing the wind system in the Dischma valley, Urfer-Henneberger and Turner (1982) suggested a categorization of the wind system into four distinct situations: undisturbed fair, Föhn, Bise, and blocking situations. Based on this analysis and considering the available data, we distinguish among ablation days characterized by synoptically induced northerly flows (Bise), thermally induced flows (undisturbed fair weather), and synoptically induced southerly flows (Föhn). Since we were only interested in the small-scale flow features, we applied a simple classification based on wind speed and wind direction to the data measured at the mobile station at the hill (Fig. A.1) to categorize between synoptic north, synoptic south, and thermally induced flows. In reference to Hennemuth and Schmidt (1985), who measured valley winds up to 4 m s^{-1} (not averaged) in the Dischma valley, the wind speed criteria to differentiate between thermic and synoptic days was set to a mean wind velocity of 3.5 m s^{-1}. The clear change from a mountain to valley wind was a further clear indicator to categorize the prevailing wind system as a thermally driven flow. The ablation season of 2015 included 48 days (the start of the melting season is here defined by the onset of snowmelt at the test site). Only 19 days could be clearly categorized and did not show precipitation during daytime and are thus considered in the following analysis.
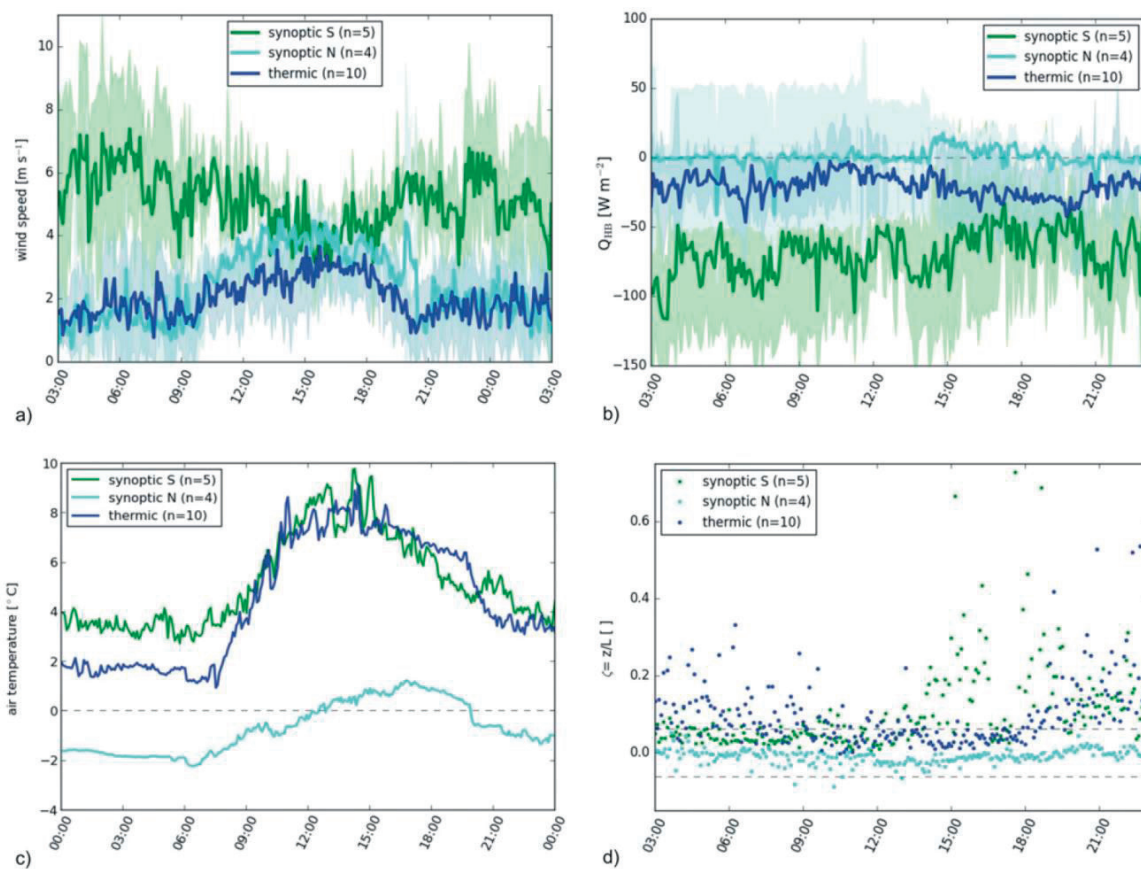

Fig A.4 Median of wind speed, median of turbulent sensible heat flux Q_{HB}, and median of air temperature for all measurement days of the corresponding weather classes. Note that negative values of Q_{HB} indicate a downward heat flux warming the surface. The variability of wind speed and buoyancy flux is shown by the correspondingly coloured translucent standard deviation. Median of the stability parameter ($\zeta = z/L$) for the three weather classes, obtained from the midlevel sensors S3 and S4.

1) Thermally driven wind systems

The highest sensitivity of the wind system to the change in land cover is revealed for days characterized by fair undisturbed weather, allowing the development of thermally driven wind systems (thermic class hereafter). Considering 48 days of the ablation season of 2015, 22 % of the days are characterized by a thermally driven up- and down-valley wind system. The development of thermally driven wind systems is strongly connected to the change from a continuous to patchy snow cover. Thermic days are thus frequent in late spring and are observed when the sun-exposed slopes in the Dischma valley become snow-free (not shown). The strong heterogeneity of snow cover distribution results in a differentiated warming of snow-free and snow-covered slopes in the morning, which modulates the thermal contrast there and thus forces the diurnal mountain wind system. For these days, wind data

evidence a change in wind direction from south (down-valley flow) to north (up-valley flow) around midday, accompanied by a significant increase in the mean wind velocity (Fig. A.5). The diurnal cycle of wind direction and speed (Figs. A.4a, A.5) is associated with a strong diurnal cycle of the time series of the turbulent sensible heat flux (Fig. A.4b). Downward turbulent sensible heat fluxes (warming the surface) are rather small during the presence of the mountain wind in the night and morning and significantly increase as the wind shifts from a down-valley to an up-valley wind. For the thermic class, stable conditions (positive stability parameter; Fig. A.4d) prevail as long as the mountain winds (down-valley winds) are present. As soon as the wind turned to an up-valley wind, stratification tended to be slightly stable or even near-neutral at approximately 1.5 m measurement height. This weak stability is in contradiction to high positive air temperatures (Fig. A.4c) and snow surface temperatures at the melting point. The strong dependency of atmospheric stability and sensible turbulent heat fluxes on the measurement height will be discussed in sections A.3c and A.3d.
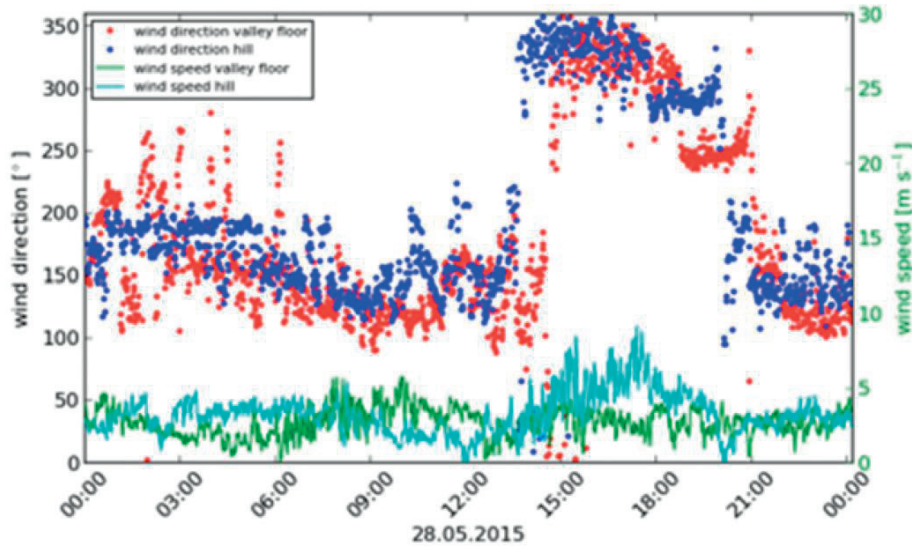

Fig A.5 Wind direction and wind velocity measured at two mobile weather stations in the Gletschboden area for a thermic day.

2) Synoptically induced wind systems

Ablation days with evidence of synoptically induced southerly winds (10 % of ablation days; synoptic south class hereafter) are characterized by high wind velocities (Fig. A.4a) and high air temperatures (Fig. A.4c), most frequently observed early in the melting season when snow coverage was still high (not shown). High air temperatures and strong winds promote strongly negative turbulent sensible heat fluxes (warming the surface) during night and day with a low temporal variation (Fig. A.4b). The atmospheric stability changes from near neutral during the night to stable conditions during daytime (Fig. A.4d).

For synoptically induced northerly flows (synoptic north class hereafter), turbulent sensible heat fluxes directed toward the snow cover (negative values) are very small during daytime, fluctuating around zero in the morning. When air temperatures slightly increased above 0 °C in the afternoon, measured sensible heat fluxes become positive (directed away from the surface) at the midlevel measurement height (0.7–2.2 m above the snow-covered ground; Fig. A.4b). The evidence of positive turbulent sensible heat fluxes despite positive air temperature gradients hints at a change in near-surface thermal boundary layer conditions. The strong heterogeneity of the land surface and the associated steps in land surface temperatures induces the formation of very shallow thermal internal boundary layers. The two upper turbulence sensors are apparently above the thermal internal boundary layer adjacent to the snow cover when air temperatures are raised above the freezing point. All synoptic north situations occurred late in the ablation season when snow cover fraction was lower than 40 % (not shown), favoring the development of thermal internal boundary layers above the heterogeneous land cover. The development of thermal internal boundary layers as a function of wind direction and snow coverage is further discussed in Section A.3b.

A.3.2 Prevailing wind systems and associated temporal and spatial patterns of snow surface warming

Figure A.6 shows an example of snow cover warming before (Fig. A.6a) and after (Fig. A.6b) sunrise on a day characterized by fair, undisturbed weather (thermic class). Two rectangles indicate areas with a strongly different response of the snow cover temperature evolution to the near-surface flow field. The average temporal evolution of snow surface temperatures for the two areas is shown for a thermic day in Fig. A6c and for a synoptic south day in Fig. A6d.

During the thermic day, late in the ablation season (28 May 2015), the measured snow surface temperatures at the flat Gletschboden test site show a high spatial and temporal variability (Figs. A.6a,b). High-resolution snow surface temperature maps obtained from the IR camera evidence some areas featuring below-average surface temperatures in the morning (rectangle B, marked in Fig.

A.6a). The temporally highly resolved sequence of measurements strongly suggests the influence of small-scale drainage flows that developed in the early morning of the thermic day (Fig. A.6a). Large avalanche deposits on the northeasterly exposed slopes (not shown) apparently allowed the surface temperatures to cool more strongly than the surrounding snow-free areas during the clear night. Colder air adjacent to the snow cover finally drained down the slope, locally cooling the snow cover on the western part of the Gletschboden (rectangle B), which is visible in the surface temperature maps obtained before sunrise at 0744 UTC (Fig. A.6a).

When the sun rises, observed drainage flows disappeared and shortwave radiation and increasing downward turbulent heat fluxes resulted in a rapid warming of the snow cover after 0800 UTC (Fig. A.6b). Areas in the eastern part of the Gletschboden area (indicated by the rectangle A) are not affected by drainage flows in the morning and thus show higher surface temperatures before sunrise. After sunrise, however, snow cover warming is significantly lower, which is also visible in the temporal evolution of the mean surface temperature within this area shown in Fig. A.6c. Small-scale spatial patterns of snow surface temperatures also reveal below-average surface temperatures at the slope of the hill Unter Schönbüel, located south of the marked area. Furthermore, small-scale stripes of very low surface temperatures at the lower part of the slope of the Unter Schönbüel (as marked in the map in Fig. A.6b) indicate the influence of very small-scale flow features there. The suppression of snow cover warming within the marked area is most probably caused by the combination of wind sheltering by the small hill upstream of the test site and the low incoming shortwave radiation at the snow-covered slopes of the hill (not exposed to the sun in the morning). Thus, locally low wind velocities due to sheltering coincide with low radiative energy input.

We expect that the negative energy balance at the snow-covered northerly exposed slopes of the hill allows the temporal development of small-scale drainage flows, explaining the small stripes of very low surface temperatures. These temporally formed drainage flows thus appear to drain toward the eastern part of the Gletschboden area, cooling the snow surface at the bottom of the hill sheltered from the larger-scale, warmer, down-valley wind. On the other hand, higher wind velocities during the synoptic south class days do not allow the formation of such very small-scale drainage flows locally changing the warming rates at the snow surface (Fig. A.6d). The temporal evolution of snow surface temperatures for synoptic south situations thus shows a low temporal (Fig. A.6d) and spatial variability (not shown) in snow surface warming at the Gletschboden area.
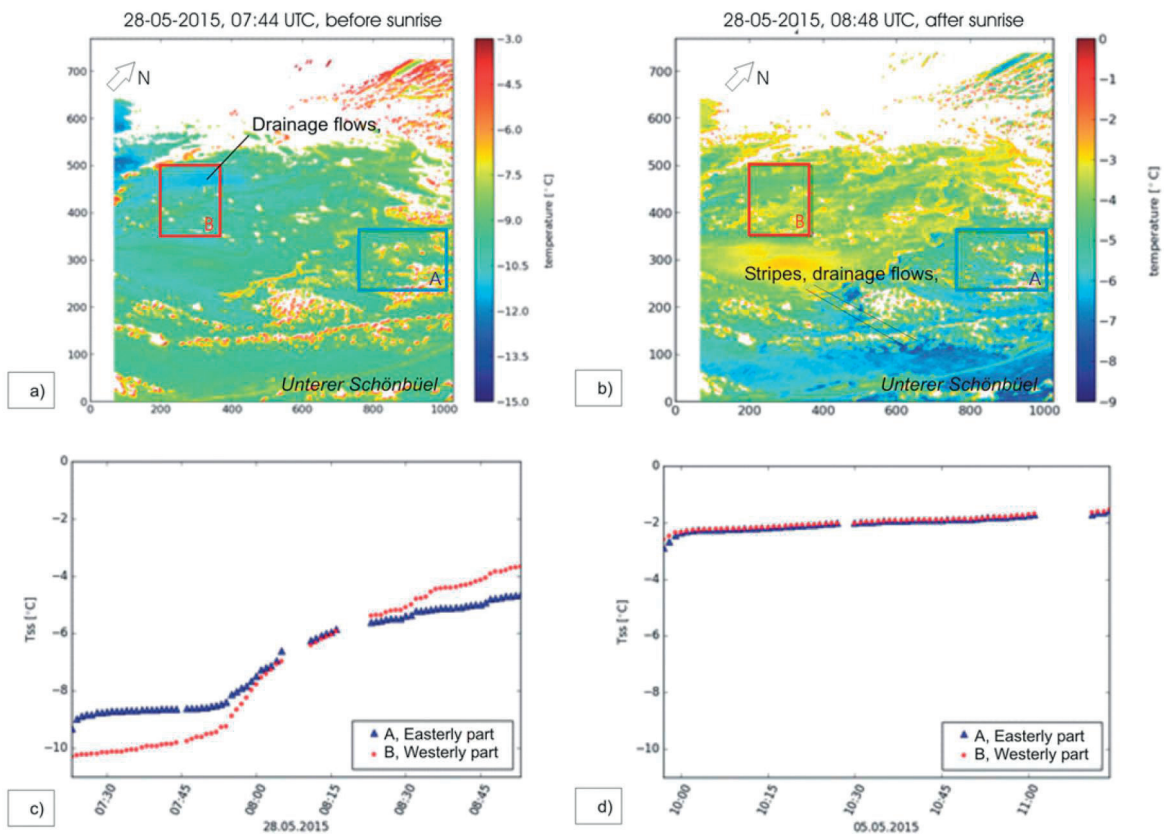

Fig A.6 Snow surface temperature maps (a) before and (b) after sunrise for a thermic day. Note that colour codes change between (a) and (b) to optimally illustrate the spatial variability of surface temperatures for both time steps. Snow surface temperature evolution of two areas for (c) the thermic day and (d) synoptically induced southerly flow. The areas selected for averaging snow surface temperatures obtained from the IR camera in (c) and (d) are indicated by blue and red rectangles in (a) and (b). The x and y axes indicate the number of measurement pixels in the corresponding direction.

A.3.3 Temporal evolution of turbulent sensible heat flux profiles during a melting season responding to changes in land surface heterogeneity

Time series of daytime turbulent heat fluxes measured at three different measurement levels (for the level heights refer to Section A.2b) above the snow surface are presented for the ablation seasons of 2014, 2015, and 2016 (Fig. A.7). Note that the measurement setup changed in spring 2016, with one turbulence tower installed over bare ground north of the reference snow patch (Fig. A.1). We only show typical time series for ablation days (air temperatures above 0°C) for different snow cover distributions and with very good data quality and without precipitation. The lowest-level sensor (0.3 m above ground) was only installed late in the ablation periods.
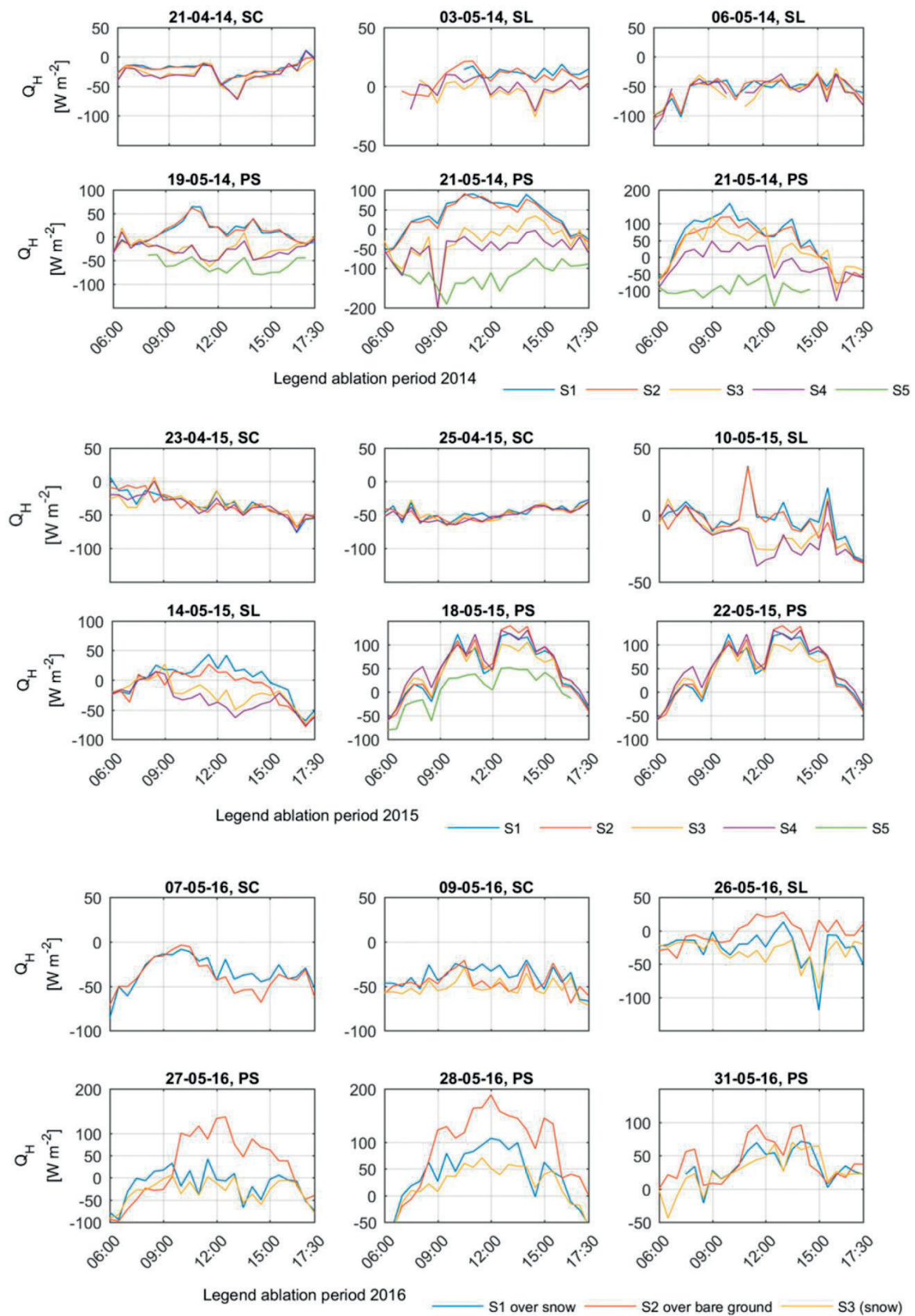
Fig A.7 Typical time series of daytime turbulent sensible heat fluxes from 0600 until 1730 UTC obtained during ablation seasons 2014, 2015, and 2016 for different snow cover distributions and for different measurement heights. SC indicates days with a full

snow cover at test site Gletschboden. SL indicates days where a sharp snow line was observed at the test site Gleschboden underneath (north to) the turbulence station. PS indicates days when the snow cover at Gletschboden was totally patchy with the snow line clearly above (south to) the turbulence station. Note that sensor S5 was only installed during selected measurement days late in the season.

In the first stage of a melting season, as long as the snow cover is continuous (days marked by SC), daytime turbulence data during ablation days of all three years evidence downward turbulent sensible heat fluxes (negative values) at all sensor heights, indicating the presence of a deep stable atmospheric layer above the snow (Fig. A.7). The vertical variability of turbulent heat fluxes is small. The second stage of a melting season starts when the snow cover distribution of the test site is dominated by the presence of a local snow line north of the Gletschboden test site in lower elevated regions (days marked by SL). During this period, the time series of turbulent flux measurements at different measurement levels showed a high sensitivity to the prevailing wind direction. For prevailing southerly winds (down-valley flows including mountain winds), all sensors measured downward turbulent sensible heat fluxes during daytime with no flux divergence (i.e., 6 and 26 May 2016). For those situations, the flow crosses very large snow-covered areas upwind of the test site featuring low heterogeneity in surface properties. Conversely, for prevailing northerly flows (including thermally driven up-valley flows and synoptic northerly flows), the flow crosses large already snow-free areas at lower elevations and experiences a step in the surface temperature when approaching the snow-covered area (i.e., 3 May 2014). Locally, the up-valley flow is connected to warm air advection from the snow-free toward the snow-covered areas. For situations favoring large flux footprints of the upper-level sensors (i.e., relatively small friction velocities with high wind velocities as favored by strong atmospheric stability), the flow at the upper-level height (S1 and S2 measured ~1.7 m in 2014 and ~2.5 m in 2015) is strongly affected by warm-air advection from snow-free areas north to the turbulence stations. The midlevel sensors (S3, S4) are, however, still within a thermal internal layer that develops above the snow. The step in surface temperature between snow-free and snow-covered areas thus induces a strong vertical variability in the turbulent sensible heat flux over snow, even showing different signs of the flux in the first meters above the surface. The strong sensitivity of local atmospheric boundary layer development to wind direction is especially visible for thermic days, such as on 10 and 14 May 2015 (Fig. A.7). For those situations, the stable internal boundary layer at the location of the turbulence station appeared to be deep as long as the mountain wind was present. As soon as the wind system changed to an up-valley flow, a shallow stable internal boundary layer developed over the reference snow patch with a depth less than 1.5 m. Sensors installed at heights above the midlevel height of 1.5 m revealed an unstable flow affected by upwind snow-free areas. At that height, the atmosphere is not affected by the underlying snow-covered ground anymore (Fig. A.7). Profiles of sensible turbulent heat fluxes thus show a strong response to the development of the thermal internal boundary layer to prevailing wind direction.

During the third stage of the melting season, the snow cover at the Gletschboden becomes patchy (days marked by PS), and the local snow line progressed to elevations higher than the test site. At this late stage of the melting period, the strong sensitivity of boundary layer development to the prevailing wind direction is not evident anymore. All prevailing wind directions and wind velocities induce the formation of shallow stable internal boundary layers during daytime with a very high vertical variability of turbulent sensible heat fluxes in the first meters above ground. As the snow cover fraction decreases, the footprints of upper- and midlevel sensors become similar or even larger than the short fetch distance over snow (results shown in the following section). The strong decrease in fetch distance over snow involves a decrease of the depth of the stable internal boundary layer at the location of the turbulence stations. Especially for the last measurement days in late May, featuring snow cover fractions lower than 25 %, upward heat fluxes are evidenced at all measurement heights despite positive air temperatures over a snow cover staying at its melting point (Fig. A.7). The evidence of near-surface upward heat fluxes and positive air temperatures at the same time indicate the presence of a very shallow stable internal boundary layer with a depth lower than 0.3 m. Given the minimum pathlengths of 0.05–0.1 m of the state-of-the-art ultrasonic anemometers applicable in the field, the supposed downward turbulent sensible heat flux adjacent to the melting snow surface (Whitemann et al., 2001) is not accessible to these measurements any more.

A.3.4 Near-surface boundary layer dynamics associated with extreme land surface heterogeneity and upwind source area

Figure A.8 shows turbulent sensible heat fluxes measured by the midlevel and low-level sensors normalized by mean air temperature and plotted against wind speed and friction velocity. We further show the relation between the distance of maximum flux contribution relative to wind fetch distance over snow (x_{max}/x_{snow}) for melting days in 2014 and 2015. The distance of maximum flux contribution is defined by the peak of the flux footprint, that is, the distance of the upwind area to which the observation is most sensitive (Schuepp et al., 1990). Fetch distances over snow were determined from snow cover distribution maps. The value of x_{max} is only an estimation of the effect of upwind areas on the single point measurements. Flux measurements at single locations are affected by the snow cover distribution of the entire upwind zone, and the distribution of flux contribution is typically right skewed, which means that flux measurements are considerably affected by areas larger than x_{max}. In this analysis, we are interested in sensible turbulent heat fluxes within the stable internal boundary layer approximately representing the heat exchange between the atmosphere and the snow cover. To ensure that measured turbulent sensible heat fluxes are not predominantly affected by bare ground, we excluded days with snow-fetch distances smaller than the distance of maximum flux contribution (x_{max}/x_{snow} larger than 1). We thus only analyse data for snow cover fractions between 94 % and 33 % for ablation season 2014 and from 100 % to 49 % for ablation season 2015. For all these days, the fetch over snow was larger than the fetch distance of the upwind area to which the sensor S3 is most sensitive (Schuepp et al., 1990). Data obtained in 2016 are excluded from the analyses because of the low number of days with evidence of stable internal boundary layer (SIBL) evolution and lack of a sufficiently large fetch distance over snow at the same time. In the following analyses, we distinguish between days with an evidence of SIBL formation (Fig. A.8, diamonds) and days without SIBL formation (Fig. A.8, circles) captured by the sensors.

Without SIBL formation, eddy covariance data at the midlevel measurement height show an increase of the downward turbulent sensible heat flux with increasing wind velocity (Fig. A.8). For situations with clear evidence of SIBL formation, midlevel measurements (S3) reveal much lower normalized heat fluxes and a significantly smaller increase of the turbulent sensible heat flux with increasing wind velocity (Figs. A8c,d). The significant lower values of turbulent sensible heat fluxes coincide with an increase in the relation between the maximum distance of flux contribution to the fetch distance over snow (Figs. A.8e, f). High coefficient values (Figs. A.8e,f) indicate large flux footprints (effective upwind source area) sensed by the observations and small fetch distances over snow at the same time. Consequently, large values indicate a significant contribution of the warmer surrounding snow-free areas on the local turbulence field captured by the sensor at the corresponding measurement height and the downwind distance over the reference snow patch. Eddy covariance measurements reveal much smaller downward turbulent sensible heat fluxes at the midlevel measurement height (~0.7 m and ~1.5 m) if the advection of upwind warm air provokes the formation of a shallow stable internal boundary layer. This is even true for situations with friction velocities high enough to produce enough inertia to mix the boundary layer (Figs. A.8a, b). On the contrary, wind situations with very large wind fetch over snow show no significant influence of snow-free areas on the turbulent structure over snow-covered areas. Deep stable layers produce significantly higher normalized turbulent sensible heat fluxes at mid- and upper-level measurement heights early in the ablation season when snow cover fraction is high or for southerly flows with a large fetch over snow.
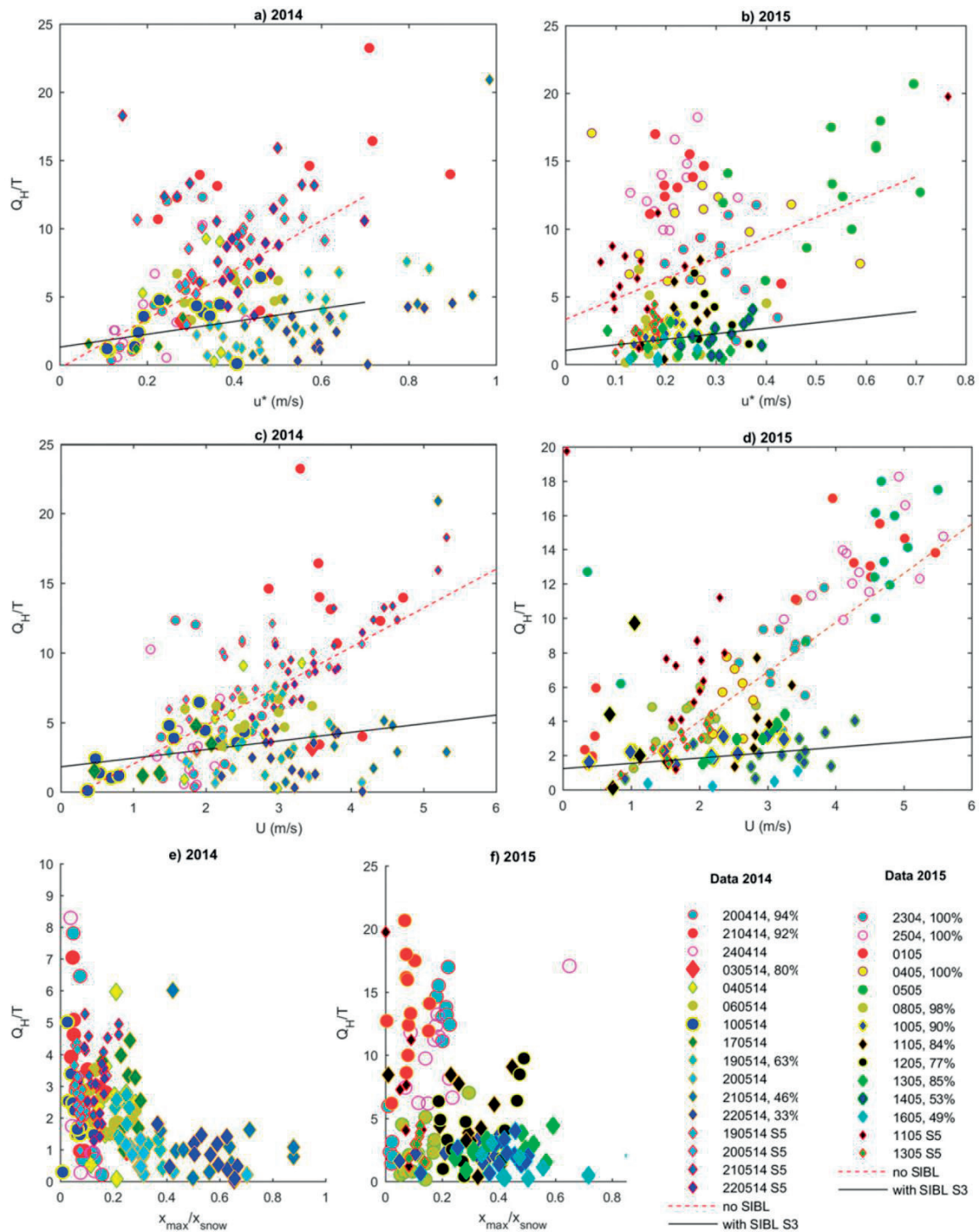
Fig A.8 Turbulent sensible heat fluxes normalized by air temperature plotted against (a), (b) friction velocity and (c), (d) mean wind velocity for data obtained in ablation periods 2014 and 2015. We distinguish between days with evidence of SIBL formation (diamonds) and days without SIBL formation (circles) captured by the sensors. (e), (f) Relation between distances of maximum flux contribution relative to wind fetch distance over snow (xmax/xsnow) is shown.

To minimize the effect of the snow-free areas on the turbulence measurements over snow, we add available measurements at the lowest measurement level above ground (S5) to the analysis featuring much lower maximum distances of flux contribution (Figs. A.8e,f). Sensors at this measurement height are thus assumed to be less affected by turbulence advected from upwind snow-free areas. While in 2014 data obtained at the 0.3 m measurement level (S5) are available for four analysed ablation days, only two days with SIBL evidence were recorded by S5 in 2015. The stability parameter and friction velocity measured at the midlevel sensor

height during days with SIBL evidence is compared against low-level measurements in Fig. A.9. Turbulent momentum and vertical turbulent heat fluxes within the stable internal boundary layer are expected to increase with decreasing distance to the snow surface (Essery et al., 2006; Mott et al., 2016). Data at 0.3 m above ground reveal significantly higher normalized turbulent sensible heat fluxes than the upper sensors reflecting the increasing temperature gradients with decreasing distance to the snow surface. At the same time, friction velocities decrease and stability parameters increase toward the 0.3-m measurement level (Fig. A.9). Consequently, warm air advection causes a decrease in atmospheric stability and an increase in friction velocity at the upper atmospheric levels of the SIBL. Some of the measurements even show slightly unstable atmospheric conditions at 0.7–1.6 m above ground. At the same time, atmospheric stability is high within atmospheric layers adjacent to the snow surface, coinciding with a suppression of friction velocity (Fig. A.9). The increase in friction velocity at higher levels is a sign of the presence of a shear layer at the upper levels of SIBL associated with a low-level jet.
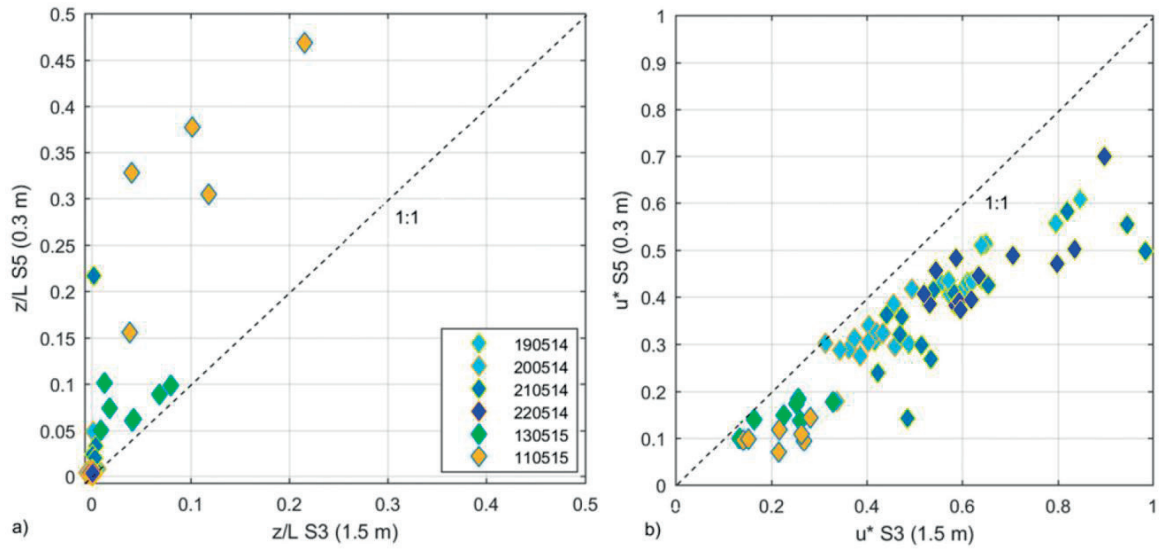

Fig A.9 (a) Stability parameter z/L and (b) friction velocity measured at midlevel sensor S3 plotted against z/L and friction velocity measured at low-level sensor S5.

A.3.5 Modelling turbulent heat exchange over an extremely heterogeneous snow cover in spring

Modelled turbulent heat fluxes using four different stability corrections are compared against measured turbulent heat fluxes in Fig. A.10. The analysis of turbulence data measured at different measurement heights showed a strong dependence of heat exchange processes over snow on the fetch distance over snow relative to the footprint at the measurement height. We expect that this strong dependency makes the comparison between modelled sensible heat fluxes at the snow surface and measured sensible heat fluxes at 0.7–2.2 m above ground strongly sensitive to SIBL occurrence.
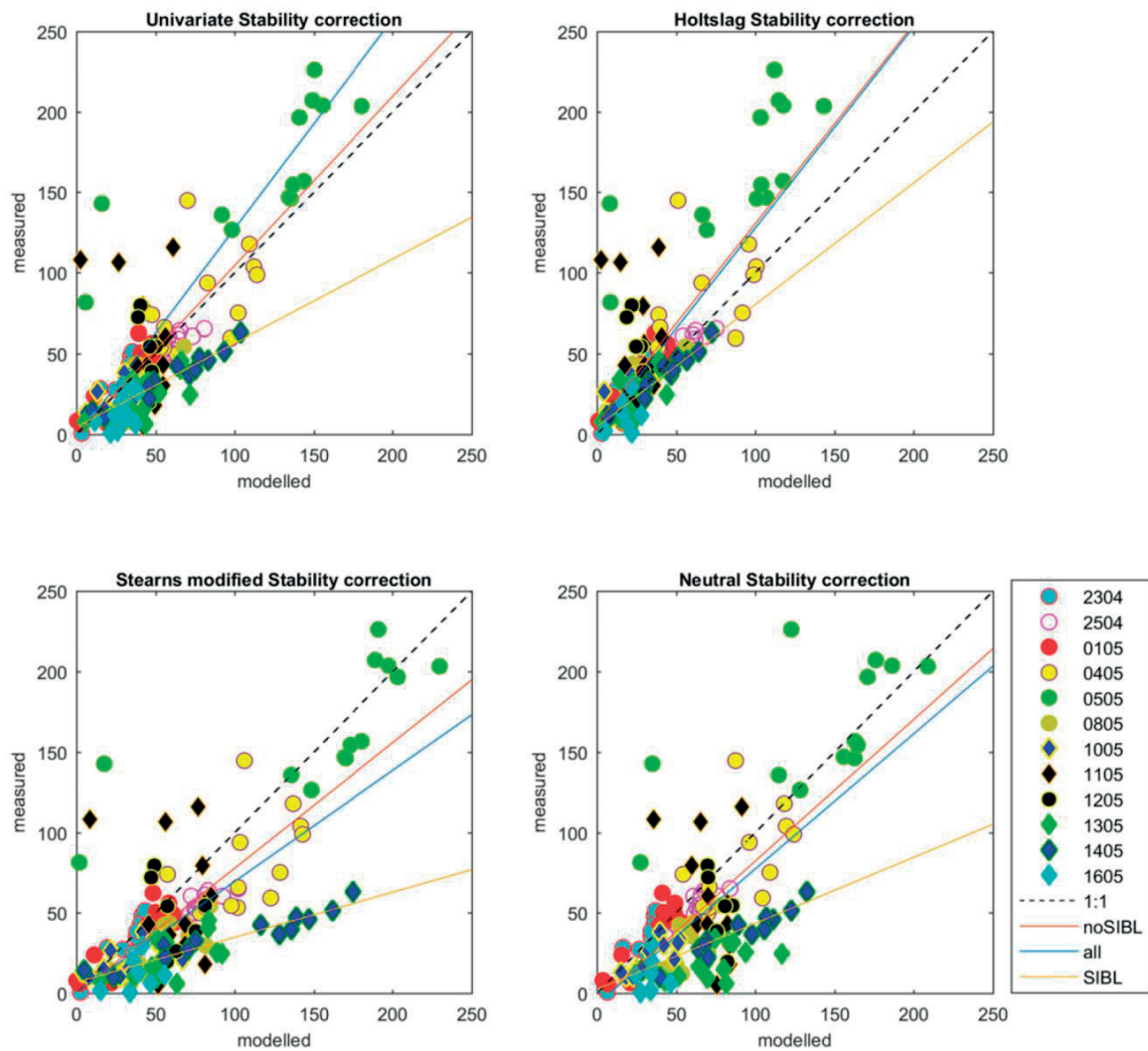
Fig A.10 Comparison between measured midlevel sensible heat flux (S3) and modelled sensible heat flux applying four different stability corrections: Univariate, Holtslag, Stearns modified, and neutral atmosphere.

During situations with a small vertical variability of downward turbulent heat fluxes within the first meters above ground, model results strongly depend on the applied stability correction as already discussed in Dadic et al. (2013) and Schlögl et al. (2017). Applying heat flux parameterizations of Stearns and Weidner (1993) (modified by Michlmayr et al., 2008) and using a neutrally forced boundary layer lead to predicted turbulent heat fluxes at the surface higher than measured at midlevel sensor height (Fig. A.10). Applying the univariate parameterization of heat fluxes (Schlögl et al., 2017) in the energy balance model even leads to smaller predicted turbulent heat fluxes at the snow surface compared to measurements. On the other hand, for situations with strong flux divergence, when the assumption of a constant flux layer totally fails [difference of sensible heat fluxes of two different vertical measurement levels is smaller than 10 % according to Stull (1988)], all models predict much higher sensible heat fluxes at the snow surface than measured at 1.6 m above the surface. This large bias results from the use of the Monin–Obukhov theory in the model for situations when constant flux layers and fully developed boundary layers do not exist. The difference for situations with SIBL occurrence is significantly reduced if model results are compared against measured sensible heat fluxes at 0.3 m above ground (Fig. A.11).
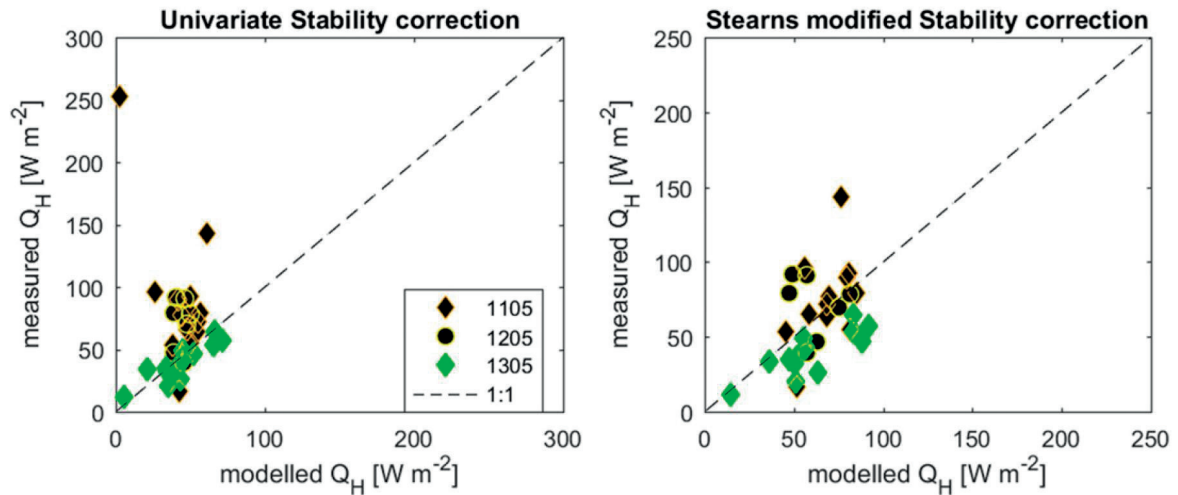
Fig A.11 Comparison between measured low-level sensible heat flux (S5) and modelled sensible turbulent heat flux at the surface applying univariate and modified Stearns stability correction.

A.4   Discussion

Turbulence data of three ablation periods show that the ablation period can be divided into three stages of snow cover distribution, considerably driving the boundary layer development and associated heat exchange at the snow cover: complete snow cover, presence of a clear snow line, and patchy snow cover distribution. Depending on winter snow cover distribution with respect to the elevation difference within the test site, an ablation season is either dominated by the snow line stage (i.e., strong elevation gradient in winter snow accumulation) or the patchy snow cover stage (i.e., small elevation gradient in winter snow accumulation). Typical mountain catchments with strong elevation gradients will typically be dominated by the snow-line stage in the early and middle stage of the ablation period. During this period, profiles of turbulent sensible heat strongly respond to the prevailing wind direction, as already found by Mott et al. (2013), with a similar snow cover distribution featuring a distinct snow line in the investigation area. For these catchments, the patchy snow cover stage is typically restricted to the late stage of the ablation period with a predominance of shallow stable internal boundary layer development above snow for all prevailing wind directions. Conversely, subpolar and polar regions will be dominated by the patchy snow cover stage over a major part of the ablation period. For these regions, which are characterized by small elevation differences and where wind transport of snow leads to often strongly varying snow depths at the beginning of the ablation season (e.g., Liston, 1999), thermal internal boundary layers typically develop as soon as the snow becomes patchy and fetch distances over snow become smaller than the flux footprint close to the snow surface. The internal thermal boundary layer development is connected with decoupling of the near-surface air from the warmer surrounding air. Decoupling of near-surface air is revealed by the data showing lower friction velocity and an increase in atmospheric stability close to the ground and high friction velocities at the top of the stable internal boundary layers, indicating the presence of a shear layer at the top of the stable internal boundary layer, similar to what has been hypothesized by Fujita et al. (2010) and what has been observed during wind tunnel experiments (Mott et al. 2016) and numerically investigated over snow patches (Mott et al., 2015).

The experimental and numerical findings show how heterogeneous land surfaces produce very unsteady boundary layers leading to a very high horizontal and vertical variability in turbulent fluxes above snow. The strong contribution of the upwind source area to the profiles of turbulent fluxes over snow has strong implications for hydrological modelling as soon as the snow cover becomes patchy. Measured air temperatures and wind velocities at single points are typically not in balance with the air adjacent to the snow cover, and thus flux predictions will be wrong. The comparison between modelled and measured turbulent sensible heat fluxes highlight the strong sensitivity of eddy covariance measurements over patchy snow cover on the measurement height, the associated footprint, and the snow cover distribution. The difference between model prediction and measured turbulent sensible heat flux increases with decreasing snow cover fraction and with increasing measurement height at the same time (i.e., increasing footprint of sensors). A comparison between predicted turbulent sensible heat fluxes at the snow surface to measured fluxes at measurement heights with footprints similar to the fetch distance over snow leads to model errors. These model errors thus become much larger than for stable conditions over continuous snow covers (e.g., Schlögl et al., 2017), who showed that the largest model errors stem from applying the Monin–Obukhov bulk formulation.

This paper mainly addresses local fluxes and does not try to synthesize the effect on large-scale models, which will be addressed in future work by explicit meteorological modelling. Although there are a number of regional and global model approaches applying subgrid fractional snow cover parameterizations (Roesch et al., 2001; Liston, 2004; Takata et al., 2003; Essery, 2008; Dutra et al., 2010; Best et al., 2011; Nitta et al., 2014), the interaction between the fractional snow cover and the overlying snow is still highly simplified. Applying simple gradient–flux relationships over patchy snow cover leads to large biases in flux estimates, which need to be addressed in regional models in particular.

A.5 Conclusions

This study presents a unique set of eddy covariance measurements obtained during three entire ablation periods. Turbulence stations consisted of two turbulence towers equipped with five ultrasonic anemometers with different pathlengths suitable to measure turbulence at different atmospheric levels. The combination with high-resolution measurements of snow cover distribution and snow surface temperatures allowed investigation of the highly complex interactions among the gradually increasing heterogeneity of land surface in spring, the near-surface atmospheric boundary layer flow, and turbulent heat exchange between the melting snow cover and the adjacent atmosphere.

The experimental study gives clear evidence on the feedback between the change in land surface variability during the course of an ablation season, the atmospheric boundary layer flow, and the heat exchange over snow. Measurements show that as soon as sun-exposed slopes in the surrounding the test site become snow-free in the ablation season, thermal contrasts stimulate the onset of a mountain valley–wind system under fair undisturbed weather. The resulting increase in wind velocity associated with the diurnal up-valley flow significantly drives the diurnal cycle of turbulent heat fluxes above the melting snow cover. Furthermore, temporally and spatially highly resolved snow surface temperature maps obtained from an IR camera indicate the formation of very small-scale drainage flows over long-lasting snow fields significantly changing the local snow cover warming and inducing a high spatial variability of snow surface temperatures, especially in the morning hours. These experiments confirm earlier numerical studies at different scales (Segal et al., 1991; Mott et al., 2015) that suggested the development of thermally driven boundary layer flows over large snow patches and an associated effect on the local energy balance over snow for fair weather conditions.

Experimental results impressively demonstrate the strong influence of land surface variability on the turbulent flux profiles measured at single points. Snow cover distribution is shown to be of vital importance for the frequency of thermal boundary layer development. We have identified three stages of snow cover distribution considerably driving the boundary layer development during the ablation period: complete snow cover, presence of a clear snow line, and patchy snow cover distribution. An ablation season is either dominated by the snow line stage or the patchy snow cover stage. The snow line stage is dominant in regions with a strong elevation gradient in winter snow accumulation or large altitudinal differences within the test site. The patchy snow cover stage is dominant in areas characterized by a small elevation gradient in winter snow accumulation or a small altitudinal difference within the test site. Deep stable boundary layers are predominantly found as long as the snow cover is complete. As soon as a clear snow line progresses from lower elevations toward the test site, the development of unsteady and shallow thermal boundary layers is strongly dependent on the prevailing wind direction. Typically, in the late stage of a melting period, when the snow cover becomes patchy, thermal boundary layers develop for all prevailing wind directions and the internal boundary layer height decreases to lower than 0.3 m.

Profiles of turbulent sensible heat exchange over a long-lasting snow patch clearly reveal a locally unsteady boundary layer during the last two stages of a melting period (snow line and patchy snow cover). The formation of thermal internal boundary layers at the Gletschboden is favored during situations forcing the advection of warmer air from snow-free toward snow-covered areas. Data reveal turbulent sensible heat flux profiles featuring a high flux divergence, even showing different signs of the fluxes in the first 2 m above the ground. Eddy covariance measurements at 1.5 m above ground reveal significantly smaller downward turbulent heat fluxes for situations with evidence of stable internal boundary layer development. For these situations, the sensible heat fluxes increased at the lowest atmospheric levels above snow, revealing a very shallow layer adjacent to the snow cover decoupled from the warm-air advection above. At the same time, friction velocities are shown to be significantly smaller at the lowest atmospheric level (0.3 m above surface), coinciding with a strong increase in atmospheric stability there. The increase in friction velocity at higher atmospheric levels is an indication for the presence of a shear layer at the top of the stable internal boundary layer similar to what has been observed during wind tunnel experiments (Mott et al., 2016) and for numerical investigations over snow patches (Mott et al., 2015).

Experimental findings show that extremely heterogeneous land surfaces induce high horizontal and vertical variability in turbulent fluxes above snow. The strong contribution of the upwind snow-free areas on the heat exchange between snow cover and the overlying atmosphere has strong implications for hydrological modelling covering an entire ablation season. Using simple parameterizations of subgrid snow cover fractions and applying simple gradient–flux relationships at the same time might lead to large biases in flux estimates that need to be addressed by regional models in the future.

Curriculum Vitae: Sebastian Schlögl

Tschuggenstrasse 7

CH-7260 Davos Dorf

Switzerland

phone: +41 76 75 22 833

Email: sebastian.schloegl86@web.de

Date of birth: 25.11.1986 in Wiesbaden, Germany

Marital status: unmarried

Education

04/2014 – 03/2018   **PhD student in meteorology**

WSL Institute for Snow and Avalanche Research SLF, Switzerland and EPFL, Lausanne, Switzerland

- Organisation of different field campaigns, data acquistion, numerical modelling and evaluation of the energy balance of a snow pack during the ablation period

- Several ISI-publications, presentations and contributions to international conferences
- Supervising tutor for the course „*Snow Physics and Hydrology*" at the EPFL

03/2007 – 11/2012   **Diploma student in meteorology**

Johannes Gutenberg University Mainz, Germany

- Diploma thesis: Atmospheric transport from MOPITT-CO data (grade: very good)
- Degree: Diploma meteorologist (grade: very good)

08/2003 – 06/2006   **Martin Niemöller secondary school, Wiesbaden, Germany**

- Graduation: general qualification for university entrance

09/1993 – 07/2003   **Theisstal school, Niedernhausen, Germany**

Work experience

06/2013 – 03/2014   **Research scientist, Research Group Snow cover and Micrometeorology, WSL Institute for Snow and Avalanche Research SLF, Switzerland**

- Analysis of snow depth sensitivities in the hydrological model Alpine3D in relation to modifications of the DEM resolution, station coverage and meteorological input parameter

12/2012 – 05/2013   **Internship, Research Group Snow cover and Micrometeorology, WSL Institute for Snow and Avalanche Research SLF, Switzerland**

- Analysis of climatological changes in the snow depth for the Swiss canton Grisons within the scope of the CH2014 Impacts report

Seit 2014   **Observer, WSL Institute for Snow and Avalanche Research SLF, Switzerland**

- Experimental measurements of several different snow parameter at the high-alpine station Weissfluhjoch during around 20 days in a year
- Measuring an Alpine snow cover with a SnowMicroPen

07/2006 – 03/2007   **Community service, Educational center Oberjosbach, Germany**

Courses and certificates

11/2015   Course *Medientraining für Forschende*, F. Allenspach, MAZ – Swiss school for journalists, Switzerland

06/2015   Course *Effective scientific presentations*, J. van Woerden, Eidg. Forschungsanstalt für Wald, Schnee und Landschaft WSL, Schweiz

03/2015   Course *Writing scientific English*, S. Dingwall, Swiss Federal Institute for Forest, Snow and Landscape Research WSL, Switzerland

03/2014 – 06/2014   Courses *Introduction intro R / Scientific visualisations using R*, J. Wunder, Swiss Federal Institute for Forest, Snow and Landscape Research WSL, Switzerland

Seit 2012   Repeated avalanche rescue courses and safety in alpine terrain, WSL Institute for Snow and Avalanche Research SLF, Switzerland

Knowlegde and skills

Languages	German: mother tongue
	English: Very good in written and spoken
Computer science	Operating system: Windows, Linux/Unix
	Programming: C++, IDL
	Data analyses: R, Matlab
	Application software: MS Office, Latex
	Other: ArcGIS
Measurements	Perennial experience in planning, organisation and exection of reaseach campaigns in alpine terrain: terrestrial laser scanning, eddy-covariance measurements, infrarot camera and the assistance and maintenance of meteorological stations
Numerical simulations	Perennial experience with the snow cover model SNOWPACK, with the hydrological model Alpine3D and with the atmospheric model ARPS
Expertise	atmospheric processes in the boundary layer, satellite data, climate change

Awards and fellowships

- SEP travel grant for young scientists for conferences: SGM 2016
- Research fellowship for the Diploma thesis
- ERASMUS fellowship for a term abroad in Svalbard/Norway (01/2011- 06/2011)

Interests and activities

- triathlon, table-tennis, travelling
- Membership at the German Meteorological Society (DMG) since 2010

References

- Prof. Michael Lehning, EPFL Lausanne, CRYOS School of Architecture, Civil and Environmental Engineering, Schweiz and Head of the Research Unit Snow and Permafrost, WSL Institute for Snow and Avalanche Research SLF, Switzerland, Phone: +41 81 417 01 58, Email: lehning@slf.ch

- Rebecca Mott, Karlsruhe Institute of Technology, Institute of Meteorology and Climate Research, Atmospheric Environmental Research (IMK-IFU), Garmisch-Partenkirchen, Germany, Phone: +49 8821 183 135, Email: rebecca.mott-gruenewald@partner.kit.edu

ISI publications

Schlögl, S., Lehning, M., Nishimura, K., Huwald, H., Cullen, N. J., and Mott, R. (2017) How do stability corrections perform in the stable boundary layer over snow?, Boundary-Layer Meteorology, 165,161-180.

Schlögl, S., Marty, C., Bavay, M., and Lehning, M. (2016) Sensitivity of Alpine3D modelled snow cover to modifications in DEM resolution, station coverage and meteorological input quantities. Environmental Modelling and Software, 83, 387-396.

Mott, R., **Schlögl, S.**, Dirks, L., and Lehning, M. (2017) Impact of extreme land-surface heterogeneity on micrometeorology over spring snow-cover, J. Hydrometeor., 18(10), 2705-2722.

Marty, C., **Schlögl, S.**, Bavay, M., and Lehning, M. (2017) How much can we save? Impact of different emission scenarios on future snow cover in the Alps, The Cryosphere, 11(1), 517-529.

Marty, C., Abegg, B., Bauder, A., Marmy, A., Lüthi, M. P., Bavay, M., Hauck, C., Hoelzle, M., Huss, M., Salzmann, N., **Schlögl, S.**, Steiger, R., and Farinotti, D. (2014) Cryospheric aspects of climate change – impacts on snow, ice and ski tourism, Chapter in CH2014 – Impacts: Toward quantitative scenarios of climate change Impacts in Switzerland, pp. 49-56.

Baker, A. K., Traud, S., Brenninkmeijer, C., Hoor, P., Neumaier, M., Oram, D. E., Rauthe-Schöch, A., Sprung, D., **Schlögl, S.**, Slemr, F., van Velthoven, P., Wernli, H., Zahn, A., and Ziereis, H. (2014) Pollution patterns in the upper troposphere over Europe and Asia observed by CARIBIC, Atmospheric Environment, 96, 245-256.

Yoon, J., Pozzer, A., Hoor, P., Chang, D. Y., Beirle, S., Wagner, T., **Schlögl, S.**, Lelieveld, J., and Worden, H. M. (2013) Technical Note: Temporal change in averaging kernels as a source of uncertainty in trend estimates of carbon monoxide retrieved from MOPITT, Atmospheric Chemistry and Physics, 13(22), 11307-11316.

Conference Contributions

(only first-autor)

Schlögl, S., Mott, R., and Lehning, M. (2017) Energy balance and melt over a patchy snow cover, Poster, In: *15th Swiss Geoscience Meeting*, Davos, Switzerland.

Schlögl, S., Mott., R., and Lehning, M. (2017) How do patchy snow covers affect turbulent sensible heat fluxes? – Numerical analysis and experimental findings, PICO, In: *EGU General Assembly Conference Abstracts*, EGU, Vienna, Austria.

Schlögl, S., Mott, R., and Lehning, M. (2016) Energy balance and melt over a patchy snow cover, Poster, In: *14th Swiss Geoscience Meeting*, Geneva, Switzerland.

Schlögl, S., Mott, R., and Lehning, M. (2016) How do stability corrections perform over snow?, Poster, In: 73*th Eastern Snow Conference (ESC)*, Columbus, United States.

Schlögl, S., Mott, R., and Lehning, M. (2016) Energy balance and melt over patchy snow covers, Vortrag, In: 73*th Eastern Snow Conference (ESC)*, Columbus, United States.

Schlögl, S., Mott, R., and Lehning, M. (2016) Energy balance and melt over patchy snow covers, Poster, In: *22nd Symposium on Boundary Layers and Turbulence*, Salt Lake City, United States.

Schlögl, S., Mott., R., and Lehning, M. (2015) Investigation of a new approach for a stability correction in complex terrain, Vortrag, In: *EGU General Assembly Conference Abstracts*, EGU, Vienna, Austria.

Schlögl, S., Mott., R., and Lehning, M. (2015) Investigation of a new approach for a stability correction in complex terrain, Vortrag, In: *EGU General Assembly Conference Abstracts*, EGU, Vienna, Austria.

Schlögl, S., Mott., R., and Lehning, M. (2015) Modelling turbulent fluxes over snow during events of constant flux layers, Vortrag, *26th IUGG General Assembly,* Prague, Czech Republic.

Schlögl, S., Marty, C., Bavay, M., and Lehning, M. (2013), Assessment of future snow pack in two Alpine regions, Poster, *C2SM Symposium "The Water Cycle in a Changing Climate",* Zürich, Switzerland.